Driven Dynamics and Pattern Formation in Bose-Einstein Condensates

विद्या वाचस्पति की
उपाधि की अपेक्षाओं की आंशिक पूर्ति में प्रस्तुत शोध प्रबंध

A thesis submitted in partial fulfillment of the requirements for the degree of Doctor of Philosophy

द्वारा / By

सांद्रा मरिया जोस/ Sandra Maria Jose

पंजीकरण सं. / Registration No.: 20182015

शोध प्रबंध पर्यवेक्षक / Thesis Supervisor:

डॉ. रेजिश नाथ / Dr. Rejish Nath

IISER PUNE

भारतीय विज्ञान शिक्षा एवं अनुसंधान संस्थान पुणे

INDIAN INSTITUTE OF SCIENCE EDUCATION AND RESEARCH PUNE

2025

CERTIFICATE

Certified that the work incorporated in the thesis entitled **"Driven dynamics and pattern formation in Bose-Einstein condensates"** submitted by **Sandra Maria Jose** was carried out by the candidate under my supervision. The work presented here or any part of it has not been included in any other thesis submitted previously for the award of any degree or diploma from any other university or institution.

Date:

Dr. Rejish Nath
(Supervisor)

Declaration of Authorship

Name of Student	: Sandra Maria Jose
Reg. No.	: 20182015
Thesis Supervisor	: Dr. Rejish Nath
Department	: Physics
Date of joining program	: August 01, 2018
Date of Pre-Synopsis Seminar	: May 28, 2025

Title of Thesis: Driven dynamics and pattern formation in Bose-Einstein condensates

I declare that this written submission represents my idea in my own words and where others' ideas have been included; I have adequately cited and referenced the original sources. I declare that I have acknowledged collaborative work and discussions wherever such work has been included. I also declare that I have adhered to all principles of academic honesty and integrity and have not misrepresented or fabricated or falsified any idea/data/fact/source in my submission. I understand that violation of the above will be cause for disciplinary action by the Institute and can also evoke penal action from the sources which have thus not been properly cited or from whom proper permission has not been taken when needed.

The work reported in this thesis is the original work done by me under the guidance of Dr. Rejish Nath.

Date: 31-07-2025

Signature:

This thesis is dedicated to Amma

Acknowledgements

I would like to begin by expressing my gratitude to my supervisor, Dr. Rejish Nath, for his guidance, encouragement, and support throughout the course of this work. His insights and constant motivation were instrumental in shaping this thesis and bringing it to completion. I would also like to thank my RAC members, Dr. Sachin Jain and Dr. Sreejith G. J., for their valuable feedback and advice. I am grateful to Dr. Aparna Deshpande for her guidance and support during my first year at IISER. I extend my thanks to all my teachers, especially Dr. Sreejith G. J. and Prof. Deepak Dhar, who were the most influential during my master's period, and to Dr. Muhammed Ashefas, for being a motivating presence during my BSc days.

During my PhD, I was fortunate to work with many peers. I thank Salman, Gautam, Ashutosh, Lokesh, Shreyas, Ratheejit, Inderpreet, and Vaishakh for their valuable contributions to this work, both direct and indirect. I would also like to thank all my past and present group members, who formed the core part of my PhD experience. I am especially grateful to my seniors Chinmayee, Yashwant, and Ankita for welcoming me into a supportive environment and for being people I could always look up to. I also thank Varna, Dhiya, Siddharth, Nargis, Pranay, Gopal, Paramjeet, Pritam, Anupam, Shobhana, Soham, and Ashwath for creating and maintaining the crazy group spirit, without which this journey would have been completely dull, and for all their support and encouragement. I would like to express my heartfelt gratitude to all my other friends; Saurabh, Basava, Shikha, Narayanan, Sajid, Charu, Vishal, Vrinda, Gokul, Snigdha, Sudiksha, and Abhishek, for making my stay at IISER a wonderful experience.

I wish to thank Imran and Inderpreet for being the older siblings I never had, and Ratheejit for being my best friend and a constant calming presence during tumultuous times. Finally, I would like to thank my family for their unwavering support, my father, for first instilling in me a love for science and encouraging me to embark on this journey; my brother and sisters, for being my pillars throughout life; my mother, for all her love and sacrifice; and my grandmother, whose strength set an enduring example for me.

List of Publications

Included in the thesis

1. **Sandra M. Jose**, Komal Sah, and Rejish Nath, *Patterns, spin-spin correlations, and competing instabilities in driven quasi-two-dimensional spin-1 Bose-Einstein condensates*, Phys. Rev. A **108**, 023308 (2023)

2. **Sandra M. Jose**, Indepreet Kaur, and Rejish Nath, *Excitation of radial modes and pattern formation in driven cylindrical BEC*, *Manuscript under preparation

3. Vaishakh Kargudri, **Sandra M. Jose**, and Rejish Nath, *Faraday patterns, spin textures, spin-spin correlations and competing instabilities in a driven spin-1 antiferromagnetic Bose-Einstein condensate*, arXiv:2510.08087, (2025)

Not included in the thesis

1. Gautam Hegde, **Sandra M. Jose**, and Rejish Nath, *Dynamics of a pair of overlapping polar bright solitons in spin-1 Bose-Einstein condensates*, Phys. Rev. A **106**, 043307 (2022)

2. Shreyas Nadiger, **Sandra M. Jose**, Ratheejit Ghosh, Inderpreet Kaur, and Rejish Nath, *Stripe and checkerboard patterns in a stack of driven quasi-one-dimensional dipolar condensates* , Phys. Rev. A **109**, 033309 (2024)

Abstract

Periodic modulation of interaction strength or external trap can create spontaneous formation of patterns in a Bose-Einstein condensate (BEC), arising from the excitation of its elementary modes. This thesis explores the dynamics of two condensate systems under periodically modulated interactions: a cylindrically confined spin-0 BEC and a homogeneous spin-1 spinor BEC.

In elongated traps, periodic driving of interaction induces spontaneous longitudinal density waves. Experiments have shown that driving the system at its transverse breathing mode frequency leads to density wave formation even at very weak modulation strength, due to coupling between transverse and longitudinal motion. We generalize this phenomenon by deriving resonance conditions for the excitation of radial modes, in a cylindrically confined BEC. These resonances are the precursor for longitudinal pattern formation, which are created as the resonantly excited radial modes spontaneously decay to lower branches of excitation spectra. Resonantly excited transverse breathing mode always decays to form longitudinal density waves. The second resonantly excitable radial mode can decay to create density waves at weaker interactions and centre-of-mass oscillations (zig-zag pattern) at larger interactions. Away from radial resonances, pattern formation occurs via second-order parametric resonance, producing density waves at the quasi-one-dimensional limit of interaction, but can also excite centre-of-mass oscillations at larger interactions.

Spin degrees of freedom significantly influence the dynamics of a driven spin-1 BEC. Condensate initialized in the ferromagnetic phase behaves like a spin-0 BEC and exhibits transient density patterns under periodic driving. We observe density and spin pattern formation in the condensate in polar and antiferromagnetic (AFM) phases. The pattern wavelength at a given driving frequency can be predicted from the Bogoliubov spectrum. Competition between density and spin dynamics exists, and the dominant process depends on the relative strength of spin-independent and spin-dependent interactions. In the polar phase, spin-density waves give rise to transverse spin textures featuring vortices and antivortices, and the radial spin-spin correlation follows a Bessel function. In the AFM phase, driving at a frequency less than the spin-mode gap creates domain structures, while higher driving frequencies lead to vortex–antivortex formation.

Contents

Acknowledgements **ix**

List of Publications **xi**

Abstract **xiii**

1 Introduction **1**

2 Background and theory **7**

2.1 Ideal Bose-Gas 7
2.2 Two-body interaction 8
2.2.1 Feshbach resonances 9
2.3 Mean-Field theory of Bose-Einstein condensate 11
2.3.1 Bogoliubov-de Gennes equation 13
2.4 Quasi-one and -two dimensional condensates 13
2.5 Bogoliubov theory 14
2.5.1 Uniform BEC 15
2.5.2 Non-uniform gas 16
2.6 Spinor BEC 18
2.6.1 Mean-field theory 21
2.6.2 Quantum phases of homogenous gas 22
2.6.3 Elementary excitations in spinor BEC 25
2.7 Floquet theory 25
2.7.1 Proof of Floquet theory 27
2.7.2 Mathieu equation 28
2.8 Faraday waves in driven condensate 29
2.8.1 Quasi-two dimensional spin-0 condensate 30
2.8.2 Quasi-two dimensional spinor condensate in ferromagnetic phase . 32

3 Excitation of radial modes and pattern formation in driven cylindrical BEC **35**

3.1 Introduction 35
3.2 Cylindrically confined Bose-Einstein condensate 36
3.3 Bogoliubov spectrum 37

3.4 Dynamics of modes under driven interaction 40
3.4.1 Excitation of radial modes 40
3.4.2 Decay of the excited modes 43
3.5 Numerical simulation using GPE 46
3.5.1 Excitation of the monopole mode 46
3.5.2 Excitation of $n_r = 2$ radial mode 47
3.6 Comparison: GPE numerics and analytical results 52
3.7 Conclusion 53

4 Parametric resonances in a cylindrically confined BEC 55
4.1 Introduction 55
4.2 System 56
4.3 Quasi-one-dimensional driven BEC 57
4.3.1 Linear stability analysis of mean-field solution 57
4.3.2 Bogoliubov theory calculation 59
4.4 Theory of driven condensate in three-dimensions 61
4.4.1 Floquet theory approach 62
Interactions beyond Q1D limit 66
4.4.2 Linear stability analysis of the mean-field solution 66
4.5 Driven dynamics in the Q1D limit of interaction 70
4.6 Beyond the Q1D limit of interaction 73
4.7 Conclusion 76

5 Faraday and spin waves in Q2D spin-1 BEC in polar phase 77
5.1 Introduction 77
5.2 Setup 78
5.2.1 System 78
5.2.2 Polar phase 79
5.3 Periodically driven scattering length 80
5.4 Details of numerical simulation 81
5.5 Linear stability analysis of driven state 81
5.6 Modulation of a_0 scattering length 83
5.6.1 Mathieu equations 83
5.6.2 Degenerate density and spin branches 84
5.7 Non-degenerate spin and density modes 88
5.7.1 Non-zero quadratic Zeeman term 89
5.8 Modulation of a_2 scattering length 89
5.8.1 a_2 Modulation: Mathieu equations 90
5.9 Simultaneous modulation of two scattering lengths 91

5.9.1 c_0 modulation . . . 91
5.9.2 c_1 modulation . . . 92
5.9.3 Competing instabilities . . . 93
5.10 Experimental considerations . . . 95
5.11 Conclusion . . . 96

6 Pattern formation in driven spin-1 BEC in AFM phase **97**
6.1 Introduction . . . 97
6.2 Anti-ferromagnetic phase . . . 98
6.2.1 Quasi-one- and quasi-two-dimensional systems . . . 100
6.3 Periodic driving of the scattering length . . . 100
6.4 GPE simulation . . . 103
6.5 Driven Q1D BEC . . . 104
6.5.1 Modulation frequency less than spin-mode gap . . . 104
6.5.2 Modulation frequency greater than the spin-mode gap . . . 105
6.5.3 Spin-spin correlation in quasi-1D condensate . . . 108
6.6 Driven quasi-2D condensate . . . 108
6.7 a_2 Modulation . . . 112
6.8 Modulation of both frequency . . . 112
6.9 Conclusion . . . 114

7 Summary and Outlook **117**

A Hamiltonian transformation in Bogoliubov basis **121**
A.1 Bogoliubov basis . . . 123

B Floquet theory calculation **125**
B.1 Mathieu equation . . . 125
B.2 Floquet exponent . . . 125

C Properties of $\hat{\mathcal{L}}_Q$ operator **129**

Bibliography **131**

List of Figures

1.1 Spontaneous density wave formation in an elongated ^{7}Li condensate. Figure reproduced from Ref. [124] . . . 2

1.2 Pattern formation in BEC of Cs atoms. Figure reproduced from Ref. [201] with permission from Springer Nature . . . 3

1.3 Star shaped pattern formation in driven ^{7}Li BEC.Reprinted figure with permission from [96]. Copyright (2021) by the American Physical Society. . . 4

2.1 (a)Schematic of open and closed channel interaction potential. (b)Variation of s-wave scattering length near a Feshbach resonance . . . 10

2.2 Phase diagram of homogeneous spin-1 BEC for spin-dependent interaction coefficient (a) $c_1 > 0$ and (b) $c_1 < 0$. . . . 23

2.3 Stability diagram for Mathieu equation (2.69) . . . 29

2.4 Formation of Faraday waves in QDS driven spin-0 condensate. . . . 31

2.5 Formation of Faraday waves in driven spin-1 spinor condensate in ferromagnetic phase . . . 34

3.1 Schematic of the setup . . . 37

3.2 The Bogoliubov spectrum of the cylindrically trapped condensate . . . 38

3.3 Density patterns under excitation of the modes from (a) gapless density ($\omega_{0,0}$) branch and (b) dipole ($\omega_{0,\pm1}$) branch. . . . 39

3.4 The excitation coefficient $\bar{\mathcal{F}}_{n_r}$ . . . 43

3.5 Decay of excited radial modes . . . 44

3.6 GPE results for transverse monopole mode excitation . . . 48

3.7 GPE results for transverse $n_r = 2$ mode excitation (Fig I) . . . 49

3.8 GPE results for transverse $n_r = 2$ mode excitation (Fig II) . . . 51

3.9 GPE results for transverse $n_r = 2$ mode excitation (Fig III) . . . 52

4.1 Mean-field evolution driven condensate of RMS radius in the xy-plane of the condensate under periodic driving . . . 61

4.2 Floquet theory results driven condensate in Q1D limit of interactions. . . . 65

4.3 Dynamics of population $\delta N_{\nu,k_z}(t)$ for Q1D limit of interaction . . . 71

4.4 The dynamics of the most unstable modes with $\nu = 0$ and $\nu = \pm1$ at Q1D limit of interaction . . . 71

4.5 The integrated densities $n_z(x, y)$(left) and $n_x(z, y)$ (right) obtained from GPE evolution for Q1D limit of interaction 72
4.6 Momentum space linear density for Q1D limit of interaction 73
4.7 Dynamics of population $\delta N_{\nu,k_z}(t)$ for interaction beyond the Q1D limit . . . 74
4.8 The dynamics of the most unstable modes with $\nu = 0$ and $\nu = \pm 1$ beyond the Q1D limit of interaction 74
4.9 The integrated densities $n_z(x, y)$ (left) and $n_x(z, y)$ (right) obtained from GPE evolution for interaction beyond the Q1D limit. 75
4.10 Momentum space linear density for interaction beyond the Q1D limit . . . 76

5.1 The polar phase dispersion relation 79
5.2 Population dynamics under a_0 modulation 85
5.3 Density pattern formed under periodic driving of scattering length a_0 . . . 86
5.4 Spin textures formation under a_0 modulation 87
5.5 Vortex dynamics under modulation of scattering length. 88
5.6 Spin-spin correlations for a_0 modulation. 89
5.7 The population dynamics under modulation of the scattering length a_0: Non-degenerate modes. 90
5.8 Non-zero Zeeman terms. 91
5.9 The ratio of the density and spin Mathieu exponents $\sigma^{(0)}/\sigma^{(+)}$ under a_2 modulation 92
5.10 Modulation of c_1 alone. 93
5.11 Competing instability among the density modes 94
5.12 Competing instability among the spin modes 95

6.1 The Bogoliubov excitation spectra of homogeneous AFM condensate. Here, $c_0 > c_1$, and the gap of the spin-mode is indicated by Δ. 99
6.2 Driven Q1D condensate ($\hbar\omega_0 < \Delta_{1D}$) 105
6.3 Pattern formation in driven Q1D AFM condensate ($\hbar\omega_0 > \Delta_{1D}$) 106
6.4 Momentum space density dynamics in driven Q1D AFM condensate ($\hbar\omega_0 > \Delta_{1D}$) 106
6.6 Density pattern formation in driven Q2D AFM condensate ($\hbar\omega_0 < \Delta_{2D}$) . . 109
6.7 Spin pattern formation in driven Q2D AFM condensate ($\hbar\omega_0 > \Delta_{2D}$) 109
6.8 Spin texture in driven Q2D AFM condensate ($\hbar\omega_0 > \Delta_{2D}$) 110
6.9 Driven Q2D AFM condensate ($\hbar\omega_0 > \Delta_{2D}$): Radial correlation 111
6.10 Simultaneous modulation of a_0 and a_2: Spin-texture 113
6.11 Simultaneous modulation of a_0 and a_2: Floquet exponent 113
6.12 Simultaneous modulation of a_0 and a_2: Population dynamics 114

List of Abbreviations

AFM	Antiferromagnetic
BdG	Bogoliubov-de Gennes
BEC	Bose-Einstein Condensate
COM	Centre-of-mass
GPE	Gross-Pitaevskii Equation
PCV	Polar-core vortex
Q1D	Quasi-one-dimensional
Q2D	Quasi-two-dimensional
RMS	Root-mean-square
TWA	Truncated Wigner Approximations

Chapter 1

Introduction

At low enough temperatures, a gas of non-interacting bosons undergoes a phase transition in which a macroscopic fraction of particles occupies the same quantum state [45, 140]. This phenomenon, known as Bose-Einstein condensation, is among the most striking consequences of quantum mechanics. Although the Bose-Einstein condensate (BEC) was predicted in 1924, it remained elusive for many decades, as most atomic gases are too strongly interacting to undergo this transition. Nevertheless, the concept remained relevant, having been hypothesized to play a role in phenomena such as the superfluidity in helium and the superconductivity. A breakthrough occurred in 1995, when BECs were experimentally realized in weakly interacting alkali gases of rubidium [3], sodium [46], and lithium [19], by independent research groups. This achievement was made possible by decades of research progress in laser cooling and magnetic trapping of atoms [138, 190]. Since then, BECs were also realized using atoms with internal spin degrees of freedom (spinor BEC) [11, 168], mixture of different species or states of atoms [70, 71, 119], long-range interacting dipolar atoms [65, 107], and most recently, in polar molecules [10].

Early experiments in BEC focused on probing the fundamental properties of the condensate and its response to external perturbations [22, 166, 167]. BEC behaves as a single coherent matter wave rather than as a collection of individual atoms [90]. It exhibits phenomena such as interference [4], long-range phase coherence [14], and quantized vortices [2, 108], similar to those observed in superfluid helium and superconductors. A key development in the field was using Feshbach resonances [15, 35], which enabled tuning the interaction in the ultracold atoms using external magnetic or optical fields. Since the experimental realization of BEC, ultracold atomic systems have also proven useful in studying other areas of physics by providing a platform for quantum simulation. In a seminal experiment, the Bose-Hubbard model was realized using ultracold atoms in an optical lattice, where a quantum phase transition between the superfluid (condensate) and a strongly correlated Mott insulator phase was observed [64]. Since then, ultracold atoms have been used to simulate various theoretical models [44, 68, 110, 170].

Ultracold atomic systems possess features that make them exceptionally suitable for quantum simulations. They exhibit a high degree of tunability of system parameters through

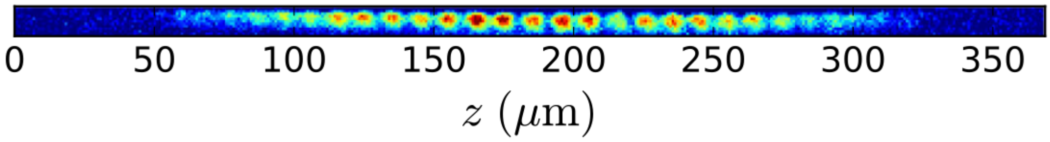

FIGURE 1.1: Spontaneous density wave formation in an elongated ^{7}Li condensate under periodic driving of s-wave scattering length. Reproduced from Ref. [124]

effective interactions and artificial gauge fields, excellent isolation from environmental decoherence, and slow dynamical timescales that allow precise control and observation. These characteristics also render them ideal for probing nonequilibrium quantum dynamics [141], including quantum quench dynamics [1, 78, 112, 149] and thermalization of isolated quantum many-body systems [38, 88, 91, 179]. Nonequilibrium dynamics also includes that of a periodically driven system. In certain scenarios, periodic driving of system parameters can be used to realize an effective Hamiltonian with desired properties. This is known as Floquet engineering [21, 48, 189]. Another class of periodically driven systems known as discrete time crystals exhibits unusually slow or a lack of thermalization and sub-harmonic response [196]. In this thesis, we are interested in the nonequilibrium dynamics of BEC under periodically modulated interactions, with particular emphasis on the spontaneous emergence of spatial patterns observed in them.

The formation of density patterns in BEC under periodic modulation of the interaction was first predicted by Staliunas et. al. [162]. This is analogous to the classical phenomena of Faraday waves observed standing wave patterns in the vertically shaken fluids [53, 114]. Both the classical Faraday wave and its quantum counterpart are sub-harmonic responses, i.e., the patterns themselves oscillate at half the driving frequency. The underlying mechanism that creates the pattern formation can be understood in terms of parametric resonance [61], where the surface modes of the fluid with natural frequencies half the driving frequency become resonantly excited.

Faraday waves in BEC were first observed experimentally in 2007 [49] in a condensate of ^{87}Rb atoms in an elongated trap. Here, they modulated the condensate's transverse trap, creating effective modulation of the interaction [163]. Under the periodic driving, spontaneous density modulations were created along the longitudinal direction, and the wavelength of the pattern decreases with increasing driving frequency. The relation between the pattern wavelength and the driving frequency gives us the dispersion relation of the longitudinal excitations of the condensate. Faraday waves are, thus, useful in probing the collective excitation of the condensate. In 2019, Faraday waves were observed in an elongated ^{7}Li condensate [124] by direct modulation of the s-wave scattering length of the system using Feshbach resonance [35]. Here too, they observed spontaneous formation of density patterns (Fig. 1.1), whose wavelengths are related to the driving frequencies as mentioned before.

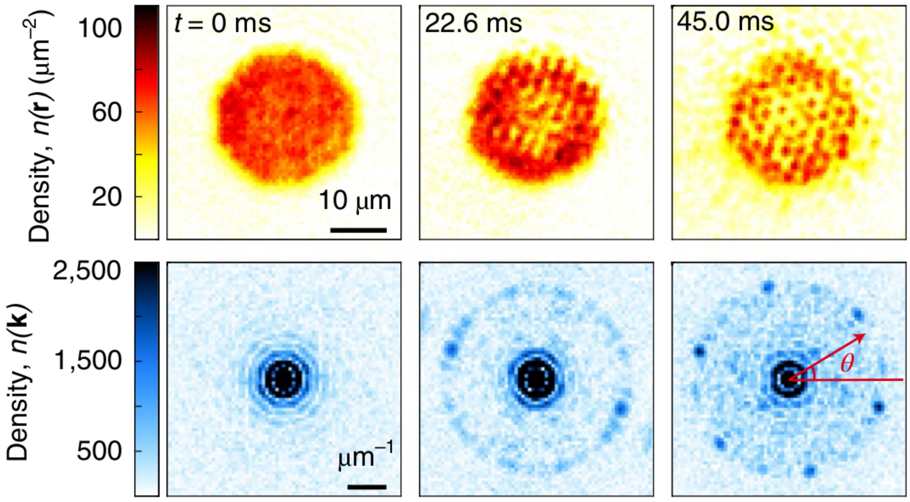

FIGURE 1.2: Pattern formation in BEC of Cs atoms under periodically driven s-wave interaction. In-situ images taken at three different times, showing the spontaneous emergence of the pattern(top row), and corresponding to its Fourier transforms (bottom row). Reproduced from Ref. [201] with permission from Springer Nature

In the experiments we discussed so far, the patterns formed were one-dimensional due to the geometry of the condensate trap. In pancake-shaped condensate, which is trapped tightly along one direction and weakly in the perpendicular plane, the Faraday waves form in the 2D plane. This was observed experimentally in a BEC of ^{133}Cs atoms [201] where the interaction was periodically modulated using the Feshbach resonance (Fig. 1.2), and later in ^{39}K BEC as well [103, 104]. The patterns we discussed so far originate from excitation of bulk modes, but periodic driving can also excite surface modes at appropriate driving frequencies. This was experimentally observed in a condensate of ^{7}Li atoms [96], where the excitation of various surface waves creates star-shaped patterns in the condensate (Fig. 1.3). The orientation of the pattern occurs at different angles for each set of realization [Fig. 1.3 (h)], demonstrating the spontaneous breaking of symmetry in the system under the periodic driving. Interestingly, this experiment in the driven superfluid has, in turn, led to the discovery of the same phenomena in a vertically shaken classical fluid [105], providing an example where exploring quantum fluids can, in turn, deepen or broaden our understanding of analogous behaviours in classical fluid systems.

The driven dynamics of multicomponent condensate are also interesting, since they can exhibit both density and spin excitation. Experimentally, this was explored by Cominotti et. al. [39] using a binary mixture containing two internal states of ^{23}Na atoms. The excitation spectra of such a condensate will have two branches, one corresponding to the total density excitation $n_1 + n_2$, and another to the "spin" excitation $n_1 - n_2$, where $n_{1,2}$ are the densities of each of the components. Periodic driving creates patterns in both these quantities with distinct wavelengths that can be related to the density and spin excitation spectra. Thus,

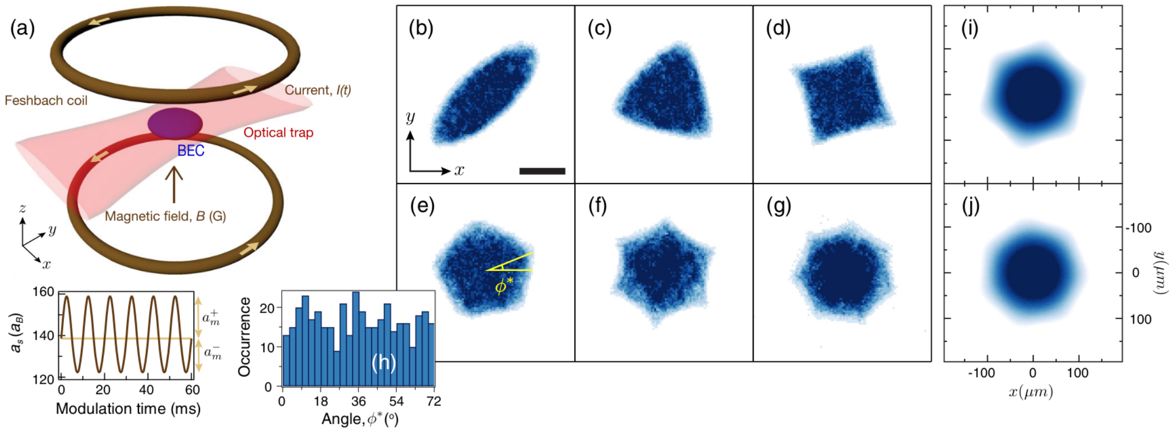

FIGURE 1.3: Star shaped pattern formation in driven ^{7}Li BEC. (a) Experimental setup. (b)-(g) Snapshots of the density pattern obtained for various driving frequencies. (h) Histogram of orientation angle ϕ of the pattern obtained for various realizations. (i),(j) Numerical simulation obtained from Gross-Pitaevskii. Reprinted figure with permission from [96]. Copyright (2021) by the American Physical Society.

Cominotti et. al [39] were able to fully map the spectra by observing the patterns, including the gap in the spin branch that arises when the sodium spin states are coherently coupled under a microwave field.

There have also been many theoretical studies on Faraday wave formation in BEC. In a dipolar condensate, for instance, it was predicted that the presence of the roton minima in the spectra can significantly change the response of the system at low frequency driving [122]. It was also shown that periodic driving of interaction can cause collective response from an array of dipolar BECs that are not overlapping [97, 120]. Other studies discuss the creation of dark soliton lattice [182] and pattern formation in binary [6, 32, 187], spin-orbit coupled [102, 198], and Rydberg-dressed [159] BEC, under periodic driving.

The study of Faraday patterns in BECs connects to the broader topic of pattern formation, specifically that in nonequilibrium systems [41, 63]. The main question is: how does an ordered pattern form spontaneously from a disordered state? This is a fundamental problem that appears in many areas, including biology [92], geology [82, 94, 111], cosmology [160], condensed matter physics [118], and more. Even though these systems are very different at the microscopic level, they often exhibit universality. Ultracold atomic systems offer a controllable setup to study pattern formation, and the insights gained can help understand similar processes in other fields. The formation of ordered patterns with square or hexagonal symmetries was observed in Ref. [103, 104, 201], and understanding this involves considering the dynamics of the system beyond the initial excitation of the modes. It has been found that decay of the excitation and other nonlinear processes can reinforce the pattern, giving it even more order [162]. More recently, long-lived square and stripe pattern formation was observed in a driven pancake condensate, which exhibited supersolid-like properties [104].

As mentioned, the origin of the pattern formation in the condensate is the parametric excitation of quasiparticles. In the presence of a shallow trap, the excited matter waves were observed to emit out in a coherent, narrow stream, resembling a firework [37, 58, 59], as periodic driving excites pairs of particles with opposite momenta, each with energy $E = \hbar\Omega/2$, with Ω being the driving frequency. This process of pair creation was also proposed as analogous to the dynamical Casimir effect, where the quantum fluctuations present in the system are amplified under periodic driving [27, 83, 151, 161]. The parametric excitation creates squeezing in spinor BEC [75]. Periodic driving is also used to probe collective excitation of system [84, 113, 155], and to generate quantum turbulence in superfluids [123].

Motivated by the wide range of fascinating phenomena exhibited by driven condensates, this thesis investigates the driven dynamics and emergent patterns in two specific systems. In the first part, we consider a spin-0 cylindrical BEC, which is trapped in the transverse plane and free along the longitudinal direction [81, 166]. We examine the role played by the transverse modes of this system in the driven dynamics. In the second part of the thesis, we look at the dynamics of a spin-1 spinor BEC under the periodic driving of interaction. The internal spin degrees of freedom give a new dimension to the driven dynamics, induced by spin-changing collisions in the system. The outline of the thesis is as follows.

In Chapter 2, we discuss the necessary background theory used in the thesis. Here we discuss the phenomena of BEC and introduce the mean-field and Bogoliubov theory. We also introduce spinor BEC and discuss the ground state phases of a homogeneous spin-1 condensate. We also take a brief look at Floquet theory, a mathematical tool used extensively in this thesis, and the Mathieu differential equation, which is particularly important to driven condensates. We then apply these tools to a driven, initially homogenous, spin-0 condensate, and discuss how the driving can cause spontaneous formation of patterns. We show that the dynamics of a driven spin-1 condensate in the ferromagnetic phase is similar to those of a spin-0 BEC.

In the next two chapters, we study the dynamics and pattern formation in a cylindrically confined condensate. Here, we explicitly look at how the transverse degrees of freedom affect the condensate dynamics, under a small amplitude driving of its s-wave scattering length. In Chapter 3, we study the resonant excitation of radial modes in cylindrically confined condensate under periodic driving of scattering length. Here we discuss in detail, the "direct excitation" (as opposed to parametric excitation) of radial modes and its subsequent decay that creates pattern formation. This phenomena of radial mode excitation occur only at specific driving frequencies, and we obtain the resonance condition through Bogoliubov theory calculations. We also examine the dynamics using numerical simulations of the 3D Gross-Pitaevskii equation (GPE). We show that excited transverse monopole mode, which is the lowest energy mode that can be directly excited under periodic drive, always decay to create longitudinal density waves. But the second directly excitable mode decays to create density patterns at weaker interaction of condensate, and centre-of-mass (COM) oscillations (zig-zag) pattern arising from dipole branch excitation at larger interaction.

In Chapter 4, we look at the parametric excitation of the cylindrically confined condensate under periodic driving, which occurs at driving frequencies away from the direct resonance points. First, we use a quasi-one-dimensional (Q1D) approximation to address the problem, which predicts density wave formation under drive. Then we use a fully 3D analysis, using both an approximate Bogoliubov approach and a linear stability analysis, using which we verified that the Q1D approximation remains valid even for a higher driving frequency, in the limit of weak interaction. For higher interactions, we find a frequency-dependent behaviour, where driving causes formation of density patterns or COM oscillations.

In the next two chapters, we study the dynamics of a driven homogeneous spin-1 condensate with antiferromagnetic interaction. A driven spin-1 BEC that is fully magnetization evolves similar to a spin-0 condensate due to conservation of the total magnetization under driving, as we saw in Chapter 2. This is no longer the case when the initial state is unmagnetized, where the internal degrees of freedom become relevant.

In Chapter 5, we study the dynamics of a quasi-two-dimensional (Q2D) spin-1 condensate initialized in the polar phase, where all atoms occupy the $m = 0$ spin-state. Periodic driving creates the density Faraday waves, as well as spin-patterns. These two dynamics can occur simultaneously only when the spin-independent and spin-dependent interaction coefficients are of nearly equal magnitudes. When the spin-independent coefficient is much larger, the spin-pattern formation dominates, creating spin-texture containing a gas of spin-vortices and anti-vortices. On the other hand, if the spin-dependent coefficient is much larger, we see density Faraday waves.

In Chapter 6, we look at the driven dynamics of condensate in the antiferromagnetic (AFM) phase, where particles are in a superposition of $m = \pm 1$ states, for both Q1D and Q2D systems. We show that when the driving frequency is below the gap of the transverse spin excitation spectrum of the system, the dynamics is similar to that of a binary condensate in the miscible phase. When the frequency exceeds the gap, the $m = 0$ component becomes populated, creating transverse spin density patterns in the system. In this case, we observe that the spin density vector is oriented along a particular direction in the transverse spin space, reflecting the underlying broken symmetry of the initial state.

We summarise the thesis and provide future outlook in Chapter 7.

Chapter 2

Background and theory

2.1 Ideal Bose-Gas

In this section, we will discuss the phenomenon of Bose-Einstein condensation in an ideal Bose gas [87, 140]. The non-interacting classical gas is described by the Maxwell-Boltzmann distribution, which treats them as distinguishable point-like objects. This theory fails at very low temperatures, where the quantum nature of the system becomes important.

Any quantum particle can be classified as a boson or a fermion based on whether its many-body wavefunction remains symmetrical under the exchange of two particles. Bosonic wavefunctions remain the same under this exchange, but fermionic wavefunctions acquire an overall negative sign. This property has huge implications for the properties of the bosonic and fermionic systems. Bosons can have multiple particles occupying the same single-particle state. In contrast, such a configuration is forbidden for fermions since it is impossible to construct a many-body wavefunction that is antisymmetric under exchange if any two particles occupy the same single-particle state. The ground state of a gas of non-interacting bosons is thus simply the product state with each boson occupying the single-particle ground state, whereas for a fermionic gas, the particles will stack up in available energy levels.

Consider an ideal gas of bosons, whose single-particle eigenstates are plane-wave momentum states. At temperature T, the occupation number of each of the momentum states is given by,

$$\langle n_K \rangle = \frac{1}{e^{\beta(E_k-\mu)} - 1} \tag{2.1}$$

where $E_k = \hbar^2 k^2/2M$ and μ denote the energy of the momentum state and chemical potential of the system, respectively, and parameter $\beta = 1/k_B T$. Since $\langle n_K \rangle$ must be non-negative, the chemical potential μ must remain less than or equal to the ground state energy, which is zero in this case; thus, $\mu \leq 0$. When μ attains this maximum value, the occupancy of the lowest energy state diverges, whereas for other states it remains finite.

The total number of particles in the excited state ($k \neq 0$) is given by,

$$N_e = \sum_{k\neq 0} \langle n_K \rangle \approx V \int \frac{d^3k}{8\pi^3} \frac{1}{z^{-1}e^{\beta E_k} - 1} \equiv \frac{V}{\lambda^3} g_{3/2}(z), \tag{2.2}$$

where we have replaced the summation with an integral, assuming a 3D system. Here, V denotes the volume, $z = e^{\beta\mu}$ is called the fugacity, and the function $g_{3/2}(z) = \frac{2}{\sqrt{\pi}} \int_0^\infty dx \frac{\sqrt{x}}{z^{-1}e^x - 1}$. We also have the thermal de Broglie wavelength,

$$\lambda = \frac{h}{\sqrt{2\pi M k_B T}}. \tag{2.3}$$

At high temperatures, the chemical potential is large and negative, and it increases as the temperature decreases until reaching zero. Decreasing the temperature further does not change μ. At the critical temperature T_C, $\mu = 0$ and $N_E \approx N$, therefore we have,

$$T_C = \frac{h^2}{2\pi M k_B} \left(\frac{n}{g_{3/2}(0)} \right)^{2/3}, \tag{2.4}$$

where $n = N/V$ is the density of the gas. Reducing the temperature below this value causes $N_e < N$, and particles start macroscopically occupying the lowest energy state. The fraction of excited population when $T < T_C$ follows the relation,

$$\frac{N_e}{N} = \left(\frac{T}{T_C} \right)^{3/2}. \tag{2.5}$$

The transition can also happen at a fixed temperature by increasing the system's density(reducing the volume). The critical density n_C in this case is given by

$$n_C \lambda^3 = g_{3/2}(0) \approx 2.612. \tag{2.6}$$

The quantity $n\lambda^3$ is known as the phase space density of the gas, which should be greater than $g_{3/2}(0)$ for condensation to occur. The above result tells us that the thermal wavelength of the gas, which is interpreted as the extent of the individual wave packets of the particles [87], must be greater than the average interparticle spacing.

2.2 Two-body interaction

In the last section, we discussed the BEC formation in a non-interacting gas of bosons below a critical temperature. However, in practice, gaseous systems are never non-interacting, and interactions play an especially greater role at lower temperatures. Most systems transition to a solid phase at low temperatures, with the notable exception of liquid helium. The gaseous BECs produced in the laboratory are metastable, since the true ground state of the system is a solid. This metastable state is maintained by keeping the gas extremely dilute, which prevents three-body collisions that can lead to the formation of bound molecules [5]. Even at these dilute conditions, interactions have a significant effect on the properties of the condensate.

The true interaction potential between two interacting atoms is fairly complex. However, since the particles have a large interparticle distance and low energies, the s-wave scattering length a_s is often sufficient to describe the interaction. This is because for low-energy collisions, the scattering cross-section is dominated by the $l = 0$ (s-wave) contribution arising from the partial wave expansion.

At large distances, the interaction experienced by atoms is described by the van der Waals potential that varies as $\sim -\alpha/r^6$, where r is the inter-atomic distance. A calculation of s-wave scattering length using an interatomic potential modelled by van der Waals interaction when $r > r_c$ and an infinite hard core potential when $r < r_c$ has been discussed in Ref. [134]. Here, the distance r_c depends on the details of the actual potential, which is repulsive at shorter distances. This calculation shows that a_s also depends on the details of the interaction at short distances, and that the scattering length can be positive or negative, which indicates a repulsive or attractive effective interaction, respectively. There can also be two different interaction potentials that produce the same a_s. In ultracold systems, the actual potential is usually replaced by a pseudo-potential given by [77, 134],

$$U_{\text{eff}}(r) = \frac{4\pi\hbar^2 a_s}{M}\delta(r), \tag{2.7}$$

where M is the mass of the interacting particles. This approximation allows one to focus on long-wavelength scattering processes.

2.2.1 Feshbach resonances

In the discussion so far, we have assumed scattering in a single channel. The scattering channel refers to a specific combination of incoming and outgoing atomic states [134]. Atoms have internal spin structure, which gives rise to multiple scattering channels and corresponding interaction potentials. This also gives rise to the possibility of inelastic collisions, which result in incoming and outgoing atoms having different internal states and kinetic energies. The scattering lengths obtained from multichannel problems can thus have an imaginary part as well, which describes the channel's atoms' loss under scattering. Usually, in the cold atom experimental setups, such losses are small, and the system can be described by an effective single-channel model.

One scenario where the inelastic scattering becomes particularly useful is the Feshbach resonance [35]. Consider a system where atoms interact via two channels: an open channel

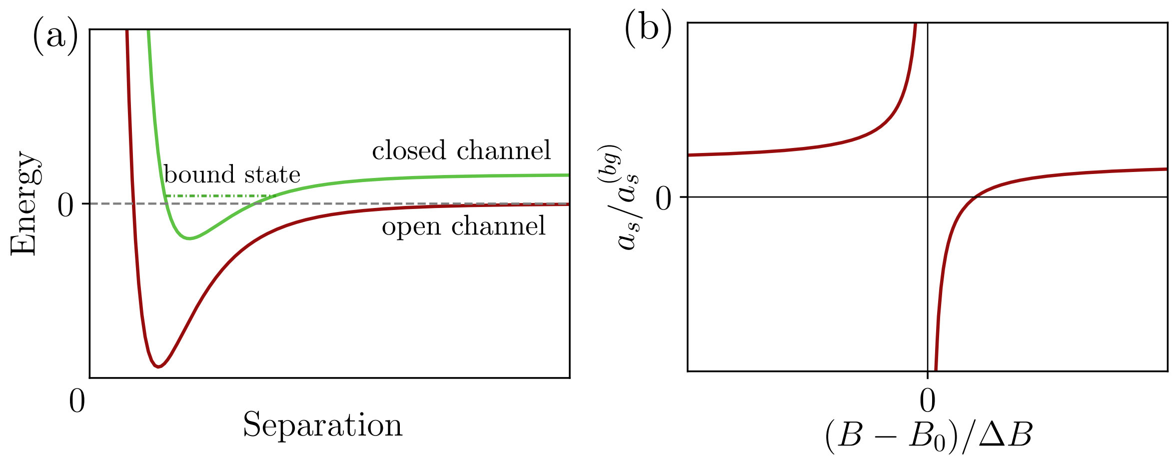

FIGURE 2.1: (a)Schematic of open and closed channel interaction potential. (b)Variation of s-wave scattering length near a Feshbach resonance

that supports scattering states, and a closed channel that supports only bound states [see Fig. 2.1(a)]. Feshbach resonance occurs when the energy of a scattering state in the open channel becomes equal to that of a bound state in a closed channel, leading to strong coupling between these channels. Such a resonance can effectively change the scattering length in the open channel. If the energies of the atomic states of the two channels can be tuned relative to each other using a magnetic field, we can induce the resonance by varying the field. If B_0 the magnetic field at which Feshbach resonance occurs, then the scattering length of the open channel varies near this field as,

$$a_s(B) = a_s^{(bg)}(B)\left(1 - \frac{\Delta B}{B - B_0}\right), \tag{2.8}$$

where B is the magnetic field applied and $a_s^{(bg)}$ is the background scattering length, far from the resonance and ΔB is known as the resonance width. The behaviour of the scattering length near a Feshbach resonance is shown in Fig. 2.1(b). At resonance field $B = B_0$, scattering length diverges, and by varying the magnetic field near this value, one can tune the effective interaction between the atoms and even change the sign of the scattering length [40, 80].

Besides the magnetic Feshbach resonance, one can also optically tune the interaction, known as the optical Feshbach resonance. Here, a laser field couples the scattering state to an excited molecular state, and by tuning the intensity and detuning, the effective scattering length can be varied. This was first proposed in [56], and later observed experimentally [54, 174, 175]. Optical Feshbach resonance suffers from atom loss due to the spontaneous emission processes occurring in the excited state.

The ability to tune the interaction of cold atom systems has opened up a whole new range of possibilities, including the experimental implementation of periodically driven interactions [37, 124, 142, 201], which is of central interest in this thesis.

2.3 Mean-Field theory of Bose-Einstein condensate

Theoretically describing a many-body system with a large number of particles is often impractical. Mean-field theory captures the properties of BEC at very low temperatures well and heavily simplifies the system, and we use it throughout this thesis. Generally speaking, there are two approaches to the mean-field theory. The first approach involves replacing the field operator $\hat{\psi}(\boldsymbol{r})$ with its expectation value $\psi(\boldsymbol{r}) \equiv \langle\hat{\psi}(\boldsymbol{r})\rangle$, which breaks the number conservation, to obtain a semiclassical description for the condensate. We can also assume that the total number of atoms is conserved and get the same results [29, 89]. In this section, we describe the mean-field theory using the number-conserving approach.

At low temperatures, a weakly interacting gas of bosons can be described by the many-body Hamiltonian,

$$\hat{H} = \int d\boldsymbol{r} \left\{ \hat{\Psi}^{\dagger}(\boldsymbol{r}) \left[-\frac{\hbar^2\nabla^2}{2M} + V_T(\boldsymbol{r}) \right] \hat{\Psi}(\boldsymbol{r}) + \frac{g}{2} \hat{\Psi}^{\dagger}(\boldsymbol{r})\hat{\Psi}^{\dagger}(\boldsymbol{r})\hat{\Psi}(\boldsymbol{r})\hat{\Psi}(\boldsymbol{r}) \right\}, \tag{2.9}$$

where the bosonic field operators $\hat{\Psi}^{\dagger}(\boldsymbol{r})$ and $\hat{\Psi}(\boldsymbol{r})$ creates and annihilates a particle at position $\boldsymbol{r}$, respectively. The first term in the integrand of Eq.(2.9) describes the single-body contribution to the Hamiltonian that includes the kinetic energy and the external trap potential $V_T(\boldsymbol{r})$. The second term describes the two-body interaction between the bosons, with interaction strength $g = 4\pi\hbar^2 a_s/M$ being proportional to the s-wave scattering length a_s. This is obtained using the pseudo-potential described in Eq. (2.7), which is valid for dilute and cold gas. Here, the diluteness condition is given as $n|a_s|^3 \ll 1$, where n is the density of the gas [45].

Particles macroscopically occupy a single mode in BEC. Let's denote this state using $\psi_C(\boldsymbol{r})$, and let the operator $\hat{a}_0$ annihilate a particle in this state. We can then construct a BEC many-body state as,

$$|\Psi\rangle_C = \left(\hat{a}_0^{\dagger}\right)^N |\Phi\rangle, \tag{2.10}$$

with $|\Phi\rangle$ denoting the vacuum state and N being the total number of particles. The expectation values of the following correlation operators for the state in Eq. (2.10) are obtained as,

$$\begin{aligned}\langle\hat{\Psi}^\dagger(\boldsymbol{r})\hat{\Psi}(\boldsymbol{r}')\rangle &= N\psi_C^*(\boldsymbol{r})\psi_C(\boldsymbol{r}')\\ \langle\hat{\Psi}^\dagger(\boldsymbol{r}_1)\hat{\Psi}^\dagger(\boldsymbol{r}_2)\hat{\Psi}(\boldsymbol{r}_3)\hat{\Psi}(\boldsymbol{r}_4)\rangle &= N(N-1)\psi_C^*(\boldsymbol{r}_1)\psi_C^*(\boldsymbol{r}_2)\psi_C(\boldsymbol{r}_3)\psi_C(\boldsymbol{r}_4)\\ &\approx N^2\psi_C^*(\boldsymbol{r}_1)\psi_C^*(\boldsymbol{r}_2)\psi_C(\boldsymbol{r}_3)\psi_C(\boldsymbol{r}_4).\end{aligned} \tag{2.11}$$

We used $N(N-1) \approx N^2$ since $N \gg 1$ in the last step, and the expectation value of the Hamiltonian is given as,

$$\langle\hat{H}\rangle = N\int d\boldsymbol{r}\left\{\psi_C^*(\boldsymbol{r})\left[-\frac{\hbar^2\nabla^2}{2M}+V_T(\boldsymbol{r})\right]\psi_C(\boldsymbol{r})+\frac{gN}{2}|\psi_C(\boldsymbol{r})|^4\right\} \equiv E_0[\psi_C]. \tag{2.12}$$

This is the mean-field energy functional of the system, and ψ_C is the condensate order parameter, also called the condensate wavefunction. While deriving this, we have completely neglected the population outside the condensate wavefunction.

For a time-independent system, the ground state order parameter, denoted by $\xi_0(\boldsymbol{r})$, can be obtained by minimizing the mean-field energy functional under the constraint that the norm of ξ_0 is conserved. We can do so by minimizing the functional $F[\psi_C] = E_0[\psi_C] - \mu N\int d\boldsymbol{r}|\psi_C(\boldsymbol{r})|^2$, where the the Lagrangian multiplier μ represents the chemical potential. From the minimization condition $\delta F[\psi]/\delta\psi = 0$, we obtain the *time-independent Gross-Pitaevskii equation (GPE)*,

$$\left[-\frac{\hbar^2\nabla^2}{2M}+V_T(\boldsymbol{r})+gN|\xi_0(\boldsymbol{r})|^2\right]\xi_0(\boldsymbol{r}) = \mu\xi_0(\boldsymbol{r}). \tag{2.13}$$

In the absence of interaction ($g = 0$), this order parameter would be the single-particle ground state of the trap potential V_T, but the interaction introduces a nonlinearity in the system, which can significantly change the condensate profile.

The dynamics of the condensate wavefunction $\psi(\boldsymbol{r}, t)$ (we dropped the subscript "C") is given by the the *time-dependent GPE*,

$$i\hbar\frac{\partial\psi}{\partial t} = \left[-\frac{\hbar^2\nabla^2}{2M}+V_T(\boldsymbol{r})+g|\psi|^2\right]\psi(\boldsymbol{r}). \tag{2.14}$$

Several approaches to derive the time-dependent GPE [29, 140] exist. One way is to minimize the action $S = \int Ldt$, where the Lagrangian is given by,

$$L = \int d\boldsymbol{r}\left(\psi^*\frac{\partial\psi}{\partial t} - \Phi\frac{\partial\psi^*}{\partial t}\right) - E_0[\psi]. \tag{2.15}$$

A rigorous derivation of the time-independent GPE under number-conservation has been discussed in Ref. [29]. As we can see, Eq. (2.14) is a nonlinear equation due to the presence of the interaction.

2.3.1 Bogoliubov-de Gennes equation

The ground state wavefunction $\xi_0(\boldsymbol{r})$ [Eq. (2.13)], is a stationary solution of the time-dependent GPE (2.14), and acquires only a phase factor $\psi(\boldsymbol{r}, t) = \xi_0(\boldsymbol{r})e^{-i\mu t}$ under evolution. The linearized solutions of the fluctuations about the ground state are often important in understanding the system, as they give us information about the stability of the condensate, as well as its response to external perturbation [45]. Consider a perturbed ground state solution,

$$\psi(\boldsymbol{r}, t) = [\xi_0(\boldsymbol{r}) + \delta\psi(\boldsymbol{r}, t)]\, e^{-i\mu t/\hbar}, \tag{2.16}$$

where μ is the chemical potential of the system, and the perturbation $\delta\psi$ is of the form,

$$\delta\psi(\boldsymbol{r}, t) = u(\boldsymbol{r})e^{-i\omega t} + v^*(\boldsymbol{r})e^{+i\omega t}. \tag{2.17}$$

Here we are looking to find solutions for amplitudes u, v with frequency ω. From the GPE. (2.14), we obtain the linearized equation for the amplitudes as,

$$\begin{pmatrix} \hat{\mathcal{L}} & gN\xi_0^2 \\ -gN\xi_0^2 & -\hat{\mathcal{L}} \end{pmatrix} \begin{pmatrix} u(\boldsymbol{r}) \\ v(\boldsymbol{r}) \end{pmatrix} = \hbar\omega \begin{pmatrix} u(\boldsymbol{r}) \\ v(\boldsymbol{r}) \end{pmatrix}. \tag{2.18}$$

Here, $\hat{\mathcal{L}} = (-\hbar^2\nabla^2/2M) + V_T + 2g|\xi_0|^2 - \mu$. This is known as the *Bogoliubov-de Gennes (BdG)* equation, and it can be solved as an eigenvalue problem to obtain the eigenvalues ω and eigenvectors (u, v). In the absence of interaction, the BdG energy spectrum coincides with the energy levels of the single particle Hamiltonian. Interaction can significantly modify this. If there are any frequencies with a non-zero imaginary part, for the system, the solution is dynamically unstable against perturbations, and small deviations can exponentially diverge from the ground state.

2.4 Quasi-one and -two dimensional condensates

For a homogeneous gas, Bose-Einstein condensation cannot occur in the dimension $d < 3$, due to divergence of N_e even when chemical potential $\mu = 0$. But in a highly anisotropic trap, the system can be described using effective 1D and 2D equations. These are called the quasi-one dimensional (Q1D) and quasi-two dimensional (Q2D) condensate [135, 136].

Consider a system of a Bose gas in a harmonic trap given as $V_T = (1/2)M(\omega_\rho^2\rho^2 + \omega_z^2 z^2)$, where $\rho^2 = x^2 + y^2$. A Q1D condensate is obtained in an elongated trap, whose radial trap frequency ω_ρ is much larger than the trap frequency ω_z, i.e. $\omega_\rho \gg \omega_z$. If all the other energies present in the system, including the kinetic and the interaction energies, are much smaller than the trap energy, then we can approximate that the transverse profile of the condensate is with the radial harmonic ground state. We then express the order parameter $\psi(\boldsymbol{r},t) = \tilde{\psi}(z,t)\Phi(\rho)$, where $\Phi(\rho) = (1/\pi l_\rho^2)^{1/2}\exp\left[-\rho^2/l_\rho^2\right]$ with $l_\rho = \sqrt{\hbar/M\omega_\rho}$ being the characteristic length of transverse trap. We use this decomposition in the 3D GPE (2.14), multiply both sides with $\Phi^*(\rho)$ and integrate over x, y directions to obtain the following Q1D GPE for longitudinal condensate wavefunction,

$$i\hbar\frac{\partial\tilde{\psi}}{\partial t} = \left[-\frac{\hbar^2}{2M}\frac{\partial^2}{\partial z^2} + \frac{1}{2}M\omega_z^2 z^2 + g_{1D}|\tilde{\psi}|^2\right]\tilde{\psi}. \tag{2.19}$$

Here, $g_{1D} = g/2\pi l_x l_y$ denotes the effective 1D interaction parameter. The validity condition for Q1D can be given as $\mu_{1D} \ll \omega_{x,y}$, where μ_{1D} is the 1D chemical potential of the system.

Similarly, by applying a strong trap along the longitudinal direction, i.e., $\omega_z \gg \omega_\rho$, we obtain the Q2D condensate. Following the same logic as in Q1D case, we can write the 3D order-parameter as $\psi(\boldsymbol{r},t) = \bar{\psi}(x,y)\Phi'(z)$, where $\Phi'(z) = (1/\pi l_z^2)^{1/4}\exp\left(-z^2/2l_z\right)$ is the ground state of the longitudinal trap. From the 3D GPE, we can then obtain the equation of motion of the 2D wavefunction as,

$$i\hbar\frac{\partial\bar{\psi}}{\partial t} = \left[-\frac{\hbar^2\nabla_\rho^2}{2M} + \frac{1}{2}M\omega_\rho^2\rho^2 + g_{2D}|\bar{\psi}|^2\right]\bar{\psi}. \tag{2.20}$$

The Q2D interaction strength is given as $g_{2D} = g/\sqrt{2\pi}l_z$.

Note that although the Q1D and Q2D gases are described by lower-dimensional theory, they are not truly lower-dimensional, as we are still using a 3D model for the two-body interaction. In fact, the lower dimensional GPEs are valid only when $l_\rho \gg a_s$ for Q1D and $l_z \gg a_z$ for Q2D gases. Additionally, for cigar shaped systems, the mean-field theory is valid only when the condition $n_{1D}l_\rho^2/a_s \gg 1$ is met, where n_{1D} is the 1D density of the condensate, as it otherwise enters the highly correlated Lieb–Lininger regime [91, 137, 140].

2.5 Bogoliubov theory

The central assumption in the mean-field theory is that all the bosons occupy a single quantum state. This is not the case when interaction exists, as there is a non-zero population outside the condensate mode, even at zero temperature. Bogoliubov theory [16] gives us the framework for describing the elementary excitation present in the condensate, when most of the atoms are in the condensate mode. In this section, we discuss the theory of uniform and non-uniform condensate and show that under the Bogoliubov transformation, the weakly interacting gas can be expressed as a non-interacting gas of quasiparticles. We also show the equivalence between the Bogoliubov quasiparticles and the BdG excitations described in Sec. 2.3.1.

2.5.1 Uniform BEC

In this section, we discuss Bogoliubov theory in its simplest setting, a weakly interacting uniform Bose gas, and derive its elementary excitation spectrum using a number-conserving approach. The Hamiltonian for a uniform gas of bosons with mass M is given in momentum space as

$$\hat{H} = \sum_{\boldsymbol{k}} E_{\boldsymbol{k}} \hat{a}^{\dagger}_{\boldsymbol{k}} \hat{a}_{\boldsymbol{k}} + \frac{g}{2V} \sum_{\boldsymbol{k}_1,\boldsymbol{k}_2,\boldsymbol{k}_3,\boldsymbol{k}_4} \hat{a}^{\dagger}_{\boldsymbol{k}_1} \hat{a}^{\dagger}_{\boldsymbol{k}_2} \hat{a}_{\boldsymbol{k}_3} \hat{a}_{\boldsymbol{k}_4} \boldsymbol{\delta}(\boldsymbol{k}_1 + \boldsymbol{k}_2 - \boldsymbol{k}_3 - \boldsymbol{k}_4). \tag{2.21}$$

The bosonic operator $\hat{a}_{\boldsymbol{k}}$ annihilates a particle in the $\boldsymbol{k}^{th}$ momentum state. The first term in Eq. (2.21) represents the single-body contribution to the Hamiltonian, with the energy of the momentum state given by $E_{\boldsymbol{k}} = \hbar^2 |\boldsymbol{k}|^2/2M$. The second term describes the interaction between particles, where $g = 4\pi\hbar^2 a_s/M$ denotes the s-wave interaction coefficient and V denotes the volume of the system. The interaction conserves the total momentum of the colliding particles, which is ensured by the delta function in the Hamiltonian.

At a very low temperature, the condensation occurs in the zero momentum state, whose population $\langle \hat{a}^{\dagger}_{\boldsymbol{0}} \hat{a}_{\boldsymbol{0}} \rangle = N_0 \approx N$. We define the number operator that counts the non-condensate population as,

$$\delta\hat{N} = \sum_{k \neq 0} \hat{a}^{\dagger}_{k} \hat{a}_{k}. \tag{2.22}$$

Since the total number of particles in the system N is conserved, we can write $\hat{a}^{\dagger}_0 \hat{a}_0 = N - \delta\hat{N}$. When $N \gg 1$, we can also expand

$$\begin{aligned} \hat{a}^{\dagger}_0 \hat{a}^{\dagger}_0 \hat{a}_0 \hat{a}_0 &= \hat{a}^{\dagger}_0 \hat{a}_0 \hat{a}^{\dagger}_0 \hat{a}_0 - \hat{a}^{\dagger}_0 \hat{a}_0 \\ &= (N - \delta\hat{N})^2 - (N - \delta\hat{N}) \\ &\approx N^2 - 2N\delta\hat{N} + O(\delta\hat{N}^2). \end{aligned}$$

Making these replacements in the Hamiltonian in Eq. (2.21), and keeping only terms that are linear in $\delta\hat{N}$, we get,

$$\hat{H} \approx \frac{gnN}{2} + \sum_{\boldsymbol{k} \neq 0} E_{\boldsymbol{k}} \hat{a}^{\dagger}_{\boldsymbol{k}} \hat{a}_{\boldsymbol{k}} + \frac{gn}{2} \sum_{\boldsymbol{k} \neq 0} \left\{ \hat{a}_{\boldsymbol{k}} \hat{a}_{-\boldsymbol{k}} + \hat{a}^{\dagger}_{\boldsymbol{k}} \hat{a}^{\dagger}_{-\boldsymbol{k}} + 2\hat{a}^{\dagger}_{\boldsymbol{k}} \hat{a}_{\boldsymbol{k}} \right\}. \tag{2.23}$$

Here, we have made two main approximations. First, we retain only the interaction terms between the condensate and the excited modes. Second, we replace the condensate mode operators with a c-number, consistent with a mean-field-like treatment. However, unlike the usual $U(1)$ symmetry-breaking approach, we employ a number-conserving formalism throughout.

We now perform the following transformation,

$$\hat{a}_{\boldsymbol{k}} = u_{\boldsymbol{k}}\hat{b}_{\boldsymbol{k}} + v^*_{-\boldsymbol{k}}\hat{b}^\dagger_{-\boldsymbol{k}}, \quad \hat{a}^\dagger_{\boldsymbol{k}} = u^*_{\boldsymbol{k}}\hat{b}^\dagger_{\boldsymbol{k}} + v_{-\boldsymbol{k}}\hat{b}_{-\boldsymbol{k}}, \tag{2.24}$$

where $b_{\boldsymbol{k}}$ are the quasiparticle operators which obey bosonic commutation relations,

$$[\hat{b}_{\boldsymbol{k}}, \hat{b}^\dagger_{\boldsymbol{k}'}] = \delta(\boldsymbol{k} - \boldsymbol{k}'), \quad \text{and} \quad [\hat{b}_{\boldsymbol{k}}, \hat{b}_{\boldsymbol{k}'}] = [\hat{b}^\dagger_{\boldsymbol{k}}, \hat{b}^\dagger_{\boldsymbol{k}'}] = 0. \tag{2.25}$$

The coefficients $u_{\boldsymbol{k}}$ and $v_{\boldsymbol{k}}$ are chosen so that the $b_{\boldsymbol{k}}$ satisfy commutation relations and the Hamiltonian Eq. (2.23) becomes diagonal. This is achieved when

$$u_{\boldsymbol{k}} = \sqrt{\frac{E_{\boldsymbol{k}} + gn}{2\epsilon(\boldsymbol{k})} + \frac{1}{2}}, \quad v_{\boldsymbol{k}} = -\sqrt{\frac{E_{\boldsymbol{k}} + gn}{2\epsilon(\boldsymbol{k})} - \frac{1}{2}}, \tag{2.26}$$

where $\epsilon(\boldsymbol{k}) = \sqrt{E_k(E_k + 2gn)}$. Under such a transformation, the Hamiltonian becomes

$$H \approx E_0^{(B)} + \sum_{\boldsymbol{k}} \epsilon(\boldsymbol{k})\hat{b}^\dagger_{\boldsymbol{k}}\hat{b}_{\boldsymbol{k}}, \tag{2.27}$$

where $E_0^{(B)} = gnN/2 - \sum_{\boldsymbol{k}} \epsilon(\boldsymbol{k})|v_{\boldsymbol{k}}|^2$. This energy, when calculated for the three-dimensional system, can shown be diverging. This divergence can be avoided by considering a higher-order correction to the interaction potential, where we replace g by $g + (g^2/V)\sum_{\boldsymbol{k}}(1/E_k)$, which would introduce an extra term to the ground state energy [140]. The Bogoliubov dispersion relation $\epsilon(\boldsymbol{k})$ gives us the energy of the quasiparticles. In the absence of interaction, this reduces to the kinetic energy $E_{\boldsymbol{k}}$. For a weakly interacting BEC, the dispersion becomes linear in the limit $|\boldsymbol{k}|/M \ll gn$, indicating phonon-like excitations. In the other limit, $|\boldsymbol{k}|/M \gg gn$, the spectrum is quadratic and free-particle-like.

2.5.2 Non-uniform gas

The approach developed in the previous section can also be extended to non-uniform systems. In this section, we show the equivalence between the Bogoliubov theory applied to the second-quantized Hamiltonian and the linearized Gross-Pitaevskii equation (GPE) around the ground state [section (2.3.1)]. As before, we adopt a number-conserving formalism [29, 30].

We start with the second-quantized Hamiltonian for the weakly interacting gas in a trap,

$$\hat{H} = \int d\boldsymbol{r} \hat{\Psi}^\dagger \hat{h}_0 \hat{\Psi} + \frac{g}{2} \int d\boldsymbol{r} \hat{\Psi}^\dagger \hat{\Psi}^\dagger \hat{\Psi} \hat{\Psi}, \tag{2.28}$$

where $\hat{h}_0 = -(\hbar^2\nabla^2/2M) + V_T$. Then the macroscopically occupied ground state mode ξ_0 can be obtained from the time-independent GPE (2.13). We expand the field operator about the condensate mode as,

$$\hat{\Psi}(\boldsymbol{r}, t) = \left[\xi_0(\boldsymbol{r})\hat{a}_0 + \delta\hat{\Psi}(\boldsymbol{r}, t)\right] e^{-i\mu t/\hbar}. \tag{2.29}$$

Here, $\hat{a}_0$ annihilates a particle in ξ_0, and $\delta\hat{\Psi}$ denotes the (non-condensate) part of the field operator that is orthogonal to ξ_0. We assume that the condensate population, $N_0 = \langle \hat{a}_0^\dagger \hat{a}_0 \rangle$, is much larger than the non-condensate population given by $\delta N = \int d\boldsymbol{r} \langle \delta\hat{\Psi}^\dagger \delta\hat{\Psi} \rangle$. Therefore, as we did in the uniform case, we can replace $\hat{a}_0^\dagger \hat{a}_0 = N - \delta\hat{N}$ and $\hat{a}_0^\dagger \hat{a}_0^\dagger \hat{a}_0 \hat{a}_0 \approx N^2 - 2N\delta\hat{N}$, where the operator $\delta\hat{N} \equiv \int d\boldsymbol{r} \delta\hat{\Psi}^\dagger \delta\hat{\Psi}$. Here we assume that the total number of particles in the system is conserved and $N \gg 1$.

After substituting Eq. (2.29) and using the replacements for operators $\hat{a}_0$ mentioned above, we can expand the Hamiltonian in powers of $\delta\hat{\Psi}$, as $\hat{H} = H_0 + \hat{H}_1 + \hat{H}_2 + \ldots$, where,

$$\begin{aligned}
H_0 &= N \int d\boldsymbol{r} \left(\xi_0^* \hat{h}_0 \xi_0 + \frac{gN}{2} |\xi_0|^4 \right) \\
\hat{H}_1 &= \hat{a}_0 \int d\boldsymbol{r} \delta\hat{\Psi}^\dagger \left[\hat{h}_0 + gN|\xi_0|^2 \right] \xi_0 + \text{H.c.} \\
\hat{H}_2 &= \int d\boldsymbol{r} \delta\hat{\Psi}^\dagger \hat{h}_0 \delta\hat{\Psi} + \frac{g}{2} \int d\boldsymbol{r} \left[\hat{a}_0^\dagger \hat{a}_0^\dagger \delta\hat{\Psi} \delta\hat{\Psi} (\xi_0^*)^2 + \text{H.c.} \right] + 2gN \int d\boldsymbol{r} |\xi_0|^2 \delta\hat{\Psi}^\dagger \delta\hat{\Psi} - \mu\delta\hat{N}.
\end{aligned} \tag{2.30}$$

H_0 is the mean field energy of the ground state given in Eq. (2.12). We can show that the linear term $\hat{H}_1$ vanishes, as the integrand in it reduces to $\mu\delta\hat{\Psi}\xi_0$ [see GPE (2.13)], and since the condensate mode is orthogonal to $\delta\hat{\Psi}$. We now introduce the following number-conserving operator [29],

$$\hat{\Lambda}(\boldsymbol{r}) = \frac{\hat{a}_0^\dagger \delta\hat{\Psi}(\boldsymbol{r})}{\sqrt{N}}, \tag{2.31}$$

which destroys a non-condensate particle and creates one in the condensate. We can write $\hat{a}_0^\dagger \hat{a}_0^\dagger \delta\hat{\Psi} \delta\hat{\Psi} = \hat{\Lambda}\hat{\Lambda}$. The term $\delta\hat{\Psi}^\dagger \delta\hat{\Psi}$ is replaced in an approximate manner as $\delta\hat{\Psi}^\dagger \delta\hat{\Psi} \approx N^{-1} \delta\hat{\Psi}^\dagger \hat{a}_0 \hat{a}_0^\dagger \delta\hat{\Psi} = \hat{\Lambda}^\dagger \hat{\Lambda}$. The quadratic term in the Hamiltonian thus becomes,

$$\hat{H}_2 \approx \int d\boldsymbol{r} \hat{\Lambda}^\dagger \left(\hat{h}_0 - \mu + 2gN \int d\boldsymbol{r} |\xi_0|^2 \right) \hat{\Lambda} + \frac{g}{2} \int d\boldsymbol{r} \left[\hat{\Lambda}^\dagger \hat{\Lambda}^\dagger (\xi_0^*)^2 + \text{H.c.} \right]. \tag{2.32}$$

The above Hamiltonian can be shown to become diagonal when expanded in the Bogoliubov basis given by,

$$\hat{\Lambda}(\boldsymbol{r},t) = \sum_i \hat{b}_i(t)\tilde{u}_i(\boldsymbol{r}) + \hat{b}_i^\dagger(t)\tilde{v}_i^*(\boldsymbol{r}), \tag{2.33}$$

where the amplitudes $\{\tilde{u}_i, \tilde{v}_i\}$ can be obtained from the BdG amplitudes we derived from (2.18) as,

$$\tilde{u}_i = u_i(\boldsymbol{r}) - \xi_0 a_i, \quad \tilde{v}_i = v_i(\boldsymbol{r}) + \xi_0 a_i, \tag{2.34}$$

where $a_i = \int d\boldsymbol{r}\xi_0^* u_i = -\int d\boldsymbol{r}\xi_0 v_i$. The above projection ensure that $\delta\hat{\Psi}$ is orthogonal to $\hat{a}_0$ [57]. These new amplitudes also obey the orthonormality condition,

$$\int d\boldsymbol{r}\left[\tilde{u}_i\tilde{u}_j^* - \tilde{v}_i\tilde{v}_j^*\right] = \delta_{ij}, \quad \int d\boldsymbol{r}\left[\tilde{u}_i\tilde{v}_j - \tilde{v}_i\tilde{u}_j\right] = 0, \tag{2.35}$$

and also has the property $\int d\boldsymbol{r}\left[\xi_0^*\tilde{u}_i + \xi_0\tilde{v}_i\right] = 0$ [13, 117]. Using the expansion in Eq.(2.33) and simplifying, the quadratic term takes the form,

$$\hat{H}_2 = \sum_i \hbar\omega_i \hat{b}_i^\dagger \hat{b}_i - \sum_i \hbar\omega_i \int d\boldsymbol{r}|v_i|^2. \tag{2.36}$$

Here, we can see the correspondence between the Bogoliubov quasiparticles and the linearized solutions obtained from the BdG equation. Both approaches give us the same set of frequencies and amplitudes[1].

2.6 Spinor BEC

In our discussion so far, we assumed that the bosons present in the condensate do not have any internal degrees of freedom, i.e. they are spin-0. Condensate of atoms with spin degrees of freedom can be attained in labs using an optical trap [89, 164]. The spin originates from the electronic and nuclear level structure of the bosonic atoms. For example, consider ^{87}Rb, which has an electronic spin $j = 1/2$ and nuclear spin of $i = 3/2$. This gives rise to total spin $f = i \pm j$ spin manifolds, which take values $f = 1, 2$. For the ^{133}Cs atom, the electronic and nuclear spins are given as $j = 1/2$ and $i = 7/2$, respectively, resulting in $f = 3, 4$ hyperfine spin manifolds. At weak magnetic fields, f is a good quantum number, and the different total spin manifolds are energetically well separated. In a given spin-f manifold, there are $2f + 1$ Zeeman sublevels denoted by $m = -f, -f + 1, \ldots, f$. When energy separations of the

[1] In the number-conserving approach, the amplitudes are related through Eq. (2.34)

sublevels due to magnetic fields are much smaller than the hyperfine splitting, the condensate retains its internal spin degrees of freedom [164], and they are called the spinor BEC.

The spin-1 bosons have three internal spin levels, denoted by $m = 1, 0, -1$. The Hamiltonian of a weakly interacting gas of these bosons can be expressed as,

$$\hat{H} = \sum_{m=-1}^{1} \hat{H}_m^{(0)} + \hat{V}. \tag{2.37}$$

Here, $\hat{H}_m^{(0)}$ is the single body Hamiltonian for a boson in spin state m, which is given by,

$$\hat{H}_m^{(0)} = \int d\boldsymbol{r} \hat{\Psi}_m^\dagger(\boldsymbol{r}) \left[-\frac{\hbar^2 \nabla^2}{2M} + V_T(\boldsymbol{r}) - pm + qm^2 \right] \hat{\Psi}_m(\boldsymbol{r}), \tag{2.38}$$

where bosonic field operator $\hat{\Psi}_m^\dagger$ destroys a boson in state m at position $\boldsymbol{r}$. The external trapping potential V_T is assumed to be the same for all three components, and p and q denote the linear and quadratic energy shifts due to external magnetic or microwave fields [89].

Now we shall look at the two-body interaction in a spin-1 Bose gas. Unlike the spin-0 gas, spin-f bosons can interact via multiple scattering channels. These channels can be labelled using the total spin of the interacting bosonic atom pairs, since the collisions conserve the total spin. For example, total spin can be $\mathcal{F} = 0$ or $\mathcal{F} = 2$ for two spin-1 bosons interacting via s-wave scattering. Only even $\mathcal{F}$ channels are allowed as s-wave states with odd F are not symmetric under exchange of particles, which is required under bosonic commutation relations [89].

Therefore, we can express the interaction between the two spin-1 bosons as $\hat{V} = \hat{V}^{(0)} + \hat{V}^{(2)}$ [73, 89, 129], where

$$\hat{V}^{(\mathcal{F})} = \frac{g_{\mathcal{F}}}{2} \sum_{\mathcal{M}=-\mathcal{F}}^{\mathcal{F}} \int d\boldsymbol{r} \hat{A}_{\mathcal{F}\mathcal{M}}^\dagger(\boldsymbol{r}, \boldsymbol{r}) \hat{A}_{\mathcal{F}\mathcal{M}}(\boldsymbol{r}, \boldsymbol{r}) \tag{2.39}$$

represents the two-body interaction in the total spin-$\mathcal{F}$ channel. Here, $\hat{A}_{\mathcal{F}\mathcal{M}}^\dagger(\boldsymbol{r}, \boldsymbol{r}')$ creates a pair of particles at $\boldsymbol{r}$ and $\boldsymbol{r}'$ in the total spin state $|\mathcal{F}\mathcal{M}\rangle$, where $\mathcal{M}$ represent the projection of spin along quantization axis. We also have the interaction coefficient $g_{\mathcal{F}} = 4\pi\hbar^2 a_{\mathcal{F}}/M$. The interaction can be represented in terms of single-particle field operators $\hat{\Psi}_m(\boldsymbol{r})$, using Clebsh-Gordon coefficients as,

$$\hat{A}_{\mathcal{F}\mathcal{M}}(\boldsymbol{r}, \boldsymbol{r}') = \sum_{m,m'=-1}^{1} \langle \mathcal{F}, \mathcal{M} | 1, m; 1, m' \rangle \hat{\Psi}_m(\boldsymbol{r}) \hat{\Psi}_m(\boldsymbol{r}'), \tag{2.40}$$

where $|f, m; f', m'\rangle$ represents the product state of two bosons with spin and projection values f, f' and m, m', respectively. Using Eq. (2.40) in (2.39), we arrive at,

$$\hat{V}^{(F)} = \frac{g_{\mathcal{F}}}{2} \sum_{\substack{m_1, m_1' \\ m_2, m_2'}} \langle 1, m_1; 1, m_1' | \hat{P}_{\mathcal{F}} | 1, m_2; 1, m_2' \rangle \int d\boldsymbol{r} \hat{\Psi}^{\dagger}_{m_1}(\boldsymbol{r}) \hat{\Psi}^{\dagger}_{m_1'}(\boldsymbol{r}) \hat{\Psi}_{m_2}(\boldsymbol{r}) \hat{\Psi}_{m_2'}(\boldsymbol{r}), \tag{2.41}$$

where operator $\hat{P}_{\mathcal{F}} = \sum_{M=-\mathcal{F}}^{\mathcal{F}} |\mathcal{F}, \mathcal{M}\rangle \langle \mathcal{F}, \mathcal{M}|$ projects a two particle spin-state onto the total spin-$\mathcal{F}$ subspace.

Now, the spin-1 spin matrices f_ν are given as,

$$f_x = \frac{1}{\sqrt{2}} \begin{pmatrix} 0 & 1 & 0 \\ 1 & 0 & 1 \\ 0 & 1 & 0 \end{pmatrix}, \quad f_y = \frac{i}{\sqrt{2}} \begin{pmatrix} 0 & -1 & 0 \\ 1 & 0 & -1 \\ 0 & 1 & 0 \end{pmatrix}, \quad f_z = \begin{pmatrix} 1 & 0 & 0 \\ 0 & 0 & 0 \\ 0 & 0 & 1 \end{pmatrix}. \tag{2.42}$$

Then, the two body operator $\boldsymbol{f}_1 \cdot \boldsymbol{f}_2$, where vector $\boldsymbol{f} = (f_x, f_y, f_z)$, can be expressed as,

$$\boldsymbol{f}_1 \cdot \boldsymbol{f}_2 = \frac{1}{2} \left[(\boldsymbol{f}_1 + \boldsymbol{f}_2)^2 - f_1^2 - f_2^2 \right]. \tag{2.43}$$

The total spin operator $(\boldsymbol{f}_1 + \boldsymbol{f}_2)^2$ has eigenvalue given by $(\boldsymbol{f}_1 + \boldsymbol{f}_2)^2 |F, M\rangle = \mathcal{F}(\mathcal{F}+1) |\mathcal{F}, \mathcal{M}\rangle$, in the total spin-$\mathcal{F}$ subspace. Since we are only dealing with spin-1 particles, f_1^2, f_2^2 can be replaced with their eigenvalue $f(f+1)$, where $f = 1$. Using these relations, and the projector operator, we can write $\boldsymbol{f}_1 \cdot \boldsymbol{f}_2 = \frac{1}{2} \sum_{\mathcal{F}=0,2} [\mathcal{F}(\mathcal{F}+1) - 4] \hat{P}_{\mathcal{F}} = \hat{P}_2 - 2\hat{P}_0$. The projection operator also satisfies $\mathbf{I} = \hat{P}_0 + \hat{P}_2$, where $\mathbf{I}$ is the identity matrix in $\mathcal{F} = 0, 2$ space. Therefore, the projection operators in Eq.(2.41) can be replaced as $\hat{P}_0 = (\mathbf{I} - \boldsymbol{f}_1 \cdot \boldsymbol{f}_2)/3$ and $\hat{P}_2 = (2\mathbf{I} + \boldsymbol{f}_1 \cdot \boldsymbol{f}_2)/3$, which gives us [73],

$$\hat{V} = \frac{1}{2} \int d\boldsymbol{r} \left[c_0 :\hat{n}^2(\boldsymbol{r}): + c_1 :\hat{\boldsymbol{F}}(\boldsymbol{r}). \cdot \hat{\boldsymbol{F}}(\boldsymbol{r}): \right] \tag{2.44}$$

Here, $c_0 = (g_0 + 2g_2)/3$ and $c_1 = (g_2 - g_0)/3$ are called the spin-independent and spin-dependent interaction coefficients, and the operators,

$$\begin{aligned} \hat{n}(\boldsymbol{r}) &= \sum_m \hat{\Psi}^{\dagger}_m(\boldsymbol{r}) \hat{\Psi}_m(\boldsymbol{r}) \\ \hat{F}_\nu(\boldsymbol{r}) &= \sum_{mm'} \hat{\Psi}^{\dagger}_m(\boldsymbol{r}) (f_\nu)_{mm'} \hat{\Psi}_{m'}(\boldsymbol{r}), \end{aligned} \tag{2.45}$$

with : : denoting the normal ordering of operators inside it.

2.6.1 Mean-field theory

In the mean-field theory (Sec. 2.3), we assume that all particles occupy the same quantum state. For the spin-1 spinor BEC, the mean-field state will have a spin part in addition to the spatial part, and can be expressed as $\boldsymbol{\psi} = (\psi_1, \psi_0, \psi_{-1})^T$. Here, $\psi_m(\boldsymbol{r})$ represents the wavefunction of the m^{th} spin state, and a many-body state can be constructed as,

$$|\Psi\rangle = \left(\sum_m \hat{a}_m^\dagger\right)^N |\Phi\rangle . \tag{2.46}$$

Here, operator $\hat{a}_m$ annihilates a particle in $\psi_m(\boldsymbol{r})$ in spin-state m. We can show that the expectation value for the mean-field state for the following operators to be [89],

$$\begin{aligned} \langle \hat{\Psi}_m^\dagger(\boldsymbol{r})\hat{\Psi}_{m'}(\boldsymbol{r}')\rangle &= N\psi_m^*(\boldsymbol{r})\psi_{m'}(\boldsymbol{r}') \\ \langle \hat{\Psi}_{m_1}^\dagger(\boldsymbol{r}_1)\hat{\Psi}_{m_2}^\dagger(\boldsymbol{r}_2)\hat{\Psi}_{m_1'}(\boldsymbol{r}_1')\hat{\Psi}_{m_2'}(\boldsymbol{r}_2')\rangle &\approx N^2\psi_{m_1}^*(\boldsymbol{r}_1)\psi_{m_2}^*(\boldsymbol{r}_2)\psi_{m_1'}(\boldsymbol{r}_1')\psi_{m_2'}(\boldsymbol{r}_2'), \end{aligned} \tag{2.47}$$

where we have used $N(N-1) \approx N^2$ for $N \gg 1$. Using the above relation, we obtain the mean-field expectation value for the spin-1 Hamiltonian (2.37) as,

$$E[\psi] = \int d\boldsymbol{r}\psi_m{}^*(\boldsymbol{r})\left[-\frac{\hbar^2\nabla^2}{2M} + V_T(\boldsymbol{r}) - pm + qm^2\right]\psi_m(\boldsymbol{r}) + \frac{1}{2}\int d\boldsymbol{r}\left[c_0 n(\boldsymbol{r})^2 + c_1|\boldsymbol{F}(\boldsymbol{r})|^2\right]. \tag{2.48}$$

Here, $n(\boldsymbol{r}) = \sum_m |\psi_m(\boldsymbol{r})|^2$ denotes the total density of the condensate. The spin-density vector $\boldsymbol{F}(\boldsymbol{r})$ has components, $F_\nu(\boldsymbol{r}) = \sum_{mm'} \psi_m^*(\boldsymbol{r})(f_\nu)\psi_{m'}(\boldsymbol{r})$, where $\nu \in \{x, y, z\}$ and the f_ν are the spin-1 spin matrices defined in (2.43). Note that here we have renormalized the mean-field order parameter to the total number of particles as $\int d\boldsymbol{r} \sum_m |\psi_m|^2 = N$. The interaction energy can be split into a spin-independent energy (containing coefficient c_0) and a spin-dependent energy (containing coefficient c_1). Spin-independent energy depends only on the total density profile of the condensate, whereas the spin-dependent energy also depends its the spin-state.

The ground state of the system can be obtained by minimizing Eq. (2.48) with the constraint that the norm of the order parameter is N. The evolution of the order-parameter is also derived similar to the spin-0 boson case [89], which gives us,

$$i\hbar\frac{\partial\psi_1}{\partial t} = \left[-\frac{\hbar^2\nabla^2}{2M} - p + q + c_0 n + c_1 F_z\right]\psi_1 + \frac{c_1}{\sqrt{2}}F_-\psi_0 \tag{2.49}$$

$$i\hbar\frac{\partial\psi_0}{\partial t} = \left[-\frac{\hbar^2\nabla^2}{2M} + c_0 n\right]\psi_0 + \frac{c_1}{\sqrt{2}}\left[F_+\psi_1 + F_-\psi_{-1}\right] \tag{2.50}$$

$$i\hbar\frac{\partial\psi_{-1}}{\partial t} = \left[-\frac{\hbar^2\nabla^2}{2M} + p + q + c_0 n - c_1 F_z\right]\psi_{-1} + \frac{c_1}{\sqrt{2}}F_+\psi_0. \tag{2.51}$$

Note that the ground state can also be obtained as the stationary solution to the time-dependent GPE by solving,

$$i\hbar\frac{\partial\psi(\boldsymbol{r})}{\partial t} = \mu\psi(\boldsymbol{r}), \tag{2.52}$$

where μ is the chemical potential of the condensate.

2.6.2 Quantum phases of homogenous gas

Even a homogeneous spinor gas has multiple ground-state phases due to its internal degrees of freedom. By varying the parameters such as the Zeeman terms p and q, one can traverse across these phases, and this is an example of a quantum phase transition [17, 78, 148].

Consider a homogenous spin-1 gas with density n. The general form of the mean-field order parameter describing the system is given as,

$$\psi = \sqrt{n}\begin{pmatrix}\zeta_1\\ \zeta_0\\ \zeta_{-1}\end{pmatrix}, \tag{2.53}$$

where the complex numbers ζ_m satisfy $\sum_m |\zeta_m|^2 = 1$, and the density of the spin-component m being $n_m = n|\zeta_m|^2$. The mean-field energy per particle for this state is,

$$\epsilon = -p\left(|\zeta_1|^2 - |\zeta_{-1}|^2\right) + q\left(|\zeta_1|^2 + |\zeta_{-1}|^2\right) + \frac{1}{2}\left[c_0 n + c_1|\boldsymbol{F}|^2\right], \tag{2.54}$$

where $F_\nu = n\sum_{mm'}\zeta_m^*(f_\nu)_{mm'}\zeta_{m'}$ denotes the uniform spin-density vector.

The ground state value of $\boldsymbol{\zeta}$ is obtained by minimizing the energy ϵ. To see how various phases arise, we first consider the case when $p = q = 0$. In this case, the minimum energy configuration depends on the sign of c_1. If $c_1 > 0$, a state which has $\boldsymbol{F} = \boldsymbol{0}$ would be the ground state, whereas if $c_1 < 0$, it would have maximum spin-density $|\boldsymbol{F}| = n$. The presence of non-zero Zeeman terms adds additional complexity. For example, a large positive p corresponds to the $m = 1$ spin state having much lower energy than the other two states. Thus, for sufficiently large p, all particles will be in the $m = 1$ state regardless of c_1, which gives us a fully magnetized condensate. The phase diagram for the spin-1 homogeneous condensate is given in Fig. (2.2) for positive and negative c_1.

In the following, we shall briefly discuss the different phases present in the spin-1 BEC.

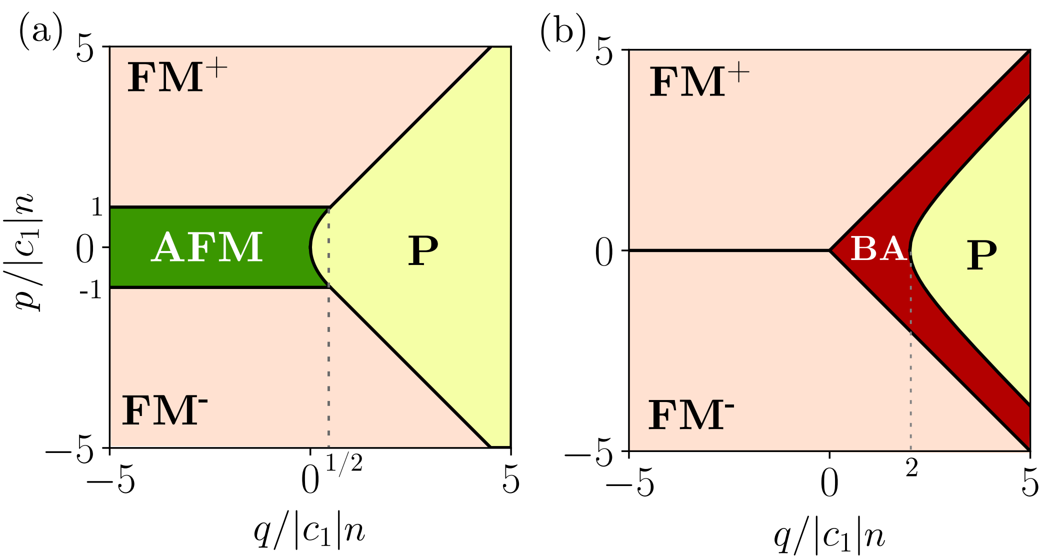

FIGURE 2.2: Phase diagram of homogeneous spin-1 BEC for spin-dependent interaction coefficient (a) $c_1 > 0$ and (b) $c_1 < 0$.

Ferromagnetic (FM) phase

In the ferromagnetic (FM) phase, the condensate is maximally polarized (i.e. $|\boldsymbol{F}|/n = 1$). In the absence of any external field ($p = q = 0$), the spin-density vector can be oriented in any direction due to the rotational symmetry, and the order-parameter (when $c_1 < 0$) takes the general form,

$$\zeta_{FM} = e^{i\phi}\begin{pmatrix} e^{-i\alpha}\cos^2(\beta/2) \\ \sin\beta/\sqrt{2} \\ e^{i\alpha}\sin^2(\beta/2) \end{pmatrix}, \tag{2.55}$$

where components of the spin-density vector is related to angles α,β as $\boldsymbol{F} = n(\cos\alpha\sin\beta,$ $\sin\alpha\sin\beta, \cos\beta)$. In this case, the system would spontaneously choose an orientation upon entering the ground state.

The rotational symmetry is lost by applying a magnetic field, and the spin vector is oriented along the field to minimize energy. If the quantization axis and the external field are along the z-direction, then in the FM phase, all the atoms occupy $m = 1$ state (FM$^+$) or $m = -1$ state (FM$^-$). When $c_1 > 0$, the FM state is the ground state when $|p| > c_1 n$ and $|p| > q + c_1 n/2$ (Fig. 2.2). On the other hand, when $c_1 < 0$, it would be the ground state if $|p| > q$.

Polar (P) phase

In the polar phase, the population is present only in the $m = 0$ state, with the order-parameter being $\zeta = (0, 1, 0)^T$. The system will have zero spin density ($\boldsymbol{F} = 0$) in this phase. We can show that, by minimizing the energy [Eq. (2.54)], the polar state would be the ground state if $q > |p| - c_1 n/2$ and $q > p^2/2c_1 n$ if the spin-dependent interaction coefficient is positive ($c_1 > 0$), or $q^2 > p^2 + 2|c_1|nq$, if the coefficient is negative ($c_1 > 0$) [89].

Antiferromagnetic (AFM) phase

In the antiferromagnetic (AFM) phase, boson are in a superposition of $m = \pm 1$ components with the order-parameter being $\zeta = (n/\sqrt{2})([1+F_z]^{1/2}, 0, e^{i\phi}[1-F_z]^{1/2})^T$, where $F_z = p/c_1$ being the component of magnetization. The phase ϕ is chosen spontaneously, making the AFM phase a symmetry-broken phase. The details of this broken symmetry are discussed in detail in chapter 6. AFM phase can only exist when $c_1 > 0$, and it would be the ground state when $|p| < c_1 n$ and $q < p^2/2c_1 n$.

When $p = q = 0$, polar and AFM are energetically degenerate. In this case, the general form of the ground state (when $c_1 > 0$) is given as,

$$\zeta_P = e^{i\phi} \begin{pmatrix} -e^{-i\alpha}\sin(\beta)/\sqrt{2} \\ \cos\beta \\ e^{i\alpha}\sin(\beta)/\sqrt{2} \end{pmatrix}, \tag{2.56}$$

where change in angles α, β corresponds to rotation in spin-space. We can also define unit vector $\hat{\boldsymbol{d}} = (\cos\alpha\sin\beta, \sin\alpha\sin\beta, \cos\beta)$, called the director. For the polar phase, $\hat{\boldsymbol{d}}$ is oriented along the z-axis, whereas for the AFM phase at $p = 0$, it is perpendicular to the axis. Thus, polar and $p = 0$ AFM phases can be transformed into each other via spin space rotation.

Broken axisymmetry phase

We shall also briefly touch upon the broken axisymmetry(BA) phase, which occurs when $c_1 < 0$. In this case, the presence of a positive quadratic Zeeman term q implies that it is energetically favourable to have the spin-density vector with a component perpendicular to the spin-space z-axis. The condensate is generally not fully magnetized in this case, with $|\boldsymbol{F}| < n$ when $q > 0$. The order-parameter for this system, when $p = 0$, is given as,

$$\zeta_{BA} = \frac{1}{2} \begin{pmatrix} e^{i\phi}\sqrt{1+q/2c_1 n} \\ \sqrt{2(1-q/2c_1 n)} \\ e^{-i\phi}\sqrt{1+q/2c_1 n} \end{pmatrix}. \tag{2.57}$$

In this case, the spin component $F_z = 0$, and $F_\perp = q\sqrt{(4c_1^2 n^2 - q^2)/2|c_1|n}$. The direction of the spin-density vector in the xy plane is determined by the phase ϕ, and by choosing a particular direction, the state breaks the rotational symmetry of the system about the z-axis. BA phase exist only when $c_1 < 0$ and it is stable when $|p| < q$ and $q^2 < |p|^2 + 2|c_1|nq$.

2.6.3 Elementary excitations in spinor BEC

In this section, we discuss the Bogoliubov theory of spin-1 condensate. An operator approach to this, similar to the one discussed in Sec . 2.5.1, is detailed in Ref. [89]. In this section, however, we outline the BdG approach, which can also be used to obtain the same results.

The BdG equations for the spin-1 homogeneous gas are obtained by using the perturbed ground state solution given by,

$$\psi(t) = [\sqrt{n}\zeta + \delta\psi(t)]e^{-i\mu t}, \tag{2.58}$$

and the perturbation $\delta\psi$ is expanded as,

$$\delta\psi(t) = e^{i\boldsymbol{k}\cdot\boldsymbol{r}}\begin{pmatrix} u_1 \\ u_0 \\ u_{-1} \end{pmatrix} e^{-i\omega t} + e^{-i\boldsymbol{k}\cdot\boldsymbol{r}}\begin{pmatrix} v_1^* \\ v_0^* \\ v_{-1}^* \end{pmatrix} e^{i\omega t}. \tag{2.59}$$

Here we see that the Bogoliubov amplitudes $\boldsymbol{u}$ and $\boldsymbol{v}$ are also three-component vectors. We have also used a plane wave ansatz for amplitudes due to the translational symmetry of the system. Using Eq. (2.58) in the GPE (2.49)-(2.51) and linearizing in u_m, v_m, we obtain the following eigenvalue equation,

$$\begin{pmatrix} \boldsymbol{B}_0(k) & \boldsymbol{B}_1(k) \\ -\boldsymbol{B}_1(k)^* & -\boldsymbol{B}_0^*(k) \end{pmatrix}\begin{pmatrix} \boldsymbol{u} \\ \boldsymbol{v} \end{pmatrix} = \hbar\omega(k)\begin{pmatrix} \boldsymbol{u} \\ \boldsymbol{v} \end{pmatrix}, \tag{2.60}$$

where $\boldsymbol{u} = (u_1, u_0, u_{-1})^T$ and $\boldsymbol{v} = (v_1, v_0, v_{-1})^T$, and $\boldsymbol{B}_{0,1}(k)$ are 3×3 matrices. We can diagonalize the matrix to obtain three distinct eigenvalues, as eigenvalues occur in pairs as $\pm\epsilon$. Thus we obtain three branches in the Bogoliubov spectra for spin-1 BEC, due to their spin degrees of freedom. The nature of the excitation can be understood from the amplitudes $\boldsymbol{u}$, $\boldsymbol{v}$. For different phases, distinct excitations occurs [179], and the dynamical stability of various phases for a given set of parameters can be seen from the excitation energies of the quasiparticles, as the energies attain an imaginary part when the system is dynamically unstable.

2.7 Floquet theory

Floquet theory is a powerful mathematical tool for analysing systems with periodic time dependence [109]. It has been applied to a wide range of driven problems, including quantum tunnelling [67], strongly correlated systems [86, 178], atoms in laser fields [36], and Floquet engineering of quantum systems [130], and its spatial analogy is Bloch's theorem in condensed matter. Although Floquet theory is only applicable to linear time-periodic systems, it remains useful for nonlinear systems as well, particularly when analyzing the linearized dynamics of small perturbations, where the theory still holds.

In this section, we introduce Floquet's theory and present a sketch of its proof, following the lecture notes by M. J. Ward [188]. We also outline a method for computing the Floquet exponents, which are crucial for understanding the stability of periodically driven systems. Finally, we discuss the Mathieu differential equation, an important example of a Floquet-type system, and examine its stability diagram.

We consider a general coupled linear differential equation of the form,

$$\frac{d\boldsymbol{x}}{dt} = \boldsymbol{A}(t)\boldsymbol{x}, \tag{2.61}$$

where the variable are written as a column vector $\boldsymbol{x} = (x_1, x_2, \ldots, x_n)^T$ and$\boldsymbol{A}(t)$ is an $n \times n$ matrix is periodic with period T, $\boldsymbol{A}(t+T) = \boldsymbol{A}(t)$. The solution to the above differential equation need not be periodic, but it will have the form,

$$\boldsymbol{x}(t) = e^{\sigma t}\boldsymbol{p}(t), \tag{2.62}$$

where $\boldsymbol{p}(t) = \boldsymbol{p}(t+T)$ is a periodic function. This is the Floquet theory, and σ is called the *Floquet exponent*. Over one period of evolution, the solution will acquire a factor $\boldsymbol{x}(t+T) = e^{\sigma T}\boldsymbol{x}(t)$. This property means that you only need to solve the solution for a single period to obtain the full information regarding the system's dynamics. The long-term dynamics of the system are determined by the value of the exponent; if $\mathrm{Re}\{\sigma\} > 0$, then the solution will grow exponentially, and if $\mathrm{Re}\{\sigma\} < 0$, it decays exponentially. If $\mathrm{Re}\{\sigma\} = 0$, then the solution is periodic or quasi-periodic. Thus, the value of the exponent will have implications for the stability of the driven system.

The Floquet exponents are a property of the differential equation (2.61) alone, and do not depend on the choice of initial state. In fact, we can show that it follows,

$$\prod_{i=1}^{n} e^{\sigma_i T} = \exp\left(\int_0^T \mathrm{tr}(A(t))dt\right), \tag{2.63}$$

where σ_i, with $i = 1, 2, \ldots, n$ are the n Floquet exponents of the system.

2.7.1 Proof of Floquet theory

In this subsection, we discuss the proof of the Floquet theory and how to find the Floquet exponents. First, we defined the fundamental matrix $\boldsymbol{X}(t)$, which is an $n \times n$ matrix, with its columns being $\boldsymbol{x}^{(i)}(t)$, the linearly independent solutions of Eq. (2.61). That is,

$$\boldsymbol{X}(t) = \left(\begin{bmatrix} \\ \boldsymbol{x}^{(1)}(t) \\ \\ \end{bmatrix} \begin{bmatrix} \\ \boldsymbol{x}^{(2)}(t) \\ \\ \end{bmatrix} \cdots \begin{bmatrix} \\ \boldsymbol{x}^{(n)}(t) \\ \\ \end{bmatrix} \right). \tag{2.64}$$

Therefore we have $d\boldsymbol{X}(t)/dt = \boldsymbol{A}(t)\boldsymbol{X}(t)$. We can then show that if $\boldsymbol{X}(t)$ is a fundamental matrix, then so is $\boldsymbol{X}'(t) = \boldsymbol{X}(t)\boldsymbol{B}_0$, where $\boldsymbol{B}_0$ is a non-singular constant matrix. This can be proved by simply taking the derivative of $\boldsymbol{X}'(t)$,

$$\frac{d}{dt}\boldsymbol{X}'(t) = \frac{d}{dt}\boldsymbol{X}(t)\boldsymbol{B}_0 = \boldsymbol{A}(t)\boldsymbol{X}(t)\boldsymbol{B}_0 = \boldsymbol{A}(t)\boldsymbol{X}'(t). \tag{2.65}$$

Now, we define matrix $\boldsymbol{B}$ such that $\boldsymbol{X}(t+T) = \boldsymbol{X}(t)\boldsymbol{B}$, where $\boldsymbol{B}$ can be proven to be time-independent. First, we note that $\boldsymbol{X}(t+T)$ is a also a fundamental matrix,

$$\frac{d}{dt}\boldsymbol{X}(t+T) = \boldsymbol{A}(t+T)\boldsymbol{X}(t+T) = \boldsymbol{A}(t)\boldsymbol{X}(t+T). \tag{2.66}$$

Consider $\boldsymbol{X}'(t) \equiv \boldsymbol{X}(t)\boldsymbol{B}(0)$, which is also a fundamental matrix as $\boldsymbol{B}(0)$ is a constant. Then we have, $\boldsymbol{X}'(0) = \boldsymbol{X}''(0)$, where we defined $\boldsymbol{X}''(t) \equiv \boldsymbol{X}(t+T) = \boldsymbol{X}(t)\boldsymbol{B}$. Since both $\boldsymbol{X}'$ and $\boldsymbol{X}''$ have the same initial condition and both satisfy the same equation, they must be equal at all times. This implies that $\boldsymbol{B}(t) = \boldsymbol{B}(0)$, i.e. the matrix is time-independent.

Now, as a final step of proof, we show that there exist solutions of the form $\boldsymbol{x}(t) = e^{\sigma t}\boldsymbol{p}(t)$. Let ρ and $\boldsymbol{b}$ be an eigenvalue and corresponding eigenvector, respectively, to matrix $\boldsymbol{B}$. The function $\boldsymbol{x}(t) = \boldsymbol{X}(t)\boldsymbol{b}$ is a solution to Eq. (2.61).

$$\frac{d\boldsymbol{x}(t)}{dt} = \frac{d\boldsymbol{X}(t)}{dt}\boldsymbol{b} = \boldsymbol{A}(t)\boldsymbol{X}(t)\boldsymbol{b} = \boldsymbol{A}(t)\boldsymbol{x}(t). \tag{2.67}$$

We can also show that $\boldsymbol{x}(t+T) = \rho\boldsymbol{x}(t)$ for such a solution. Now chose exponent $\sigma = (1/T)\log(\rho)$ or $\rho = e^{\sigma T}$. If we define $\boldsymbol{p}(t) = e^{-\sigma t}\boldsymbol{x}(t)$, then $\boldsymbol{p}(t)$ is periodic with period T.

$$\begin{aligned} \boldsymbol{p}(t+T) &= e^{-\sigma(t+T)}\boldsymbol{x}(t+T) \\ &= \rho^{-1}e^{-\sigma t}\rho\boldsymbol{x}(t) \\ &= e^{-\sigma t}\boldsymbol{x}(t) = \boldsymbol{p}(t). \end{aligned} \tag{2.68}$$

Thus, we have proved the Flqouet theory for equation Eq. (2.61).

Calculating the Floquet exponent

In order to numerically calculate the Floquet exponent for a linear differential equation with periodic coefficients, we obtain the fundamental matrix for a single time period $\boldsymbol{X}(T)$. Then the monodromy matrix can be found as $\boldsymbol{B}_T = \boldsymbol{X}(0)^{-1}\boldsymbol{X}(T)$. We usually chose $\boldsymbol{X}(0) = \boldsymbol{I}$ without loss of generality, thus $\boldsymbol{B}_T = \boldsymbol{X}(T)$. The characteristic multipliers ρ are then the eigenvalues of $\boldsymbol{B}_T$ and the Floquet exponents are given as $\sigma = (1/T)\log(\rho)$. Solving for $\boldsymbol{X}(T)$ can be implemented using methods such as RK4, where we solve for n different initial conditions chosen from $\boldsymbol{X}(0) = \boldsymbol{I}$.

2.7.2 Mathieu equation

Consider the equation of the following form,

$$\frac{d^2u}{dt^2} + [A + 2B\cos(2t)]\,u = 0. \tag{2.69}$$

Choosing $u_0(t) = u(t)$ and $u_1(t) = du/dt$, we get,

$$\frac{d}{dt}\begin{pmatrix} u_0 \\ u_1 \end{pmatrix} = \begin{pmatrix} 0 & 1 \\ -[A + 2B\cos(2t)] & 0 \end{pmatrix}\begin{pmatrix} u_0 \\ u_1 \end{pmatrix}, \tag{2.70}$$

which is of the form given in Eq. (2.61). Therefore, we can use Floquet theory and look for solutions of form $u(t) = e^{\sigma t}p(t)$. From the relation Eq. (2.63), we can see that $\rho_1\rho_2 = 1$, or

$$\sigma_1 = -\sigma_2. \tag{2.71}$$

The stability of the solutions is determined from the exponent. For the Mathieu equations, two cases can occur,

1. If $\mathrm{Re}\{\sigma\} > 0$ for any of the exponents, the system is unstable
2. If $\mathrm{Re}\{\sigma\} = 0$ for all of the exponents, the system is stable.

The stability diagram is obtained by numerically solving the equation for various values of A and B, shown in Fig. 2.3.

When the coefficient of the periodic term, B, is zero, the system is always stable. For infinitesimally small B, the instability occurs near $A = j^2$, where $j = 1, 2, 3$. These are the resonance points where even a weak driving cause an instability, and the strongest resonance, as characterized by magnitude of σ, occurs at $A = 1 (m = 1)$

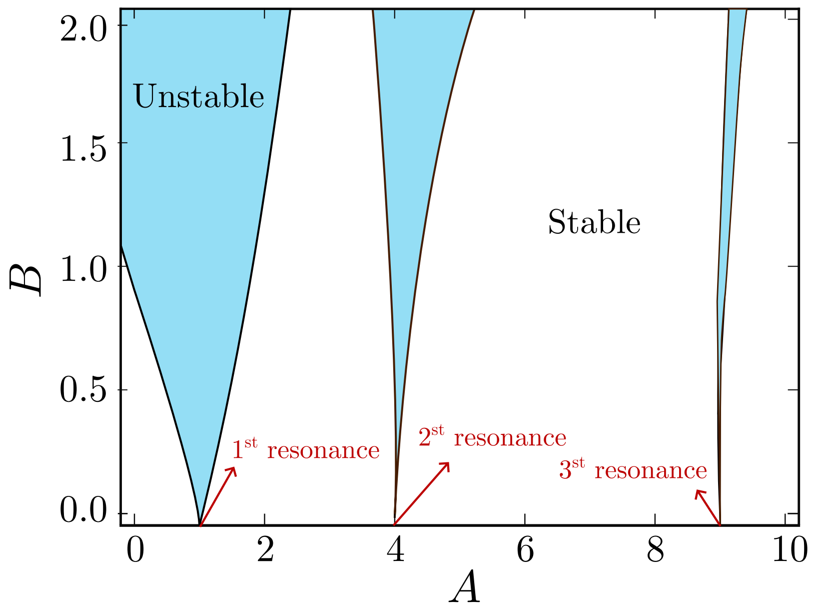

FIGURE 2.3: Stability diagram for Mathieu equation (2.69)

We shall also briefly discuss Bloch's theorem, which is the Floquet theory applied to a quantum system of a particle in a periodic potential. We have the Schrödinger equation,

$$\frac{\hbar^2}{2M}\frac{d^2\psi}{dx^2} + [V_0\cos(k_0 x) - E]\psi = 0, \tag{2.72}$$

where V_0 is the depth of the potential. Bloch's theorem states that the solutions are of the form $\psi(z) = e^{ikx}u(x)$, where $u(x + 2\pi/k_0) = u(x)$ is a periodic function. After converting it into standard form Eq. (2.69), we can show that the instability region corresponds to the energy gaps, where the exponentially diverging unphysical solution occurs.

2.8 Faraday waves in driven condensate

The phenomenon of formation of regular standing waves on the surface of a vibrating fluid was first reported by Michael Faraday in 1831 [53, 114]. He noted that the frequency of the waves was half that of the driving frequency. Benjamin and Ursell gave a theoretical explanation for this phenomenon in 1954 [9] using linear stability analysis of the surface modes of the fluids. Analogous phenomena occur in BEC as well [49, 162] under modulation of the interaction between the particles. In this section, we discuss the theory of Faraday wave formation in BEC, and find that we obtain a Mathieu equation for the linearized dynamics for the unstable modes, which explains the wave number selection and the sub-harmonic response of the system.

In the second part of this section, we look at the driven dynamics of a spin-1 spinor BEC which is initialized in the ferromagnetic phase, where we see that the dynamics are analogous to those of a spin-0 condensate [85].

2.8.1 Quasi-two dimensional spin-0 condensate

Here, we consider a homogeneous Q2D condensate [see Sec. 2.4] with its s-wave scattering length driven as,

$$a_s(t) = \bar{a}_s\,[1 + 2\alpha\cos 2\omega t]\,, \tag{2.73}$$

where $\bar{a}_s$ is the mean scattering length, and α and ω are the amplitude and (half the) frequency of the periodic driving. The following Q2D GPE describes such a system,

$$i\hbar\frac{\partial\bar{\psi}}{\partial t} = \left[-\frac{\hbar^2\nabla_\rho^2}{2M} + g_{2D}(t)|\bar{\psi}|^2\right]\bar{\psi}, \tag{2.74}$$

where $\bar{\psi}(x, y)$ is the Q2D mean-field order parameter of the system, and $g_{2D}(t) = \bar{g}_{2D}[1 + 2\alpha\cos 2\omega t]$ with $\bar{g}_{2D} = 4\pi\hbar^2\bar{a}_s(t)/\left(\sqrt{2\pi}Ml_z\right)$ is Q2D interaction coefficient. Here, $l_z = \sqrt{\hbar/M\omega_z}$ is the characteristic length of the longitudinal trap of the system, with trap frequency ω_z. We assume that the trap is sufficiently strong to confine the dynamics along the xy-plane, thus allowing us to use the Q2D GPE (2.74).

In the absence of periodic driving, i.e. $a_s(t) = \bar{a}_s$, the ground state of the system is homogeneous in the xy-plane, due absence of transverse trap. In presence of the driving as given in Eq. (2.73), the uniform solution $\bar{\psi}_H(t) = \sqrt{n_H}\exp[i\theta(t)]$ satisfy the GPE (2.74), where the time dependent phase is given as,

$$\theta(t) = \bar{g}_{2D}n_H\left[t + \frac{\alpha}{\omega}\sin(2\omega t)\right]. \tag{2.75}$$

Here, n_H denotes the 2D homogeneous density of the condensate. Although the driven GPE has a uniform solution, it's not stable against the growth of density patterns when perturbed. To see this, we consider the ansatz $\bar{\psi}(t) = \left[\sqrt{n_H} + w(t)\cos(\boldsymbol{k}\cdot\boldsymbol{\rho})\right]\exp[i\theta(t)]$, where $\boldsymbol{\rho} = x\hat{x} + y\hat{y}$. Here we have the amplitude of the modulated perturbation $w(t) = u(t) + iv(t)$, with $|w(0)| \ll 1$, and $\boldsymbol{k}$ represents the amplitude and the wave vector of the plane wave perturbation, respectively. Using this ansatz in the GPE (2.74), and linearizing in u, v, we arrive at the following equations of motion for the perturbation amplitude,

$$\hbar\frac{du}{dt} = E_k v, \quad \hbar\frac{dv}{dt} = -[E_k + 2g_{2D}(t)n_H]u \tag{2.76}$$

which can then be expressed as [162],

$$\hbar^2\frac{d^2u}{dt^2} + \left[\epsilon^2(k) + 4E_k\alpha\bar{g}_{2D}n_H\cos(2\omega t)\right]u = 0. \tag{2.77}$$

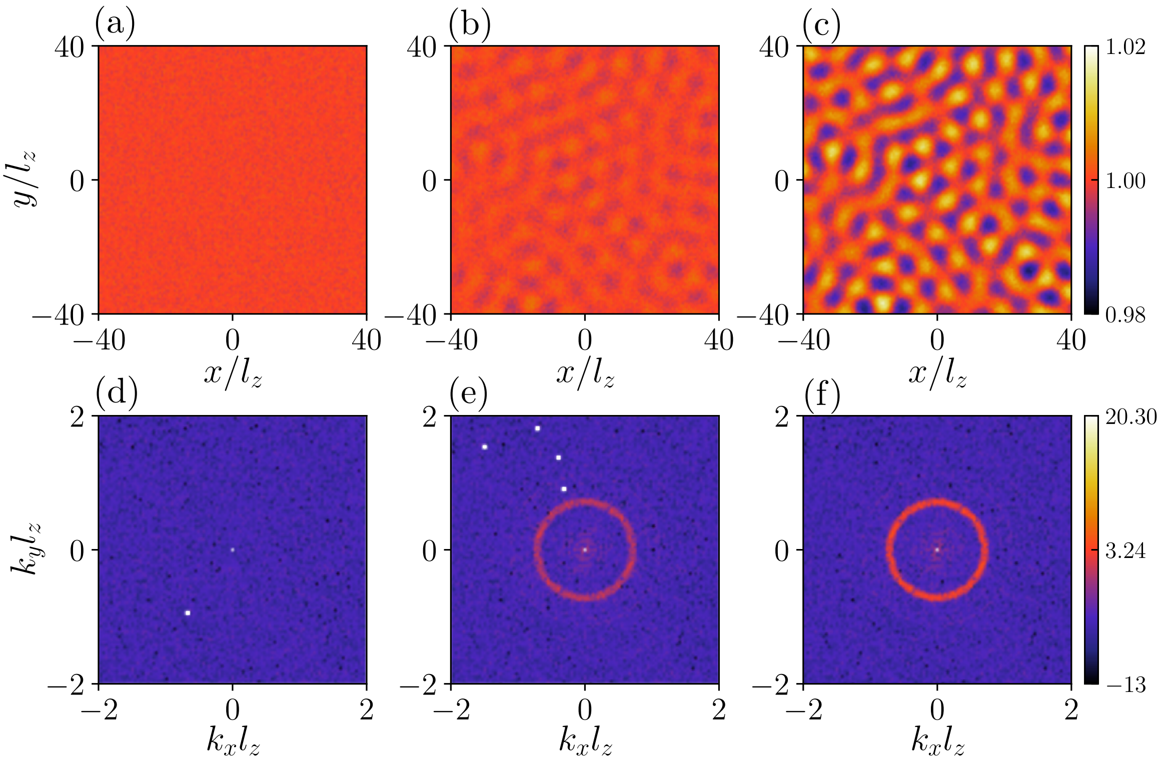

FIGURE 2.4: *Formation of Faraday waves in driven condensate*: The [(a)-(c)] real space density $n_{2D} = |\bar{\psi}|^2$ and [(e)-(f)] the log of moment space density $\tilde{n}_{2D} = |\bar{\psi}'|^2$ at three different times for driven spin-0 condensate. The system parameters are $\bar{g}_{2D} n_H = 0.2\hbar\omega_z$, $\alpha = 0.4$, and $\omega = 0.4\omega_z$.

Here, $E_k = \hbar^2 k^2/2M$ and $\epsilon(k) = \sqrt{E_k(E_k + 2\bar{g}_{2D} n_H)}$ is the Q2D dispersion relation of the system (see Sec. 2.5.1). Eq. (2.77) is a Mathieu equation. As discussed in Sec . 2.7.2, the Mathieu equation has unstable solutions if its Floquet exponent σ has a positive real part. For very weak driving amplitude, $\alpha \to 0$, the instability occur if $j\hbar\omega = \epsilon(k)$, where $j = 1, 2, \ldots$. The strongest resonance, i.e. the one with largest $\mathrm{Re}\{\sigma\}$, occur for mode with momenta k_u which satisfy $\hbar\omega = \epsilon(k_u)$ ($j = 1$). Since the growth of the unstable mode is exponential, the most unstable mode dominates the dynamics. The condensate density under the perturbation is given as,

$$n(x, y) = n_H + 2\sqrt{n_H} u(t) \cos(\boldsymbol{k}_u \cdot \boldsymbol{\rho}) + O(w^2). \tag{2.78}$$

Thus, the presence of unstable modes results in pattern formation in the initially homogeneous condensate. In 1D geometry, instability causes sinusoidal patterns with wavelength $2\pi/k_u$, whereas in 2D geometry, there are many unstable wave vectors with magnitudes $|\boldsymbol{k}| = k_u$, which lie on a ring in the k_x-k_y momentum space. The superposition of these individual density waves gives rise to a distinct pattern that features a Bessel function density correlation [128].

In Fig. 2.4, we show the density formation under periodic driving of scattering length in a Q2D condensate, obtained from the numerical simulation of the GPE (2.74). To trigger the instability, we add a small random noise to the initial wavefunction at each grid point [58], which mimics the quantum fluctuations present in the real condensate. Under the modulation of scattering length, the uniform state becomes unstable to the formation of patterns, which can be seen in Fig. 2.4 (a)-(c). From the momentum space density of the system (Fig. 2.4 (d)-(f)), defined as $\tilde{n}(k_x, k_y) = |\bar{\psi}'(k_x, k_y)|^2$ with $\bar{\psi}'$ being the Fourier transform of $\bar{\psi}$, we see population spike in the annular region in the k_x-k_y plane with radius k_u. This shows how the driving excites modes with the momentum satisfying the resonance condition.

We also note the condensate response is sub-harmonic, resulting from the parametric excitation of the modes. The condensate is driven with a frequency 2ω, and the density patterns oscillate with frequency ω. The linear stability analysis only captures the dynamics during the initial phase of the driving, when the population in the excited ($\boldsymbol{k} \neq 0$) states is much lower than the condensate mode ($\boldsymbol{k} = 0$) population. The patterns that we observe are transient, and under the continuous modulation, the system absorbs energy, leading to heating and eventual destruction of the condensate of the BEC.

2.8.2 Quasi-two dimensional spinor condensate in ferromagnetic phase

This section has been adapted from the research article titled "Patterns, spin-spin correlations, and competing instabilities in driven quasi-two-dimensional spin-1 Bose-Einstein condensates" [85].

In this section, we look at a driven spin-1 spinor Q2D condensate, which is initially in a ferromagnetic phase. Here, all the atoms are in the $m = 1$ spin state, and the Q2D order parameter can be expressed as,

$$\bar{\psi}_{FM} = \sqrt{n_H} \begin{pmatrix} 1 \\ 0 \\ 0 \end{pmatrix}, \tag{2.79}$$

where n_H is the uniform density of the system. This state is maximally magnetized in the z-direction in spin space.

For the spin-1 condensate, there are two relevant scattering lengths, a_0 and a_2, which arise due to the total spin $\mathcal{F} = 0$ and $\mathcal{F} = 2$ channel of collision. For the ferromagnetic phase, however, a_0 scattering length is not relevant, since the colliding pair will always have total spin $\mathcal{F} = 2$ due to their polarization. Under the periodic driving of scattering length a_2 as $a_2(t) = \bar{a}_2[1 + 2\alpha_2 \cos(2\omega_2 t)$, while $a_0(t) = \bar{a}_0$ remains constant, the spin-independent coefficient c_0 and spin-dependent coefficient c_1 evolve as,

$$\begin{aligned} \tilde{c}_0(t) &= \bar{c}_0 + (4\alpha_2\bar{g}_2/3)\cos(2\omega_2 t) \\ \tilde{c}_1(t) &= \bar{c}_1 + (2\alpha_2\bar{g}_2/3)\cos(2\omega_2 t), \end{aligned} \tag{2.80}$$

where the Q2D interaction coefficients $\bar{c}_0 = (\bar{g}_0 + 2\bar{g}_2)/3$ and $\bar{c}_1 = (\bar{g}_2 - \bar{g}_0)/3$ with $\bar{g}_j = 4\pi\hbar^2\bar{a}_j/(M\sqrt{2\pi}l_z)$.

Under this drive, the coupled GPE (2.49)-(2.51) has the uniform solution of form, $\bar{\psi}(t) = \bar{\psi}_{FM}\exp(-i\theta(t)/\hbar)$ where $\psi_H(t) = (\psi_1, \psi_0, \psi_{-1})^T$ is the spinor order parameter, and $\bar{\psi}_{FM}$ is defined in Eq. (2.79). The evolution of the overall phase is given as,

$$\theta(t) = qt + n_H \int_0^t [\tilde{c}_0(t') + \tilde{c}_1(t')]\, dt'. \tag{2.81}$$

The stability of the uniform phase is analyzed by looking at the perturbed state given by,

$$\psi(\boldsymbol{r}, t) = \left[\bar{\psi}_{FM} + \boldsymbol{w}(t)\cos(\mathbf{k}\cdot\boldsymbol{\rho})\right] e^{-i\theta(t)/\hbar}, \tag{2.82}$$

where $\boldsymbol{w}(t) = (w_1, w_0, w_{-1})^T$ is the amplitude of modulations. We use the ansatz in the Q2D coupled spin-1 GPE [of form Eqs. (2.49)-(2.51)] with driven interactions, and linearize in $\boldsymbol{w}(t)$. Writing $\boldsymbol{w}(t) = \boldsymbol{u}(t) + i\boldsymbol{v}(t)$ where $\boldsymbol{u} = (u_1, u_0, u_{-1})^T$ and $\boldsymbol{v} = (v_1, v_0, v_{-1})^T$ are real-valued vectors, we obtain the relevant Mathieu equation [85, 150],

$$\frac{d^2 u_1}{dt^2} + \frac{1}{\hbar^2}\left[\epsilon_{k,1}^2 + 4n_H E_k \alpha_2 \bar{g}_2 \cos(2\omega_2 t)\right] u_1 = 0, \tag{2.83}$$

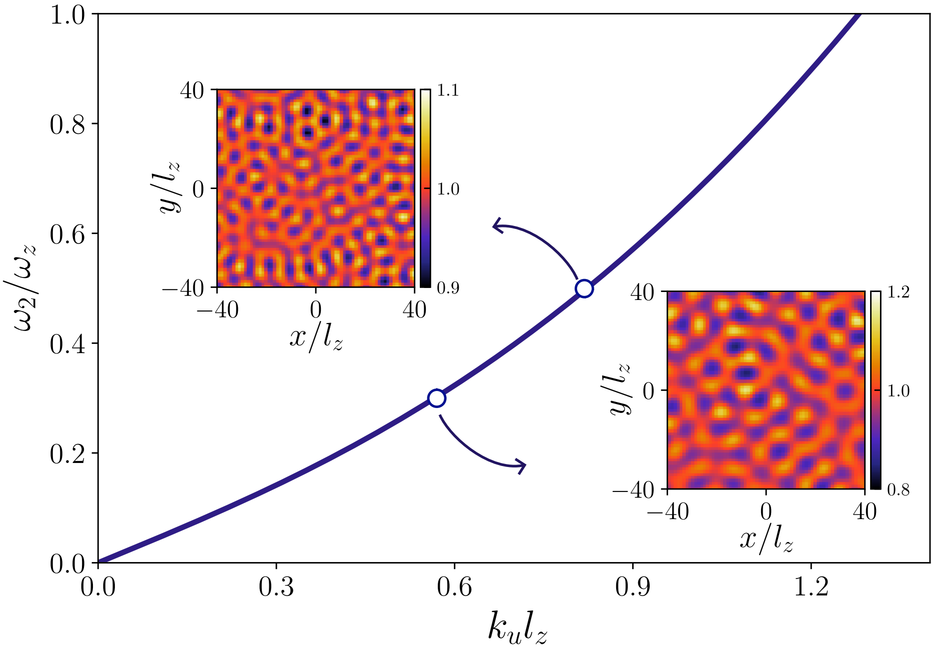

FIGURE 2.5: *Formation of Faraday waves in driven spinor condensate in ferromagnetic phase*: The most unstable mode k_u as a function of driving frequency. The inset shows pattern formation under periodic driving at two frequencies $\omega_2 = 0.3\omega_z$ and $\omega_2 = 0.5\omega_z$. The other parameters are $\bar{c}_0 n_H = 0.3\hbar\omega_z$, $\bar{c}_1 n_H = -0.1\hbar\omega_z$, $p = -0.3\hbar\omega_z$, and $q = 0$. The driving amplitude is $\alpha_2 = 0.4$.

where

$$\epsilon_1(k) = \sqrt{E_k[E_k + 2(\bar{c}_0 + \bar{c}_1)n_H]}, \tag{2.84}$$

is the Bogoliubov dispersion describing the density excitations. The equation of motion of the fluctuations in two components does not accommodate any instability. Therefore, the population of those modes remain close to zero. The Mathieu equation (2.83) remains valid even in the presence of a_0 modulation, as this has no effect on the dynamics of the ferromagnetic condensate. Like the scalar case, the momenta k_u of the most unstable mode can be obtained as $\hbar\omega_2 = \epsilon_1(k_u)$.

In Fig. 2.5, we show the results for the patterns observed in the driven ferromagnetic phase spin-1 condensate. We see the formation of density patterns similar to a spin-0 BEC. There is no transfer of population to other modes, which is expected as the system is maximally magnetized and the magnetization remains conserved during dynamics. Similar to the spin-0 Faraday waves, these patterns are also transient, and driving eventually destroys the BEC.

The dynamics of the spinor BEC crucially depend on its initial state. In Chapter 5 and Chapter 6, we examine the driven dynamics of spin-1 spinor BEC initialized in the polar phase and antiferromagnetic (AFM) phase, where the spin degrees of freedom play a role in the dynamics.

Chapter 3

Excitation of radial modes and pattern formation in driven cylindrical BEC

This chapter is adapted from a manuscript currently under preparation titled “Excitation of radial modes and pattern formation in driven cylindrical BEC”.

3.1 Introduction

The simplest models used to study Faraday wave formation in driven Bose–Einstein condensates (BECs) often assume a uniform condensate, in which the trapping potential merely reduces the system’s effective dimensionality [27, 100, 162, 201]. This approach has also been extended to BECs confined in nontrivial geometries, such as bubble [20] and ring traps [202]. While such simplified models can capture the essential features of the dynamics, they may overlook significant effects introduced by the trap itself. In many cases, the trap plays a direct role in shaping the condensate’s response to external driving. Notable examples include the emergence of star-shaped patterns at specific resonant frequencies, triggered by the excitation of surface modes [96], and the stabilization of square-shaped patterns due to trapping effects [103]. Several theoretical studies have also investigated the dynamics of driven trapped systems [144, 145, 183, 184].

Faraday waves in BECs were first observed experimentally in 2007 in an elongated trap, where the transverse confinement was periodically modulated [49], and later through interaction modulation in a similarly elongated geometry [124]. These elongated traps effectively realize a quasi-one-dimensional (Q1D) system when the transverse confinement is sufficiently strong [136]. However, under certain conditions, transverse (radial) modes can significantly influence the condensate’s dynamics [34, 116]. For instance, when the driving frequency resonates with the transverse monopole mode, the resulting dynamics deviate qualitatively from the one-dimensional picture [49, 124], necessitating a description that accounts for the coupling between radial and axial excitations [126]. In this chapter, we investigate a periodically driven condensate, focusing on the resonant excitation of transverse modes and their subsequent decay, which gives rise to longitudinal density patterns. Using

Bogoliubov theory and numerical simulations based on the Gross–Pitaevskii equation (GPE), we show that under certain conditions, the driving can lead to the excitation of dipole-branch modes.

The outline of this chapter is as follows. In Sec . 3.2, we introduce the setup of cylindrically confined BEC, and in Sec . 3.3, we study its Bogoliubov spectrum, which consists of multiple branches due to the transverse trap [55, 176]. In Sec . 3.4 we use Bogoliubov theory to examine the dynamics of the condensate under periodic driving of interaction. We find that at specific driving frequencies, the radial modes can get "directly excited" [77], a response which dominates the parametric resonance of the modes that causes the usual Faraday waves. Such a radial mode excitation can spontaneously decay to lower branches, creating a longitudinal density pattern. In Sec . 3.5, we study this phenomenon using 3D GPE simulations. Here we find that, when the driving directly excites the transverse monopole mode, its subsequent decay creates longitudinal density waves [49, 125]. The dynamics under the excitation of the second radial mode ($n_r = 2$), excited at a higher driving frequency, turned out to be more complex. For very weak interaction strengths, its decay creates longitudinal density waves; however, as the interaction increases, we observe a zig-zag (centre-of-mass oscillation) pattern from dipole branch excitation at higher interaction strengths.

3.2 Cylindrically confined Bose-Einstein condensate

Our system consists of a dilute gas of bosons with mass M trapped in the xy-plane and free along the z-axis (See Fig. 3.1). It is described by the second-quantized Hamiltonian,

$$\hat{H}(t) = \int d\boldsymbol{r}\hat{\Psi}^\dagger \left[-\frac{\hbar^2\nabla^2}{2M} + V_\rho\right]\hat{\Psi} + \frac{g(t)}{2}\int d\boldsymbol{r}\hat{\Psi}^\dagger\hat{\Psi}^\dagger\hat{\Psi}\hat{\Psi}. \tag{3.1}$$

Here, $\hat{\Psi}(\boldsymbol{r})$ is the field operator that annihilates a boson at position $\boldsymbol{r}$, $V_\rho(\rho) = M\omega_\rho^2\rho^2/2$ is the transverse harmonic trap, and $g(t) = 4\pi\hbar^2 a_s/M$ is the time-dependent interaction coefficient, with a_s being the s-wave scattering length. At very low temperatures, the system can be described using the mean-field theory, where the dynamics of the condensate order-parameter $\psi(\boldsymbol{r}, t)$ is governed by the Gross-Pitaevskii equation (GPE),

$$i\hbar\frac{\partial\psi(\boldsymbol{r}, t)}{\partial t} = \left[-\frac{\hbar^2\nabla^2}{2M} + V_\rho(\rho) + g(t)|\psi(\boldsymbol{r}, t)|^2\right]\psi(\boldsymbol{r}, t). \tag{3.2}$$

The interaction strength in cylindrically confined BEC can be characterized by the following dimensionless quantity [125, 176],

$$\eta(t) \equiv 4\pi a_s(t)n_H = g(t)n_H\frac{M}{\hbar^2}. \tag{3.3}$$

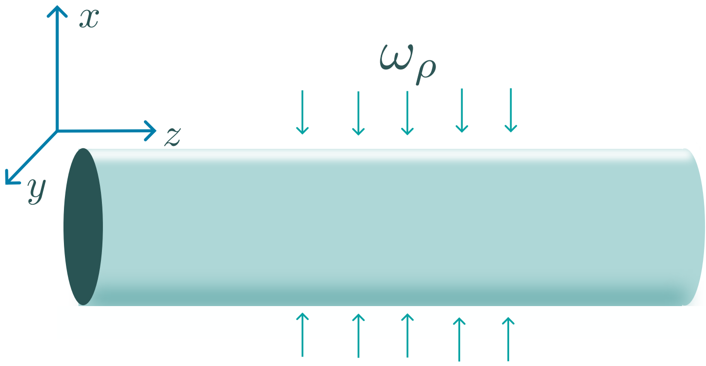

FIGURE 3.1: Schematic of the setup: Gas of bosons confined in the transverse plane with a harmonic trap of frequency ω_ρ, and free along the z-direction.

Here, $n_H = N/L_z$ denotes the linear density of the condensate along the z-axis, with N being the total number of bosons and L_z, the length of the system along the z axis. For a time-independent system with constant interaction $g(t) = \bar{g}$, the ground state order parameter can be obtained from the time-independent 2D GPE,

$$\left[-\frac{\hbar^2\nabla^2_{xy}}{2M} + V_\rho(\rho) + \bar{g}n_H|\xi_0|^2 - \mu\right]\xi_0 = 0, \tag{3.4}$$

where the operator $\nabla^2_{xy} = \partial_{xx} + \partial_{yy}$ and μ is the chemical potential. Here, we have also chosen the following normalization for the ground state,

$$\int dxdy|\xi_0|^2 = 1. \tag{3.5}$$

The 3D ground state is then obtained as, $\xi_0^{(3D)} = \sqrt{n_H}\xi_0$. The ground state is translationally symmetric along the z-direction and rotationally symmetric about the z-axis.

3.3 Bogoliubov spectrum

To understand the response of the condensate to the periodic driving, we need to first study elementary excitations of the undriven condensate. The excitation spectrum of the elongated condensate has been studied theoretically as well as experimentally [55, 166, 176, 197], and can be obtained by solving the Bogoliubov-de Gennes (BdG) equation,

$$\begin{pmatrix} \hat{\mathcal{H}}_{GP} + \bar{g}n_H|\xi_0|^2 & \bar{g}n_H\xi_0^2 \\ -\bar{g}n_H(\xi_0^*)^2 & -\hat{\mathcal{H}}_{GP} - \bar{g}n_H|\xi_0|^2 \end{pmatrix}\begin{pmatrix} u \\ v \end{pmatrix} = \hbar\omega\begin{pmatrix} u \\ v \end{pmatrix}. \tag{3.6}$$

Here, $\hat{\mathcal{H}}_{GP} = -\hbar^2\nabla^2/2M + V_\rho(\rho) + \bar{g}n_H|\xi_0|^2 - \mu$, and $\{u(\boldsymbol{r}), v(\boldsymbol{r})\}$ and ω are the amplitudes and frequency of the Bogoliubov quasiparticle, respectively. Due to rotational and translational

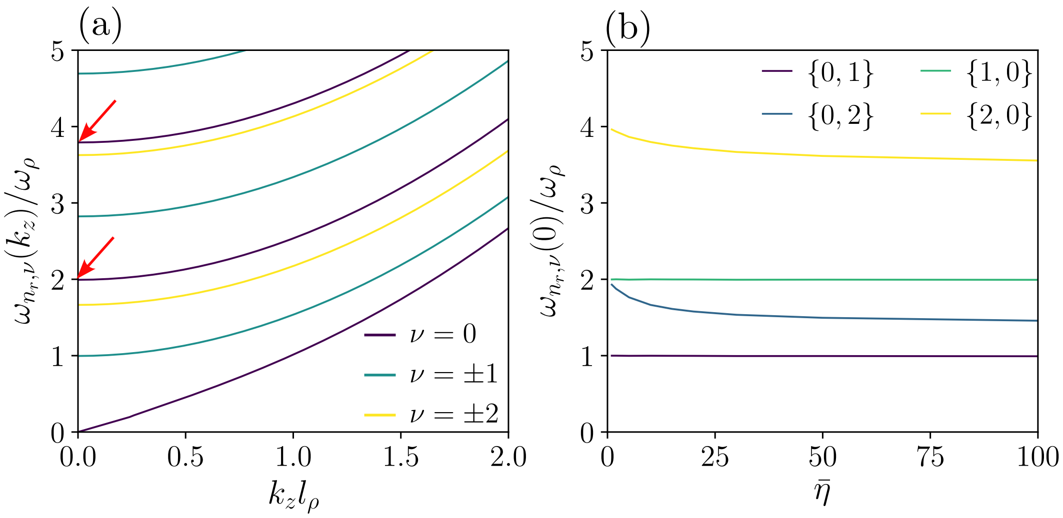

FIGURE 3.2: (a) The Bogoliubov spectrum of the cylindrically trapped condensate for mode with quantum numbers $\nu = 0, \pm 1, \pm 2$, for interaction strength $\bar{\eta} = 10.0$. The red arrows indicate the modes that can be excited under the periodic driving of interaction at frequency $\Omega = \omega_{n_r,0}(0)$ [Eq. (3.25)]. (b) The gap of branches with quantum number $\{n_r, \nu\}$ as a function of interaction strength.

symmetries of the system, we can parametrize the quasiparticle amplitudes as,

$$u(\boldsymbol{r}) = \frac{1}{\sqrt{2\pi L_z}}\bar{u}(\rho)e^{ik_z z}e^{i\nu\varphi}, \quad v(\boldsymbol{r}) = \frac{1}{\sqrt{2\pi L_z}}\bar{v}(\rho)e^{ik_z z}e^{i\nu\varphi}, \tag{3.7}$$

where ν (integer) and k_z (real number) denote the azimuthal number and longitudinal momentum of the mode, respectively. The radial amplitudes are normalized such that $\int d\rho\rho[|\bar{u}(\rho)|^2 - |\bar{v}(\rho)|^2] = 1$. We use Eq. (3.7) in Eq. (3.6) to obtain the following equation for the radial amplitudes,

$$\begin{pmatrix} \hat{\mathcal{L}}_{\nu k_z}(\rho) & \bar{g}n_H\xi_0^2 \\ -\bar{g}n_H(\xi_0^*)^2 & -\hat{\mathcal{L}}_{\nu k_z}(\rho) \end{pmatrix}\begin{pmatrix} \bar{u}_{\nu k_z} \\ \bar{v}_{\nu k_z} \end{pmatrix} = \hbar\omega \begin{pmatrix} \bar{u}_{\nu k_z} \\ \bar{v}_{\nu k_z} \end{pmatrix}. \tag{3.8}$$

Here, we have defined $\hat{\mathcal{L}}_{\nu k_z}(\rho) = -\hbar^2[\nabla_\rho^2 - (\nu/\rho)^2 - k_z^2]/2M + V_T + 2\bar{g}n_H|\xi_0|^2 - \mu$, where,

$$\nabla_\rho^2 = \frac{1}{\rho}\frac{\partial}{\partial\rho}\left(\rho\frac{\partial}{\partial\rho}\right).$$

We diagonalize Eq. (3.8) for various $\{k_z, \nu\}$ to obtain the excitation frequencies and amplitudes. The excitation frequencies are plotted as a function of k_z in Fig. 3.2(a), for interaction strength $\bar{\eta} = 10$. The spectrum contains branches, each labelled as $\omega_{n_r,\nu}(k_z)$, where $n_r = 0, 1, 2\ldots$ denotes the number of nodes in the radial amplitude $\bar{u}$ and $\bar{v}$. We note that $\omega_{n_r,\pm\nu}$ are degenerate pairs of excitations due to the rotational symmetry of the system about the z-axis.

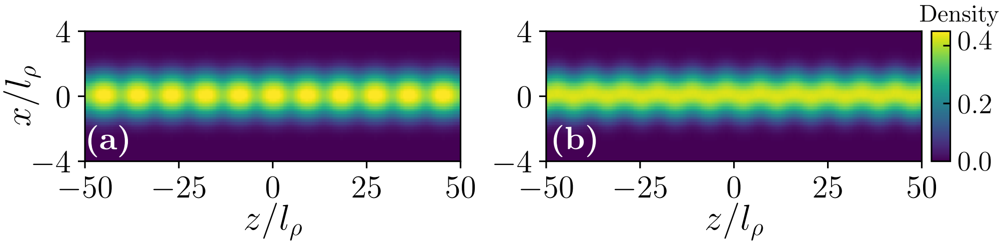

FIGURE 3.3: Density patterns under excitation of the modes from (a) gapless density ($\omega_{0,0}$) branch and (b) dipole ($\omega_{0,\pm1}$) branch.

Lowest lying branches

In the following, we discuss the properties of a few of the lowest lying branches that would become important during the later discussions in this chapter. The lowest branch, $\omega_{0,0}(k_z)$, is gapless and phonon-like at small k_z. These are purely axial excitations and in the quasi-one-dimensional limit $\mu \approx \hbar\omega_\rho$ takes the form $\omega_{0,0}(k_z) = \sqrt{E_{k_z}(E_{k_z} + 2\bar{g}_{1D}n_H)}$, where $E_{k_z} = \hbar^2k_z^2/2M$ and $\bar{g}_{1D} = \bar{g}/(2\pi l_\rho^2)$ with the characteristic trap length $l_\rho = \sqrt{\hbar/M\omega_\rho}$. The excitations in the gapped branches ($n_r > 0$ or $\nu \neq 0$) at $k_z \to 0$ represent the purely radial excitations. The second branch, $\omega_{0,\pm1}(k_z)$, is the dipole branch, which in the limit $k_z \to 0$ describes collective centre-of-mass (COM) oscillation of the condensate in the transverse plane. As the result, the gap of this branch $\omega_{0,\pm1}(0) = \omega_\rho$, is independent of the interaction strength [169].

We also have $\omega_{1,0}(k_z)$, called the monopole branch, which at $k_z \to 0$, describes the transverse breathing oscillations of the condensate. The gap of this branch $\omega_{1,0}(0) = 2\omega_\rho$ is also independent of the interaction strength due to the symmetry properties of the effective two-dimensional equations obtained at $k_z = 0$ [34, 139]. The gap of $\omega_{0,\pm2}(k_z)$ (quadrupole branch) decreases with increasing interaction strength $\bar{\eta}$, varying from $2\omega_\rho$ in the non-interacting limit to $\sqrt{2}\omega_\rho$ in the Thomas-Fermi limit [33, 169]. The gaps of the monopole, dipole, and quadrupole branches are given in Fig. 3.2 (b) as a function of increasing repulsive interaction strength.

Excitations from different branches at non-zero k_z induce distinct dynamics in the condensate [see Fig. (3.3)]. For instance, excitation from the lowest branch $\omega_{1,0}(k_z)$ generate density modulations along the z- axis with wavelength $2\pi/k_z$, and $\omega_{0,\pm1}(k_z)$ branch excitation causes modulations in the radial COM of the condensate along the z- axis with wavelength $2\pi/k_z$. Therefore, excitations from the gapped branches can create patterns besides the usual density modulations in the condensate.

3.4 Dynamics of modes under driven interaction

In this section, we discuss the dynamics of the Bogoliubov modes under the periodic driving of the scattering length. First, we discuss the resonant excitation of radial modes and derive the resonance condition using the Bogoliubov theory. Then, we look at the spontaneous decay of the excited mode, which creates excitations in the lower branch. We identify the dominant channels of decay using Beliaev theory approach [8, 62].

We start from the ground state ξ_0 of the system with interaction $\bar{\eta}$, and when $t > 0$, the interaction is periodically driven as,

$$a_s(t) = \bar{a}_s + \Delta a_s \cos(\Omega t). \tag{3.9}$$

Here, Δa_s and Ω are the driving amplitude and frequency, respectively. The interaction coefficient is therefore modulated as $g(t) = \bar{g} + \Delta g \cos(\Omega t)$ $[\eta(t) = \bar{\eta} + \Delta\eta \cos(\Omega t)]$, with the amplitude $\Delta g = 4\pi\hbar^2 \Delta a_s/M$ $[\Delta\eta = 4\pi\Delta a_s n_H]$. This can be experimentally implemented using Feshbach resonance [35, 124], which we have discussed in Sec . 2.2.1.

3.4.1 Excitation of radial modes

The initial dynamics of the condensate under the periodic driving of interaction [Eq. (3.9)] can be described under Bogoliubov theory. First, we write the Hamiltonian (3.1) as $\hat{H}(t) = \hat{H}_0 + \hat{V}_I(t)$, where,

$$\hat{H}_0 = \int d\boldsymbol{r} \hat{\Psi}^\dagger \left[-\frac{\hbar^2\nabla^2}{2M} + V_\rho \right] \hat{\Psi} + \frac{\bar{g}}{2} \int d\boldsymbol{r} \hat{\Psi}^\dagger \hat{\Psi}^\dagger \hat{\Psi} \hat{\Psi}, \tag{3.10}$$

is the time-independent part, and the time-dependent perturbation is given by

$$\hat{V}_I(t) = \frac{\Delta g \cos(\Omega t)}{2} \int d\boldsymbol{r} \hat{\Psi}^\dagger \hat{\Psi}^\dagger \hat{\Psi} \hat{\Psi}. \tag{3.11}$$

We then expand the field operator about the initial state as

$$\hat{\Psi}(\boldsymbol{r}, t) = \left[\frac{1}{\sqrt{L_z}} \xi_0(\rho) \hat{a}_0 + \delta\hat{\Psi}(\boldsymbol{r}, t) \right] e^{-i\mu t}. \tag{3.12}$$

Here, $\hat{a}_0$ annihilates a particle in the ground state $\xi_0(\rho)$. The second term in Eq. (3.12) denotes the component that is orthogonal to $\xi_0(\rho)$, i.e. $\int d\boldsymbol{r} \xi_0^* \delta\hat{\Psi} = 0$, and the population outside this mode is defined as $\delta\hat{N} = \int d\boldsymbol{r} \delta\hat{\Psi}^\dagger \delta\hat{\Psi}$. In our formalism, we assume that the total number of particles in the system, $N = n_H L_z$, is conserved. Therefore, we define the following number-conserving operator [29],

$$\hat{\Lambda}(\boldsymbol{r},t) = \hat{a}_0^{\dagger}\delta\hat{\Psi}(\boldsymbol{r},t)/\sqrt{N}, \tag{3.13}$$

which creates a particle in the ξ_0 mode and destroys one outside this mode.

Time-independent Hamiltonian

When the population in the excited modes $\langle\delta\hat{N}\rangle \ll N$, the time-independent Hamiltonian can be approximated using the expansion Eq. (3.12) and Eq. (3.13) as (Appendix A),

$$\hat{H}_0 \approx E_0 + \int d\boldsymbol{r}\hat{\Lambda}^{\dagger}\left(\hat{\mathcal{L}}\right)\hat{\Lambda} + \frac{\bar{g}n_H}{2}\int d\boldsymbol{r}\xi_0^2\left[\hat{\Lambda}^{\dagger}\hat{\Lambda} + \text{H.c.}\right], \tag{3.14}$$

where E_0 is the mean-field energy of the ground state and $\hat{\mathcal{L}} = \hat{\mathcal{H}}_{GP} + \bar{g}n_H|\xi_0|^2$, with $\hat{\mathcal{H}}_{GP}$ being defined below Eq. (3.6). The field operator $\hat{\Lambda}(\boldsymbol{r},t)$ is then expanded in the Bogoliubov basis of $\hat{H}_0$,

$$\hat{\Lambda}(\boldsymbol{r},t) = \sum_{n_r,\nu,k_z}\hat{b}_{n_r,\nu,k_z}(t)\tilde{u}_{n_r,\nu,k_z}(\boldsymbol{r})e^{-i\omega_{n_r,\nu}(k_z)t} + \hat{b}^{\dagger}_{n_r,\nu,k_z}(t)\tilde{v}^*_{n_r,\nu,k_z}(\boldsymbol{r})e^{+i\omega_{n_r,\nu}(k_z)t}, \tag{3.15}$$

where each excitation is labelled using quantum numbers n_r, ν, k_z. Here, $\hat{b}_{n_r,\nu,k_z}(t)$ is the (number-conserving) Bogoliubov operator that creates an excitation and $\omega_{n_r,\nu}(k_z)$ is the corresponding quasiparticle frequency. The functions $\tilde{u}_{n_r,\nu,k_z}$ and $\tilde{v}_{n_r,\nu,k_z}$ are related to the usual Bogoliubov amplitudes u_{n_r,ν,k_z} and v_{n_r,ν,k_z} [Eq. (3.7)] as ,

$$\tilde{u}_{n_r,\nu,k_z}(\boldsymbol{r}) = u_{n_r,\nu,k_z}(\boldsymbol{r}) - \int d\boldsymbol{r}\xi_0^*(\rho)u_{n_r,\nu,k_z}(\boldsymbol{r}). \tag{3.16}$$

Such a projection ensures the orthogonality of Bogoliubov modes with the ground state modes [29]. Note that, in Eq.(3.15), we have assumed that the quasiparticle operators are time-dependent while the amplitudes are not.

Upon expansion using Eq. (3.12) and Eq. (3.15), $\hat{H}_0$ becomes diagonal as (Appendix A),

$$\hat{H}_0 = \text{Const.} + \sum_{n_r,\nu,k_z}\hbar\omega_{n_r,\nu}(k_z)\hat{b}^{\dagger}_{n_r,\nu,k_z}\hat{b}_{n_r,\nu,k_z} + O(\hat{\Lambda}^3). \tag{3.17}$$

Here, the constant term contains ground state energy of the system , and terms that contain quasiparticle operators in linear order vanish (see Sec. 2.5.2). In deriving this, we have used the relation $\hat{a}_0^{\dagger}\hat{a}_0 = N - \delta\hat{N}$ and $\hat{a}_0^{\dagger}\hat{a}_0^{\dagger}\hat{a}_0\hat{a}_0 \approx N^2 - 2N\delta\hat{N}$. As expected, the excited modes population remains constant under $\hat{H}_0$. We have ignored terms of cubic order and higher in non-condensate operators, since those terms describe the interactions between the excited particles, and are negligible when the non-condensate population in the system is small.

Periodic driving: Resonant excitation of modes

Now we shall look at the time-dependent part of the Hamiltonian, $\hat{V}_I(t)$. Here, we use Eq. (3.12) and expand it in powers of $\hat{\Lambda}$ as $\hat{V}_I(t) \approx \hat{V}_I^{(0)}(t) + \hat{V}_I^{(1)}(t) + \hat{V}_I^{(2)}(t)$, with

$$\hat{V}_I^{(0)}(t) = \frac{\Delta g n_H^2 \cos(\Omega t)}{2} \int d\boldsymbol{r} |\xi_0|^4 \tag{3.18}$$

$$\hat{V}_I^{(1)}(t) = \Delta g n_H^{3/2} \cos(\Omega t) \int d\boldsymbol{r} |\xi_0|^2 \left[\xi_0 \hat{\Lambda} + \text{H.c.}\right] \tag{3.19}$$

$$\hat{V}_I^{(2)}(t) = \Delta g n_H \cos(\Omega t) \int d\boldsymbol{r} \left\{\left[(\xi_0^*)^2 \hat{\Lambda}\hat{\Lambda} + \text{H.c.}\right] + [2|\xi_0|^2 - \Xi]\hat{\Lambda}^\dagger \hat{\Lambda}\right\}, \tag{3.20}$$

where we have defined the quantity $\Xi = \int dxdy |\xi_0|^4$. We can see that the linear term $\hat{V}_I^{(1)}(t)$ no longer vanishes when periodic driving is present. In the Bogoliubov basis (Eq. (3.15)), we have,

$$\hat{V}_{I,B}^{(1)}(t) = \Delta g n_H^{3/2} \sum_{n_r} \mathcal{F}_{n_r} \hat{b}_{n_r,0,0}(t) e^{-i\omega_{n_r,0}(0)t} + \text{H.c.}, \tag{3.21}$$

with the coefficient given as,

$$\mathcal{F}_{n_r} = \int d\boldsymbol{r} |\xi_0(\rho)|^2 \left[\xi_0(\rho) \tilde{u}_{n_r,0,0}(\boldsymbol{r}) + \xi_0^*(\rho) \tilde{v}_{n_r,0,0}(\boldsymbol{r})\right]. \tag{3.22}$$

Operator $\hat{V}_{I,B}^{(1)}(t)$ creates and annihilates quasiparticles with quantum numbers $\{\nu = 0, k_z = 0\}$. Only such modes are created due to conservation of angular and linear momenta. The dynamics of $\hat{b}_{n_r,\nu,k_z}(t)$ under the linear Hamiltonian is obtained from the Heisenberg equation of motion,

$$i\hbar \frac{d\hat{b}_{n_r,\nu,k_z}}{dt} = \left[\hat{b}_{n_r,\nu,k_z},\ \hat{V}_{I,B}^{(1)}(t)\right] = \Delta g n_H^{3/2} \cos(\Omega t) \bar{\mathcal{F}}_{n_r}^* \,\delta_{\nu,0}\delta_{k_z,0}, \tag{3.23}$$

The above equation can be integrated to obtain excite mode populations as [13],

$$\left\langle \hat{b}_{n_r,0,0}^\dagger(t) \hat{b}_{n_r,0,0}(t)\right\rangle \approx \frac{\Delta g^2 \left|\bar{\mathcal{F}}_{n_r}\right|^2 n_H^3 \sin^2[(\omega_{n_r,0}(0) - \Omega)\, t/2]}{[\omega_{n_r,0}(0) - \Omega]^2} + \left\langle \hat{b}_{n_r,0,0}^\dagger(0) \hat{b}_{n_r,0,0}(0)\right\rangle, \tag{3.24}$$

When the driving frequency matches with excitation frequency of a particular mode as

$$\Omega = \omega_{n_r,0}(0), \tag{3.25}$$

that mode gets resonantly populated. Such a coherent mode excitation under the periodic driving only occurs for trapped systems [27], as $\hat{V}_{I,B}^{(1)}$ vanishes if the system is uniform. We have plotted coefficient $\bar{\mathcal{F}}_{n_r}$ for different n_r in Fig. 3.4(a). The coefficient is greatest for the

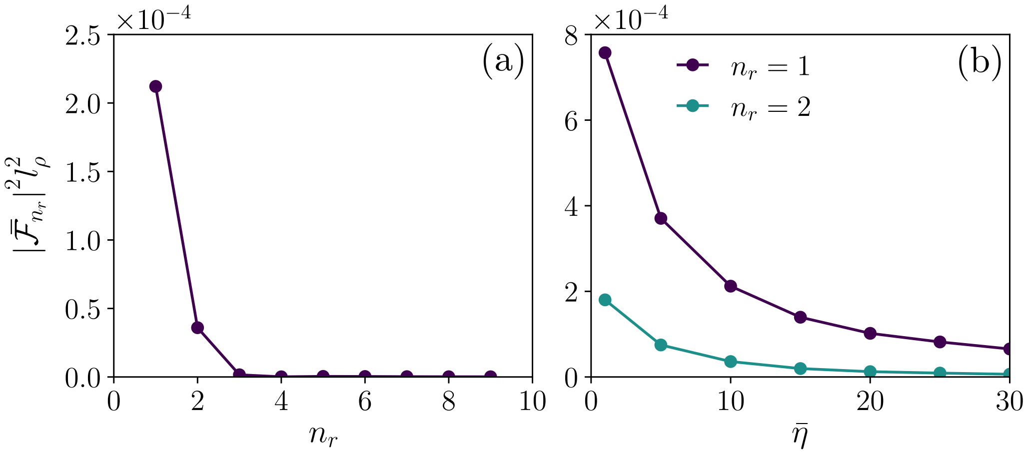

FIGURE 3.4: (a) The excitation coefficient $\bar{\mathcal{F}}_{n_r}$, defined in Eq. (3.22), for various values of radial node number n_r, at $\bar{\eta} = 10.0$. (b) The coefficients for the two lowest modes ($n_r = 1, 2$) for various interaction strengths.

lowest lying mode, i.e. the radial monopole mode ($n_r = 1, \nu = 0, k_z = 0$), and falls off for higher modes, indicating that the higher modes are significantly harder to excite under driving.

We have neglected the quadratic terms $V_I^{(2)}(t)$ in the analysis so far, as the dynamics will be dominated by the linear terms when the resonance condition (3.25) is satisfied. The quadratic terms are responsible for the parametric excitation of modes, which leads to the formation of Faraday waves in the condensate [27, 49, 124]. The parametric resonance causes excitation of modes with quasiparticle frequencies half the driving frequency, i.e. at $\Omega = 2\omega_{n_r,\nu}(k_z)$, whereas in this chapter we look at the "direct resonance" of the modes, which dominates for driving frequencies given by Eq. (3.25). Such a direct resonance was observed in trapped 3D gas under modulation of scattering length [142]. This phenomenon is studied in detail in chapter 4.

3.4.2 Decay of the excited modes

In the last section, we saw that certain radial modes get resonantly excited under driving of the two-body interaction [Eq. (3.25)]. The Bogoliubov theory captures the initial dynamics under driving when the excited population is much smaller than the ground state population. However, at longer times, this approximation breaks down as the quasiparticle population becomes significant. At this point, the interaction between the excited modes can no longer be ignored, and it will lead to the decay of modes [132]. At very low temperatures, this occurs via a process known as Beliaev damping [8, 62], where the excited mode decays to create a pair of modes. Since this process conserves energy, Beliaev damping is rare in trapped systems due to its discrete energy levels [69, 76]. However, the elongated structure

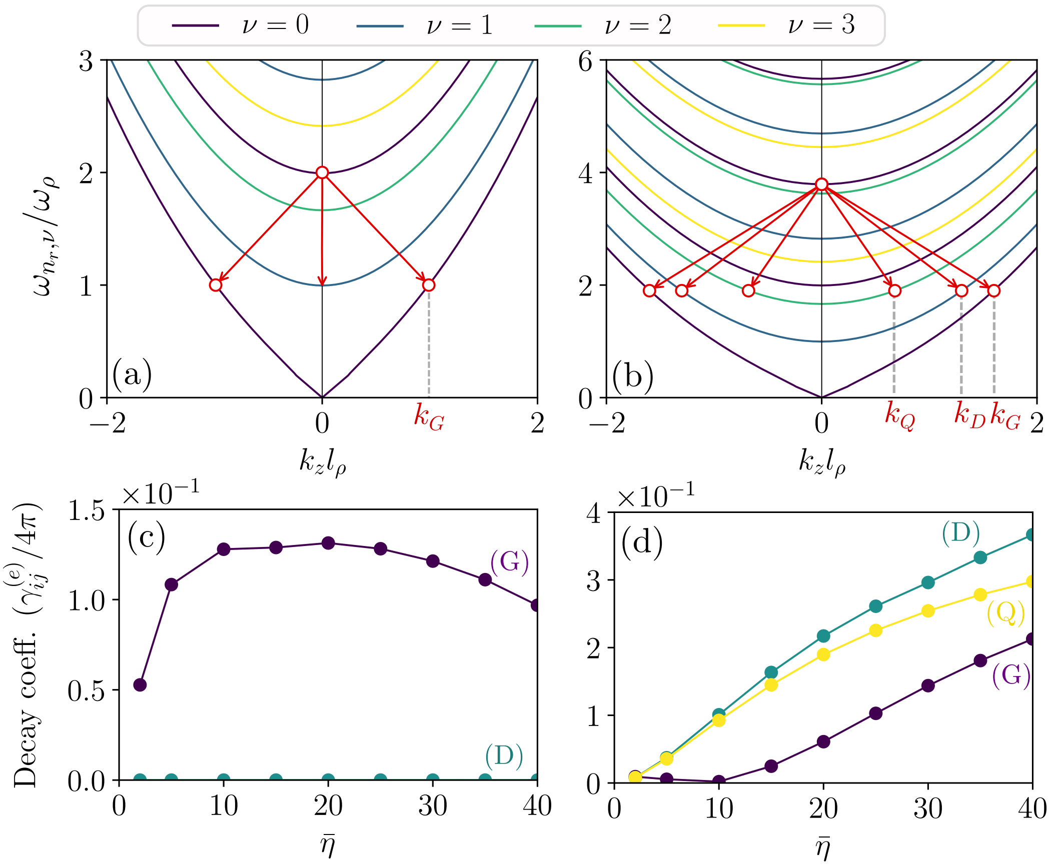

FIGURE 3.5: The energetically allowed decay processes for (a) $n_r = 1$ (monopole) and (b) $n_r = 2$ modes. The decay coefficients for each of these processes as a function of interaction strength $\bar{\eta}$ for (c) $n_r = 1$ (monopole) and (d) $n_r = 2$ modes. Here decay of the excited mode into gapless, dipole and quadrupole branches are indicated by (G), (D), and (Q), respectively in (c), (d) plots and k_G, k_D, and k_Q denotes the longitudinal momenta of the modes that are creates under the decay from each of these branches.

of our system allows several transitions that conserve energy as well as linear and angular momenta [see Fig. 3.5 (a), (b)].

The probability of decay into various channels can be compared by calculating the damping rate [62, 147],

$$\gamma_{i,j}^{(e)} = 4\pi\bar{g}^2 n_H |B_{ij}^{(e)}|^2, \tag{3.26}$$

where the matrix element associated with the decay is given by,

$$B_{ij}^{(e)} = \int d\boldsymbol{r} \left[u_e(u_i^* v_j^* + v_i^* u_j^* + u_i^* u_j^*) + v_e(u_i^* v_j^* + v_i^* u_j^* + v_i^* v_j^*)\right] \xi_0, \tag{3.27}$$

where $u_{i,j}$ and $v_{i,j}$ denote the quasiparticle amplitudes of the modes that are created as a result of the decay, and u_e, v_e denote the amplitudes of the mode that has undergone the decay. This formula was obtained using a perturbative approach, assuming a weak quasiparticle interaction. For simplicity, we also assume that the periodic driving has been terminated once the modes are excited.

Consider the excitation of the monopole mode ($n_r = 1$) at $k_z = 0$ under the resonant driving. The allowed transitions via which this mode can decay are given in Fig. 3.5(a). A single monopole excitation can decay to create two excitations with momenta $\pm k_G$ in the gapless density branch. The energy conservation under this process implies $2\omega_{0,0}(\pm k_G) = \omega_{1,0}(0)$, and thus the decay creates longitudinal density waves with wavelength $2\pi/k_G$. It is also energetically allowed for the monopole mode to decay into two dipole modes with $\nu = \pm 1, k_z = 0$. The damping rates associated with these two processes are plotted against the interaction strength $\bar{\eta}$ in Fig. 3.5(c), where (G) and (D) labels indicate the decay to gapless and dipole branches, respectively. The damping rates show that the decay occurs predominantly into the gapless branch, while that to the dipole branch is heavily suppressed.

We also examine the excitation of the $n_r = 2, \nu = 0, k_z = 0$ mode. Since it is a high-lying mode, more allowed decay transitions exist for it as compared to the monopole mode [Fig. 3.5(b)]. At very low interaction $\eta \to 0$, the $n_r = 2$ mode has twice the frequency of the monopole mode at $\omega_{2,0}(0) \to 4\omega_\rho$ [see Fig. 3.2(b)], and the decay process is dominated by the transition to this mode. This is due to the decay rate of this transition, calculated at $\bar{\eta} = 2$, being an order of magnitude larger than for other transitions. At higher interactions, however, the decay to monopole mode is suppressed due to energy conservation. By comparing the decay rate for three channels, we see that the damping rate for the decay to dipole and quadrupole branches is relatively higher than to the gapless branch.

3.5 Numerical simulation using GPE

In this section, we numerically solve the 3D GPE (3.2) with periodically driven interaction, where we consider the resonant excitation of the two lowest ($\nu = 0, k_z = 0$) modes, with $n_r = 1$ (monopole mode) and $n_r = 2$ mode. The linear dynamics of the Bogoliubov modes are captured within the time-evolution of the order parameter under GPE [29]. However, the decay process requires us to consider the quantum fluctuation present in the system. We mimic the fluctuations by adding a small random noise to the initial condensate. We compare the GPE results with the predictions from the Bogoliubov theory and the Beliaev damping calculations.

3.5.1 Excitation of the monopole mode

First, we consider the excitation of the monopole mode ($n_r = 1$) under a periodically driven interaction. Here, the resonant driving frequency,

$$\Omega = 2\omega_\rho, \tag{3.28}$$

is independent of the interaction parameter $\bar{\eta}$ [Fig. 3.2(b)]. Excitation of the monopole mode induces radial breathing oscillation in the condensate, which is seen from the dynamics of the average root-mean-square (RMS) radius of the condensate in the xy-plane given by

$$\rho^2_{\text{rms}}(t) = \frac{\int d\boldsymbol{r}\rho^2|\psi(\boldsymbol{r},t)|^2}{\int d\boldsymbol{r}|\psi(\boldsymbol{r},t)|^2}, \tag{3.29}$$

From Fig. 3.6(a), we see that $\rho^2_{\text{rms}}(t)$ oscillates with frequency $2\omega_\rho$, with the oscillation amplitude increasing linearly in time under the driving. At this stage, radial breathing occurs uniformly along the z-direction.

The excited monopole mode eventually decays into the gapless branch [Fig.3.5(a)], creating excitations with wavenumber $\pm k_G$ that satisfy the energy conservation criteria

$$\omega_{0,0}(\pm k_G) = \omega_{1,0}(0)/2 = \omega_\rho. \tag{3.30}$$

The decay process can be seen from the population in modes with non-zero k_z [Fig. 3.6(a)] defined as,

$$N_k(t) = \int_{k_z>0} d\boldsymbol{k}|\tilde{\psi}(\boldsymbol{k},t)|^2, \tag{3.31}$$

where $\tilde{\psi}(\boldsymbol{k},t)$ is the momentum space wave function. This quantity will remain close to zero in the initial stage of monopole excitation. Later, we see $N_k(t)$ increasing simultaneously as

$\rho_{\rm rms}$ oscillation amplitude dips, indicating the decay of the monopole mode. We observe several oscillations of the population between the axial and radial excitations. The condensate is later destroyed as excited modes become highly populated. The GPE results at the later stages are unreliable due to a large non-condensate population.

Density modulations form along the z-direction due to the monopole decay to the gapless branch. We see this from the integrated 2D densities in the xy and xz planes given by,

$$n_y(x,z) = \int dy|\psi(\boldsymbol{r})|^2, \quad n_z(x,y) = \int dz|\psi(\boldsymbol{r})|^2, \tag{3.32}$$

which are shown in Fig. 3.6 (b)-(e). The wavelength of the density patterns observed indeed matches the predicted value at $\lambda = 2\pi/k_G$, where k_G can be determined from Eq. (3.30).

We note that density patterns also form for nonresonant driving frequencies due to the parametric resonance of the phonons [127, 162] which creates the usual Faraday waves. But pattern formation under parametric resonance requires continuous driving, whereas direct excitation of the radial mode can lead to pattern formation even after the termination of periodic driving, since the decay of the mode is spontaneous. Triggering parametric pattern formation also requires a much larger driving amplitude, as it originates from a higher-order process. The decay of the radial breathing mode and subsequent creation of density patterns have been observed experimentally [49, 124]. Theoretically, the pattern formation at the resonant driving frequency has been explored using variational techniques in Ref. [127]. Monopole decay has also been discussed recently for an elongated condensate in two dimensions, in the context of analog simulation [24].

We observe qualitatively similar dynamics across various interaction strengths for monopole excitation and decay. However, the time scales associated with the excitation and decay process may vary depending on the interaction and amplitude of the periodic driving and the quantum fluctuation present in the system, and accurately capturing it requires one to consider the beyond-mean-field effects systematically.

3.5.2 Excitation of $n_r = 2$ radial mode

Now we consider the resonant excitation of the $\{n_r = 2, \nu = 0, k_z = 0\}$ mode, for which the resonance condition given in Eq. (3.25) becomes,

$$\Omega = \omega_{2,0}(0). \tag{3.33}$$

The frequency $\omega_{2,0}(0)$ depends on the interaction strength [see Fig. 3.4], unlike for the monopole mode. For the non-interacting gas, the $n_r = 2$ mode frequency is twice that of the monopole frequency at $\omega_{2,0}(0) = 4\omega_\rho$, and it decreases as the interaction increases. This mode also has a smaller excitation coefficient as compared to the monopole mode, i.e.

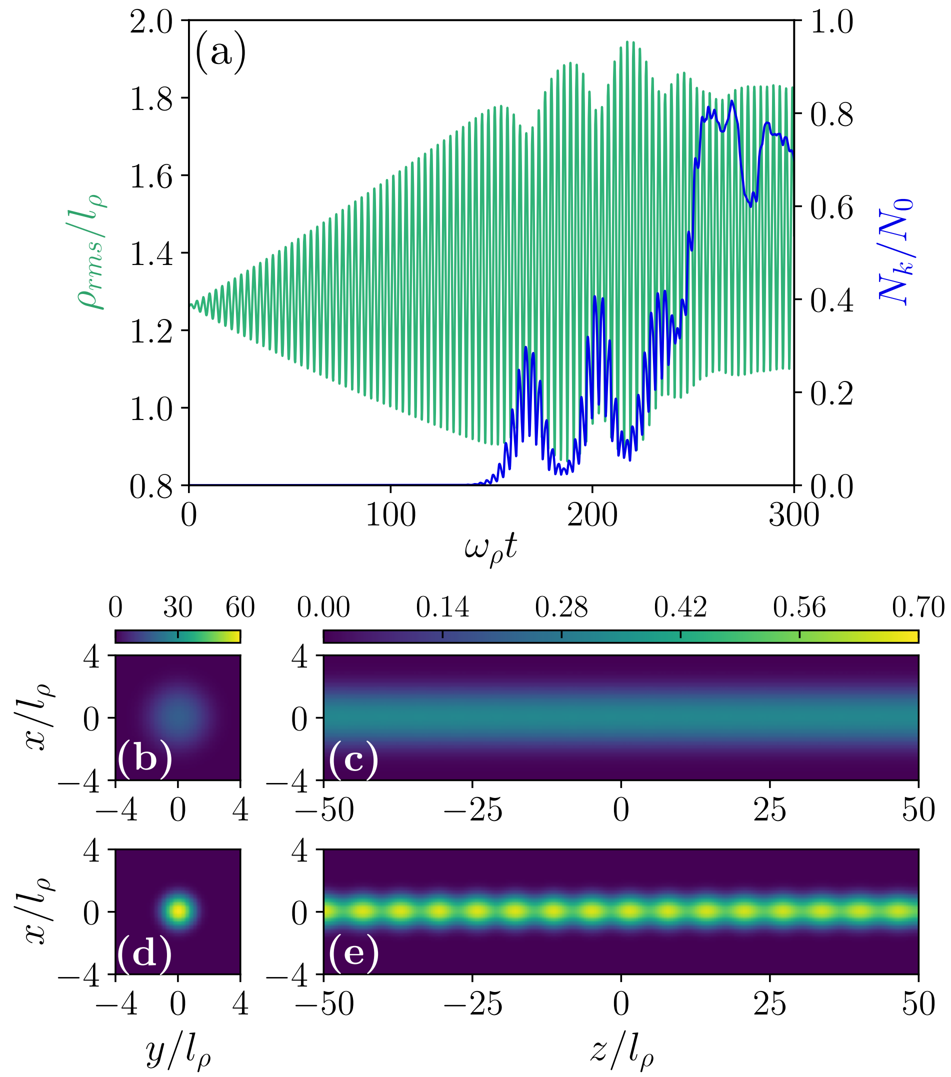

FIGURE 3.6: $n_r = 1$ *(monopole) mode excitation*: (a) Dynamics of $\rho_{\rm rms}(t)$ and $N_k(t)$ under modulation of scattering length with frequency $\Omega = 2\omega_\rho$. (b)-(e) The integrated 2D densities (left) $n_z(x, y)$ and (right) $n_y(x, z)$at times [(b), (c)] $\omega_\rho t = 120$ and [(d), (e)] $\omega_\rho t = 150$, under the periodic driving of interaction with frequency $\Omega = 2\omega_\rho$ and amplitude $\Delta\eta/\bar{\eta} = 0.016$. Here $\bar{\eta} = 10.0$.

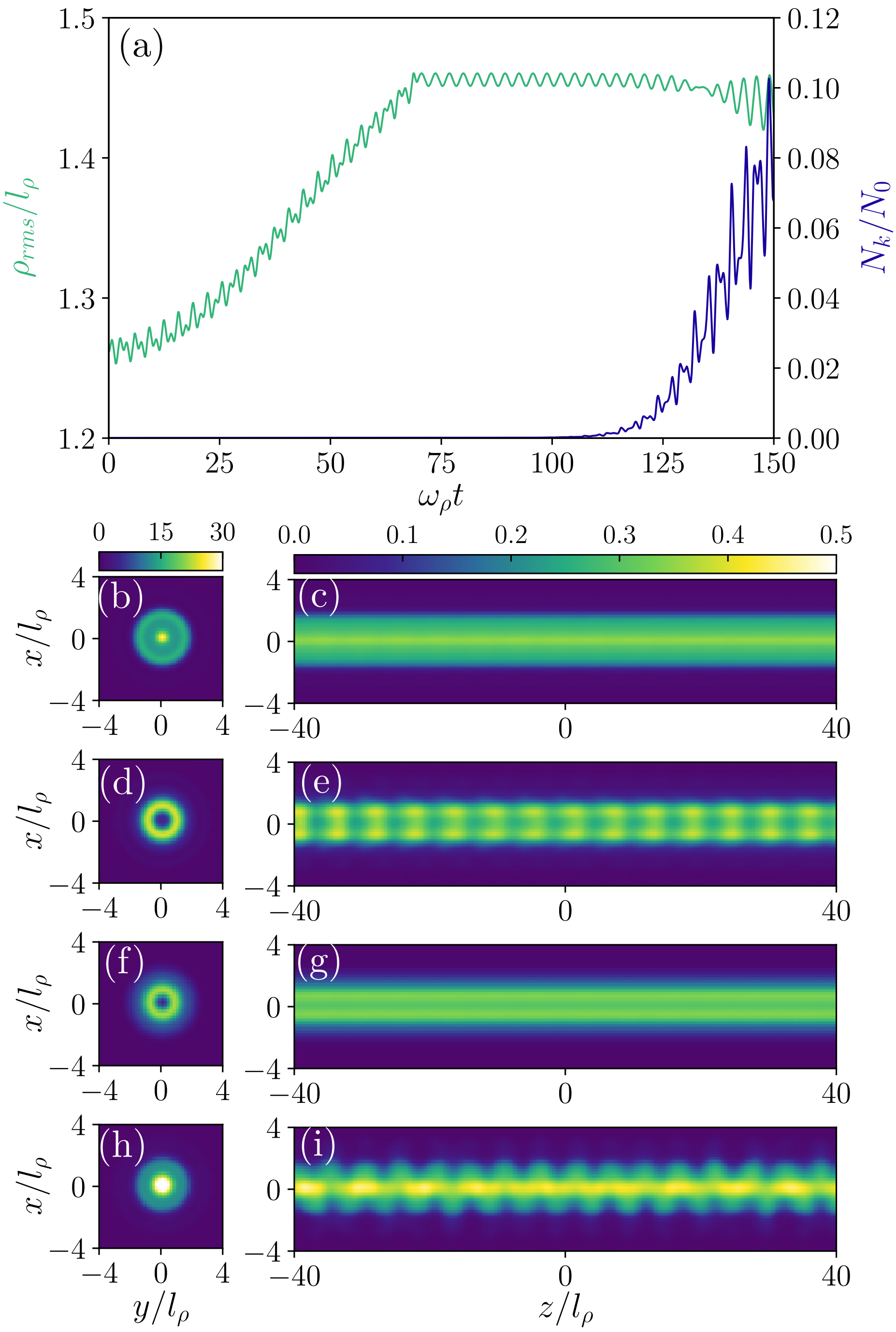

FIGURE 3.7: $n_r = 2$ *mode excitation*: (a) Dynamics of $\rho_{\rm rms}(t)$ and $N_k(t)$ under modulation of interaction at resonant frequency. [(b)-(i)] The snapshot of integrated 2D densities (left) $n_z(x, y)$ and (right) $n_y(x, z)$. Results are given for two values of interaction strengths, [(b)-(e)] $\bar{\eta} = 10.0$ ($\Omega = 1.90\omega_\rho$) and [(f)-(i)] $\bar{\eta} = 20.0$ ($\Omega = 1.86\omega_\rho$), before and after longitudinal patterns formation. The snapshots are taken at [(b), (c)]$\omega_\rho t = 70$, [(d), (e)] $\omega_\rho t = 100$, [(f), (g)] $\omega_\rho t = 70$, and [(h), (i)] $\omega_\rho t = 110$. The interaction is driven with amplitude $\Delta\eta = 1.6$ in both cases. The driving is terminated at $t_D = 70/\omega_\rho$.

$\bar{\mathcal{F}}_2 < \bar{\mathcal{F}}_1$, thereby requiring a larger driving amplitude Δg to observe the excitation dynamics around the same time-scales.

In this set of simulations, we drive interaction at the resonance frequency as,

$$g(t) = \begin{cases} \bar{g} + \Delta g \cos(\Omega t), & 0 < t < t_D \\ \bar{g}, & t > t_D \end{cases}. \tag{3.34}$$

where we terminate the driving after time t_D. During the drive ($t < t_D$), the $n_r = 2$ mode excitation causes change in the radial density profile condensate. This can be seen from the average RMS radius $\rho_{\text{rms}}(t)$ plotted in Fig. 3.7 (a), which increases steadily under driving. Once the driving is terminated, $\rho_{\text{rms}}(t)$ oscillates about its new value at a frequency close to the original monopole frequency.

The $n_r = 2$ mode excitation can also be seen from the radial density profile of the condensate, which develops annular patterns [Fig. 3.7 (b), (d), (f), (h)]. During the initial phase of the periodic driving, the longitudinal density remains uniform as $k_z \neq 0$ modes are mostly unpopulated. We terminate the drive before observing longitudinal pattern formation. This ensures that the patterns formed are due to the decay of the resonantly excited mode alone, not parametric excitation.

The longitudinal pattern formation formed after the termination of the drive, at two different interaction strengths $\bar{\eta}$, is given in Fig. 3.7 (e) and (i). At the weaker interaction, the decay creates the formation of longitudinal density waves [Fig. 3.7 (e)], whereas for the larger interaction values, we see a zig-zag pattern in the $n_y(x, z)$ density resulting from oscillation of radial COM [Fig. 3.7 (i)].

We also see that the wavenumber of the density pattern, denoted as k_G, formed at the weaker interaction strength, in Fig. 3.7(e), indicates that its does not occur due to the decay of $n_r = 2$ mode to gapless branch, i.e. $\omega_{0,0}(k_G) \neq \omega_{2,0}(0)/2$. Instead, it is closer to the wavenumber expected under monopole mode decay, at $\omega_{0,0}(k_G) \approx \omega_\rho$. This suggests that the monopole mode may have played an intermediate role in the axial density wave formation. At larger interactions, however, wavenumber of the COM oscillations (k_D) that emerge does satisfy the $\omega_{0,\pm 1}(k_D) = \omega_{2,0}(0)/2$, indicating that it does originates due to the decay of $n_r = 2$ mode to the dipole branch.

To quantify the growth of different types of patterns, we define the following quantities. The longitudinal density is given by,

$$n_{xy}(z, t) = \int dxdy |\psi(\boldsymbol{r}, t)|^2. \tag{3.35}$$

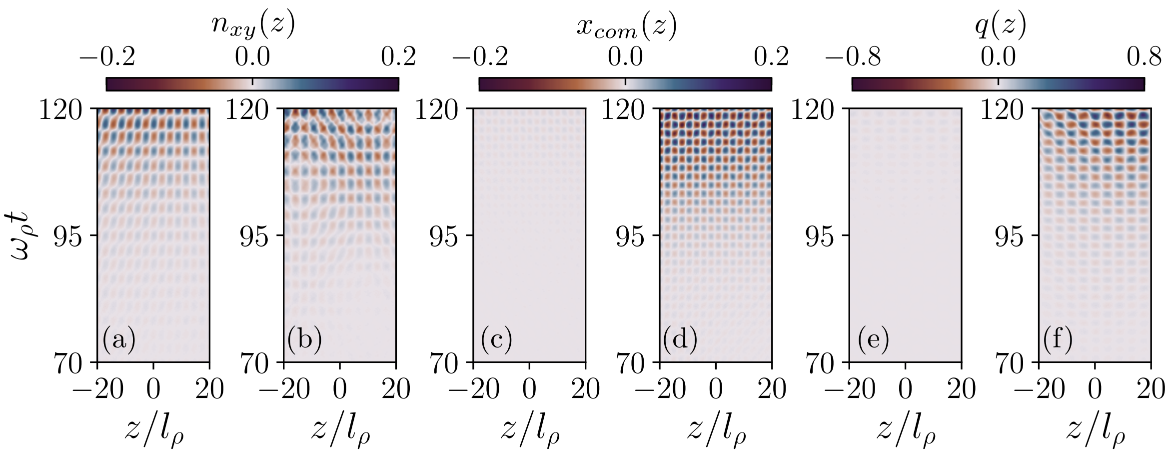

FIGURE 3.8: $n_r = 2$ *excitation*: The dynamics of [(a), (b)] $n_{xy}(z)$, [(c), (d)] $x_{\text{com}}(z)$, and [(e), (f)] $q(z)$, for interaction strengths [(a), (c), (e)] $\bar{\eta} = 10.0$ ($\Omega = 1.90\omega_\rho$) and [(b), (e), (f)] $\bar{\eta} = 20.0$ ($\Omega = 1.86\omega_\rho$). The interaction is driven with amplitude $\Delta\eta = 1.6$. The driving is terminated at $t_D = 70/\omega_\rho$.

The x component of the COM of the condensate in the radial plane,

$$x_{\text{com}}(z,t) = \frac{\int dxdy\ x|\psi(\boldsymbol{r},t)|^2}{n_{xy}(z,t)}, \tag{3.36}$$

We also define the quantity associated with the radial quadrupole branch excitation,

$$q(z,t) = \frac{\int dxdy\ (x^2 - y^2)|\psi(\boldsymbol{r},t)|^2}{n_{xy}(z,t)}. \tag{3.37}$$

In Fig. 3.8, we plot the dynamics of these three quantities for the two interactions, $\bar{\eta} = 10$ and $\bar{\eta} = 20$. For the weaker interaction [Fig. 3.8 (a)-(c)], longitudinal density patterns form, while the dipole and quadrupole excitation signatures are very weak. For the stronger interaction, on the other hand, [Fig. 3.8 (d)-(f)], the excitations from dipole and quadrupole branches become prominent. The wavenumber of the quadrupole excitation k_Q satisfy the relation $\omega_{0,\pm 2}(k_Q) = \omega_{2,0}(0)/2$, indicating that it originate from the decay of the $n_r = 2$ mode.

The decay of the excited mode is triggered by the noise present in the simulation, and the exact moment it occurs varies from one run of the simulation to another. A more qualitative assessment requires considering the role of quantum fluctuations in the system. The truncated Wigner method (TWA) [12] accomplishes this task, but the divergences in 3D systems such as ours make it difficult to implement. In general, larger Δg and t_D would create the pattern form faster as these would transfer a larger population to the $n_r = 2$ mode.

To better under the transition between two types of pattern a function of the interaction strength, we consider the Fourier transform of the $n_{x,y}$, x_{com}, and q, denoted as $\tilde{n}_{x,y}(k_z)$, $\tilde{x}_{\text{com}}(k_z)$

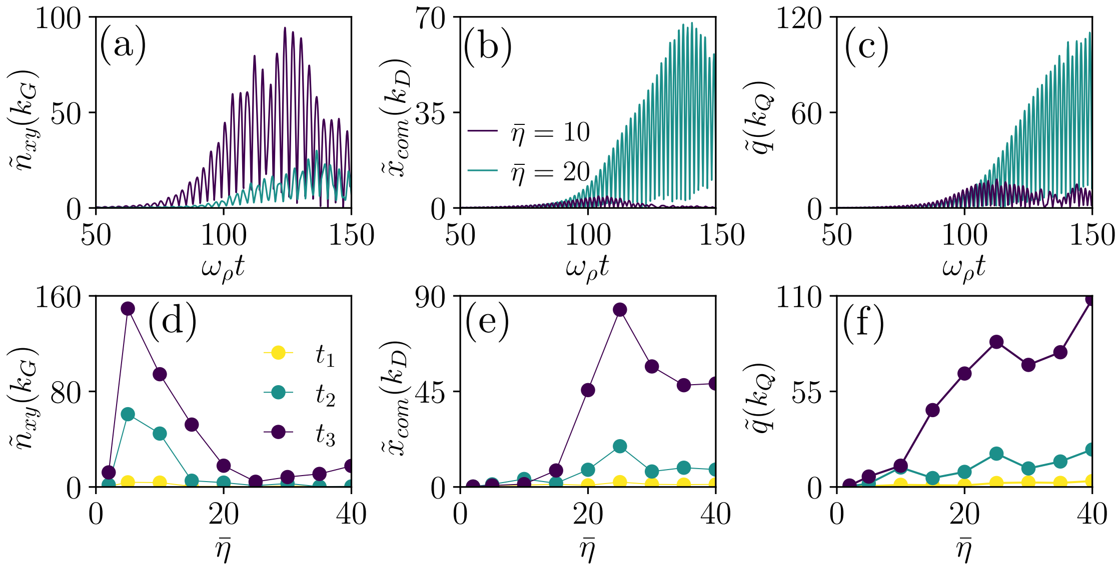

FIGURE 3.9: $n_r = 2$ excitation: The dynamics of Fourier peak values (a) $\tilde{n}_{x,y}(k_G)$, (b) $\tilde{x}_{\text{com}}(k_D)$, and (c) $\tilde{q}(k_Q)$ for two different interaction strengths. The peak values taken near three different times $\omega_\rho t_1 = 75$, $\omega_\rho t_2 = 100$, and $\omega_\rho t_3 = 125$, as a function of interaction strength. Here, we take the peak value at the nearest maxima of the particular time.

and $\tilde{q}(k_z)$, respectively. These quantities develop peaks at their respective pattern wavenumbers under the decay of the $n_r = 2$ mode. The peak values, given by $\tilde{n}_{x,y}(k_G)$, $\tilde{x}_{\text{com}}(k_D)$ and $\tilde{q}(k_Q)$, as plotted as a function of time for the two values of interaction strengths in Fig. 3.9 (a)-(c). These function oscillates in time, with $\tilde{x}_{\text{com}}(k_D)$ and $\tilde{q}(k_Q)$ oscillating at half the driving frequency Ω, while $\tilde{n}_{x,y}(k_G)$ having a much smaller frequency, closer to ω_ρ. We can also see that the density pattern dominates at smaller interactions, whereas the dipole and quadrupole mode signatures are prominent at higher interactions. We also plotted the value of $\tilde{n}_{x,y}(k_G)$, $\tilde{x}_{\text{com}}(k_D)$, and $\tilde{q}(k_Q)$, at three times t_1, t_2, and t_3, as a function of interaction $\bar{\eta}$ in Fig. 3.9 (d)-(f). We chose the maxima of the Fourier peak closest to these times. Here we see a transition of pattern type, which is clearly showing the density pattern formation dominating at lower values of interaction, whereas $\tilde{x}_{\text{com}}(k_D)$ and $\tilde{q}(k_Q)$ become prominent for larger interactions.

3.6 Comparison: GPE numerics and analytical results

In this section, we compare the results obtained from the theoretical calculations in Sec. 3.4 with those obtained by the GPE simulations in Sec. 3.5, for the driven cylindrical condensate. The initial excitation of the radial modes is a coherent process [13, 27, 29] which is captured well within the mean-field GPE evolution. The mode decay, however, is beyond the Bogoliubov theory and cannot be captured in the mean-field picture [66]. We introduce a small perturbation to the initial state by adding a random noise to the mean-field state. The GPE results remain qualitatively independent of the strength noise, which only influences the decay time of the excited mode. Methods such as the Truncated Wigner approximation (TWA) [12] fail in our system, as it causes divergence of energy. This issue has been noted for 3D systems [143]. Ref. [24] has studied the spontaneous decay of excited modes using TWA in a two-dimensional elongated condensate.

From the GPE dynamics, for weaker interaction values, we saw that the decay of the $n_r = 2$ mode created density waves with wavelength much larger than what was expected from the Beliaev theory predictions. Here, the wavelength of the pattern is closer to that obtained from monopole ($n_r = 1$) decay. This, along with the fact that at vanishing interaction strength, the Beliaev theory predicts the decay of $n_r = 2$ mode into radial monopole modes, suggests that at weaker interaction, monopole mode may have played an intermediate role. However, we do not observe any increase in radial breathing motion at weaker interactions. At larger interaction, both the theory and simulations show that $n_r = 2$ radial mode decays predominantly to dipole and quadrupole branches, leading to interesting longitudinal patterns. We do observe weak $n_{x,y}$ density wave formation for larger interactions, but the pattern wavenumber k_D now satisfies $\omega_{0,\pm 2}(k_D) = \omega_{2,0}(0)/2$.

Thus, GPE simulation qualitatively matches the Beliav predictions. We note that Beliaev decay could be understood in terms of non-linear mixing of modes under the GPE [146]; however, no rigorous connections have been established to our best knowledge.

3.7 Conclusion

In this chapter, we have looked at the resonant excitation and subsequent decay of radial modes in a cylindrically confined and axially free condensate, under the periodic modulation of s-wave scattering length. We found that the condensate exhibits several direct resonance points, and driving at these frequencies leads to strong radial excitations in the condensate, and the nature of the excitation depends on the quasiparticle that is resonant under driving. When the driving frequency matches the transverse monopole frequency, the condensate exhibits radial breathing that gets amplified in time, whereas when it matches the second resonance point ($n_r = 2$), the radial density profile of the condensate develops annular patterns, along with the RMS radius of the condensate steadily increasing under drive.

The radial modes excited under such resonant drive spontaneously decay to create pairs of excitation in the lower branches of the Bogoliubov spectrum via Beliaev damping. The monopole mode decays to create density waves with half its characteristic frequency. The wavelength of the pattern can be determined from the gapless density branch of the excitation spectra. For the resonantly excited $n_r = 2$ mode, the decay process is more complex due to the existence of multiple decay channels. When the initial interaction of the system is relatively weak, the decay creates density waves, whose wavelength suggests that monopole modes may have an intermediate role. In a condensate with larger values of interaction strengths, the decay creates density and COM oscillation (zig-zag) patterns along the condensate, with COM oscillations being more prominent, and their wavelength can be determined from the Bogoliubov spectrum.

We have used both Bogoliubov theory and GPE simulation to study the dynamics, and the results are in agreement. We look at the response of the system driven with frequencies away from these direct resonances in the next chapter.

Chapter 4

Parametric resonances in a cylindrically confined BEC

This work in this chapter is currently ongoing.

4.1 Introduction

Parametric resonances arise in many driven systems, including optical [52], superconducting [193], and plasmonic systems [153], as well as in vibrating fluids [31] and driven Bose-Einstein condensates (BECs), where they can lead to the spontaneous formation of density waves [49, 162]. The classical parametric oscillator is described by the equation

$$\frac{d^2x}{dt^2} + \omega_{PO}^2(t)x = 0, \tag{4.1}$$

where the oscillator's natural frequency is periodically modulated as $\omega_{PO}^2(t) = \bar{\omega}_{PO}^2[1 + \alpha\cos(\Omega t)]$, with $\alpha \ll 1$. This equation models, for instance, a pendulum with a vertically oscillating suspension point, or an LC circuit with a periodically varying inductance. Equation (4.1) admits the trivial solution $x_0(t) = 0, \dot{x}_0(t) = 0$, indicating that an initially stationary oscillator remains at rest despite the periodic drive. However, this solution is not always stable. A linear stability analysis shows that when the driving frequency satisfies,

$$\Omega = 2\omega_{P0}, \tag{4.2}$$

the trivial solution becomes unstable, and any small perturbation grows exponentially. This phenomenon is known as parametric resonance [25, 99]. In BECs, periodic modulation of the interaction strength or the trapping potential can similarly induce spontaneous pattern formation. Such modulations have led to observations of periodic density waves in elongated condensates [49, 124], two-dimensional density patterns [103, 104, 201], and star-shaped surface waves in pancake-shaped condensates [96]. Similar effects have also been reported in two-component condensates [39]. Beyond pattern formation, parametric resonances in

BECs have been used to generate squeezed states [75], simulate the dynamical Casimir effect [83], and are of particular relevance in Floquet engineering, where they can cause unwanted heating [100, 192].

In Chapter 3, we saw that the radial modes of a driven cylindrical condensate exhibit resonances at specific driving frequencies given by

$$\Omega = \omega_{n_r,0}(0), \tag{4.3}$$

where denotes the frequency of the Bogoliubov mode. Away from these direct resonance points, the condensate dynamics are dominated by parametric resonances, which we examine in detail in this chapter.

The outline of the chapter is as follows. In section 4.2, we briefly reintroduce the system under consideration. In section 4.3, we study its response to periodic driving of interaction, under a quasi-one-dimensional (Q1D) approximation. Here, we use a linear stability analysis of the uniform mean-field state and the Bogoliubov theory. The Q1D approach does not consider the role of radial modes in the dynamics. In section 4.4, we consider the dynamics of the excited modes in a 3D driven cylindrical condensate, using an approximate approach which allows Floquet theory and a linear stability of the driven GPE solution. The results are compared with the GPE evolution of a perturbed initial ground state in sections 4.5 and 4.6. We find that the Q1D approximation captures the relevant dynamics for weak interaction, away from the resonances in Eq. (4.3). For interaction strength beyond the Q1D limit, radial modes play a more substantial role.

4.2 System

The system we study in this chapter is the same as the one described in the last chapter. We consider a weakly interacting gas of bosons with mass M that is harmonically trapped in the radial xy-plane, with the trap potential $V_\rho(\rho) = (1/2)M\omega_\rho^2\rho^2$, and free along the longitudinal z direction. The trapped bosons interact via two-body collisions, characterized by the s-wave scattering length a_s. The dimensionless parameter characterizing the interaction is given by

$$\eta = 4\pi a_s n_H, \tag{4.4}$$

where $n_H = N/L_z$ is the linear density, with N and L_z being the particle number and length of the system along the z-direction, respectively. The second quantized Hamiltonian describing this system is given in Eq. (3.1). At very low temperature, when the system is Bose condensed, it is also described using the mean-field order-parameter $\psi(\boldsymbol{r})$ that obeys the

Gross-Pitaevskii equation,

$$i\hbar\frac{\partial\psi(\boldsymbol{r},t)}{\partial t} = \left[-\frac{\hbar^2\nabla^2}{2M} + V_\rho(\rho) + g(t)|\psi(\boldsymbol{r},t)|^2\right]\psi(\boldsymbol{r},t). \tag{4.5}$$

At time $t = 0$, the system is at the ground state with constant interaction $\bar{\eta}$, and when $t > 0$, the scattering length is driven periodically. as,

$$a_s(t) = \bar{a}_s + \Delta a_s \cos(\Omega t). \tag{4.6}$$

The interaction coefficient also evolve periodically as $\eta(t) = \bar{\eta} + \Delta\eta\cos(\Omega t)$ with $\Delta\eta = 4\pi\Delta a_s n_H$.

4.3 Quasi-one-dimensional driven BEC

The system we mentioned above can be described using a quasi-one-dimensional (Q1D) approximation when the transverse trap energy is much larger than all other energy scales in the system [see Sec. 2.4]. In this case, the radial motion of atoms is assumed to be frozen in the harmonic ground state, and dynamics can be reduced to that in the longitudinal direction.

The approximation is valid if $\mu_{1D} \ll \hbar\omega_\rho$, where μ_{1D} is the 1D chemical potential of the system and ω_ρ is the transverse trap frequency. However, in a time-periodic system, the approximation can break down even if this condition is met. The simplest example is periodically driving the system at a frequency resonant with a radial excitation. We discussed this scenario in the last chapter, where we saw the condensate exhibiting radial dynamics even at a very small driving amplitude. Despite these shortcomings, the quasi-1D picture can capture the qualitative dynamics when the driving frequency is not resonant with the radial modes.

In this section, we look at the dynamics of a periodically driven Q1D homogeneous system. We do so using two approaches: the linear stability analysis of the mean-field solution and the Bogoliubov theory. We show that these methods give us the same quantitative predictions for the system.

4.3.1 Linear stability analysis of mean-field solution

In Sec. 2.8.1, we discuss the pattern formation in a driven homogeneous 2D system, where linear stability analysis was used to predict the wavelength of the patterns formed in the system. Here, we employ the same analysis to a Q1D driven BEC.

The dynamics of the Q1D wavefunction $\tilde{\psi}(z)$ of the condensate is given by the GPE,

$$i\hbar\frac{\partial\tilde{\psi}}{\partial t} = \left[-\frac{\hbar^2}{2M}\frac{\partial^2}{\partial z^2} + g_{1D}(t)|\tilde{\psi}|^2\right]\tilde{\psi}, , \tag{4.7}$$

where the 1D coefficient interaction $g_{1D}(t) = 2\hbar^2 a_s(t)/Ml_\rho^2$. In the absence of any driving, the ground state of the equation is uniform given by $\tilde{\psi}_0(z) = \sqrt{n_H}$ and the 1D chemical potential being $\mu_{1D} = \bar{g}_{1D}n_H$, where $\bar{g}_{1D} = 2\hbar^2\bar{a}_s/Ml_\rho^2$ denoting the constant interaction.

Under the periodic driving of interaction as given in Eq. (4.6), the 1D coefficient evolve as $g_{1D}(t) = \bar{g}_{1D} + \Delta g_{1D}\cos(\Omega t)$, where $\Delta g_{1D} = 2\hbar^2\Delta a_s/Ml_\rho^2$. In this case, the uniform state becomes unstable to the formation of density modulation. To see this, we do a linear stability analysis on the uniform solution of the driven GPE (4.7) [162], given by $\tilde{\psi}(t) = e^{-i\theta_H(t)}$ with

$$\theta_H(t) = \bar{g}_{1D}n_H t + \Delta g_{1D}n_H\frac{\sin(\Omega t)}{\Omega}. \tag{4.8}$$

A spatially modulated perturbation is added to this solution as $\tilde{\psi}(t) = [1+w(t)\cos(kz)]e^{-i\theta_H(t)}$, where $w(t)$ and k are the amplitude and momentum of the perturbation, respectively. We then seek linearized solutions to $w(t)$ from the GPE (4.7), and after simplifying we arrive at,

$$\hbar^2\frac{d^2u}{dt^2} + \left[\epsilon_{1D}^2(k) + 2E_k\Delta g_{1D}n_H\cos(\Omega t)\right]u = 0, \tag{4.9}$$

where,

$$\epsilon_{1D}(k) = \sqrt{E_k(E_k + 2\mu_{1D})}, \tag{4.10}$$

is the Bogoliubov spectrum of the homogeneous 1D system, with $E_k = \hbar^2k^2/2M$. Eq. (4.9) is a Mathieu equation. Floquet theory states that solutions of the form $u(t) = e^{\sigma t}p(t)$ exist for Eq. (4.9), where $p(t + 2\pi/\Omega) = p(t)$ is a periodic function and σ is the known as the Floquet exponent. If $\mathrm{Re}\{\sigma\} > 0$ for a particular k, the uniform state is unstable to the formation of density modulation at that wavenumber under driving. The most unstable momentum k_u is the momentum for which $\mathrm{Re}\{\sigma\}$ is the largest. We can show when $\Delta g_{1D} \to 0$, k_u satisfy,

$$\hbar\Omega = 2\epsilon_{1D}(k_u), \tag{4.11}$$

and Floquet exponent at this point is given as $\mathrm{Re}\{\sigma\}_{\Delta g_{1D}\to 0} = \Delta g_{1D}n_H E_{k_u}/\hbar^2\Omega$ [122]. This is parametric resonance, where surface modes with a characteristic frequency half that of the driving frequency get excited. Here we have ignored dissipation, which introduces a minimum amplitude above which one has to modulate if wave formation is to be observed [162].

4.3.2 Bogoliubov theory calculation

We now demonstrate that the same results as above can be obtained using Bogoliubov theory. Similar calculations were done in Ref. [27], focusing on density correlations. The second-quantized Hamiltonian for a Q1D Bose gas is given by [140],

$$\hat{H}_{1D}(t) = \sum_k E_k \hat{a}_k^\dagger \hat{a}_k + \frac{g_{1D}}{2L_z} \sum_{\substack{k_1,k_2 \\ k_3,k_4}} \hat{a}_{k_1}^\dagger \hat{a}_{k_2}^\dagger \hat{a}_{k_3} \hat{a}_{k_4}\ \delta(k_1 + k_2 - k_3 - k_4), \tag{4.12}$$

where $\hat{a}_k$ annihilates a particle in the longitudinal momentum state k, in the ground state of radial trap. As in the previous section, we assume that the transverse degrees of freedom are frozen to the ground state of the harmonic trap. The delta function in the second term ensures the momentum conservation of interacting pair of particles under the two-body interaction.

Under Bose–Einstein condensation, the zero-momentum mode becomes macroscopically occupied, thus the population in this mode $N_0 = \langle \hat{a}_0^\dagger \hat{a}_0 \rangle \approx N$. We define the number of particles in the non-zero momentum modes as,

$$\delta\hat{N} = \sum_{k\neq 0} \hat{a}_k^\dagger \hat{a}_k. \tag{4.13}$$

Assuming particle number conservation, we can write $\hat{a}_0^\dagger \hat{a}_0 = N - \delta\hat{N}$. For small non-condensate population $\langle \delta N \rangle \ll N$, we also have $\hat{a}_0^\dagger \hat{a}_0^\dagger \hat{a}_0 \hat{a}_0 \approx N^2 - 2N\delta\hat{N}$. Substituting these into the Hamiltonian,

$$\hat{H}_{1D}(t) \approx \sum_{k\neq 0} E_k \hat{a}_k^\dagger \hat{a}_k + \frac{g_{1D}}{2L_z} \left\{ \sum_{k\neq 0} [N \hat{a}_k \hat{a}_{-k} + \text{H.c.}] + 4N \hat{a}_k^\dagger \hat{a}_k + N(N - 2\delta\hat{N}) \right\}. \tag{4.14}$$

Here, we have neglected cubic order and higher order terms in $\hat{a}_{k\neq 0}$, which is justified for a small non-condensate population. Under the periodic driving of the scattering length, we can split the Hamiltonian into a time-independent part,

$$\hat{H}_{1D}^{(0)} = \frac{1}{2} g_{1D} n_H N + \sum_{k\neq 0} E_k \hat{a}_k^\dagger \hat{a}_k + \frac{g_{1D} n_H}{2} \sum_{k\neq 0} \left\{ \hat{a}_k \hat{a}_{-k} + \hat{a}_k^\dagger \hat{a}_{-k}^\dagger + 2\hat{a}_k^\dagger \hat{a}_k \right\}, \tag{4.15}$$

and a periodic perturbation,

$$V_{1D}^{(T)}(t) = \frac{1}{2} \Delta g_{1D} n_H \cos(\Omega t) \left[N + \sum_{k\neq 0} \left\{ \hat{a}_k \hat{a}_{-k} + \hat{a}_k^\dagger \hat{a}_{-k}^\dagger + 2\hat{a}_k^\dagger \hat{a}_k \right\} \right]. \tag{4.16}$$

The time-independent Hamiltonian can be diagonalized by the Bogoliubov transformation of the operators [see Sec. 2.5.1],

$$\hat{a}_k = u_k \hat{b}_k + v^*_{-k} \hat{b}^\dagger_{-k}, \quad \hat{a}^\dagger_k = u^*_k \hat{b}^\dagger_k + v_{-k} \hat{b}_{-k}, \tag{4.17}$$

Here, the Q1D Bogoliubov operators satisfy bosonic commutation relations $[\hat{b}_k, \hat{b}^\dagger_{k'}] = \delta_{kk'}$ and the coefficients are given by

$$u_k = \sqrt{\frac{E_k + \mu_{1D}}{2\epsilon_{1D}(k)} + \frac{1}{2}}, \quad v_k = -\sqrt{\frac{E_k + \mu_{1D}}{2\epsilon_{1D}(k)} - \frac{1}{2}}, \tag{4.18}$$

where $\epsilon_{1D}(k)$ is the homogeneous 1D spectrum defined in Eq. (4.10). Under the transformation, we get,

$$\hat{H}^{(I)}_{1D} = E^{(1D)}_0 + \sum_{k \neq 0} \epsilon_{1D}(k) \hat{b}^\dagger_k \hat{b}_k. \tag{4.19}$$

From here, we see that the Bogoliubov quasiparticle population remains constant as $\langle \hat{b}^\dagger_k(t) \hat{b}_k(t) \rangle = \langle \hat{b}^\dagger_k(0) \hat{b}_k(0) \rangle$ in the absence of modulation. The evolution in the presence of modulation is given by the Heisenberg equation of motion,

$$i\hbar \frac{\partial}{\partial t} \hat{b}_k = \left[\hat{b}_k, \hat{H}^{(I)}_{1D} + V^{(T)}_{1D}(t) \right] \tag{4.20}$$

Using the commutation relations of the Bogoliubov operators, we arrive at the following equation of motion for the operators under driving given by,

$$i\hbar \frac{\partial}{\partial t} \begin{pmatrix} \hat{b}_k \\ \hat{b}^\dagger_{-k} \end{pmatrix} = \begin{pmatrix} \hbar\omega_{k,1D} + \frac{\Delta g_{1D} n_H E_k}{\epsilon_{1D}(k)} \cos(\Omega t) & \frac{\Delta g_{1D} n_H E_k}{\epsilon_{1D}(k)} \cos(\Omega t) \\ -\frac{\Delta g_{1D} n_H E_k}{\epsilon_{1D}(k)} \cos(\Omega t) & -\hbar\omega_{k,1D} - \frac{\Delta g_{1D} n_H E_k}{\epsilon_{1D}(k)} \cos(\Omega t) \end{pmatrix} \begin{pmatrix} \hat{b}_k \\ \hat{b}^\dagger_{-k} \end{pmatrix}. \tag{4.21}$$

We can seek solution to this equation of the following form,

$$\begin{aligned} \hat{b}_k(t) &= c_k(t) \hat{b}_k(0) + \tilde{c}_k(t) \hat{b}^\dagger_{-k}(0) \\ \hat{b}^\dagger_{-k}(t) &= c'_k(t) \hat{b}_k(0) + \tilde{c}'_k(t) \hat{b}^\dagger_{-k}(0). \end{aligned} \tag{4.22}$$

The time-dependent coefficient can then be shown to follow the same set of equations as $\hat{b}_k, \hat{b}^\dagger_{-k}$. Since this is a linear equation with periodic coefficients, we can apply Floquet theory (Sec. 2.7), which predicts solutions of the form,

$$\begin{pmatrix} c_k \\ \tilde{c}^*_k \end{pmatrix} = e^{\sigma_k t} \begin{pmatrix} p_{1,k} \\ p_{2,k} \end{pmatrix}, \tag{4.23}$$

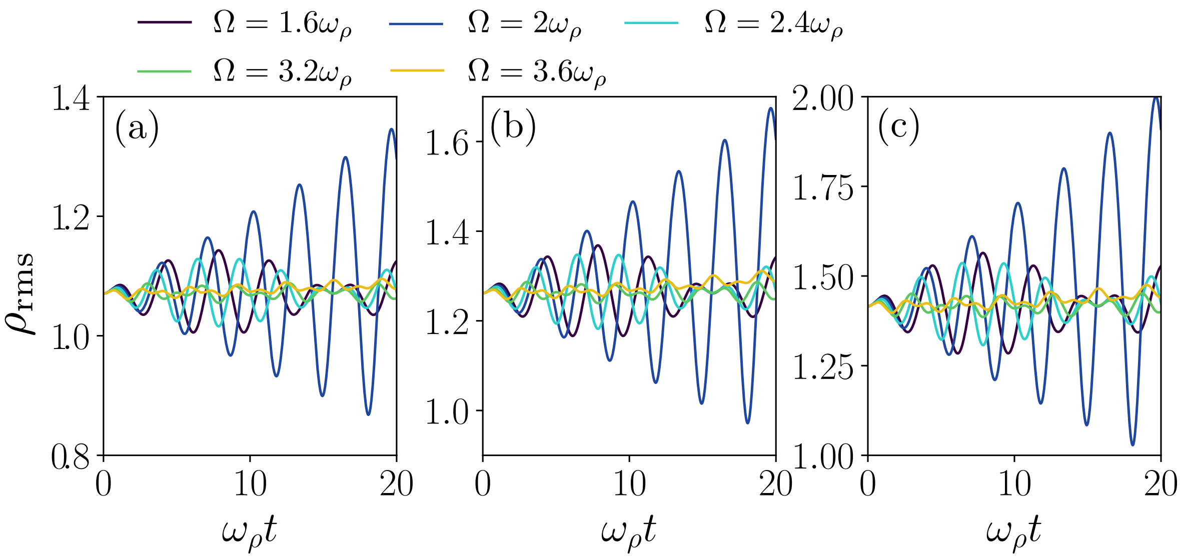

FIGURE 4.1: *Mean-field evolution of driven cylindrical BEC*: Dynamics of RMS radius in the xy-plane, $\rho_{\rm rms}(t) = (1/L_z)\int d\boldsymbol{r}\rho|\psi(\boldsymbol{r},t)|^2$, under modulation for scattering length at mean-interaction and driving amplitude values (a) $\bar{\eta} = 2$ and $\alpha = 0.1$, (b) $\bar{\eta} = 10$ and $\alpha = 0.05$, and (c) $\bar{\eta} = 20$. The results are given for various driving frequencies Ω.

where $p_{1/2,k}(t + 2\pi/\Omega) = p_{1/2,k}(t)$ is a periodic function, and σ_k is the Floquet exponent. At timescales larger than the driving period, the evolution determined by σ_k, and the mode population grows as,

$$\langle \hat{b}_k^\dagger(t)\hat{b}_k(t)\rangle \sim e^{2\,\mathrm{Re}\{\sigma_k\}t}. \tag{4.24}$$

If $\mathrm{Re}\{\sigma_k\} > 0$, the corresponding mode becomes unstable as its population increases exponentially under the drive. We show that (Appendix B) that when Δg_{1D} is infinitesimally small, the instability occur for the mode with momentum k_u satisfying,

$$\hbar\Omega = 2\epsilon_{1D}(k_u), \tag{4.25}$$

and the Floquet exponent for the most unstable mode is $\mathrm{Re}\{\sigma_k\} = \Delta g_{1D} n_H k_u^2/2\hbar^2\Omega$. These predictions match the ones we obtain from the linear stability analysis.

4.4 Theory of driven condensate in three-dimensions

In the Q1D analysis, we have neglected the radial degrees of freedom of the condensate. In this section, we look at the full 3D dynamics of the driven cylindrically confined system, which allows us to verify the validity Q1D approximation for low interactions. We also extend the study to higher interaction regimes beyond this approximation.

Extending the quasi-1D analysis to 3D trapped condensate is challenging due to the motion of the background condensate, due to the driving [180]. For the homogeneous 1D system, the uniform state satisfies the driven GPE, and the perturbations about this solution can be expanded in the momentum basis. For an inhomogeneous condensate, there are no stationary solutions under periodic driving, as the condensate expands and contracts radially under the modulation. Therefore, the dynamics of the longitudinal excitation are not only affected by the driving itself, but they can also be affected by the radial motion of the condensate [126]. The radial dynamics of the mean-field solution are also not periodic [see Fig. 4.1], thus making the use of Floquet theory questionable.

In this section, we attempt to include the radial degrees of freedom of condensate into the theoretical analysis in two ways.

i. Floquet theory approach: In this method, we ignore the radial dynamics of the GPE mean-field solution and derive the equations of motion of the Bogoliubov operators of the 3D cylindrical system. This is an extension of the method discussed in Sec. 4.3.2, and we use the Floquet theory to find the unstable modes in the system

ii. Linear stability analysis of mean-field solution: Here we follow the method developed in Ref. [29], using which we study the dynamics of the Bogoliubov modes. This approach is more tedious, but it enables us to take into account the effect of radial motion in the mode dynamics.

4.4.1 Floquet theory approach

Here, we expand the field operator as follows,

$$\hat{\Psi}(\boldsymbol{r}, t) = \left[\frac{\xi_0(\rho)}{\sqrt{L_z}} \hat{a}_0 + \delta\hat{\Psi}(\boldsymbol{r}, t) \right] e^{-i\mu t}. \tag{4.26}$$

where $\xi_0(\rho)$ is the mean-field ground state of the condensate in the absence of driving. This expansion holds an implicit assumption that the condensate wavefunction is stationary in time, which we justify by assuming that the driving amplitude of the scattering length is weak enough to ignore the radial motion of the condensate. We have already discussed the expansion of the Hamiltonian using Eq. (4.26) in Sec. 3.4, where we saw that the term $\hat{V}_I^{(1)}(t)$ that is linear in $\delta\hat{\Psi}$ causes radial mode excitation at resonant driving frequency Ω Eq. (4.3). When Ω is not at these resonant values, the quadratic Hamiltonian $\hat{V}_I^{(2)}(t)$ can no longer be ignored. Expanding the $\hat{V}_I^{(2)}(t)$ in the Bogoliubov basis Eq. (3.15), we arrive at the following,

$$\hat{V}_I^{(2)}(t) = \Delta g n_H \cos(\Omega t) \sum_{\substack{n_r,n_r' \\ \nu,k_z}} P_{n_r,n_r'}^{(\nu,k_z)} \hat{b}^\dagger_{n_r,\nu,k_z}(t) \hat{b}_{n_r',\nu,k_z}(t) + \left[Q_{n_r,n_r}^{(\nu,k_z)} \hat{b}^\dagger_{n_r,\nu,k_z}(t) \hat{b}^\dagger_{n_r',-\nu,-k_z}(t) + \text{H.c.} \right], \tag{4.27}$$

where the coupling coefficients are given as,

$$\begin{aligned} P_{n_r,n_r'}^{(\nu,k_z)} &= \int \rho d\rho \left(|\xi_0|^2 [\bar{u}^*_{n_r,\nu,k_z} \bar{v}_{n_r',\nu,k_z} + \bar{v}^*_{n_r,\nu,k_z} \bar{u}_{n_r',\nu,k_z}] + (2|\xi_0|^2 - \Xi)[\bar{v}^*_{n_r,\nu,k_z} \bar{v}_{n_r',\nu,k_z} + \bar{u}_{n_r,\nu,k_z} \bar{u}^*_{n_r',\nu,k_z}] \right) \\ Q_{n_r,n_r'}^{(\nu,k_z)} &= \int \rho d\rho \left[\frac{|\xi_0|^2}{2} (\bar{u}^*_{n_r,\nu,k_z} \bar{u}^*_{n_r',\nu,k_z} + \bar{v}^*_{n_r,\nu,k_z} \bar{v}^*_{n_r',\nu,k_z}) + (2|\xi_0|^2 - \Xi) \bar{v}^*_{n_r,\nu,k_z} \bar{u}^*_{n_r',\nu,k_z} \right]. \end{aligned} \tag{4.28}$$

As we can see in Eq. (4.27), $V_I^{(2)}(t)$ describes the creation and annihilation of pairs of excitations with quantum numbers $\pm\nu$ and $\pm k_z$. Thus, the dynamics of Bogoliubov modes are no longer uncoupled when driving is present.

We now restrict our analysis to the modes with non-zero ν and k_z quantum numbers, for which the lowest order dynamics is given by $\hat{V}_I^{(2)}(t)$. The equations of motion of these modes are obtained using the Heisenberg equation,

$$i\hbar \frac{d\hat{b}_{n_r,\nu,k_z}}{dt} = \Delta g n_H \cos(\Omega t) e^{i\omega_{n_r,\nu}(k_z)t} \sum_{n_r'} P_{n_r,n_r'}^{(\nu,k_z)} \hat{b}_{n_r',\nu,k_z} e^{-i\omega_{n_r',\nu}(k_z)t} + \tilde{Q}_{n_r,n_r'}^{(\nu,k_z)} \hat{b}^\dagger_{n_r',-\nu,-k_z} e^{i\omega_{n_r',-\nu}(-k_z)t}, \tag{4.29}$$

where $\tilde{Q}_{n_r,n_r'}^{(\nu,k_z)} \equiv Q_{n_r,n_r'}^{(\nu,k_z)} + Q_{n_r',n_r}^{(\nu,k_z)}$. By making the transformation $\hat{b}_{n_r,\nu,k_z} e^{-i\omega_{n_r,\nu}(k_z)t} \to \hat{b}_{n_r,\nu,k_z}$, we finally arrive at the following set of equations,

$$i\hbar \frac{d}{dt} \begin{pmatrix} \boldsymbol{B}_{\nu,k_z} \\ \bar{\boldsymbol{B}}_{-\nu,-k_z} \end{pmatrix} = \begin{pmatrix} \boldsymbol{M}^{(0)}_{\nu,k_z} & \boldsymbol{M}^{(1)}_{\nu,k_z} \\ -\left[\boldsymbol{M}^{(1)}_{\nu,k_z}\right]^* & -\left[\boldsymbol{M}^{(0)}_{\nu,k_z}\right]^* \end{pmatrix} \begin{pmatrix} \boldsymbol{B}_{\nu,k_z} \\ \bar{\boldsymbol{B}}_{-\nu,-k_z} \end{pmatrix}. \tag{4.30}$$

Here the column vectors $\boldsymbol{B}_{\nu,k_z} = (\hat{b}_{0,\nu,k_z}, \hat{b}_{1,\nu,k_z}, \dots)^T$ and $\bar{\boldsymbol{B}}_{\nu,k_z} = (\hat{b}^\dagger_{0,\nu,k_z}, \hat{b}^\dagger_{1,\nu,k_z}, \dots)^T$ and the matrices contains the following elements,

$$\left[\boldsymbol{M}^{(0)}_{\nu,k_z}(t)\right]_{n_r n_r'} = \hbar\omega_{n_r,\nu}(k_z)\delta_{n_r,n_r'} + \Delta g n_H \cos(\Omega t) P_{n_r,n_r'}^{(\nu,k_z)}, \tag{4.31}$$

$$\left[\boldsymbol{M}^{(1)}_{\nu,k_z}(t)\right]_{n_r n_r'} = \Delta g n_H \cos(\Omega t) \tilde{Q}_{n_r,n_r'}^{(\nu,k_z)}, \tag{4.32}$$

The set of coupled equations can be solved numerically to obtain the population of various excited modes. We use Floquet theory to further simplify the problem, as described in the next section.

Floquet theory

We can apply Floquet theory to Eq. (4.30), since it is a set of linear equations with periodic coefficients. The long-time dynamics (as compared to the driving period) of the modes are contained within the Floquet exponents, which can be used to definitively identify the instability of the modes.

First, we note that the solution to Eq. (4.30) can be sought of the forms,

$$\hat{b}_{n_r,\nu,k_z}(t) = \sum_{n'_r} c_{n_r n'_r}(t)\hat{b}_{n'_r,\nu,k_z}(0) + \tilde{c}_{n_r n'_r}(t)\hat{b}^{\dagger}_{n'_r,-\nu,-k_z}(0). \tag{4.33}$$

The time-dependent coefficients follow the same equations as modes, given by

$$i\hbar\frac{d}{dt}\begin{pmatrix} \boldsymbol{C}_{n_r} \\ \tilde{\boldsymbol{C}}^*_{n_r} \end{pmatrix} = \begin{pmatrix} \boldsymbol{M}^{(0)}_{\nu,k_z} & \boldsymbol{M}^{(1)}_{\nu,k_z} \\ -\left[\boldsymbol{M}^{(1)}_{\nu,k_z}\right]^* & -\left[\boldsymbol{M}^{(0)}_{\nu,k_z}\right]^* \end{pmatrix}\begin{pmatrix} \boldsymbol{C}^*_{n_r} \\ \tilde{\boldsymbol{C}}_{n_r} \end{pmatrix}, \tag{4.34}$$

where the column vector $\boldsymbol{C}_{n_r} = (c_{n_r,1}, c_{n_r,2}, \dots)^T$ and $\tilde{\boldsymbol{C}}_{n_r} = (\tilde{c}_{n_r,1}, \tilde{c}_{n_r,2}, \dots)^T$. Floquet theory states that there exist solutions of the form,

$$\begin{pmatrix} \boldsymbol{C}_{n_r}(t) \\ \tilde{\boldsymbol{C}}^*_{n_r}(t) \end{pmatrix} = e^{\sigma t}\begin{pmatrix} \boldsymbol{P}_{n_r}(t) \\ \tilde{\boldsymbol{P}}^*_{n_r}(t) \end{pmatrix}, \tag{4.35}$$

where $\boldsymbol{P}_{n_r}(t)$ and $\tilde{\boldsymbol{P}}_{n_r}(t)$ are periodic with time-period $T = 2\pi/\Omega$. The Floquet exponents σ can be obtained numerically by solving the set of equations over one modulation period, using the method we outlined in Sec. 2.7. If $\mathrm{Re}\{\sigma\} > 0$, it indicates an instability under driving that creates an exponential increase in the population of excited modes.

There are n distinct exponents for a system of n coupled differential equations, but the solution with the exponent having the largest real part dominates the dynamics. We use σ_{ν,k_z} to denote the exponent with the largest real part for a given value of $|\nu|, |k_z|$. If $\mathrm{Re}\{\sigma_{\nu,k_z}\} > 0$, we expect the instability to cause longitudinal pattern formation with wavelength $2\pi/k_z$.

Q1D interaction limit

We first look at the Floquet theory results for driven condensate interaction in the Q1D limit. We restrict our analysis to driving frequencies $0 < \Omega < 4\omega_\rho$, which lie in the experimentally achievable region [124]. The unstable modes are determined by solving Eq. (4.34) for various ν, k_z values, after truncating it to include coupling between $n_r = 0, 1$ modes only. We verified that including more modes in the calculation does not affect the result.

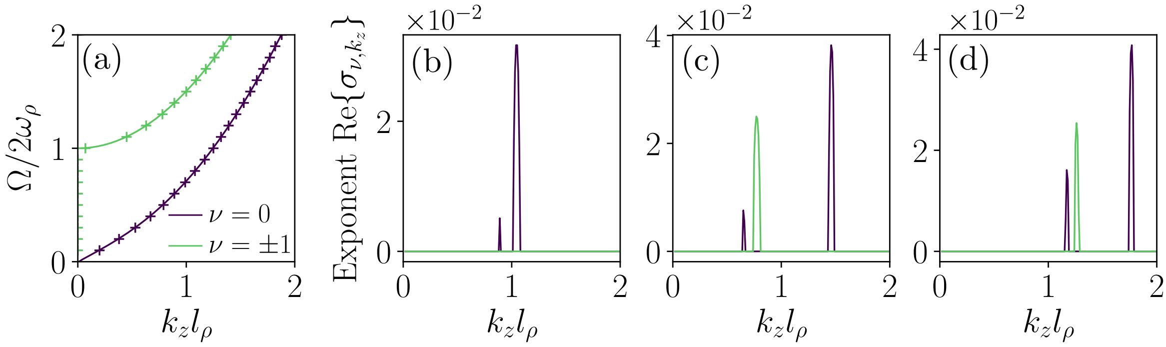

FIGURE 4.2: (a) The momenta (marked by "+") of the most unstable modes in the gapless branch ($\nu = 0$) and dipole branch ($\nu = \pm 1$) obtained from Eq. (4.34) plotted as function of driving frequency Ω (y-axis). Solid lines indicate the Bogoliubov dispersion relations $\omega_{0,\nu}(k_z)$. The real part of the Floquet exponent σ_{ν,k_z} for various k_z at driving frequencies (b) $\Omega/2 = 0.75\omega_\rho$, (c) $\Omega/2 = 1.2\omega_\rho$, and (d) $\Omega/2 = 1.8\omega_\rho$. Peaks indicate instability at the corresponding momenta. Here $\bar{\eta} = 2.0$ and $\Delta\eta = 1.2$.

Here we see that, under periodic driving, parametric resonance occurs for modes from radial branches as well, with the general resonance condition being,

$$\Omega = 2\omega_{n_r,\nu}(k_z). \tag{4.36}$$

In Fig. 4.2 (a), we plot the axial momenta k_z of the most unstable modes for $\nu = 0$ and $\nu = \pm 1$, as a function of driving frequencies. The predictions for the modes from the gapless branch match those from the Q1D analysis. The resonance in Eq. (4.36) occurs due to the strong mixing between modes with $\pm\nu$ and $\pm k_z$, creating pairs of such excitation with total energy $\hbar\Omega$ [201].

Although we see instability arising from both the gapless branch ($n_r = 0, \nu = 0$) and the dipole branch ($n_r = 0, \nu = \pm 1$), the condensate dynamics will be dominated by the unstable mode with the larger Floquet exponent. Fig. 4.2 (b)-(c) show the $\mathrm{Re}\left\{\sigma_{\nu,k_z}\right\}$ for $\nu = 0, \pm 1$ for different driving frequencies. The peak position in these plots gives us the momenta of the unstable modes. When driving frequency $\Omega < 2\omega_\rho$, the dipole branch ($\nu = \pm 1$) modes are not unstable. When $\Omega > 2\omega_\rho$, dipole branch modes are unstable, but the Floquet exponent $\mathrm{Re}\left\{\sigma_{0,k_z}\right\} > \mathrm{Re}\left\{\sigma_{\pm 1,k_z}\right\}$. The dynamics are thus dominated by the gapless branch modes, which create longitudinal density waves upon excitation.

The pair creation process can also occur for modes with different radial node numbers n_r. This process must conserve energy, longitudinal momentum, and angular momentum, which gives us the most general resonance condition as,

$$\Omega = \omega_{n_r,\nu}(k_z) + \omega_{n_r',-\nu}(-k_z) \tag{4.37}$$

This describes a process that creates a pair of excitations with quantum numbers $\{n_r, \nu, k_z\}$ and

$\{n'_r, -\nu, -k_z\}$. In Fig. 4.2 (b)-(c), as well as in the later GPE simulations, we see a signature of resonance creating pairs of modes with $n_r \neq n'_r$. This is seen as the smallest peak in these figures. Due to the very small value of their Floquet exponent, such processes do not play any significant role in the dynamics.

Thus, the 3D analysis here shows that, although the modes from the gapped radial branches are unstable under driving, the dynamics are dominated by the density pattern formation resulting from the lowest branch instability. Thus, Q1D theory remains valid at weak interaction, even when driving frequency $\Omega > 2\omega_\rho$.

Interactions beyond Q1D limit

The Q1D interaction picture is not expected to be valid at regimes where $\mu\hbar \gtrapprox \omega_\rho$. We also find, however, that the Floquet Hamiltonian approach incorporating the radial modes also fails to accurately capture the dynamics of the condensate, as we find discrepancies with the GPE results. The Floquet calculations predict the dipole branch modes to be more unstable than the gapless branch modes at driving frequencies greater than but close to $2\omega_\rho$, and vice versa when the driving frequency is larger. The GPE results predict the exact opposite results. In order to understand this deviation, we turn to an approach that does not ignore the radial oscillations of the condensate under periodic driving (Fig. 4.1).

4.4.2 Linear stability analysis of the mean-field solution

To understand the effect of radial condensate motion under driving on the evolution of quasi-particles, we use the method described in Ref. [29]. First, we will briefly discuss some background here.

In general, the response of a condensate in the presence of a time-dependent interaction or trap can be classified into two types;

i. The collective motion of the condensate mode

ii. The evolution of the non-condensate atoms

Condensate mode is the macroscopically populated mode, which in the number-conserving formalism is defined as the eigenvector of the one-body density matrix with the largest eigenvalue. The corresponding eigenvalue, $N_0 \approx N$, gives the condensate population. For the cylindrically confined system, the condensate mode dynamics is given by time-dependent 2D GPE,

$$i\hbar\frac{\partial\psi_0(\rho,t)}{\partial t} = \left[-\frac{\hbar^2\nabla^2_{x,y}}{2M} + V_\rho(\rho) + g(t)|\psi_0(\rho,t)|^2\right]\psi_0(\rho,t), \tag{4.38}$$

as the system remains uniform along the z-direction under the driving. Here, we use the subscript to differentiate the condensate mode $\psi_0(\rho, t)$ from the 3D GPE solution $\psi(\boldsymbol{r}, t)$, which is the evolved from a perturbed initial ground state, and these two solutions diverge from each other due to the parametric instabilities in the system.

The particles can also leave and enter the condensate mode, and the mean-field does not capture this dynamics. The dynamics of the non-condensate particles can be expressed in terms of the evolution of Bogoliubov modes, and at the lowest/ linear order, it follows the equation [28, 29],

$$i\hbar\frac{d}{dt}\begin{pmatrix}|u_n(t)\rangle\\|v_n(t)\rangle\end{pmatrix} = \hat{\mathcal{L}}_Q(t)\begin{pmatrix}|u_n(t)\rangle\\|v_n(t)\rangle\end{pmatrix}. \tag{4.39}$$

Here $|u_n(t)\rangle$ and $|v_n(t)\rangle$ denote the quasiparticle amplitude at time t. In this formalism, we assume the quasiparticle operator $\hat{b}_n$ is time-independent, while the amplitudes evolve. At time $t = 0$, the $|u_n(t)\rangle$ and $|v_n(t)\rangle$ are the Bogoliubov amplitudes of the undriven condensate as defined in Eq. (2.34) (see Sec. 3.3 as well), and these functions are orthogonal to the condensate mode. The operator $\hat{\mathcal{L}}_Q(t)$ is given by,

$$\mathcal{L}_Q(t) = \begin{pmatrix}\hat{\mathcal{H}}_{GP}(t) + gn_H\hat{Q}(t)|\psi(t)|^2\hat{Q}(t) & gn_H\hat{Q}(t)\psi_0^2(t)\hat{Q}^*(t)\\ -gn_H\hat{Q}^*(t)(\psi_0^2)^*(t)\hat{Q}(t) & -\hat{\mathcal{H}}_{GP}(t) - gn_H\hat{Q}(t)|\psi_0(t)|^2\hat{Q}(t)\end{pmatrix}. \tag{4.40}$$

Here we have $\hat{\mathcal{H}}_{GP}(\boldsymbol{r}, t) = -(\hbar^2\nabla^2/2M) + V_\rho(\rho) + g(t)n_H|\psi_0(t)|^2 - \mu$, with $\psi(t)$ being the GPE solution with $\psi_0(0) = \xi_0$ (ground state of order-parameter). We also have the operator $\hat{Q}(t)$ which projects a function to the space orthogonal to the condensate mode $\psi_0(t)$, i.e. $\hat{Q}(t) = \mathbf{I} - |\psi_0(t)\rangle\langle\psi_0(t)|$, where $\mathbf{I}$ is the identity matrix. The initial solution of the amplitudes $u_n(0), v_n(0)$ also turned out to be the eigenfunctions of $\mathcal{L}_Q(0)$ (Appendix C).

The non-condensate population can be obtained from $|u_n(t)\rangle$ and $|v_n(t)\rangle$ as,

$$\langle\delta\hat{N}(t)\rangle = \sum_n \langle v_n(t)|v_n(t)\rangle + \langle\hat{b}_n^\dagger\hat{b}_n\rangle[\langle u_n(t)|u_n(t)\rangle + \langle v_n(t)|v_n(t)\rangle].,\tag{4.41}$$

The first and second terms in the above equation give us the quantum and thermal depletions of the condensate, respectively. Since we assume zero temperature, the contribution from thermal depletion remains zero, i.e. $\langle\hat{b}_n^\dagger\hat{b}_n\rangle = [\exp(\epsilon_n/k_BT) - 1]^{-1} = 0$. We are then left with the quantum depletion,

$$\langle\delta\hat{N}(t)\rangle = \sum_n \langle v_n(t)|v_n(t)\rangle\,. \tag{4.42}$$

The exponential growth of $\delta N(t)$ indicates condensate instability [28]. Eq. (4.39) is valid as long as the condensate population is much greater than the non-condensate population, thus capturing the early time-dynamics in the presence of instability.

We note that the perturbations in mean-field solutions evolve under equations similar to Eq. (4.39) [29]. Therefore, here we are effectively doing a linear stability test on the time-dependent mean-field solution of the GPE.

In Bogoliubov basis

The equations of motion (4.39) can be efficiently solved in the Bogoliubov basis of undriven condensate, i.e., in the basis of $\hat{\mathcal{L}}_Q(0)$. First, we obtain $|u_n(0)\rangle, |v_n(0)\rangle$ by diagonalizing $\hat{\mathcal{L}}_Q(0)$, or equivalently, solving the usual BdG equation (2.18) and then orthogonalizing the amplitudes using Eq. (2.34). The solution at a later time, $|u_n(t)\rangle, |v_n(t)\rangle$, can then be expanded in the Bogoliubov basis of the initial Hamiltonian as (see Appendix C),

$$\begin{pmatrix} |u_n(t)\rangle \\ |v_n(t)\rangle \end{pmatrix} = \alpha_0^{(n)}(t)\begin{pmatrix} |\xi_0\rangle \\ |0\rangle \end{pmatrix} + \beta_0^{(n)}(t)\begin{pmatrix} |0\rangle \\ |\xi_0^*\rangle \end{pmatrix} + \sum_{n'\neq 0}\alpha_{n'}^{(n)}(t)\begin{pmatrix} |u_{n'}(0)\rangle \\ |v_{n'}(0)\rangle \end{pmatrix} + \beta_{n'}^{(n)}(t)\begin{pmatrix} |v_{n'}^*(0)\rangle \\ |u_{n'}^*(0)\rangle \end{pmatrix}. \tag{4.43}$$

Here, the summation is over the Bogoliubov modes with frequency $\omega \neq 0$, and the coefficients are given as,

$$\begin{aligned} \alpha_{n'}^{(n)}(t) &= \langle u_{n'}(0)|u_n(t)\rangle - \langle v_{n'}(0)|v_n(t)\rangle \\ \beta_{n'}^{(n)}(t) &= -\langle v_{n'}^*(0)\big|u_n(t)\rangle + \langle u_{n'}^*(0)\big|v_n(t)\rangle . \end{aligned} \tag{4.44}$$

This expansion transforms the partial differential equations (4.39) to a set of ordinary linear equations of $\alpha_{n'}^{(n)}, \beta_{n'}^{(n)}$.

The problem can be further simplified by considering the symmetries of the condensate. We know that for the cylindrically confined system, the amplitudes are of the form,

$$\begin{aligned} u_{n_r,\nu,k_z}(\boldsymbol{r},0) &= \bar{u}_{n_r,\nu,k_z,0}(\rho)e^{i\nu\varphi}e^{ik_z z} \\ v_{n_r,\nu,k_z}(\boldsymbol{r},0) &= \bar{v}_{n_r,\nu,k_z,0}(\rho)e^{i\nu\varphi}e^{ik_z z}. \end{aligned} \tag{4.45}$$

We also note that the mean-field solution $\psi_0(t) = \psi_0(\rho, t)$ retains its translational symmetry along the z axis and rotationally symmetry about the z-axis. Using these facts, it is possible to show that evolution only couples modes with the same $|\nu|, |k_z|$ (Appendix C). The dynamics of the coefficients become separated as,

$$i\hbar\frac{d}{dt}\begin{pmatrix} \boldsymbol{\alpha}_{n_r}^{(\nu,k_z)} \\ \boldsymbol{\beta}_{n_r}^{(\nu,k_z)} \end{pmatrix} = \begin{pmatrix} \tilde{\boldsymbol{M}}_{\nu,k_z}^{(1)} & \tilde{\boldsymbol{M}}_{\nu,k_z}^{(2)} \\ -\left(\tilde{\boldsymbol{M}}_{\nu,k_z}^{(2)}\right)^* & -\left(\tilde{\boldsymbol{M}}_{\nu,k_z}^{(1)}\right)^* \end{pmatrix}\begin{pmatrix} \boldsymbol{\alpha}_{n_r}^{(\nu,k_z)} \\ \boldsymbol{\beta}_{n_r}^{(\nu,k_z)} \end{pmatrix}. \tag{4.46}$$

Here, column matrices are given by $\boldsymbol{\alpha}^{(\nu,k_z)}_{n_r} = (\alpha^{(\nu,k_z)}_{n_r,1}, \alpha^{(\nu,k_z)}_{n_r,2}, ...)^T$ and $\boldsymbol{\beta}^{(\nu,k_z)} = (\beta^{(\nu,k_z)}_{n_r,1}, \beta^{(\nu,k_z)}_{n_r,2}, ...)^T$ where the coefficients of the radial modes given by

$$\begin{aligned}\alpha^{(\nu,k_z)}_{n_r,n_r'} &= \int d\rho\rho[\bar{u}_{n_r',\nu,k_z}(0)\bar{u}_{n_r,\nu,k_z}(t) - \bar{v}_{n_r',\nu,k_z}(0)\bar{v}_{n_r,\nu,k_z}(t)]\\ \beta^{(\nu,k_z)}_{n_r,n_r'} &= \int d\rho\rho[\bar{u}_{n_r',\nu,k_z}(0)\bar{v}_{n_r,\nu,k_z}(t) - \bar{v}_{n_r',\nu,k_z}(0)u_{n_r,\nu,k_z}(t)].\end{aligned} \tag{4.47}$$

And the elements of the matrices are given by,

$$\begin{aligned}[\tilde{\boldsymbol{M}}^{(1)}{}_{\nu,k_z}]_{n_r,n_r'} &= \left(\left\langle\bar{u}_{n_r,\nu,k_z}(0)\right|, -\left\langle\bar{v}_{n_r,\nu,k_z}(0)\right|\right)\hat{\mathcal{L}}^{\nu,k_z}_Q(t)\begin{pmatrix}\left|\bar{u}_{n_r',\nu,k_z}(0)\right\rangle\\ \left|\bar{v}_{n_r',\nu,k_z}(0)\right\rangle\end{pmatrix}\\ [\tilde{\boldsymbol{M}}^{(2)}{}_{\nu,k_z}]_{n_r,n_r'} &= \left(\left\langle\bar{u}_{n_r,\nu,k_z}(0)\right|, -\left\langle\bar{v}_{n_r,\nu,k_z}(0)\right|\right)\hat{\mathcal{L}}^{\nu,k_z}_Q(t)\begin{pmatrix}\left|\bar{v}_{n_r',\nu,k_z}(0)\right\rangle\\ \left|\bar{u}_{n_r',\nu,k_z}(0)\right\rangle\end{pmatrix}.\end{aligned} \tag{4.48}$$

with matrix $\hat{\mathcal{L}}^{\nu,k_z}_Q$ is obtained from the relation $\hat{\mathcal{L}}_Q(t)u_{n_r,\nu,k_z} = e^{i\nu\varphi}e^{ik_z z}\hat{\mathcal{L}}^{\nu,k_z}_Q(t)\bar{u}_{n_r,\nu,k_z}$.

We can see that Eqs. (4.46) is similar to the Eqs. (4.30) obtained from the Floquet theory approach. The difference here is that the $\boldsymbol{M}(t)$ matrices used in the Floquet approach are periodic in time, whereas $\tilde{\boldsymbol{M}}(t)$ matrices defined in the equation set above are not due to their dependence on the mean-field solution $\psi_0(t)$.

The steps for solving the equation of motion for the quasiparticle amplitude under driving are as follows.

i) Solve for the Bogoliubov amplitudes of the undriven cylindrical condensate to obtain $\left|\bar{u}_{n_r,\nu,k_z}(0)\right\rangle$ and $\left|\bar{v}_{n_r,\nu,k_z}(0)\right\rangle$.

ii) Obtain the mean field $\psi_0(\rho, t)$ from GPE. (4.38).

iii) Obtain $\tilde{\boldsymbol{M}}^{(1)}{}_{\nu,k_z}(t)$ and $\tilde{\boldsymbol{M}}^{(1)}{}_{\nu,k_z}(t)$ using Eqs. (4.48).

iv) Solve Eq. (4.46) to obtain the dynamics of various modes, with the initial conditions $\alpha^{(\nu,k_z)}_{n_r,n_r} = \delta_{n_r n_r'}$ and $\beta^{(\nu,k_z)}_{n_r,n_r} = 0$

The population of each mode can be calculated from the coefficients as,

$$\langle v_n(t)|v_n(t)\rangle = \begin{pmatrix}\boldsymbol{\alpha}^\dagger_n & \boldsymbol{\beta}^\dagger_n\end{pmatrix}\begin{pmatrix}\boldsymbol{C}^{\alpha\alpha} & \boldsymbol{C}^{\alpha\beta}\\ \boldsymbol{C}^{\beta\alpha} & \boldsymbol{C}^{\beta\beta}\end{pmatrix}\begin{pmatrix}\boldsymbol{\alpha}_n\\ \boldsymbol{\beta}_n\end{pmatrix}, \tag{4.49}$$

where $n = \{n_r, \nu, k_z\}$ denotes the mode index and the time-independent matrices are given by,

$$\begin{aligned}\boldsymbol{C}^{\alpha\alpha}_{n,n'} &= \langle v_n(0)|v_{n'}(0)\rangle, \qquad & \boldsymbol{C}^{\alpha\beta}_{n,n'} &= \langle u^*_n(0)\big|v_{n'}(0)\rangle\\ \boldsymbol{C}^{\beta\alpha}_{n,n'} &= \langle v_n(0)\big|u^*_{n'}(0)\rangle, \qquad & \boldsymbol{C}^{\beta\beta}_{n,n'} &= \langle u^*_n(0)\big|u^*_{n'}(0)\rangle.\end{aligned}$$

In the rest of the chapter, we look at the dynamics of excited modes under periodic driving using the linear stability analysis of the mean-field GPE solution, and compare the results with the dynamics of the perturbed ground state.

4.5 Driven dynamics in the Q1D limit of interaction

In this section, we examine the dynamics of a weakly interacting 3D cylindrical condensate in the quasi-1D (Q1D) regime, using linear stability analysis of Bogoliubov modes as discussed in Sec. 4.4.2. We compare these predictions with Gross-Pitaevskii equation (GPE) simulations of an initially perturbed ground state, which also exhibit instability of the longitudinally uniform state. To initiate the dynamics, we perturb the ground state by adding small random noise of the form,

$$\psi(\boldsymbol{r}_i, t) = \sqrt{n_H}\xi_0(\rho_i) + |\xi_0(\rho_i)|(s_i + it_i), \tag{4.50}$$

where i denotes the grid point index, and s_i and t_i are small uniform random variable. The perturbation added mimics the inherent quantum fluctuations in the system [50, 58], which triggers the pattern formation. We also assume a weak modulation with amplitude $\Delta a_s/\bar{a}_s \ll 1$, and the modulation frequencies restricted to $\Omega < 4\omega_\rho$.

Here, the mean interaction strength is $\bar{\eta} = 2$, which corresponds to a chemical potential $\mu \approx 0.28\,\hbar\omega_\rho$, well within the Q1D limit. The driving does not cause significant excitation in the modes with $|\nu| > 1$ in the driving frequency range we consider. The population dynamics of the excited mode from the gapless branch ($\nu = 0$) and dipole branch ($\nu = \pm 1$), at the initial stages of modulation, is given in Fig. 4.3 for four different driving frequencies. Here, we defined the excited population for the unstable mode as,

$$\delta N_{\nu,k_z}(t) = \left\langle v_{0,\nu,k_z}(t) \middle| v_{0,\nu,k_z}(t) \right\rangle, \tag{4.51}$$

which gives the population of modes which was at $t = 0$ in the lowest branches (i.e. $n_r = 0$).

In Fig. 4.3, we see that the population in the modes grows sharply under the periodic driving. These are modes with excitation frequency half the driving frequency as $\omega_{n_r,\nu}(k_z) = \Omega/2$, indicating the parametric excitation. The unstable gapless density mode population grows at a faster rate than that of dipole branch mode, fully in agreement with the Floquet theory calculations done in Sec. 4.4.1. We compare the growth of unstable modes from the two branches in Fig. 4.4, where we see the gapless mode ($\nu = 0$) being more unstable than the dipole mode ($\nu = \pm 1$), at the three different driving frequencies considered.

We also look at the 3D GPE dynamics of the perturbed ground state under periodic driving of the interaction. The results are shown in Fig. (4.5) for three driving frequencies.

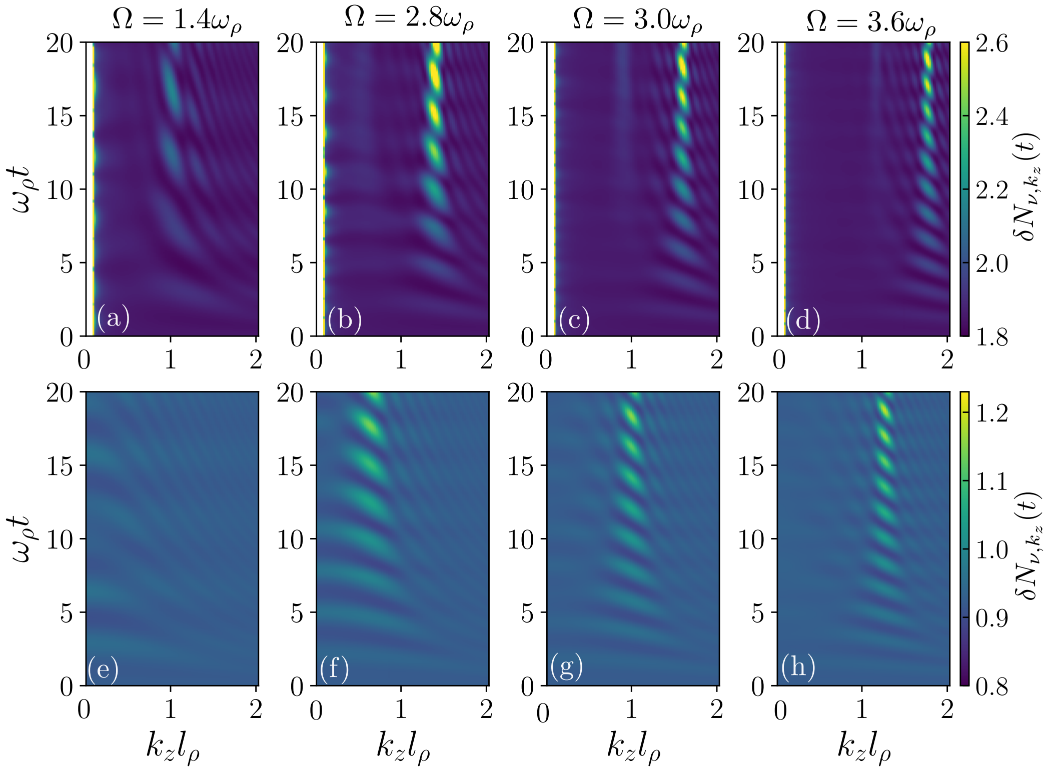

FIGURE 4.3: Dynamics of population $\delta N_{\nu,k_z}(t)$ at Q1D limit of interaction for $\nu = 0$ (top row) and $\nu = \pm 1$ (bottom row), for various driving frequencies. Here, interaction $\bar{\eta} = 2.0$ and $\bar{\eta} = 1.2$.

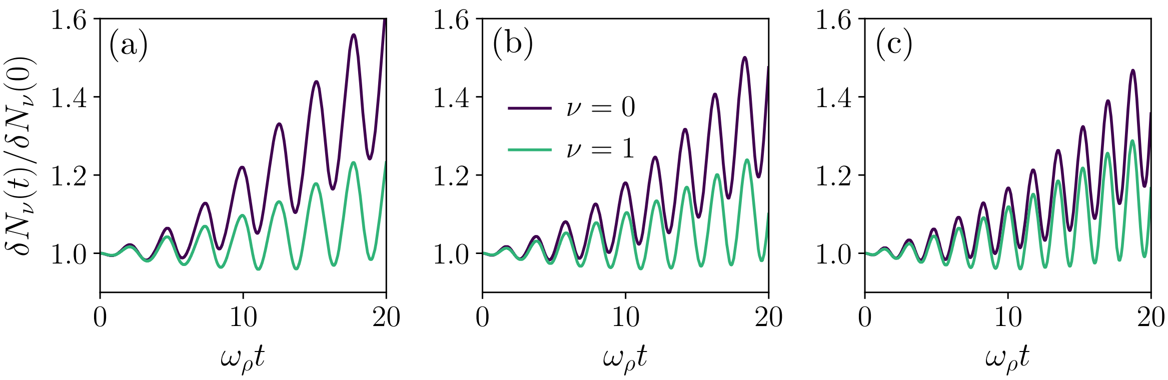

FIGURE 4.4: The dynamics of the most unstable modes with $\nu = 0$ and $\nu = \pm 1$ at Q1D limit of interaction, for driving frequencies (a) $\Omega = 2.4\omega_\rho$, (b) $\Omega = 3.0\omega_\rho$, and (c) $\Omega = 3.6\omega_\rho$. Here, interaction $\bar{\eta} = 2.0$ and $\bar{\eta} = 1.2$.

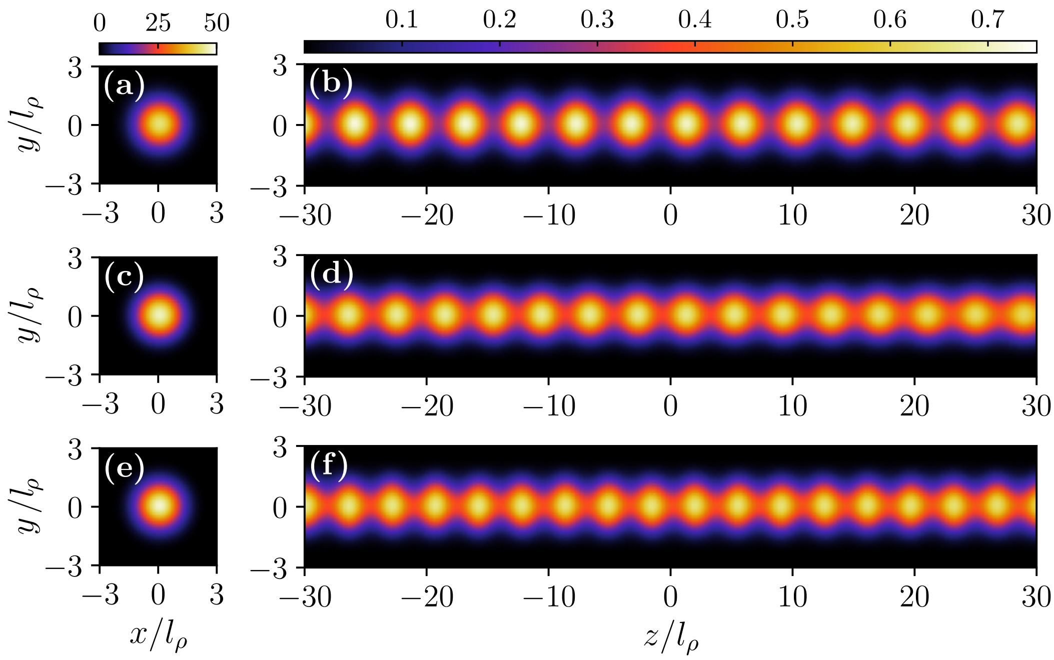

FIGURE 4.5: The integrated densities $n_z(x, y)$(left) and $n_x(z, y)$ (right) for obtained from GPE evolution for Q1D limit of interaction at driving frequencies [(a), (b)] $\Omega = 2.4\omega_\rho$ ($\omega_\rho t = 120$), [(c), (d)] $\Omega = 3.0\omega_\rho$ ($\omega_\rho t = 140$), and [(d), (e)] $\Omega = 3.6\omega_\rho$ ($\omega_\rho t = 150$). Here, interaction $\bar{\eta} = 2.0$ and $\bar{\eta} = 1.2$.

Here, we plot the integrated 2D densities in the xy and yz planes, given by,

$$n_z(x, y, t) = \int dz|\psi(\boldsymbol{r}, t)|^2 \quad \text{and} \quad n_x(y, z, t) = \int dx|\psi(\boldsymbol{r}, t)|^2. \tag{4.52}$$

From the $n_x(y, z)$ (Fig. (4.5)), we see the formation of longitudinal density patterns with wavelength $\lambda \sim 2\pi/k_u^{(0)}$, where $k_u^{(0)}$ is the momenta of the unstable mode from the lowest branch, given by $\omega_{0,0}(k_u^{(0)}) = \Omega/2$. These are the usual Faraday waves observed in driven BEC [49, 124, 163]. The density patterns do not reveal any sign of the dipole branch mode excitation, but it can be seen from the momentum space density of the system. In Fig. 4.6, we plot the momentum space density of the condensate along the z-direction, which is defined as,

$$\tilde{n}_z(k_z, t) = \int dk_x dk_y |\psi'(\boldsymbol{k}, t)|, \tag{4.53}$$

where $\psi'(\boldsymbol{k}, t)$ is the momentum space wavefunction. Here, we can see the peaks (beside at $k_z = 0$) at $\pm k_u^{(0)}$ arising due to excitation of axial density modes. We can also see smaller peaks at the momenta $\pm k_u^{(1)}$, given $\omega_{0,1}(k_u^{(1)}) = \Omega/2$, due to resonant dipole mode.

Since only the lowest branch plays a significant role in the pattern formation, the Q1D picture captures the dynamics well, even when the driving frequency is large enough to cause excitation of modes from radial branches.

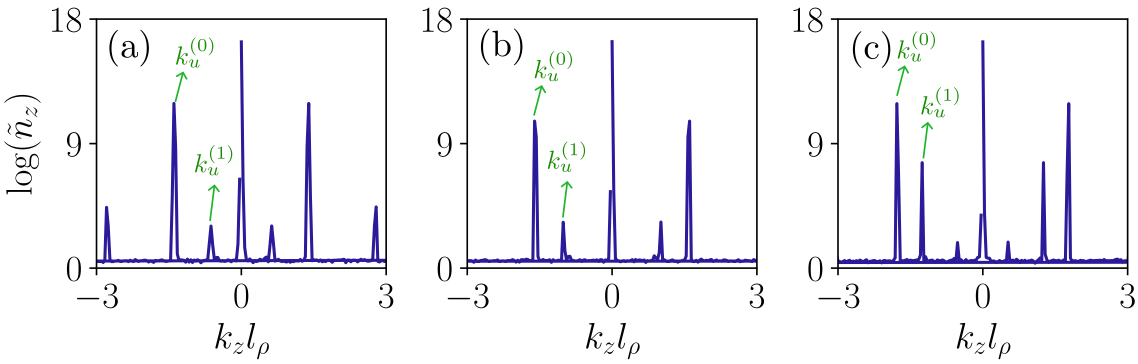

FIGURE 4.6: Momentum space linear density of the condensate obtained from GPE evolution, for driving frequencies (a) $\Omega = 2.4\omega_\rho$ ($\omega_\rho t = 120$), (b) $\Omega = 3.0\omega_\rho$ ($\omega_\rho t = 140$), and (c) $\Omega = 3.6\omega_\rho$ ($\omega_\rho t = 150$). Here, interaction $\bar{\eta} = 2.0$ and $\bar{\eta} = 1.2$.

4.6 Beyond the Q1D limit of interaction

In this section, we look at the dynamics of a driven cylindrical BEC, whose chemical potential $\mu \gtrapprox \hbar\omega_\rho$ is no longer in the Q1D limit. Unsurprisingly, the Q1D approximation fails here to capture the important aspects of the dynamics. Despite considering the radial modes, the Floquet theory approach in Sec. 4.4.1 also fails. Here, consider a mean interaction strength of $\bar{\eta} = 10$, corresponding to a chemical potential $\mu \approx 1.06\omega_\rho$.

In Fig. 4.7, we show the population of modes from the branches with $\nu = 0 \pm 1$ for various k_z under periodic driving of the scattering length, obtained using the linear stability analysis discussed in Sec. 4.4.2. We generally see parametric excitation, where the modes with an excitation frequency that is half the driving frequency are resonantly populated. When the driving frequency $\Omega < 2\omega_\rho$, we do not observe any excitation in the dipole branch modes ($\nu = \pm 1$), as frequency is not sufficient to cause the parametric excitation. The growth of unstable gapless density modes ($\nu = 0$) is significantly slower at these frequencies than at larger driving frequencies.

When $\Omega > 2\omega_\rho$, both the axial density modes and the dipole branch modes are unstable, but we see a frequency-dependent behaviour in the system in this frequency range. For instance, when $\Omega = 2.4\omega_\rho$ [Fig. 4.7 (b),(f)], the gapless density modes are more unstable than the dipole branch, causing formation of longitudinal density waves in the system, which is also seen from the GPE dynamics [Fig. 4.9 (b)]. But when the driving frequency is increased to $\Omega = 3.6\omega_\rho$ [Fig. 4.7 (d),(h)], this behaviour seems to be reversed, as the dipole branch mode grows at a faster rate than the density branch mode. The growth rate of the most unstable modes from both branches is given in Fig. 4.8, where a clear switching of behaviour is seen as driving frequency is varied.

This transition of response under driving can also be seen from the GPE dynamics of the perturbed ground state, Fig. 4.9 when the frequency $\Omega = 2.4\omega_\rho$, the periodic driving creates

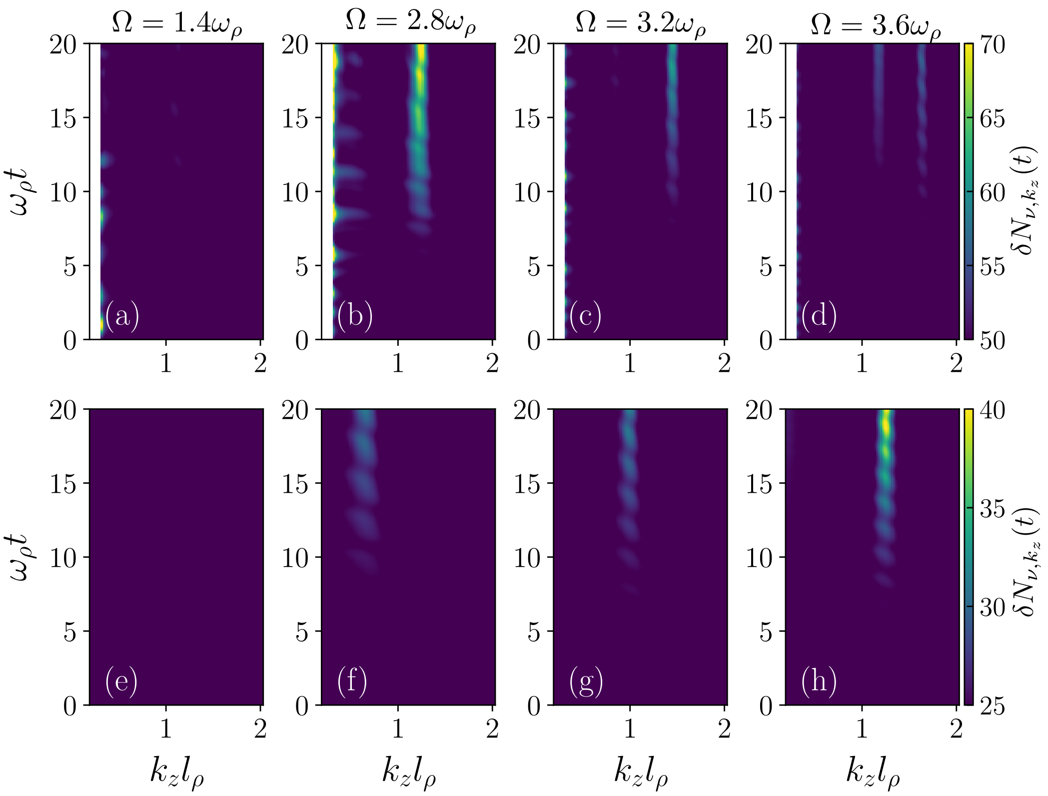

FIGURE 4.7: Dynamics of population $\delta N_{\nu,k_z}(t)$ for $\nu = 0$ (top row) and $\nu = \pm 1$ (bottom row) for interaction beyond the Q1D limit, at various driving frequencies. Here $\bar{\eta} = 10.0$ and $\Delta\eta = 2$.

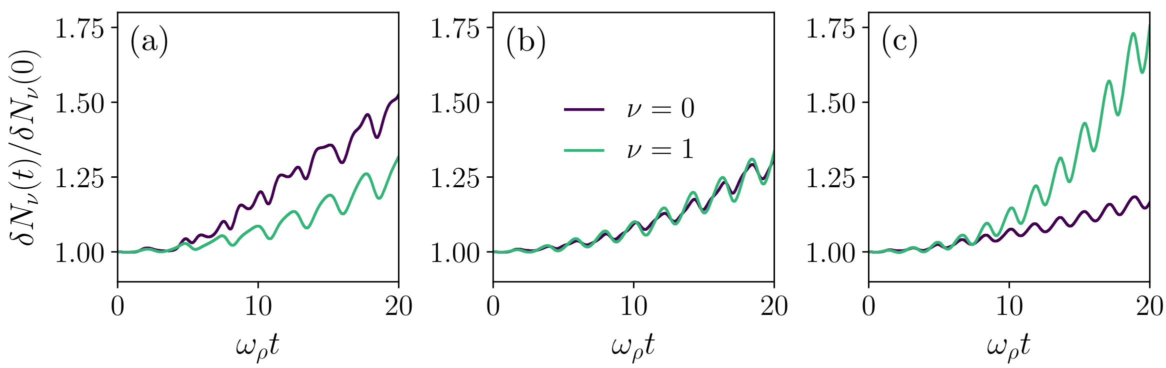

FIGURE 4.8: The dynamics of the most unstable modes with $\nu = 0$ and $\nu = \pm 1$ for interaction beyond the Q1D limit, at driving frequencies (a) $\Omega = 2.4\omega_\rho$, (b) $\Omega = 3.2\omega_\rho$, and (c) $\Omega = 3.6\omega_\rho$. Here, the interaction $\bar{\eta} = 10.0$ and $\Delta\eta = 2$.

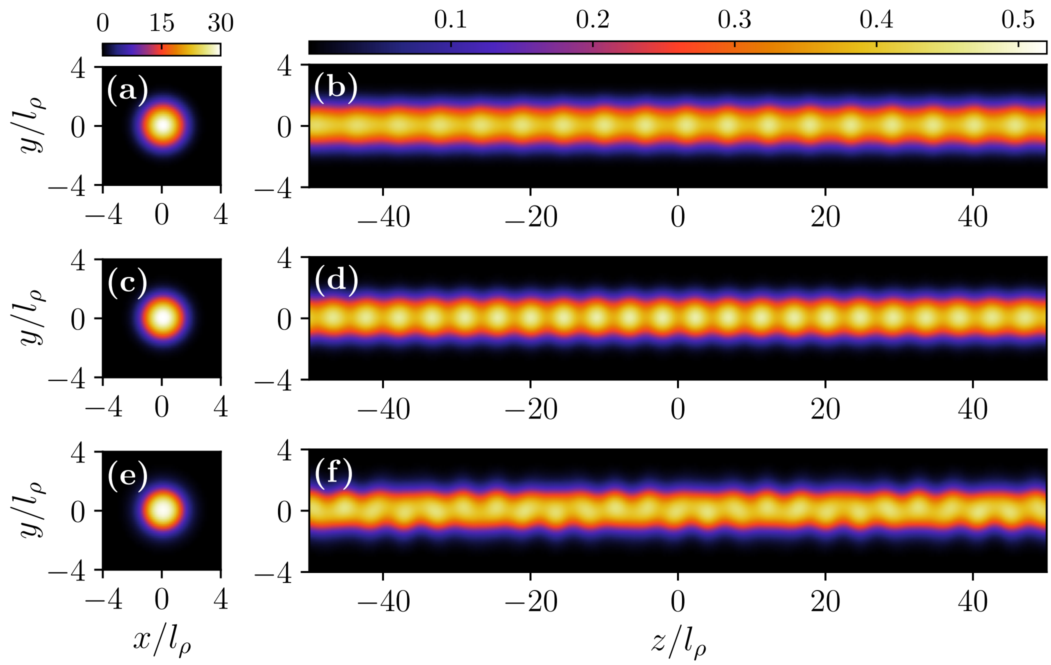

FIGURE 4.9: The integrated densities $n_z(x,y)$(left) and $n_x(z,y)$ (right) for obtained from GPE evolution interaction beyond the Q1D limit, at driving frequencies [(a),(b)] $\Omega = 2.4\omega_\rho$, [(c),(d)] $\Omega = 3.2\omega_\rho$, and [(d),(e)] $\Omega = 3.6\omega_\rho$. Here, interaction $\bar{\eta} = 10.0$ and $\Delta\eta = 2$.

formation of density waves with wavelength $2\pi/k_u^{(0)}$ [Fig. 4.9 (a)], where the momenta is determined from the relation $\omega_{0,0}(k_u^{(0)}) = \Omega/2$. At a higher driving frequency ($\Omega = 3.6\omega_\rho$), the pattern resembles the centre-of-mass oscillation (zig-zag) waves arising from dipole branch excitation, The wavelength of the is pattern is given by $2\pi/k_u^{(1)}$, where the momenta of the unstable dipole mode is determined from $\omega_{0,\pm1}(k_u^{(0)}) = \Omega/2$. The 1D momentum space density along k_z Eq. (4.53) is given in Fig. 4.10. Here we see a larger population at the $k_z = \pm k_u^{(0)}$ for the smaller driving frequency, whereas $k_z = \pm k_u^{(1)}$ also attains a significant population at the larger driving frequency.

Note that the driving frequencies we consider throughout this chapter do not cause the direct excitation discussed in the last section. The pattern formation occurs due to the parametric excitation alone. We also note that the linear stability predictions are only valid when the population of the excited modes are much smaller than the condensate population, thus only capturing the initial time dynamics. Continuous driving eventually causes the heating and destruction of the condensate.

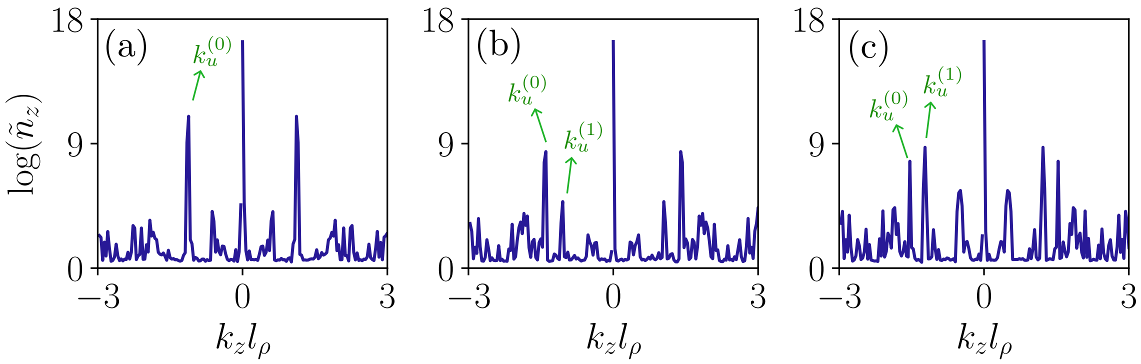

FIGURE 4.10: Momentum space linear density of the condensate obtained from GPE evolution for interaction beyond the Q1D limit, at driving frequencies (a) $\Omega = 2.4\omega_\rho$ ($\omega_\rho t = 160$), (b) $\Omega = 3.2\omega_\rho$ ($\omega_\rho t = 150$), and (c) $\Omega = 3.6\omega_\rho$ ($\omega_\rho t = 150$). Here, interaction $\bar{\eta} = 10.0$ and $\Delta\eta = 2$.

4.7 Conclusion

In this chapter, we looked at the parametric excitation of a cylindrically confined BEC with a periodically driven scattering length. The driving causes excitation of Bogoliubov modes with frequency half the driving frequency, away from the direct resonance points [Eq. (4.3)]. When the interactions are weak enough to be in the Q1D limit, the prominent excitation arise from the lowest branch of the Bogoliubov spectra, leading to longitudinal density patterns with wavelength $2\pi/k_u$, and where the momenta of the unstable mode k_u can be obtained from the parametric resonance condition $\Omega = 2\epsilon_{1D}(k_u)$. The density mode remains the most unstable even for large driving frequencies ($\Omega > 2\omega_\rho$), where dipole branch modes are also unstable. When the interaction is beyond the Q1D limit, the unstable dipole branch modes play a more prominent role, and we see frequency-dependent pattern formation.

Further work is needed to explore the condensate dynamics across a broader range of interaction strengths.

Chapter 5

Faraday and spin waves in Q2D spin-1 BEC in polar phase

This section has been adapted from the research article titled "Patterns, spin-spin correlations, and competing instabilities in driven quasi-two-dimensional spin-1 Bose-Einstein condensates" [85].

5.1 Introduction

Spinor Bose-Einstein condensates, composed of bosons with non-zero spin, offer a rich platform to explore phenomena such as spin textures and magnetic phases [89, 149, 164] in quantum fluids. Driven spinor condensates have been shown to exhibit interesting phenomena, including dynamical stabilization [74], spin squeezing [75, 151], Shapiro resonances [51, 79], parametric resonances [194], and quantum walks in momentum space [42, 43]. As we already discussed in Sec. 2.8.2, a spin-1 condensate in the ferromagnetic phase behaves similarly to a spin-0 condensate [49, 162], when a density pattern forms under periodic driving. But this is no longer the case with the polar phase BEC, where the particles can scatter from $m = 0$ state to $m = \pm 1$ states while conserving magnetization.

In this chapter, we investigate the formation of density and spin patterns under periodic modulation of the s-wave scattering lengths in a quasi-two-dimensional (Q2D) homogeneous spin-1 condensate in the polar phase. We consider three driving protocols: modulating a_0 alone, a_2 alone, and both simultaneously. In all cases, the modulation affects both spatial and spin degrees of freedom.

Unlike the ferromagnetic phase, a polar-phase condensate exhibits non-trivial dynamics, as both density and spin Bogoliubov modes become unstable. This results in a competition between density modulations and spin-mixing dynamics. When spin-mixing dominates, polar core vortices (PCVs) and antivortices with distinct spin textures emerge, producing spin-density patterns described by Bessel functions, with their argument determined by the momentum of the unstable spin mode. The momentum of the unstable density mode sets the wavelength of the Faraday pattern, while that of the spin mode controls the vortex density. If spin-dependent interaction is stronger than the spin-independent one, density Faraday patterns dominate the dynamics, and conversely, when spin dynamics dominate, the spin-spin correlations follow a different scaling behaviour.

When both scattering lengths are modulated at the same frequency, the driving amplitudes can be tuned to excite the density or spin mode selectively. If the modulation frequencies differ, competing instabilities arise—two modes (from density or spin channels) can become equally unstable, leading to interference between patterns of different wavelengths. In classical fluids, such competing instabilities lead to the coexistence of patterns with distinct symmetries [95]. This results in a superposition of Faraday patterns or spatial correlations with different wavelengths and time-dependent amplitudes.

5.2 Setup

5.2.1 System

We consider a weakly interacting gas of spin-1 bosons with mass M, which is tightly trapped along the z-direction, while free in the xy-plane. For sufficiently strong axial trap $V_z(z) = (1/2)M\omega_z^2 z^2$, the order parameter of each component takes the form $\Psi_m(\boldsymbol{r}) = \psi_m(\rho)\phi(z)$, where $\phi(z)$ is the single-particle ground state of the axial trap. The dynamics of the two-dimensional order-parameter $\psi_m(\rho)$ can then be shown to follow the quasi-two-dimensional Gross-Pitaevskii equation (Q2D GPE),

$$i\hbar\frac{\partial\psi_1}{\partial t} = \left[-\frac{\hbar^2\nabla_\rho^2}{2M} - p + q + \tilde{c}_0\tilde{n} + \tilde{c}_1\tilde{F}_z\right]\psi_1 + \frac{\tilde{c}_1}{\sqrt{2}}\tilde{F}_-\psi_0 \tag{5.1}$$

$$i\hbar\frac{\partial\psi_0}{\partial t} = \left[-\frac{\hbar^2\nabla_\rho^2}{2M} + \tilde{c}_0\tilde{n}\right]\psi_0 + \frac{\tilde{c}_1}{\sqrt{2}}\left[\tilde{F}_+\psi_1 + \tilde{F}_-\psi_{-1}\right] \tag{5.2}$$

$$i\hbar\frac{\partial\psi_{-1}}{\partial t} = \left[-\frac{\hbar^2\nabla_\rho^2}{2M} + p + q + \tilde{c}_0\tilde{n} - \tilde{c}_1\tilde{F}_z\right]\psi_{-1} + \frac{\tilde{c}_1}{\sqrt{2}}\tilde{F}_+\psi_0. \tag{5.3}$$

Here, p and q are the linear and quadratic Zeeman terms. The interaction between the particles is characterized through $\tilde{c}_0$ and $\tilde{c}_1$, the two-dimensional spin-independent and spin-dependent coefficients, respectively. These are related to the 3D coefficients $c_{0,1}$ through the relation $\tilde{c}_{0,1} = c_{0,1}/\sqrt{2\pi l_z^2}$, where $l_z = \sqrt{\hbar/M\omega_z}$ is the length scale associated with the axial trap and $c_0 = 4\pi\hbar^2(a_0 + 2a_2)/3M$ and $c_1 = 4\pi\hbar^2(a_2 - a_0)/3M$, with a_F being the s-wave scattering length in the collision channel with total spin F. We also have 2D total density $\tilde{n}(\rho) = \sum_m |\psi_m(\rho)|^2$ and spin-density vector $\tilde{F}_i(\rho) = \sum_{mm'} \psi_m^*(\rho)\,(f_i)_{mm'}\,\psi_{m'}(\rho)$, and $\tilde{F}_\pm = \tilde{F}_x \pm i\tilde{F}_y$.

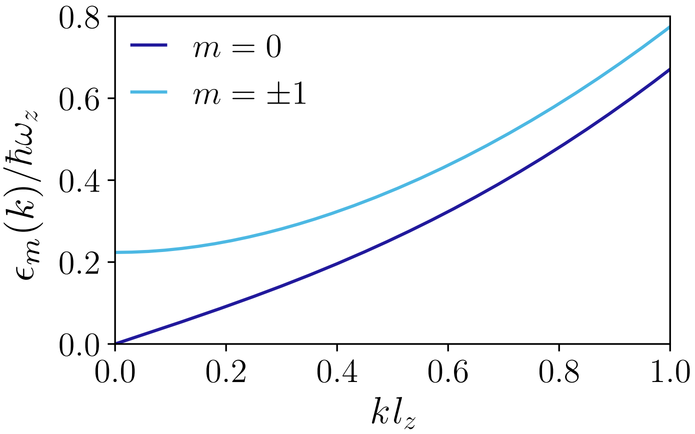

FIGURE 5.1: The polar phase dispersion relation for $\tilde{c}_0\tilde{n}_0 = 0.2\hbar\omega_z$, $\tilde{c}_1\tilde{n}_0 = 0.05\hbar\omega_z$, $q = 0.1\hbar\omega_z$, and $p = 0$.

5.2.2 Polar phase

In the absence of trap in the xy plane, the system will have a uniform ground state density. We chose the Zeeman terms p and q such that the ground state of the system will be the polar phase, in which all atoms occupy the $m = 0$ spin state [89]. The ground state order parameter for this state is given by $\psi_P = \left(0, \sqrt{\tilde{n}_0}, 0\right)^T$, where $\tilde{n}_0 = N/(L_x L y)$ is the 2D density of the system, where N is the total number of particles and L_x and L_y are the system lengths along the x and y directions, respectively. In this state, the spin density vector $\tilde{F}(\rho)$ vanishes in all three spin directions.

In the polar phase, the Bogoliubov excitation spectrum of the homogeneous condensate consists of three branches. The gapless density dispersion branch,

$$\epsilon_0(k) = \sqrt{E_k(E_k + 2\tilde{c}_0\tilde{n}_0)}, \tag{5.4}$$

where $E_k = \hbar^2 k^2/2M$, describes the phonon excitations that occur within the $m = 0$ component. We also have two spin-dispersion branches,

$$\epsilon_{\pm 1}(k) = \sqrt{(E_k + q)(E_k + q + 2\tilde{c}_1\tilde{n}_0)} \mp p, \tag{5.5}$$

that describe spin-waves in $\tilde{F}_x$ and $\tilde{F}_y$ spins-space and arise from the elementary spin-changing collisions of form $(\mathbf{0}, 0) + (\mathbf{0}, 0) \rightleftarrows (\boldsymbol{k}, \pm 1) + (-\boldsymbol{k}, \mp 1)$, where the condensate atoms scatter into $m = \pm 1$ spin states.

5.3 Periodically driven scattering length

We prepare the system in the ground-state polar phase and then subject it to periodic modulation of the s-wave scattering lengths, described by

$$a_F(t) = \bar{a}_F\,[1 + 2\alpha_F \cos(2\omega_F t)]\,, \tag{5.6}$$

where α_F and ω_F denotes the amplitude and frequency of the drive in total spin-Fchannel,respectively. We consider three scenarios;

i) a_0 being modulated, while a_2 remain constant

ii) a_2 being modulated, while a_0 remain constant

iii) Both scattering lengths, a_0 and a_2, are modulated simultaneously

For case (i), where only a_0 is driven, the interaction coefficients evolve as

$$\begin{aligned}\tilde{c}_0(t) &= \bar{c}_0 + \frac{2}{3}\alpha_0\bar{g}_0\cos(2\omega_0 t),\\ \tilde{c}_1(t) &= \bar{c}_1 - \frac{2}{3}\alpha_0\bar{g}_0\cos(2\omega_0 t),\end{aligned} \tag{5.7}$$

while for case (ii), with only a_2 modulated, the coefficients take the form

$$\begin{aligned}\tilde{c}_0(t) &= \bar{c}_0 + \frac{4}{3}\alpha_2\bar{g}_2\cos(2\omega_2 t),\\ \tilde{c}_1(t) &= \bar{c}_1 + \frac{2}{3}\alpha_2\bar{g}_2\cos(2\omega_2 t).\end{aligned} \tag{5.8}$$

In the general case (iii), where both a_0 and a_2 are independently driven with a relative phase Φ, the interaction coefficients evolve as

$$\begin{aligned}\tilde{c}_0(t) &= \bar{c}_0 + \frac{2}{3}\alpha_0\bar{g}_0\cos(2\omega_0 t) + \frac{4}{3}\alpha_2\bar{g}_2\cos(2\omega_2 t + \Phi),\\ \tilde{c}_1(t) &= \bar{c}_1 - \frac{2}{3}\alpha_0\bar{g}_0\cos(2\omega_0 t) + \frac{2}{3}\alpha_2\bar{g}_2\cos(2\omega_2 t + \Phi).\end{aligned} \tag{5.9}$$

Here, effective 2D coupling constant $\bar{g}_F = (4\pi\hbar^2/Ml_z\sqrt{2\pi})\bar{a}_F$ and mean values of coefficients $\bar{c}_0 = (\bar{g}_0 + 2\bar{g}_2)/3$ and $\bar{c}_1 = (\bar{g}_2 - \bar{g}_0)/3$. In this work, we explore all three scenarios mentioned above.

Tuning the scattering length in a spinor BEC using magnetic Feshbach resonance [35] is challenging due to the large magnetic fields required. Alternative ways to control the interaction using radio-frequency or microwave [47, 72, 133, 177], and independent control of two scattering lengths [199] have been proposed in the literature.

5.4 Details of numerical simulation

We numerically study the dynamics of the driven spin-1 condensate by solving the time-dependent Gross-Pitaevskii equations (5.1)–(5.3), incorporating the periodic interaction coefficients described previously. The equations are integrated using the second-order symplectic algorithm introduced in Ref. [172].

Although the initial state is stationary under the periodic modulation, it is unstable with respect to small perturbations. The quantum fluctuations are simulated in the numerics by choosing a perturbed initial state based on the truncated Wigner prescription [7, 12, 151, 191] in the limit $q \to \infty$ at zero temperature. Here we have $\psi(\boldsymbol{\rho}, t = 0) = \psi_P + \delta\psi(x, y)$, with ψ_P the uniform polar phase state and

$$\delta(\boldsymbol{\rho}) = \frac{1}{\sqrt{L_x L_y}} \sum_{\boldsymbol{k}} \begin{pmatrix} \alpha^1_{\boldsymbol{k}} \exp(i\boldsymbol{k}\cdot\boldsymbol{\rho}) \\ \alpha^0_{\boldsymbol{k}} u_{\boldsymbol{k}} \exp(i\boldsymbol{k}\cdot\boldsymbol{\rho}) + v_{\boldsymbol{k}} \left(\alpha^0_{\boldsymbol{k}}\right)^* \exp(-i\boldsymbol{k}\cdot\boldsymbol{\rho}) \\ \alpha^{-1}_{\boldsymbol{k}} \exp(i\boldsymbol{k}\cdot\boldsymbol{\rho}). \end{pmatrix} \tag{5.10}$$

Here $\alpha^m_{\boldsymbol{k}}$ are complex Gaussian random variable with zero mean and satisfy $\langle \alpha^m_{\boldsymbol{k}} \alpha^{m'}_{\boldsymbol{k}'} \rangle = (1/2)\delta_{mm'}\delta(\boldsymbol{k} - \boldsymbol{k}')$. The amplitudes are given as,

$$u_{\boldsymbol{k}} = \sqrt{\frac{E_k + \bar{c}_0 \tilde{n}_0}{2\sqrt{E_k(E_k + 2\bar{c}_0\tilde{n}_0)}} + \frac{1}{2}}, \quad v_{\boldsymbol{k}} = \sqrt{1 - u^2_{\boldsymbol{k}}}. \tag{5.11}$$

We also note that qualitatively similar results are obtained for the initial state perturbed using uniform random noise,

$$\psi(\boldsymbol{\rho}, t = 0) = \sqrt{\tilde{n}_0} \begin{pmatrix} p_1 \exp(i\theta_1) \\ [1 - p_1^2 - p_{-1}^2] \exp(i\theta_0) \\ p_{-1} \exp(i\theta_{-1}) \end{pmatrix}, \tag{5.12}$$

where $p_{\pm 1}, \theta_0 \in [0, \epsilon]$ and $\theta_{\pm 1} \in [0, 2\pi]$ are uniform random variables, with $\epsilon \ll 1$.

5.5 Linear stability analysis of driven state

Under the periodic driving of the scattering lengths, the uniform state becomes unstable to the spontaneous formation of density and spin patterns. The state given by $\psi_H(t) = \psi_P e^{i\theta(t)}$, where $\theta(t) = \int_0^t dt\ \bar{c}_0(t)\tilde{n}_0$, is the uniform polar phase solution of the coupled GPE with modulated interaction. We employ a linear stability analysis on the uniform solution. We consider a perturbed ground-state solution of the form,

$$\psi(\boldsymbol{r}) = \{\psi_P + [\boldsymbol{u}(t) + i\boldsymbol{v}(t)] \cos(\boldsymbol{k}\cdot\boldsymbol{r})\} e^{i\theta(t)}, \tag{5.13}$$

where ψ_P is uniform state in polar phase and $\boldsymbol{u}(t) = (u_1, u_0, u_{-1})^T$ and $\boldsymbol{v}(t) = (v_1, v_0, v_{-1})^T$ are the real-valued amplitudes of the spatially modulated perturbation. Using Eq. (5.13) in the coupled GPE with driven interactions and linearizing, we arrive at the equation of motion for $u_m(t), v_m(t)$. The first set of equations gives us the evolution of the perturbation in the $m = 0$ component,

$$\hbar \frac{d}{dt}\begin{pmatrix} u_0 \\ v_0 \end{pmatrix} = \begin{pmatrix} 0 & E_k \\ -\left[E_k + 2\tilde{c}_0(t)\tilde{n}_0\right] & 0 \end{pmatrix}\begin{pmatrix} u_0 \\ v_0 \end{pmatrix}, \tag{5.14}$$

which can be written as a second-order differential equation,

$$\frac{d^2 u_0}{dt^2} + \frac{E_k}{\hbar^2}\left[E_k + 2\tilde{c}_0(t)\tilde{n}_0\right] u_0 = 0. \tag{5.15}$$

For the perturbation in $m = \pm 1$ components, we obtain a set of four coupled equations,

$$i\hbar \frac{d}{dt}\begin{pmatrix} u_1 \\ u_{-1} \\ v_1 \\ v_{-1} \end{pmatrix} = \begin{pmatrix} 0 & 0 & \mathcal{E}_k^{(+)} & \tilde{c}_1(t)\tilde{n}_0 \\ 0 & 0 & \tilde{c}_1(t)\tilde{n}_0 & \mathcal{E}_k^{(-)} \\ -\mathcal{E}_k^{(+)} & -\tilde{c}_1(t)\tilde{n}_0 & 0 & 0 \\ -\tilde{c}_1(t)\tilde{n}_0 & -\mathcal{E}_k^{(-)} & 0 & 0 \end{pmatrix}\begin{pmatrix} u_1 \\ u_{-1} \\ v_1 \\ v_{-1} \end{pmatrix}. \tag{5.16}$$

Here, we have defined $\mathcal{E}_k^{(\pm)} = E_k + q \mp p + \tilde{c}_1(t)\tilde{n}_0$. If the linear Zeeman term $p = 0$, these equations simplifies as,

$$\hbar^2 \frac{d^2 u_+}{dt^2} + (E_k + q)\left[E_k + q + 2\tilde{c}_1(t)\tilde{n}_0\right] u_+ = 0 \tag{5.17}$$

$$\hbar^2 \frac{d^2 v_-}{dt^2} + (E_k + q)\left[E_k + q + 2\tilde{c}_1(t)\tilde{n}_0\right] v_- = 0, \tag{5.18}$$

with $u_\pm = u_1 \pm u_{-1}$ and $v_\pm = v_1 \pm v_{-1}$. The quantities u_0, u_+, and v_- are related to the fluctuations in various physical quantities in the system. For instance, the total density under the perturbed system is modulated as,

$$n(\boldsymbol{r}, t) = n_0 + 2\sqrt{\tilde{n}_0}\, u_0(t)\cos(\boldsymbol{k}\cdot\boldsymbol{r}) + O(u_m^2, v_m^2). \tag{5.19}$$

We can see that the density fluctuation about the mean value is linearly proportional to u_0. Similarly, transverse spin-density vectors become,

$$F_x(\boldsymbol{r}, t) = \sqrt{2\tilde{n}_0}\, u_+ \cos(\boldsymbol{k}\cdot\boldsymbol{r}) + O(u_m, v_m) \tag{5.20}$$

$$F_y(\boldsymbol{r}, t) = \sqrt{2\tilde{n}_0}\, v_- \cos(\boldsymbol{k}\cdot\boldsymbol{r}) + O(u_m, v_m), \tag{5.21}$$

which are proportional to u_+ and v_-. The longitudinal spin component $F_z(\boldsymbol{r}, t)$ is perturbed only in quadratic order of u_m, v_m. Therefore, the instabilities in u_0 manifest as density modulations, while that in u_+ and v_- cause the formation of spin-texture in transverse spin components $F_x(\boldsymbol{t})$ and $F_y(\boldsymbol{r}, t)$. In the following sections, we look at the specific modulation protocols where we use these equations to gain insight into the system dynamics.

5.6 Modulation of a_0 scattering length

5.6.1 Mathieu equations

When a_0 driven periodically while a_2 is held constant, the time evolution of $\tilde{c}_0$ and $\tilde{c}_1$ are given by Eq. (5.7). In this scenario, the density amplitude equation (5.15) becomes,

$$\frac{d^2u_0}{dt^2} + \frac{1}{\hbar^2}\left[\epsilon_0(k)^2 + \frac{4}{3}E_k\alpha_0\bar{g}_0\tilde{n}_0\cos(2\omega_0 t)\right]u_0 = 0, \tag{5.22}$$

where α_0 and ω_0 are the amplitude and frequency of the periodic driving. Eq. (5.22) is a Mathieu differential equation, for which Floquet theory predicts solutions of the form $u_0(t) = b_0(t)\exp\left(\sigma^{(0)}t\right)$, with $b_0(t + \pi/\omega_0) = b_0(t)$ being a periodic function. The stability of the equation depends on the Floquet exponent $\sigma^{(0)}$, and the system is unstable against perturbation if $\mathrm{Re}\{\sigma^{(0)}\} > 0$, where, even a small initial value of $u_0(t)$ grows exponentially in time.

For vanishing driving amplitude $\alpha_0 \to 0$, the instability occur when for the momenta $\boldsymbol{k}$ that satisfies $\epsilon_0(k) = j\hbar\omega_0$, where $j \in \mathbb{N}$ [109] (see Sec. 2.7.2). Although multiple $\boldsymbol{k}$ values satisfy these conditions, at various j, the solution with the largest Floquet exponent will dominate the dynamics due to the exponential growth rates. The strongest instability occurs for $j = 1$ (first resonance). When $\alpha_0 \to 0$, the Floquet exponent's value at first resonance is given by $\sigma^{(0)} = (k_u^{(0)})^2\alpha_0\bar{g}_0\tilde{n}_0/6M\omega_0$. Here, $k_u^{(0)}$ is the wave number of the most unstable mode that satisfies

$$\epsilon_0(k_u^{(0)}) = \hbar\omega_0. \tag{5.23}$$

The instability leads to the formation of density Faraday patterns in the density of wavelength $\lambda \sim 2\pi/k_u^{(0)}$. Using the resonance condition Eq. (5.23) we get the Floquet exponent,

$$\sigma^{(0)} \approx \frac{\alpha_0\bar{g}_0\tilde{n}_0}{3\hbar^2\omega_0}\left[\sqrt{\bar{c}_0^2\tilde{n}_0^2 + \hbar^2\omega_0^2} - \bar{c}_0\tilde{n}_0\right], \tag{5.24}$$

which gives us the growth rate of the density patterns in the system.

Now we turn to the spin-wave excitations governed by Eqs. (5.17) and (5.18). When only a_0 is modulated, these equations take the form,

$$\frac{d^2u_+}{dt^2} - \frac{1}{\hbar^2}\left[\epsilon_1^2(k) + \frac{4}{3}(E_k + q)\alpha_0\bar{g}_0\tilde{n}_0\cos(2\omega_0 t)\right]u_+ = 0,$$
$$\frac{d^2v_-}{dt^2} - \frac{1}{\hbar^2}\left[\epsilon_1^2(k) + \frac{4}{3}(E_k + q)\alpha_0\bar{g}_0\tilde{n}_0\cos(2\omega_0 t)\right]v_- = 0, \tag{5.25}$$

which are Mathieu equations as well. Similar to the case of density equation Eq. (5.22), spin equations will have solutions of the form $u_+, v_-(t) = b_\pm(t)\exp\left(\sigma^{(\pm)}t\right)$, with $b_\pm(t + \pi/\omega_0) = b_\pm(t)$ being a periodic. For small driving frequencies, the instability occurs for spin modes satisfying $\epsilon_{\pm 1}(k) = j\hbar\omega_0$. The Floquet exponent at the first resonance is $\sigma^{(\pm)} \approx [(\hbar^2(k_u^{(\pm)})^2/2M) + q]\alpha_0\bar{g}_0\tilde{n}_0/3\hbar^2\omega_0$, where $k_u^{(\pm)}$ is the wavenumber of the most unstable spin-mode,

$$\epsilon_{\pm 1}(k_u^{(\pm)}) = \hbar\omega_0. \tag{5.26}$$

Transverse spin-density patterns of wavelength $\lambda \sim 2\pi/k_u^{(\pm)}$ form as a result of spin-mode instability, and the growth rate of the spin-waves is given by,

$$\sigma^{(\pm)} \approx \frac{\alpha_0\bar{g}_0\tilde{n}_0}{3\hbar^2\omega_0}\left[\sqrt{\bar{c}_1^2\tilde{n}_0^2 + \hbar^2\omega_0^2} - \bar{c}_1\tilde{n}_0\right]. \tag{5.27}$$

5.6.2 Degenerate density and spin branches

When the interaction coefficients are equal, i.e. $\bar{c}_0 = \bar{c}_1$, and the quadratic Zeeman term $q = 0$, all three branches of the polar-phase condensate spectrum are degenerate. Therefore, the density and spin instabilities that occur under periodic driving of scattering length a_0 will have the same Floquet exponent, i.e $\sigma^{(0)} = \sigma^{(\pm)}$, causing the density patterns and the spin patterns to grow at the same rate. The wavelengths of the spin and density patterns are equal as well, since $k_u^{(0)} = k_u^{(\pm)} \equiv k_u$.

In Fig. 5.2, we show the mean-field dynamics of population in each spin-level, defined as $N_m(t) = \int d\boldsymbol{\rho}|\psi_m(\rho, t)|^2$ under a_0 modulation, where we can see transfer occurring from $m = 0$ to $m = \pm 1$ modes under the driving. The spin-mode instability causes the population transfer and occurs at a rate determined by $\sigma^{(\pm)}$. The total magnetization along F_z remains zero due to conservation of angular momentum, thus $N_+(t) = N_-(t)$. We have also given the population of non-zero momentum modes in $m = 0$, denoted by $N_{0,k\neq 0}$, which grows due to the density mode instability. The population growth in the excited modes is exponential during the initial period, as predicted from the stability analysis, with the exponent matching the linear stability analysis predictions. At later times, as the perturbations grow larger, the linear

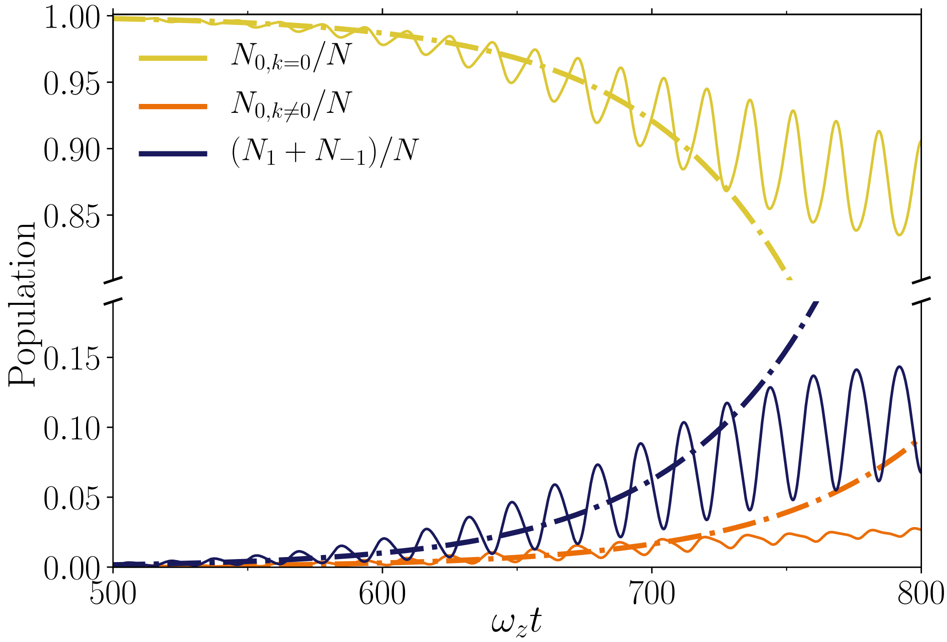

FIGURE 5.2: Population dynamics under a_0 modulation. The population of the states $m = \pm1$ is defined as $N_{\pm1} = \iint |\psi_{\pm1}(x, y)|^2 dxdy$. The excited population in $m = 0$ is $N_{0,k\neq0} = \iint_{k\neq0} \left|\tilde{\psi}_0(k_x, k_y)\right|^2 dk_x dk_y$. The driving frequency and amplitudes are $\omega_0 = 0.2\omega_z$ and $\alpha_2 = 0.4$ respectively. Other parameters are $\bar{c}_0\tilde{n}_0 = \bar{c}_1\tilde{n}_0 = 0.2\hbar\omega_z$ and $q = 0$. The dashed lines show the exponential fit to the data.

approximation becomes invalid and the growth rate deviates from the initial exponential behaviour.

Density pattern formation

The periodic driving creates density patterns in all three components [Fig. 5.3(a)-(c)]. In the $m = 0$ component, the excited modes interfere with the condensate, creating patterns with wavelength $2\pi/k_u$, whereas in $m = \pm1$, we observe density waves with wavelength $\sim \pi/k_u$. The pattern in the total density is only affected by the $m = 0$ component contribution, as the density patterns in the other two components are orders of magnitude smaller. The excitations also appear in the momentum space density [Fig. 5.3(d)-(f)], where momenta modes with $|\boldsymbol{k}| \approx k_u$ are populated under the driving.

Later on, we see population growth in other momentum modes as well. These are formed due to secondary scattering processes where initially excited atoms with momenta $(\boldsymbol{k}_1, \boldsymbol{k}'_1)$, where $|\boldsymbol{k}| = |\boldsymbol{k}'| = k_u$, scatter into $(\boldsymbol{k}_2, \boldsymbol{k}'_2)$ states, satisfying momentum conservation $\left|\boldsymbol{k}_1 + \boldsymbol{k}'_1\right| = \left|\boldsymbol{k}_2 + \boldsymbol{k}'_2\right|$. These excitations can be seen as a fainter halo in Fig. 5.3 (e) around the ring at radius k_u. We also note an enhancement of population in the modes that satisfy the second resonance condition given by $\epsilon_{k,m} = 2\hbar\omega_0$. These density patterns are transient as continuous driving eventually destroys the BEC due to depletion [18, 200].

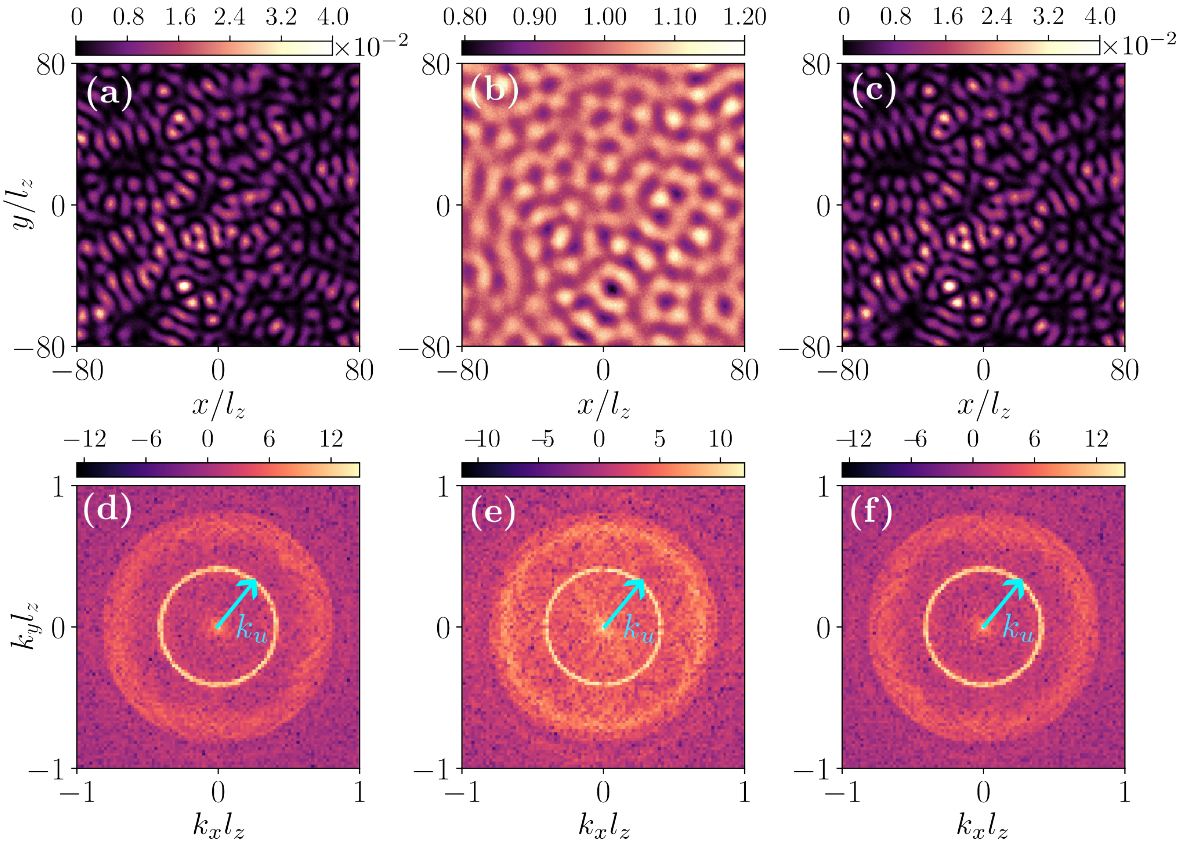

FIGURE 5.3: Density pattern formed under periodic driving of scattering length a_0 in (a) $m = 1$, (b) $m = 0$, and (c) $m = -1$ components, snapshot taken at $\omega_z t = 570$. Bottom row contains the momentum space density of (d) $m = 1$, (e) $m = 0$, and (f) $m = -1$ The driving frequency and amplitudes are $\omega_0 = 0.2\omega_z$ and $\alpha_2 = 0.4$ respectively. Other parameters are $\bar{c}_0\tilde{n}_0 = \bar{c}_1\tilde{n}_0 = 0.2\hbar\omega_z$.

Magnetization dynamics

The initial state has a null spin-density vector $\boldsymbol{F}(\boldsymbol{\rho})$. The spin-mode instability creates spin-texture in the transverse spin components, shown in Fig. 5.4 (a). Interestingly, the velocity field of the transverse spin-density vector $\boldsymbol{F}_\perp$ in Fig. 5.4 (b) reveals the formation of polar-core vortices (PCVs) and antivortices [81, 115, 149]. The polar-core spin vortices appear due to phase windings $m = 1$ and $m = -1$ components, which create a vortex and antivortex in these components, respectively. The density of the $m = \pm 1$ components vanishes at the centre of the spin-vortex, which is filled with particles in the $m = 0$ component.

In Fig. 5.5 (a), we show the dynamics of the spin-vortex density N_v/L^2, L being the length of the box. The vortex number is numerically computed by taking small loops around each grid point to determine the phase winding of the spin-vector F_x, F_y along it. This method outputs a large vortex number for the initial state, although $|\boldsymbol{F}|$ is nearly zero. This is due to the random noise added at the initial state that introduces a small spin-density, oriented along arbitrary directions, at each grid point. As a result, the decrease in the vortex density due to the driving should be interpreted as the growth of polar-core spin vortices, which mask the

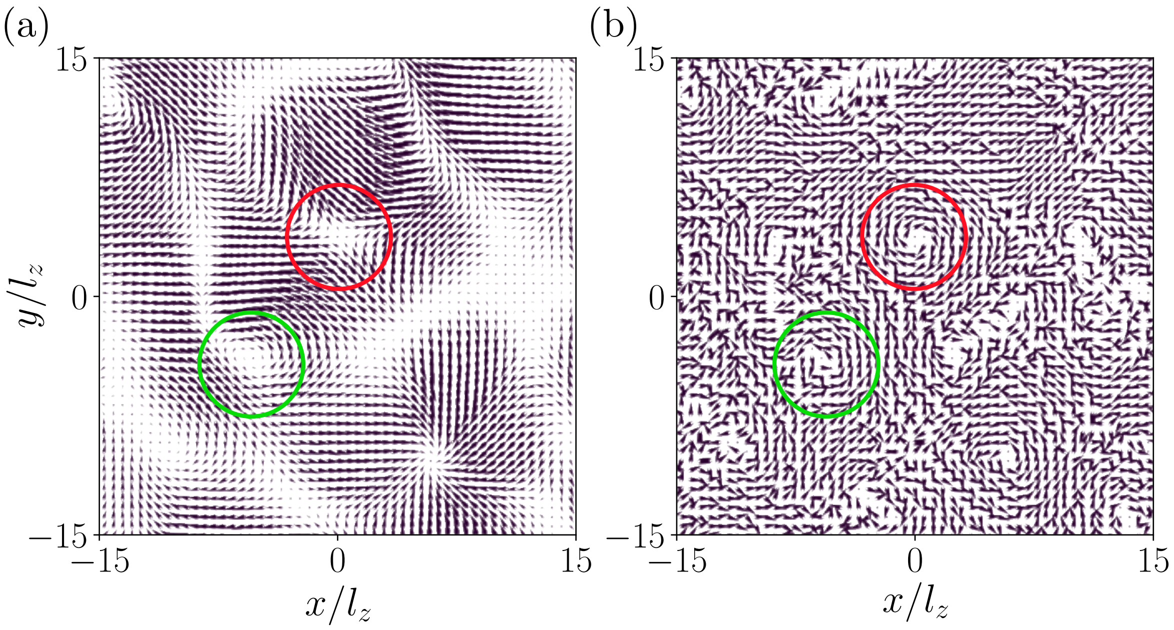

FIGURE 5.4: Spin textures formation under a_0 modulation. (a) The transverse spin density $\boldsymbol{F}_\perp(x, y)$ and (b) the velocity field of $\boldsymbol{F}_\perp(x, y) = (F_x, F_y)$, i.e., $\vec{\nabla}\phi/|\vec{\nabla}\phi|$, where $\phi = \arctan\left(F_x/F_y\right)$ at $\omega_z t = 670$ or $\sigma^{(+)}t = 14.74$. Other parameters are the same as in Fig. 5.3. Vortex (green) and antivortex (red) are marked using circles.

initial random noise. Once the spin-texture growth attains a certain amplitude, the number of vortices settles to a constant value [region shown in inset of Fig. 5.5 (a)], at which point, almost all of the spin-vortices counted are PCV. The decay rate of the vortex number is thus determined by the spin Floquet exponent $\sigma^{(+)}$.

The number density of PCVs once the spin-texture is formed is determined by the unstable momentum k_u, as shown in Fig. 5.5 (d), and it is proportional k_u^2. This implies that the larger the modulation frequency is, the denser the spin-vortex gas is. At longer times ($\sigma^{(+)}t > 16$), we observed that the $m = 0$ homogeneous condensate gets significantly depleted, and PCVs disintegrate into independent gases of vortices in the $m = 1$ and $m = -1$ components.

Further, we analyze the scaled spin-spin correlations,

$$C_\nu = \frac{1}{A_\nu} \iint d\boldsymbol{\rho}' F_\nu(\boldsymbol{\rho} + \boldsymbol{\rho}', t) F_\nu(\boldsymbol{\rho}', t) \tag{5.28}$$

where $\nu \in \{x, y, z\}$ and $N_\nu = \iint d\boldsymbol{\rho} F_\nu^2(\boldsymbol{\rho})$. The radial correlation function for the transverse and longitudinal spin-components is given in Fig. 5.6 (a). The radial correlation function $C_\nu(\rho, r) = (1/2\pi) \int_0^{2\pi} C_\nu(\boldsymbol{\rho}, t) d\varphi$ is a Bessel function [Fig. 5.6 (b)]. The Bessel function relation indicates that the patterns are formed from the superposition of spin-waves of the same wavelength $\lambda = 2\pi/k_u$ travelling in random directions in the xy-plane, and such correlations have been predicted for quantum quenches as well [7, 98, 152].

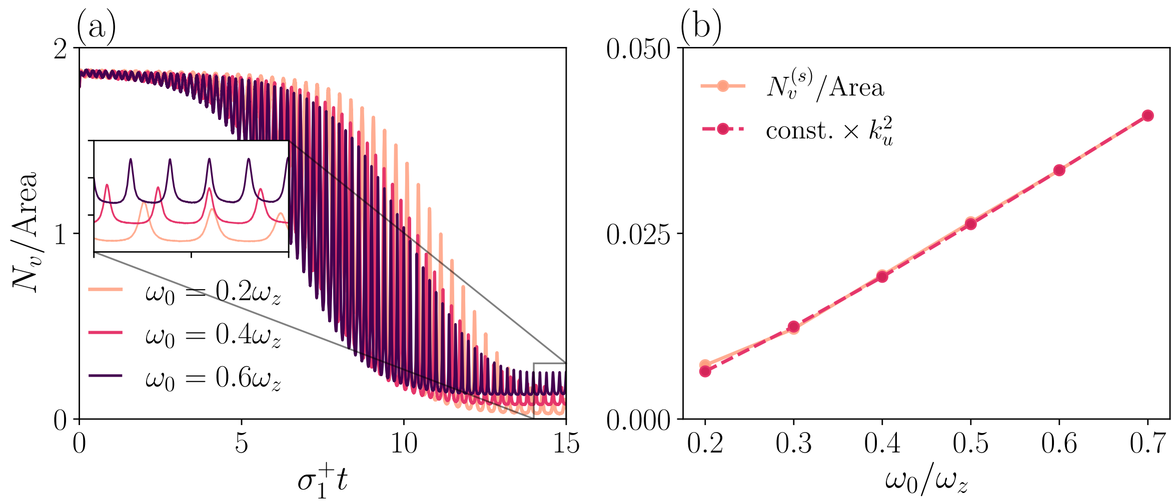

FIGURE 5.5: (a)The dynamics of spin-vortex number density N_v/L^2, where L is the box size, as a function of scaled time $\sigma_1^+ t$. The inset indicates the vortex dynamics after the formation of the patterns. The results are averaged over 10 runs. (b) The vortex number density at $\sigma^{(+)}t = 14.74$ for various driving frequencies is proportional to the k_u^2. Parameters are the same as in Fig. 5.3.

5.7 Non-degenerate spin and density modes

So far, we have discussed the case where the density and spin Bogoliubov branches are degenerate. However, this is no longer the case when a non-zero Zeeman term q is present or if the spin and density interaction coefficients are unequal, i.e. $\bar{c}_1 \neq \bar{c}_0$. In such cases, the momenta of the unstable density and spin modes under periodic driving are different, i.e. $k_u^{(0)} \neq k_u^{(+)}$, and corresponding Mathieu exponents $\sigma^{(+)}, \sigma^{(0)}$ are unequal as well. The dynamics of the driven condensate are significantly altered if the magnitudes of the two interaction coefficients differ substantially.

When $\bar{c}_1 \ll \bar{c}_0$, the spin-mode is soft and hence $k_u^{(0)} \ll k_u^{(+)}$ and the spin Mathieu exponent is much greater than the density exponent as $\sigma^{(0)} \ll \sigma^{(+)}$. Under periodic driving, spin mixing dominates the dynamics. At the same time, excitation occurs in the non-zero momentum modes of $m = 0$ spin component remains small due to a relatively small density exponent, as seen from Fig. 5.7 (b). The transverse spin-spin correlation would be a Bessel function in this case.

On the other hand, when $\bar{c}_1 \gg \bar{c}_0$, the density mode is soft and $k_u^{(0)} \gg k_u^{(+)}$. Therefore, $\sigma^{(0)} \gg \sigma^{(+)}$ and the density pattern formation dominate the dynamics over spin-mixing [Fig. 5.7 (a)], and the spin-spin correlation in this case would be exponentially decaying, instead of a Bessel function as in the previous cases.

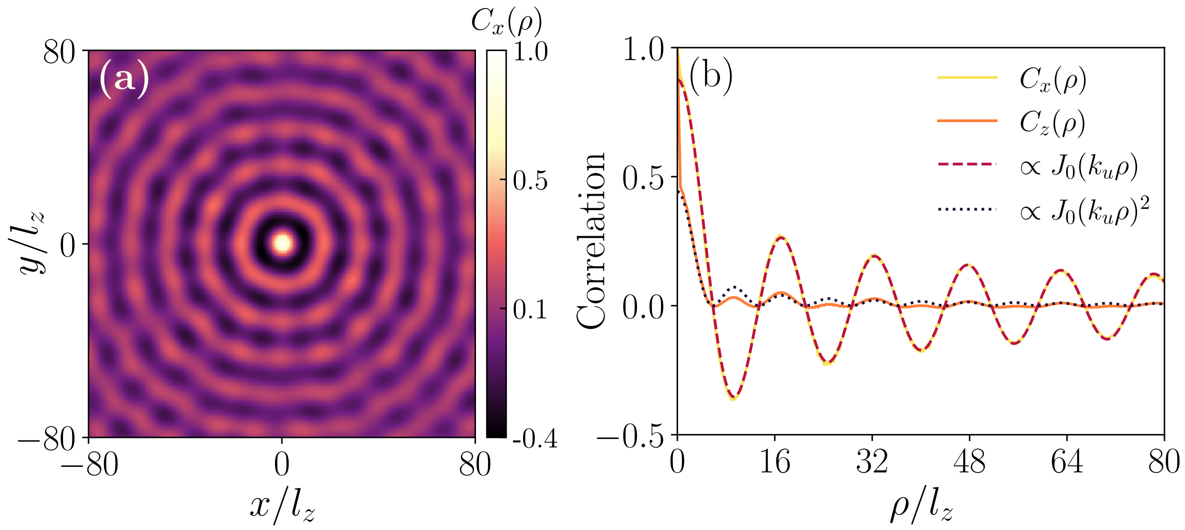

FIGURE 5.6: Spin-spin correlations for a_0 modulation. (a) The transverse magnetization correlation $C_x(\boldsymbol{\rho}, t)$ in the xy-plane and (b) the radial correlation function $C_{x,z}(\rho)$ at $\omega_z t = 500$. Other parameters are the same as in Fig. 5.3. We see that $C_{x,y}(\rho) \propto J_0(k_u\rho)$ and $C_z(\rho) \propto J_0^2(k_u\rho)$. The plots are obtained by taking an average of the results from ten different realizations of initial noise.

5.7.1 Non-zero quadratic Zeeman term

When the quadratic Zeeman term is non-zero, the density and spin modes become non-degenerate as it introduces a gap, $\Delta = \sqrt{q(q + \bar{c}_1\tilde{n}_0)}$ [Fig. 5.8 (a)], in the spin modes. When the driving frequency $\hbar\omega_0 < \Delta$, none of the spin modes satisfy the first resonance condition. The spin-mixing dynamics and spin pattern formation only occur when $\hbar\omega_0 > \Delta$.

Consider $\bar{c}_0 = \bar{c}_1$ and $\hbar\omega_0 > \Delta$. In this case, Mathieu exponent for the density and spin modes are equal and exponents are independent of q [see Eqs. (5.24) and (5.27)]. However, momenta of the unstable spin and density pattern will be different, i.e. $k_u^{(0)} \neq k_u^{(\pm)}$.

In Fig. 5.8 (b), we see the implicit dependent of Mathieu exponent $\sigma^{(+)}$ on q. When $\hbar\omega_0 > \Delta$, the exponent values are determined from the first resonance of the Mathieu equation, whereas when $\hbar\omega_0 < \Delta$, it is determined from the second resonance at which the exponent is much smaller. Thus, in the second scenario, density pattern formation dominates the dynamics. A case of particular interest is when $\bar{c}_1 \ll \bar{c}_0$, where the density pattern formation dominates when $\hbar\omega_0 < q$ and spin-dynamics dominates when $\hbar\omega_0 > q$.

5.8 Modulation of a_2 scattering length

The discussion so far has been on the modulation of a_0 scattering length. In this section, we will discuss the dynamics of a_2 scattering length, highlighting the main differences from the previous case.

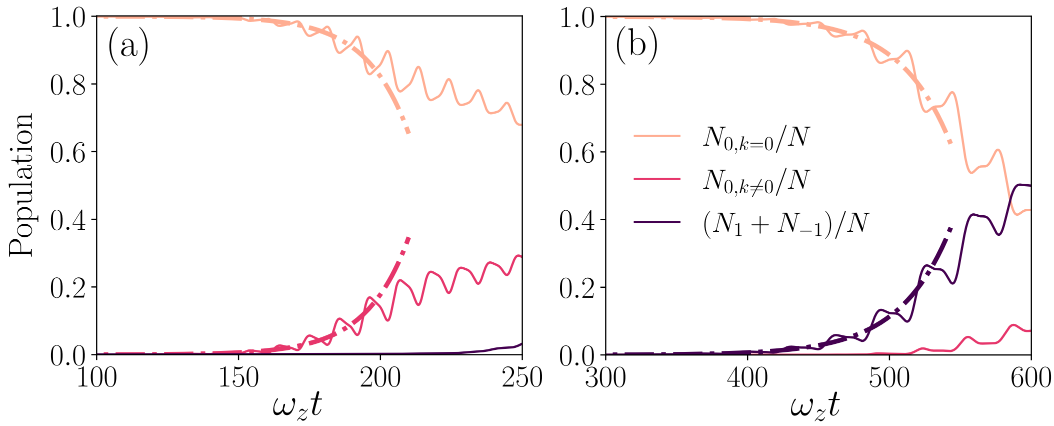

FIGURE 5.7: The population dynamics under modulation of the scattering length a_0 for $q = 0$. (a) $\bar{c}_0\tilde{n}_0 = 0.2\hbar\omega_z$, $\bar{c}_1\tilde{n}_0 = 4.0\hbar\omega_z$, $\alpha_0 = 0.03$, and $\omega_0 = 0.3\omega_z$. (b) $\bar{c}_0\tilde{n}_0 = 0.4\hbar\omega_z$, $\bar{c}_1\tilde{n}_0 = 0.05\hbar\omega_z$, $\alpha_0 = 0.25$, and $\omega_0 = 0.1\omega_z$. N_m denotes the population of each component and $N = \sum_m N_m$ is the total population. $N_{0,k=0}$ denotes the population in the zero momentum mode in the $m = 0$ component, while $N_{0,k\neq 0}$ is the population of the non-zero modes in the same component.

5.8.1 a_2 Modulation: Mathieu equations

When the a_2 is driven as $a_2(t) = \bar{a}_2\,[1 + 2\alpha_2\cos(2\omega_2 t)]$, equation describing the density fluctuation Eq. (5.15) becomes

$$\frac{d^2u_0}{dt^2} + \frac{1}{\hbar^2}\left[\epsilon_0^2(k) + \frac{8}{3}E_k\alpha_2\bar{g}_2\tilde{n}_0\cos(2\omega_0 t)\right]u_0 = 0, \tag{5.29}$$

Similarly from the spin equation (5.17) we get,

$$\begin{aligned}\frac{d^2u_+}{dt^2} + \frac{1}{\hbar^2}\left[\epsilon_{\pm1}^2(k) + \frac{4}{3}(E_k + q)\alpha_2\bar{g}_2\tilde{n}_0\cos(2\omega_2 t)\right]u_+ = 0,\\ \frac{d^2v_-}{dt^2} + \frac{1}{\hbar^2}\left[\epsilon_{\pm1}^2(k) + \frac{4}{3}(E_k + q)\alpha_2\bar{g}_2\tilde{n}_0\cos(2\omega_2 t)\right]v_- = 0.\end{aligned} \tag{5.30}$$

These are Mathieu equations as well, and the condition for instability in a mode has been discussed before, which is given by $\epsilon_0(k) = j\hbar\omega_2$ for the density mode and $\epsilon_{\pm1}(k) = j\hbar\omega_2$ for the spin mode, for $j = 1, 2, ...$ The density and spin Floquet exponents for a_2 modulation are given by,

$$\begin{aligned}\sigma^{(0)} &\approx \frac{2\alpha_2\bar{g}_2\tilde{n}_0}{3\hbar^2\omega_0}\left[\sqrt{\bar{c}_0^2 n_0^2 + \hbar^2\omega_0^2} - \bar{c}_0\tilde{n}_0\right]\\ \sigma^{(\pm)} &\approx \frac{\alpha_2\bar{g}_2\tilde{n}_0}{3\hbar^2\omega_0}\left[\sqrt{\bar{c}_1^2\tilde{n}_0^2 + \hbar^2\omega_0^2} - \bar{c}_1\tilde{n}_0\right].\end{aligned} \tag{5.31}$$

By inspecting the above exponent, we can see an extra factor of two for $\sigma^{(0)}$. This is due to the difference in the dependence of c_0 and c_1 on the scattering length a_2. Driving a_2 causes twice the modulation in c_0 as compared to that in c_1 [Eq. (5.8)]. Hence, density dynamics

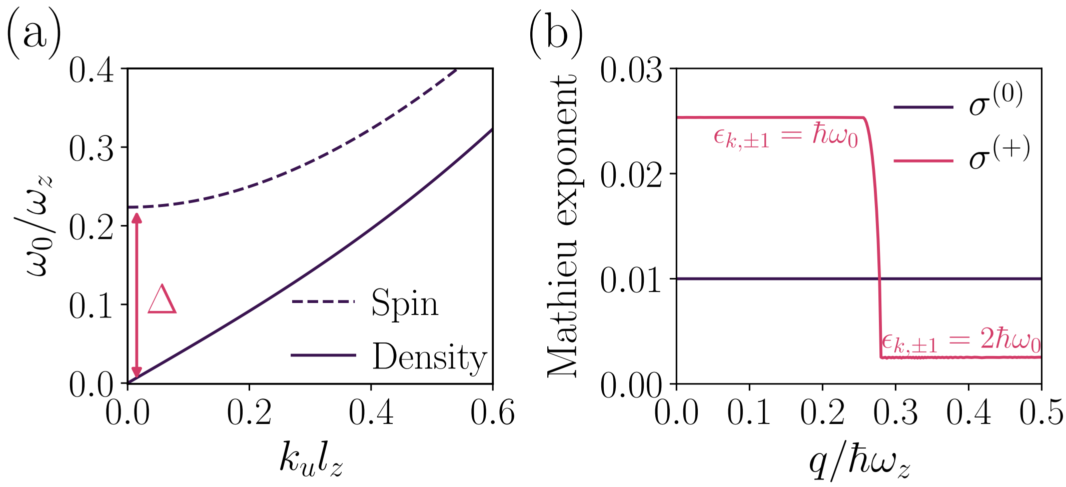

FIGURE 5.8: (a) The Bogoliubov spectrum for $\bar{c}_0\tilde{n}_0 = \bar{c}_1\tilde{n}_0 = 0.2\hbar\omega_z$, $\omega_0/\omega_z = 0.3$, and $q = 0.1\hbar\omega_z$. The unstable momenta as a function of ω_0 map the spectrum in the limit $\alpha \to 0$. (b) The Mathieu exponents of density and spin modes as a function of q for $\bar{c}_0\tilde{n}_0 = 0.4\hbar\omega_z$, $\bar{c}_1\tilde{n}_0 = 0.05\hbar\omega_z$, $\omega_0/\omega_z = 0.3$ and $\alpha_0 = 0.3$. Δ is the gap of the spin modes at $k = 0$. In (b), the primary resonance associated with the spin mode changes from $\epsilon_{\boldsymbol{k},\pm1} = \hbar\omega_0$ to $\epsilon_{\boldsymbol{k},\pm1} = 2\hbar\omega_0$ as a function of q, leading to a significant decrease in the Mathieu exponent $\sigma^{(+)}$.

dominates when $\bar{c}_0 = \bar{c}_1$, unlike in the case of a_0 modulation, where both dynamics occur at the same rate. This is see from Fig. 5.9, where $\sigma^{(0)} = 2\sigma^{(+)}$ for equal interaction coefficients.

We also see an interesting frequency-dependent behaviour with a_2 modulation, when $\bar{c}_1 \ll \bar{c}_0$, where dominant spin-dynamics occur at smaller driving frequencies and dominant density dynamics occur at larger frequencies. The crossover from spin to density-dominant dynamics is given in Fig. 5.9.

5.9 Simultaneous modulation of two scattering lengths

In this section, we look at the case of simultaneous modulation of the two scattering lengths as given in Eq. (5.9). First, we discuss two specific scenarios, where the scattering lengths are driven such that only one of the interaction coefficients is modulated, by modulating a_2 with a relative phase as $a_2(t) = \bar{a}_2[1 + 2\alpha_2 \cos(2\omega_2 t + \phi)]$. We also discuss a general case, where the modulation with multiple frequencies with appropriately chosen amplitudes is shown to create instabilities with different wavelengths.

5.9.1 c_0 modulation

When $\omega_0 = \omega_2$, $\alpha_2\bar{g}_2 = \alpha_0\bar{g}_0$ and $\phi = 0$, we have the $c_0(t)$ being varied in time, whereas modulation in c_1 is cancelled out. From Eq. (5.15), we get a Mathieu equation for density

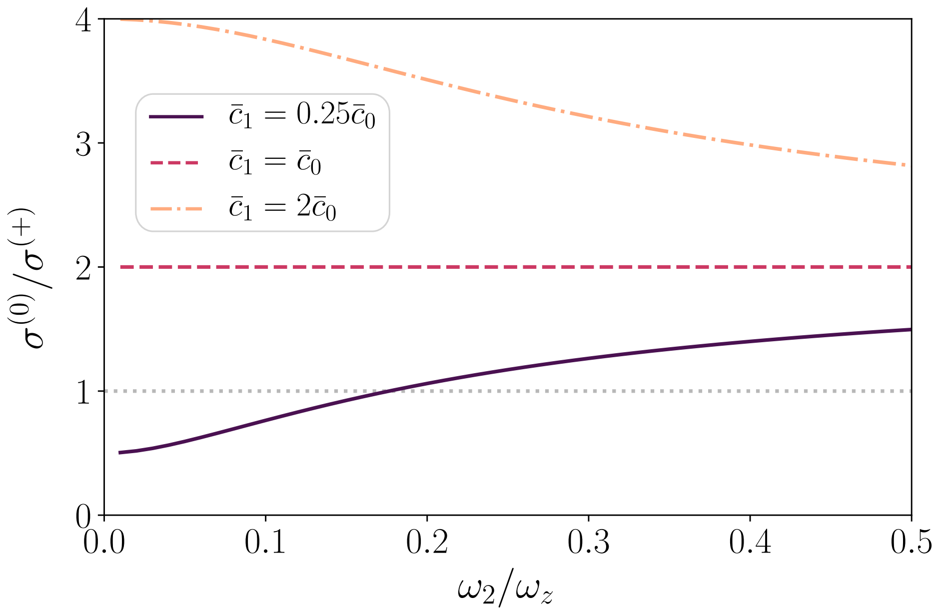

FIGURE 5.9: The ratio of the density and spin Mathieu exponents $\sigma^{(0)}/\sigma^{(+)}$ under a_2 modulation, as a function of the driving frequency ω_2 for three different c_1 values, for $\bar{c}_0\tilde{n}_0 = 0.2\hbar\omega_z$. The grey dotted line indicates $\sigma^{(0)} = \sigma^{(+)}$. When $\bar{c}_1 = 0.25\bar{c}_0$, we see a change in the dynamics as a function of driving frequency as the $\sigma^{(0)}/\sigma^{(+)}$ crosses unity at the critical frequency $\omega_2 \approx 0.18\omega_2$.

fluctuations

$$\frac{du_0}{dt^2} + \frac{1}{\hbar^2}\left[\epsilon_0(k)^2 + 4E_k\alpha_0\bar{g}_0\tilde{n}_0\cos(2\omega_0 t)\right]u_0 = 0, \tag{5.32}$$

which indicate that density modes with wavenumber $\epsilon_0(k_u^{(0)}) = \hbar\omega_0$ are unstable, whereas spin-fluctuations evolve under [Eq. (5.17), (5.18)]

$$\frac{d^2u_+}{dt^2} + \frac{1}{\hbar^2}\epsilon_{\pm 1}^2(k)u_+ = 0. \tag{5.33}$$

All the spin-modes are stable in the absence of c_1 modulation, thus spin-pattern formation and spin-mixing do not occur.

5.9.2 c_1 modulation

Now, consider when $\omega_0 = \omega_2$, $2\alpha_2\bar{g}_2 = \alpha_0\bar{g}_0$ and $\phi = \pi$. In this case, we have c_1 being modulated while c_0 is held constant. The equation of evolution of density fluctuations becomes,

$$\frac{d^2u_0}{dt^2} + \frac{1}{\hbar^2}\epsilon_0^2(k)u_0 = 0. \tag{5.34}$$

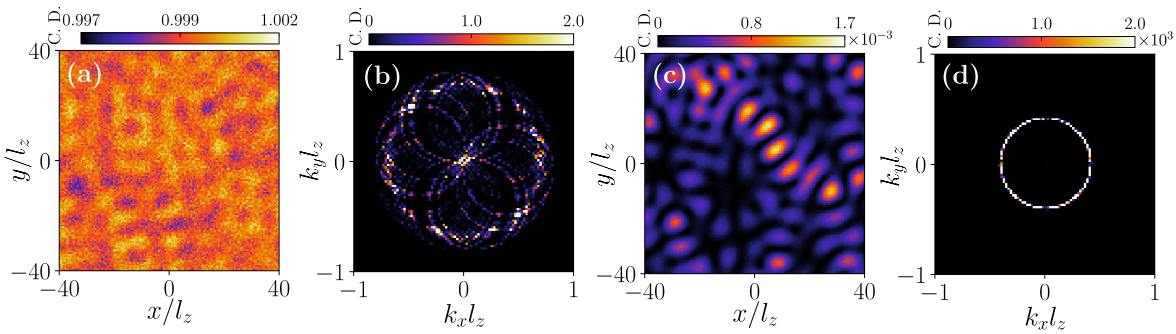

FIGURE 5.10: The real space density pattern for (a) $m = 0$ and (c) $m = \pm 1$ components under simultaneous modulation of a_0 and a_2 scattering length with phase difference π. The momentum space density of the component (b) $m = 0$ and (d) $m = \pm 1$ is also given. Here $\bar{c}_0\tilde{n}_0 = \bar{c}_1\tilde{n}_0 = 0.2\hbar\omega_z$, $\alpha_0 = 0.2$,$\alpha_2 = 0.05$, and $\omega_0 = \omega_2 = 0.2\omega_z$. The results are taken at time $\omega_z t = 800$.

which indicates that the density modes are stable under driving. As for the spin modes, we get,

$$\frac{d^2u_+}{dt} + \frac{1}{\hbar^2}\left[\epsilon_{\pm 1}^2(k) + 2\tilde{n}_0(E_k + q)\alpha_0\bar{g}_0\cos(2\omega_0 t)\right]u_+ = 0, \tag{5.35}$$

which indicate instability for modes with wavenumber $k_u^{(+)}$ satisfying $\epsilon_{\pm 1}(k_u^{(+)}) = \hbar\omega_0$. The instability leads to population transfer to $m = \pm 1$ components and spin texture formation. The depletion of the density in the $m = 0$ component causes the formation of a local depletion in the same [Fig. 5.10 (a), (c)]. In the momentum space density of $m = \pm 1$, we see the bright ring arising from the instability [Fig. 5.10 (d)]. For the $m = 0$ component, we see a distribution of density pattern as an array of rings [Fig. 5.10 (b)]. This is due to secondary mixing processes that scatter atoms back into $m = 0$ from $m = \pm 1$ under the process $(\boldsymbol{k}, \pm 1) + (-\boldsymbol{k}, \mp 1) \leftrightarrow (\boldsymbol{k} + \boldsymbol{k}', \pm 1) + (-\boldsymbol{k} - \boldsymbol{k}', \mp 1)$.

5.9.3 Competing instabilities

In this section, we discuss the modulation of both scattering lengths with different frequencies, i.e. $\omega_0 \neq \omega_2$. Here, we stick to two cases; when $\bar{c}_1 \gg \bar{c}_0$ and when $\bar{c}_1 \ll \bar{c}_0$.

When $\bar{c}_1 \gg \bar{c}_0$, the density dynamics are given by

$$\frac{d^2u_0}{dt^2} + \frac{1}{\hbar^2}\left[\epsilon_0^2(k) + \frac{4E_k\tilde{n}_0}{3}(\alpha_0\bar{g}_0\cos 2\omega_0 t + 2\alpha_2\bar{g}_2\cos 2\omega_2 t)\right], \tag{5.36}$$

which is a quasi-periodic Mathieu equation. Such a system can be non-trivial, and the Floquet theory may no longer apply. They have been explored using an approximation method, which revealed a very complex stability diagram [93]. The problem simplifies if ω_0/ω_2 is a rational number, as the system will then have an overall periodicity and we can still apply the Floquet theory. We numerically solve Eq. (5.36) for various momenta k to obtain the

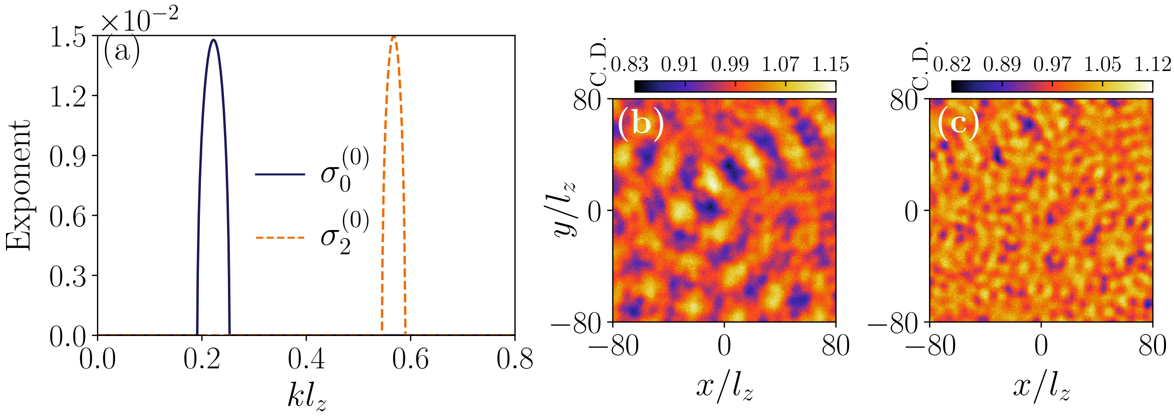

FIGURE 5.11: Competing instability among the density modes. (a) The two primary peaks in Mathieu exponent vs k from the simultaneous modulation of a_0 and a_2 for $\bar{c}_0\tilde{n}_0 = 0.2\hbar\omega_z$, $\bar{c}_1\tilde{n}_0 = 4\hbar\omega_z$, $q = 0$, $\alpha_0 = 0.024$, $\omega_0 = 0.1\omega_z$, $\alpha_2 = 0.01$, and $\omega_2 = 0.3\omega_z$. The solid line is for a_0, and the dashed line is for a_2 modulations. (b) and (c) show the density of $m = 0$ component at $\omega_z t = 420$ and $\omega_z t = 460$, respectively, exhibiting the change in wavelength of patterns in time. (b) has a wavelnegth of $1/k_{u0}^{(0)}$ and (c) has a wavelength of $1/\bar{k}_u^{(0)}$ with $k_u^{(0)} < \bar{k}_u^{(0)}$.

Floquet exponents (see Sec. 2.7.1), which are plotted for a given set of driving frequencies in Fig. 5.11(a). For small modulation amplitudes, the instability occurring under driving with two different frequencies is then found to be a union of the individual scattering length modulations [158]. The two unstable momenta $k_u^{(0)}$ and $\bar{k}_u^{(0)}$ found from,

$$\hbar\omega_0 = \epsilon_0(k_u^{(0)}), \quad \hbar\omega_2 = \epsilon_0(\bar{k}_u^{(0)}). \tag{5.37}$$

The density pattern contains both wavelengths, and when amplitudes are chosen so that the exponents are nearly equal for the two unstable momenta, we observe oscillations between the two patterns [Fig. 5.11(b),(c)]. When $\bar{c}_1 \gg \bar{c}_0$, spin dynamics does not happen within the same time-scales, as we discussed in 5.7, thus we do not observe it.

Conversely, when $\bar{c}_1 \ll \bar{c}_0$, we observe the spin, but not density, pattern formation. And the equation for the dynamics of spin fluctuations is given by,

$$\frac{d^2u_+}{dt^2} + \frac{1}{\hbar^2}\left[\epsilon_{k,\pm1}^2 + \frac{4(E_k+q)\tilde{n}_0}{3}\left(\alpha_0\bar{g}_0\cos 2\omega_0 t - \alpha_2\bar{g}_2\cos 2\omega_2 t\right)\right], \tag{5.38}$$

and $v_-(t)$ also obeys the same equation. Similar to the case before, Floquet theory can be applied if ω_0/ω_2 is a rational number, and the corresponding exponents are given in Fig. 5.12 (a). The unstable spin modes have momenta that are obtained from,

$$\hbar\omega_0 = \epsilon_{\pm1}(k_u^{(+)}), \quad \hbar\omega_2 = \epsilon_{\pm1}(\bar{k}_u^{(+)}). \tag{5.39}$$

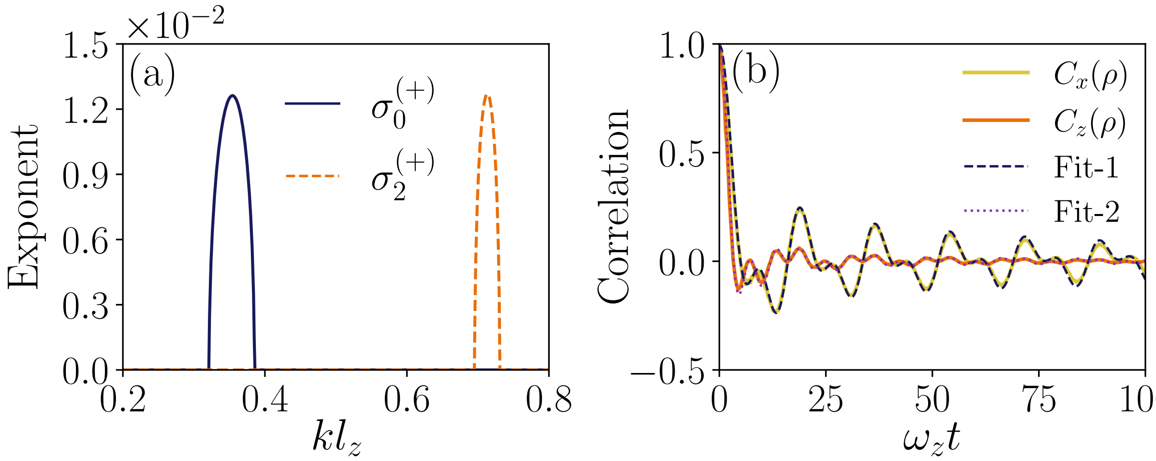

FIGURE 5.12: Competing instability among the spin modes. (a) The two primary peaks in Mathieu exponent vs k from the simultaneous modulation of a_0 and a_2 for $\bar{c}_0\tilde{n}_0 = 0.4\hbar\omega_z$, $\bar{c}_1\tilde{n}_0 = 0.05\hbar\omega_z$, $q = 0$, $\alpha_0 = 0.205$, $\omega_0 = 0.1\omega_z$, $\alpha_2 = 0.1$, and $\omega_2 = 0.3\omega_z$. The solid line is for a_0, and the dashed line is for a_2 modulations. (b) shows the spin-spin correlation functions $C_x(\rho)$ and $C_z(\rho)$. Fit-1 and Fit-2 are respectively the Eqs. (5.40) and (5.41). The numerical results in (b) are obtained by taking the average over ten realizations of noise.

The spin pattern is thus a combination of patterns with both wavelengths, as this is reflected in the radial transverse spin-spin correlation function,

$$C_{x,y}(\rho, t) = D(t)J_0(k_u^{(+)}\rho) + [1 - D(t)]J_0(\bar{k}_u^{(+)}\rho), \tag{5.40}$$

which is the sum of two Bessel functions, with $D(t)$ being a time-dependent amplitude and $k_u^{(+)}$ and $\bar{k}_u^{(+)}$ being the momenta of unstable mode for modulation frequencies ω_0 and ω_2. The longitudinal spin-spin correlation is given by

$$C_z(\rho, t) = J_0(k_u^{(+)}\rho)J_0(\bar{k}_u^{(+)}\rho). \tag{5.41}$$

We have plotted these functions in Fig. 5.12 (b).

5.10 Experimental considerations

Here, we briefly examine the experimental possibilities of our study. The emergent spin textures leading to PCVs can be observed as long as $|\bar{c}_1| \leq \bar{c}_0$ for which the spin mode dominates the instability dynamics. This condition is satisfied by spin-1 system of for ^{23}Na, where the ratio $\bar{c}_1/\bar{c}_0$ is 0.036 [89]. In a given atomic setup, Feshbach resonances are required to access different regimes of interaction strengths we consider, and in particular, independent control of a_0 and a_2 is needed. The latter has been proposed to achieve via combining magnetic and rf-field-induced Feshbach resonances [199]. Note that longitudinal and transverse spin-spin correlations are computed once the corresponding magnetizations are measured and demonstrated in Ref. [78].

5.11 Conclusion

In conclusion, we analyzed the density patterns and spin textures in a periodically driven Q2D spin-1 condensate for two initial states in polar phase, which revealed interesting dynamics; for instance, a gas of polar core vortices and antivortices is seen, with its density determined by the momentum of the unstable spin mode. We see competition between density patterns and spin-mixing dynamics, which can be controlled by tuning the interaction strengths, quadratic Zeeman field, or driving frequencies. When spin-mixing dynamics dominate, the spin-spin correlation functions exhibit a Bessel function behaviour as a function of the relative distance. Otherwise, they decay exponentially with a correlation length of the order of a spin healing length. Modulating both scattering lengths creates an exciting scenario of competing instabilities among density or spin modes. It produces the superposition of density patterns or spin correlation functions of two distinct wavelengths.

Chapter 6

Pattern formation in driven spin-1 BEC in AFM phase

6.1 Introduction

The driven dynamics of a spinor condensate can depend critically on which scattering length is modulated and on the initial magnetic phase of the system. For instance, in the ferromagnetic phase, modulating the a_0 scattering length has no effect, whereas modulation of a_2 leads to dynamics similar to those observed in a driven scalar condensate. In contrast, a polar phase quasi-two-dimensional condensate a competition between density modulations and spin-mixing dynamics exists. When the latter dominates, this competition can lead to the formation of polar-core spin vortices. In general, the characteristic wavelengths of the patterns emerging during the driven dynamics can be predicted from the Bogoliubov spectrum of the condensate's initial state.

In this chapter, we investigate the response of a spin-1 Bose-Einstein condensate (BEC) in the antiferromagnetic (AFM) phase to periodic modulation of the s-wave scattering length. In a spin-1 condensate with antiferromagnetic interactions ($c_1 > 0$), the spin density minimized in the ground state of the system. When the quadratic Zeeman energy q is positive, the polar phase, where all atoms occupy the $m = 0$ component, is energetically favored. However, for $q < 0$, the condensate forms a coherent superposition of the $m = \pm 1$ components, realizing the AFM phase [89]. In the absence of a linear Zeeman shift, both the polar and AFM phases exhibit vanishing spin density across all spin components, but they are distinguished by the expectation value of the spin nematic tensor, $\mathcal{N}_{\nu\nu'} = (1/2)\langle f_\nu f_{\nu'} + f_{\nu'} f_\nu \rangle$, which exhibits anisotropy in the xy spin plane, perpendicular to the quantization axis [89, 171, 203]. As a result, the condensate shows spin-nematic order without magnetic ordering.

Similar nematic phases also appear in spin-1 lattice models [121, 131, 165], where the magnetization vanishes isotropically, but components of the spin-nematic tensor still break symmetry spontaneously. The AFM phase in a spin-1 BEC supports novel topological excitations, including half-quantum vortices [101, 156, 157] and nematic spin vortices [106, 173, 181]. Quenching the quadratic Zeeman shift q from positive to negative across the phase boundary has been shown to induce such excitations [17, 172, 185, 186].

In this work, we examine the formation of density and spin-density patterns in quasi-one-dimensional (Q1D) and quasi-two-dimensional (Q2D) homogeneous systems. Our findings reveal that the system's response depends on the driving frequency. When the frequency is below the energy gap of the transverse spin branch in the Bogoliubov spectrum, the dynamics resemble those of a two-component BEC without coherent coupling between components [39]. However, when the driving frequency exceeds this gap, the response becomes anisotropic in the xy spin space, reflecting the broken spin symmetry of the AFM phase. We analyze in detail the spin textures formed in both Q1D and Q2D systems and discuss the distinct features of the emergent patterns.

6.2 Anti-ferromagnetic phase

In this section, we briefly discuss the properties of the AFM state in a spin-1 homogeneous BEC. In the absence of linear Zeeman shift p, the order parameter of the condensate in the antiferromagnetic (AFM) phase is given as [89],

$$\psi_{AFM} = \sqrt{\frac{n}{2}} \begin{pmatrix} 1 \\ 0 \\ e^{i\phi} \end{pmatrix}, \tag{6.1}$$

where n is the condensate density. Here, the bosons are in a coherent superposition of $m = \pm 1$ states, while the population in the $m = 0$ state remains zero. Energy of the system is independent of the phase difference between the $m = \pm 1$ states, and choosing a particular value of ϕ breaks the symmetry of the system in the F_x-F_y spin-space. This can be seen from the expectation value of the spin nematic tensor given by,

$$\mathcal{N}_{\nu\nu'} = \frac{1}{2} \sum_{mm'} \psi_m^* \left(f_\nu f_{\nu'} + f_{\nu'} f_\nu \right) \psi_{m'}, \tag{6.2}$$

where f_ν are the spin-1 matrices defined in Sec. 2.6. $\mathcal{N}_{\nu\nu'}$ describes the fluctuation of the spin-components. The anisotropy of the AFM phase can be seen from the tensor components $\mathcal{N}_{xx} = \cos^2(\phi/2)$ and $\mathcal{N}_{yy} = \sin^2(\phi/2)$, which indicate the spin-fluctuation in xy spin space. Another way to understand the anisotropy is by noting that $\boldsymbol{\xi} = (1, 0, 1)/\sqrt{2}$ is an eigenvector of spin matrix f_y with eigenvalue zero, while $\boldsymbol{\xi} = (1, 0, -1)/\sqrt{2}$ is an eigenvector of f_x with the same eigenvalue. Thus, these states exhibit anisotropic properties in the xy plane despite both having null spin vector $\langle \boldsymbol{f} \rangle$. We can also define the spin nematic director $\hat{\boldsymbol{d}} = (d_x, d_y, d_z) = (\sin\phi, -\cos\phi, 0)$ [181] which characterises the AFM phase. In the polar phase,

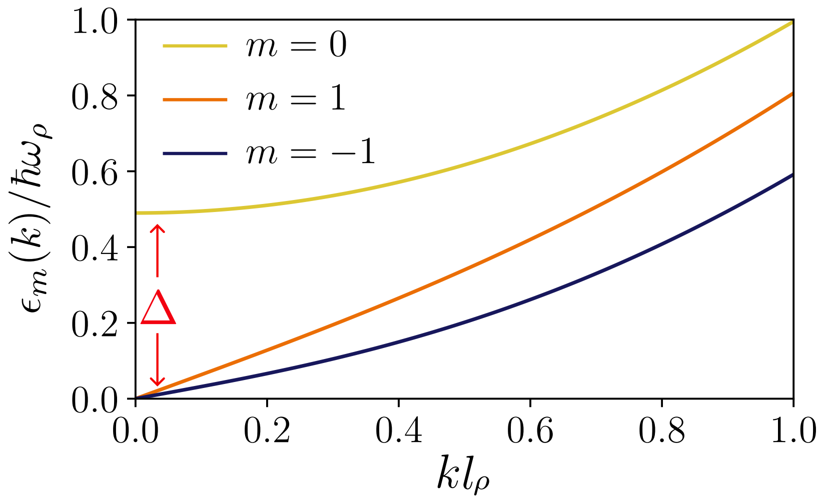

FIGURE 6.1: The Bogoliubov excitation spectra of homogeneous AFM condensate. Here, $c_0 > c_1$, and the gap of the spin-mode is indicated by Δ.

the director points along the F_z direction, whereas for the AFM phase, it spontaneously chooses a direction in the F_x- F_y plane.

Now we shall look at the elementary excitation of the homogeneous spin-1 BEC in the AFM phase. The excitation spectrum contains three branches. The first two are the gapless density and spin branches, given respectively by,

$$\epsilon_1(k) = \sqrt{E_k(E_k + 2c_0 n)}, \tag{6.3}$$

$$\epsilon_{-1}(k) = \sqrt{E_k(E_k + 2c_1 n)}, \tag{6.4}$$

where $E_k = \hbar^2 k^2/2M$, and c_0 and c_1 are the spin-independent and -dependent coefficients of interactions, respectively. These modes describe coupled in-phase and out-of-phase excitations in $m = \pm 1$ components. The density mode excitation creates patterns in the total density, and the spin mode excitation creates patterns in the F_z spin density. The third branch is gapped when the quadratic Zeeman energy q is negative, given by,

$$\epsilon_0(k) = \sqrt{(E_k - q)(E_k - q + 2c_1 n)}. \tag{6.5}$$

These modes describe anisotropic spin-excitation in xy-spin space (transverse spin-density). If the phase between the spin-components $\phi = 0$ ($\phi = \pi/2$), the excitation are spin-wave in F_x (F_y) spin-density. The three branches are plotted in Fig. (6.1), where $\Delta = \sqrt{q(q - 2c_1 n)}$ denotes the gap of the spin mode. By inspecting the modes, we see that the AFM phase is stable only when $c_1 > 0$ and $c_0 > 0$.

In the absence of an external magnetic field, i.e. when $q = p = 0$, the polar and AFM phases are degenerate, and can be interconverted by a spin space rotation [89].

6.2.1 Quasi-one- and quasi-two-dimensional systems

As we have discussed in Sec. 2.4, the Q1D system is obtained by applying a strong radial confinement which freezes its motional freedom along the confined plane, while being homogeneous along the third, unconfined direction. Similarly, the Q2D system is obtained by applying a strong external confinement along the z-direction while homogeneous in the xy-plane. In this case, we assume that along the tightly trapped direction, atoms in all three spin states are in the ground state of the harmonic trap, and remain so during the dynamics.

The spectra of excitations of the Q1D (Q2D) condensates, along the untrapped direction, have the same form as given in Eqs. (6.3)-(6.5), except we replace the interaction coefficients with their 1D (2D) counterparts given by,

$$c_{0,1}^{(1D)} = \frac{c_{0,1}}{2\pi l_\rho^2} \left(c_{0,1}^{(2D)} = \frac{c_{0,1}}{\sqrt{2\pi} l_z} \right), \tag{6.6}$$

and 3D density n with the uniform 1D (2D) density. Here $l_\rho = \sqrt{\hbar/M\omega_\rho}$ ($l_z = \sqrt{\hbar/M\omega_z}$) denotes the characteristic length of the radial (longitudinal) harmonic trap with frequency ω_ρ (ω_z).

The validity of the Q1D approximation under periodic driving has been discussed for a spin-0 condensate in chapter 4, where we found that the approximation remains valid as long as the interaction energies are weak compared to the trap energy and the driving frequencies are not resonant with radial (in Q1D) modes.

6.3 Periodic driving of the scattering length

In this section, we discuss the stability of the uniform AFM condensate under the periodic driving of the s-wave scattering length. We only consider the periodic driving of scattering length a_0, which is given as,

$$a_0(t) = \bar{a}_0[1 + 2\alpha_0 \cos(2\omega_0 t)], \tag{6.7}$$

while a_2 is assumed to be constant in time. The results, however, remain qualitatively the same under a_2 modulations. Under the modulation of a_0, both c_0 and c_1 interaction coefficient evolve periodically as given by,

$$c_0 = \bar{c}_0 + \frac{2\alpha_0 \bar{g}_0}{3} \cos(2\omega_0 t), \quad c_1 = \bar{c}_1 - \frac{2\alpha_0 \bar{g}_0}{3} \cos(2\omega_0 t), \tag{6.8}$$

where $\bar{g}_{0,2} = 4\pi\hbar^2 a_{0,2}/2M$ and $\bar{c}_{0,1}$ are the mean-value of the interaction coefficients.

The response of the system to the modulation can be understood using a linear stability analysis of the homogeneous AFM state. The uniform solution of the Gross-Pitaevskii equation (GPE) [Eqs. (2.49)-(2.51)] under the periodic driving can be obtained as,

$$\psi_0(t) = \sqrt{\frac{n_H}{2}} \begin{pmatrix} 1 \\ 0 \\ 1 \end{pmatrix} e^{i\theta(t)}, \tag{6.9}$$

where the phase $\theta(t)$ is time dependent. Here, n_H denotes the constant density, and we have chosen $\phi = 0$. The overall phase of the uniform state evolves as $\theta(t) = \mu t + (\alpha_0 \bar{g}_0 n_H / 3\omega_0) \sin(2\omega_0 t)$, where $\mu = q + \bar{c}_0 n_H$ is the chemical potential of the condensate in the absence of the periodic driving.

We then consider a perturbed solution of the form $\psi = [\psi_0(0) + \boldsymbol{w}(t) \cos(\boldsymbol{k} \cdot \boldsymbol{r})] e^{i\theta(t)}$, where the amplitude of the perturbation is given by,

$$\boldsymbol{w}(t) = \begin{pmatrix} w_1(t) \\ w_0(t) \\ w_{-1}(t) \end{pmatrix} = \begin{pmatrix} u_1(t) \\ u_0(t) \\ u_{-1}(t) \end{pmatrix} + i \begin{pmatrix} v_1(t) \\ v_0(t) \\ v_{-1}(t) \end{pmatrix}, \tag{6.10}$$

with u_m, v_m being real numbers. The equation of motion for the $\boldsymbol{w}(t)$ is obtained by inserting the perturbed solution in the coupled GPE and linearizing in u_m, v_m. We obtain the following second-order differential equation for the dynamics of u_0,

$$\hbar^2 \frac{d^2 u_0}{dt^2} + \left[\epsilon_0^2(k) + \frac{4\alpha_0 \bar{g}_0 n_H (E_k - q)}{3} \cos(2\omega_0 t) \right] u_0 = 0. \tag{6.11}$$

This equation governs the excitation in the $m = 0$ component, which is uncoupled from the other components at linear order. We get two more equations which describe the excitations in $m = \pm 1$,

$$\hbar^2 \frac{d^2 u_\pm}{dt^2} + \left[\epsilon_{\pm 1}^2(k) + \frac{4\alpha_0 \bar{g}_0 n_H E_k}{3} \cos(2\omega_0 t) \right] u_\pm = 0, \tag{6.12}$$

where $u_\pm = u_1 \pm u_{-1}$. We can see that the dynamics of $m = \pm 1$ components are coupled.

Eqs. (6.11) and (6.12) are Mathieu equations [109]. Floquet theory states that these equations have solutions of the form $u_{0,\pm} = p_{0,\pm}(t) e^{\sigma_{0,\pm} t}$ where $p_{0,\pm}(t + \pi/\omega_0)$ is a periodic function, and $\sigma_{0,\pm}$ is the complex Floquet exponent. The instability of the uniform solution occurs is $\mathrm{Re}\{\sigma_{0,\pm}\} > 0$ at any value of momenta k, as it leads to the exponential growth of the initially small perturbation. When the driving strength is vanishingly small ($\alpha_0 \to 0$), the instability occur if the momenta k of the perturbation satisfy the condition

$$\epsilon_{0,\pm 1}(k) = j\hbar\omega_0, \tag{6.13}$$

where $j = 1, 2, \ldots$. The primary resonance, with the largest $\mathrm{Re}\{\sigma_{0,\pm}\}$, occur at $j = 1$.

As we can see, three primary resonances occur for the spin-1 condensate when the interactions are periodically driven. The first two resonances results in the excitation in $m = \pm 1$ spin states, with $k_u^{(+)}$ and $k_u^{(-)}$ being the momenta resulting instability. The value of the momenta of unstable modes is given by,

$$k_u^{(+)} = \left[\frac{2M}{\hbar^2}\left(\sqrt{\bar{c}_0^2 n_H^2 + \hbar^2\omega_0^2} - \bar{c}_0 n_H\right)\right]^{1/2} \tag{6.14}$$

$$k_u^{(-)} = \left[\frac{2M}{\hbar^2}\left(\sqrt{\bar{c}_1^2 n_H^2 + \hbar^2\omega_0^2} - \bar{c}_1 n_H\right)\right]^{1/2}. \tag{6.15}$$

This instability can be understood as the parametric excitation of the Bogoliubov modes in the gapless density and longitudinal spin branches of the AFM phase under driving. The instability of the density modes induces total density patterns with wavelength $2\pi/k_u^{(+)}$, and that of the spin modes induces f_z spin patterns with wavelength $2\pi/k_u^{(-)}$.

The third resonance results in excitation in the $m = 0$ state with momentum $k_u^{(0)}$ given by,

$$k_u^{(0)} = \left[\frac{2M}{\hbar^2}\left(\sqrt{\bar{c}_1^2 n_H^2 + \hbar^2\omega_0^2} - \bar{c}_1 n_H + q\right)\right]^{1/2}. \tag{6.16}$$

This instability occurs due to the parametric excitation of the mode from the gapped transverse spin branch $\epsilon_0(k)$, resulting in the formation of a spin-density pattern in the xy-spin space. The direction of the transverse spin-density pattern vector depends on the spin nematic order of the initial system. It will be perpendicular to the nematic director $\hat{\boldsymbol{d}}$. Thus, if $\phi = 0$, we see pattern formation in the F_x spin density, and if $\phi = \pi/2$, it will be along the F_y spin density. The transverse spin mode instability only occurs when the driving frequency is greater than the spin branch gap, i.e. $\hbar\omega_0 > \Delta$.

The growth rate of the unstable modes is determined by the real part of the Floquet exponents $\sigma_{\pm,0}$. For the most unstable density modes, the exponent is obtained as [122],

$$\sigma_+ = \frac{\alpha_0 \bar{g}_0}{3\hbar^2\omega_0}\left(\sqrt{\bar{c}_0^2 n_H^2 + \hbar^2\omega_0^2} - \bar{c}_0 n_H\right), \tag{6.17}$$

and for the most unstable spin-modes,

$$\sigma_- = \sigma_0 = \frac{\alpha_0 \bar{g}_0}{3\hbar^2\omega_0}\left(\sqrt{\bar{c}_1^2 n_H^2 + \hbar^2\omega_0^2} - \bar{c}_1 n_H\right). \tag{6.18}$$

The Floquet exponents of unstable longitudinal and transverse spin modes are equal. But their momenta of the unstable mode might differ, resulting in $F_\perp$ and F_z spin density patterns with different wavelengths. While three primary resonances exist for the spinor condensate, the dynamics will be dominated by density pattern formation if $\sigma_+ \gg \sigma_-$, which occurs when $c_0 \ll c_1$. Similarly, spin-density pattern formation dominates when $\sigma_+ \ll \sigma_-$, i.e.

when $c_0 \gg c_1$. This scenario is similar to what we have seen from the case of polar phase, where a larger spin-independent coefficient leads to dominant spin-dynamics, while a larger spin-dependent coefficient leads to dominant density pattern (Faraday wave) formation.

The linear stability analysis predictions are valid when fluctuations about the initial states are small. Therefore, in the presence of an instability, it only captures the initial stages of the dynamics.

6.4 GPE simulation

We study the driven dynamics in Q1D and Q2D geometry by solving the spin-1 GPE equations numerically. To simulate the quantum fluctuations that trigger the pattern formation, we add random noise to the initial AFM state under the TWA prescription [12] as $\psi(\boldsymbol{r},0) = \zeta_{AFM} + \delta\psi(\boldsymbol{r})$, where the fluctuations about the mean field is given by

$$\begin{aligned}
\delta\psi_1(\boldsymbol{r},0) &= \sum_k [\beta_k^{(1)}\bar{u}_{k,1} + \beta_k^{(-1)}\bar{u}_{k,-1}]e^{i\boldsymbol{k}\cdot\boldsymbol{r}} + [\beta_k^{(1)}\bar{v}_{k,1} + \beta_k^{(-1)}\bar{v}_{k,-1}]^* e^{-i\boldsymbol{k}\cdot\boldsymbol{r}} \\
\delta\psi_0(\boldsymbol{r},0) &= \sum_k \beta_k^{(0)}\bar{u}_{k,0}e^{i\boldsymbol{k}\cdot\boldsymbol{r}} + (\beta_k^{(0)})^*\bar{v}_{k,0}e^{-i\boldsymbol{k}\cdot\boldsymbol{r}} \\
\delta\psi_{-1}(\boldsymbol{r},0) &= \sum_k [\beta_k^{(1)}\bar{u}_{k,1} - \beta_k^{(-1)}\bar{u}_{k,-1}]e^{i\boldsymbol{k}\cdot\boldsymbol{r}} + [\beta_k^{(1)}\bar{v}_{k,1} - \beta_k^{(-1)}\bar{v}_{k,-1}]^* e^{-i\boldsymbol{k}\cdot\boldsymbol{r}},
\end{aligned} \tag{6.19}$$

where $\beta_k^{(m)}$ are independent Gaussian random variables with mean zero and variance 1/2. The coefficients are given as [89],

$$\bar{u}_{k,1} = \sqrt{\frac{E_k + \bar{c}_0 n_H + \epsilon_1(k)}{4\epsilon_1(k)}} \tag{6.20}$$

$$\bar{u}_{k,0} = \sqrt{\frac{E_k - q + \bar{c}_1 n_H + \epsilon_0(k)}{2\epsilon_0(k)}} \tag{6.21}$$

$$\bar{u}_{k,-1} = \sqrt{\frac{E_k + \bar{c}_1 n_H + \epsilon_{-1}(k)}{4\epsilon_{-1}(k)}}, \tag{6.22}$$

and $\bar{v}_{k,m} = \sqrt{\bar{u}_{k,m}^2 - 1}$. Thus, the noise present in $m = \pm 1$ components is correlated. The results remain qualitatively the same if the noise is a uniform random variable between $\pm\epsilon$ for $\epsilon \ll 1$.

In the rest of the chapter, we analyze the driven dynamics of spin-1 BEC in an initial AFM state. Here, we assume spin-independent and dependent coefficients of the same orders of magnitude, thereby observing both density and spin-density pattern formation simultaneously under periodic driving. However, in the experimentally realized system of antiferromagnetic ^{23}Na condensate [11, 154], the spin-dependent interaction is about 3% of the spin-independent interaction. In this case, we assume that the spin-pattern formation dominates, whereas the total density of the condensate remains nearly constant.

6.5 Driven Q1D BEC

In this section, we look at the driven dynamics of Q1D BEC in an initial AFM state. The evolution of the Q1D spinor order-parameter $\tilde{\psi}(z,t)$ is follows the coupled GPE,

$$i\hbar\frac{\partial\tilde{\psi}_1}{\partial t} = \left[-\frac{\hbar^2}{2M}\frac{\partial^2}{\partial z^2} - p + q + c_0^{(1D)}n^{(1D)} + c_1^{(1D)}F_z^{(1D)}\right]\tilde{\psi}_1 + \frac{c_1^{(1D)}}{\sqrt{2}}F_-^{(1D)}\tilde{\psi}_0 \tag{6.23}$$

$$i\hbar\frac{\partial\tilde{\psi}_0}{\partial t} = \left[-\frac{\hbar^2}{2M}\frac{\partial^2}{\partial z^2} + c_0^{(1D)}n^{(1D)}\right]\tilde{\psi}_0 + \frac{c_1^{(1D)}}{\sqrt{2}}\left[F_+^{(1D)}\tilde{\psi}_1 + F_-^{(1D)}\tilde{\psi}_{-1}\right] \tag{6.24}$$

$$i\hbar\frac{\partial\tilde{\psi}_{-1}}{\partial t} = \left[-\frac{\hbar^2}{2M}\frac{\partial^2}{\partial z^2} + p + q + c_0^{(1D)}n^{(1D)} - c_1^{(1D)}F_z^{(1D)}\right]\tilde{\psi}_{-1} + \frac{c_1^{(1D)}}{\sqrt{2}}F_+^{(1D)}\tilde{\psi}_0. \tag{6.25}$$

The Q1D interaction coefficients $c_{0,1}^{(1D)}$ are defined in Eq. (6.6), and $n^{(1D)} = n_1^{(1D)} + n_0^{(1D)} + n_{-1}^{(1D)}$ the denotes the linear density of condensate, with $n_m^{(1D)} = |\tilde{\psi}_m|^2$ being the density of spin state m. The spin density components are given as $F_z^{(1D)} = |\tilde{\psi}_1|^2 - |\tilde{\psi}_{-1}|^2$, and $F_+^{(1D)} = (F_-^{(1D)})^* = \sqrt{2}(\tilde{\psi}_1\tilde{\psi}_0^* + \tilde{\psi}_0^*\tilde{\psi}_{-1})$. The transverse spin-density vectors is obtained from $F_x^{(1D)} = \mathrm{Re}\left\{F_+^{(1D)}\right\}$ and $F_y^{(1D)} = \mathrm{Im}\{F_+^{(1D)}\}$.

Under the periodic driving of scattering length a_0 as specified in Eq. (6.7), the interactions coefficients evolve as,

$$\begin{aligned} c_0^{(1D)} &= \bar{c}_0^{(1D)} + \frac{\alpha_0\bar{g}_0}{3\pi l_\rho}\cos(2\omega_0 t) \\ c_1^{(1D)} &= \bar{c}_1^{(1D)} - \frac{\alpha_0\bar{g}_0}{3\pi l_\rho}\cos(2\omega_0 t). \end{aligned} \tag{6.26}$$

In the following, we look at the driven dynamics of the condensate by solving the GPEs (6.23)-(6.25). Here we add an initial noise to the system, which triggers the growth of instabilities, as discussed in Sec. 6.4.

6.5.1 Modulation frequency less than spin-mode gap

We first look at the case when a_0 is driven with frequency $\hbar\omega_0 < \Delta_{1D}$, where $\Delta_{1D} = \sqrt{q(q - \bar{c}_1^{(1D)}n_H^{(1D)})}$ denotes the gap of Q1D transverse spin branch ϵ_0, with $n_H^{(1D)}$ being uniform linear density of the condensate. In this case, the primary instabilities only occur in the

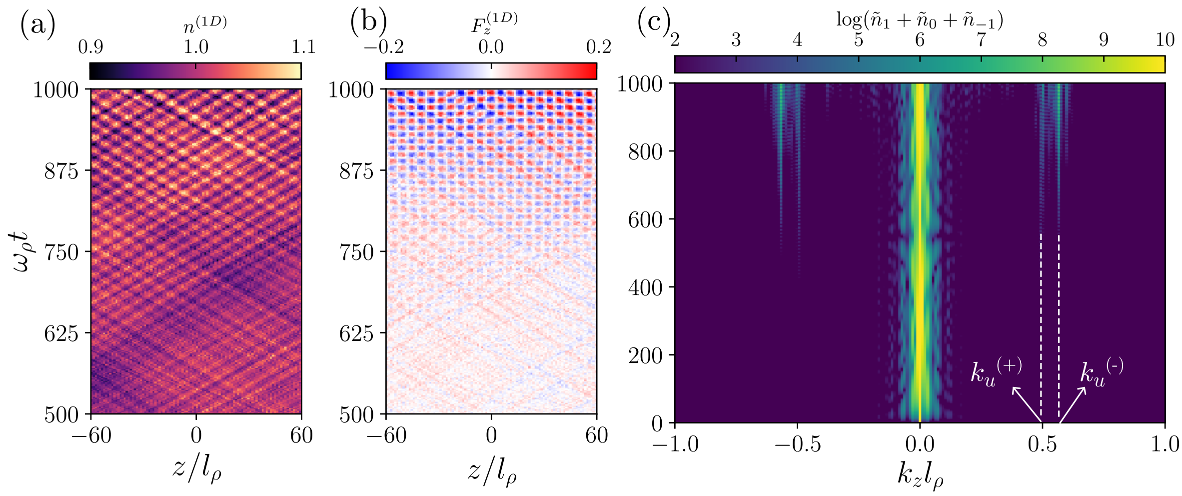

FIGURE 6.2: *Driven Q1D condensate* ($\hbar\omega_0 < \Delta_{1D}$): The dynamics of the (a) total density $n^{(1D)}(z,t)$ and (b) spin-density $F_z^{(1D)}(z,t)$. (c) The dynamics of the momentum state population of the condensate. The frequency and amplitude of the driving of scattering length a_0 are $\omega_0 = 0.3\omega_\rho$ and $\alpha_0 = 0.4$ respectively. The other parameters are $\bar{c}_0^{(1D)} n_{1D} = 0.3\hbar\omega_\rho$, $\bar{c}_1^{(1D)} n_H^{(1D)} = 0.2\hbar\omega_\rho$, $q = -0.3\hbar\omega_\rho$, and $p = 0$.

gapless branches $\epsilon_{\pm 1}$, whereas the modes in the transverse spin branch ϵ_0 are not unstable. As a result, the $m = 0$ population remains close to its initial value of zero.

The dynamics of the total density $n_1^{(1D)} + n_{-1}^{(1D)}$ and spin-density $n_1^{(1D)} - n_{-1}^{(1D)}$ is given in Fig. 6.2 (a),(b). Here we see the spontaneous emergence of patterns in both quantities due to the parametric instability of the Bogoliubov modes. In the driven Q1D condensate, the density and spin density patterns arising are sinusoidal, with wavelengths $\lambda_d \sim 2\pi/k_u^{(+)}$ and $\lambda_s \sim 2\pi/k_u^{(-)}$, respectively. The momenta of the unstable mode can also be observed from the momentum space density shown in Fig. 6.2 (c), where $\tilde{n}_m$ denotes the momentum space density of the spin state m. The peak near $k_z = 0$ corresponds to the condensate mode, and two new peaks emerge at $\pm k_u^{(\pm)}$ under periodic driving.

When the AFM condensate is driven at a frequency below the spin-mode gap, the resulting dynamics resembles that of a driven binary condensate in the miscible phase. Such parametric excitation and pattern formation in binary condensates have been observed experimentally in Ref. [39]. This analogy holds in the absence of coherent coupling between the two components of the binary condensate. The phase difference between the two components does not influence the dynamics when the driving frequency remains below the transverse spin-mode gap.

6.5.2 Modulation frequency greater than the spin-mode gap

When the driving frequency $\hbar\omega_0 > \Delta_{1D}$, transverse spin-mode also become unstable, along with the density mode and the longitudinal spin-mode. Therefore, under the periodic driving, we observe a transfer of population to the $m = 0$ mode [Fig.6.3(a)]. The population growth

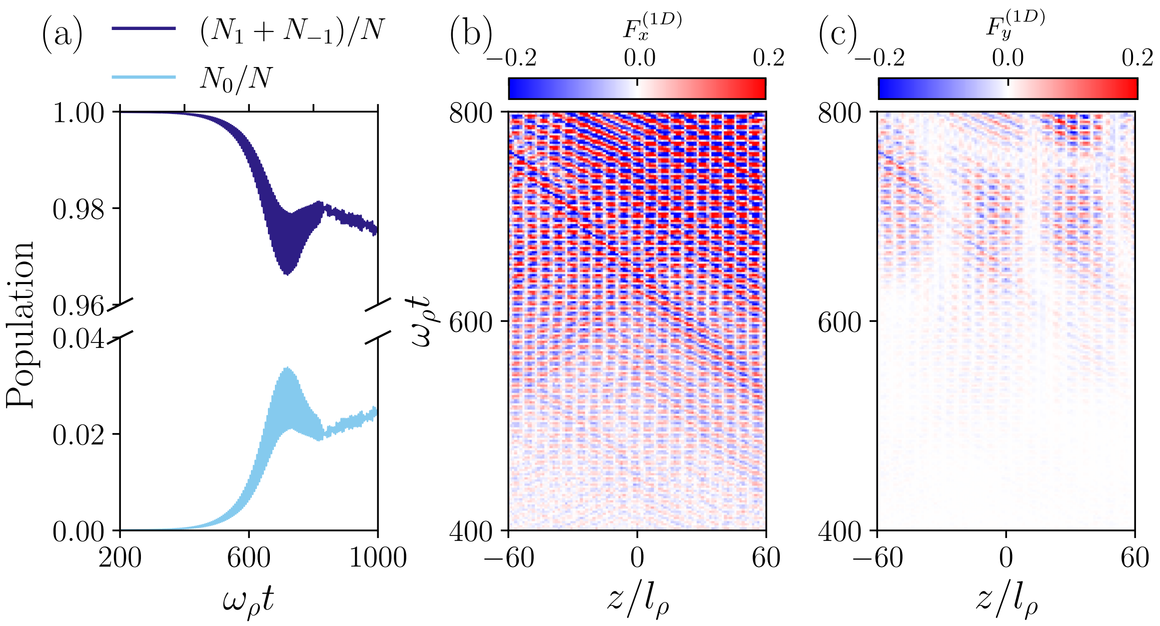

FIGURE 6.3: *Driven Q1D condensate* ($\hbar\omega_0 > \Delta_{1D}$): Dynamics of (a) spin state population under periodic driving of scattering length a_0. Dynamics of transverse spin-densities (b) $F_x^{(1D)}(z,t)$ and (c) $F_y^{(1D)}(z,t)$. The frequency and amplitude of the driving are $\omega_0 = 0.45\omega_\rho$ and $\alpha_0 = 0.3$ respectively. The other parameters are given as $\bar{c}_0^{(1D)} n_H^{(1D)} = 0.3\hbar\omega_\rho$, $\bar{c}_1^{(1D)} n_H^{(1D)} = 0.2\hbar\omega_\rho$, $q = -0.3\hbar\omega_\rho$, and $p = 0$.

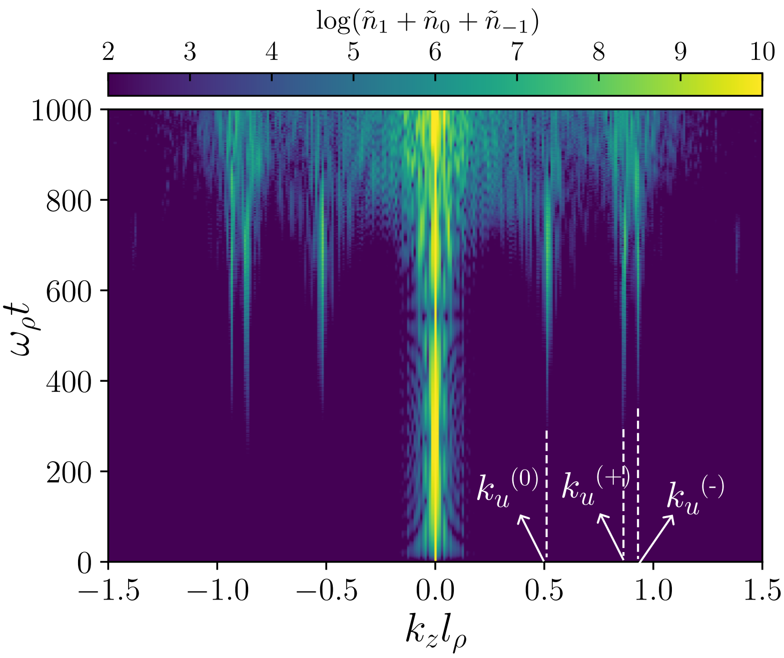

FIGURE 6.4: *Driven Q1D condensate* ($\hbar\omega_0 > \Delta_{1D}$): The dynamics of the momentum state population of the condensate under periodic driving of scattering length a_0. The frequency and amplitude of the driving are $\omega_0 = 0.45\omega_\rho$ and $\alpha_0 = 0.3$ respectively. The other parameters are $\bar{c}_0^{(1D)} n_H^{(1D)} = 0.3\hbar\omega_\rho$, $\bar{c}_1^{(1D)} n_H^{(1D)} = 0.2\hbar\omega_\rho$, $q = -0.3\hbar\omega_\rho$, and $p = 0$.

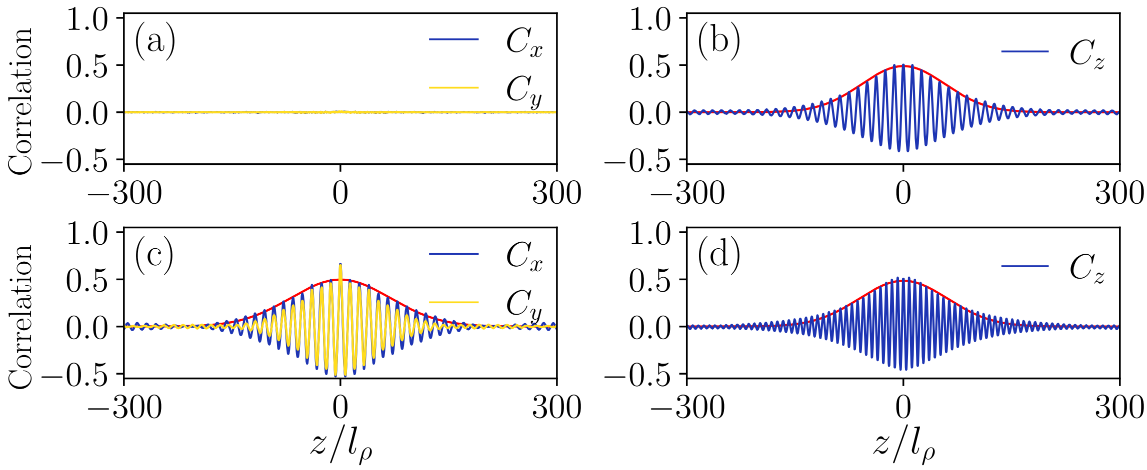

FIGURE 6.5: Q1D spin-spin correlations of for driving frequency [(a),(b)] $\omega_0 = 0.2\omega_\rho$ ($\hbar\omega_0 < \Delta_{1D}$) and [(c),(d)] $\omega_0 = 0.4\omega_\rho$ ($\hbar\omega_0 > \Delta_{1D}$). Here we show [(a),(c)] C_x and C_y and [(b),(d)] C_z. The solid red line is obtained from a Gaussian envelope fit. The correlation is time-averaged from [(a),(c)] $\omega_\rho t_i = 300$ to $\omega_\rho t_f = 650$ and [(b),(d)] $\omega_\rho t_i = 200$ to $\omega_\rho t_f = 600$. We further take an average over 40 realizations of TWA noises. The other parameters are $\bar{c}_0^{(1D)} n_H^{(1D)} = 0.1\hbar\omega_\rho$, $\bar{c}_1^{(1D)} n_H^{(1D)} = 0.1\hbar\omega_\rho$, $q = -0.2\hbar\omega_\rho$, $p = 0$, and $\alpha_0 = 0.45$. The central peak, $C_\alpha(z = 0) = 1$ is removed for clarity.

is initially exponential, with the rate determined by the Floquet exponent σ_0 [see Eq. (6.18)]. We can also see an additional peak at $k_u^{(0)}$ in the momentum space densities of the condensate [Fig. 6.4], which arises from the transfer of particles occurring to the $m = 0$ spin state. Here, we define the total population for spin state m as,

$$N_m = \int dz \left|\tilde{\psi}_m\right|^2, \tag{6.27}$$

and $N = \sum_{m=-1}^{1} N_m$ denotes the total population. Due to the conservation of total longitudinal magnetization, we have $N_1 = N_{-1}$.

Along with the spin transfer to the $m = 0$ spin-state, we can also see formation of spin-texture in the transverse spin components [Fig.6.3 (b)]. The initial phase difference between the $m = \pm 1$ components plays a significant role here, as it determines the orientation of the transverse spin-density vector $\boldsymbol{F}_\perp$. In our simulations, we chose the initial phase $\phi = 0$, causing the spin-density pattern formation along F_x. The wavelength of the transverse spin-density patterns is $\lambda_{s\perp} \sim 2\pi/k_u^{(+)}$. We can also see weaker patterns forming in the F_y spin component as well [Fig.6.3 (c)], and we attribute this to the fluctuations of the nematic order along the condensate.

6.5.3 Spin-spin correlation in quasi-1D condensate

We analyse the spin-texture using the 1D spin-spin correlation defined by,

$$C_\nu(z) = \frac{\int dz' F_\nu^{(1D)}(\boldsymbol{r}')F_\nu^{(1D)}(z'+z)}{\int dz'(F_\nu^{(2D)}(z'))^2}, \quad \nu \in \{x, y, z\}. \tag{6.28}$$

which is shown in Fig. 6.5. Here, the spin-correlation is averaged over time period between t_i and t_f, during which the pattern formation is prominent. It is further averaged over 40 different realization of initial TWA noise. As we can see, when $\omega_0 < \Delta$, the spin-texture in the $F_{x,y}$ spin-densities exhibit zero correlation, whereas that in the F_z spin-density exhibit a sinusoidal correlation with wavelength $2\pi/k_u^{(-)}$ and an overall Gaussian envelope. The width of the Gaussian envelope is found to be related to the driving amplitude α_0, with smaller α_0 leading to wider envelope. When the driving frequency $\omega_0 > \Delta$, we see such oscillation in $C_{x,y}$ as well. The C_y has a narrower envelope, due to the choice of the initial phase difference ϕ between the $m = \pm 1$ spin-components.

6.6 Driven quasi-2D condensate

In this section, we look at the dynamics of the driven AFM condensate in Q2D geometry. The evolution of 2D order-parameter $\bar{\psi}(x, y, t)$ is given by the following GPE,

$$i\hbar\frac{\partial\bar{\psi}_1}{\partial t} = \left[-\frac{\hbar^2\nabla_{xy}^2}{2M} - p + q + c_0^{(2D)}n^{(2D)} + c_1^{(2D)}F_z^{(2D)}\right]\bar{\psi}_1 + \frac{c_1^{(2D)}}{\sqrt{2}}F_-^{(2D)}\bar{\psi}_0 \tag{6.29}$$

$$i\hbar\frac{\partial\bar{\psi}_0}{\partial t} = \left[-\frac{\hbar^2\nabla_{xy}^2}{2M} + c_0^{(2D)}n^{(2D)}\right]\bar{\psi}_0 + \frac{c_1^{(2D)}}{\sqrt{2}}\left[F_+^{(2D)}\bar{\psi}_1 + F_-^{(2D)}\bar{\psi}_{-1}\right] \tag{6.30}$$

$$i\hbar\frac{\partial\bar{\psi}_{-1}}{\partial t} = \left[-\frac{\hbar^2\nabla_{xy}^2}{2M} + p + q + c_0^{(2D)}n^{(2D)} - c_1^{(2D)}F_z^{(2D)}\right]\bar{\psi}_{-1} + \frac{c_1^{(2D)}}{\sqrt{2}}F_+^{(2D)}\bar{\psi}_0. \tag{6.31}$$

The Q2D interaction coefficients are defined in Eq.(6.6), and the $n^{(2D)} = \sum_m |\bar{\psi}_m|^2$ denotes the 2D density of the system. We also have the 2D spin-density component $F_z^{(2D)} = |\bar{\psi}_1|^2 - |\bar{\psi}_{-1}|^2$, and the transverse components $F_x^{(2D)} = \mathrm{Re}\left\{F_+^{(2D)}\right\}$ and $F_y^{(2D)} = \mathrm{Im}\{F_+^{(2D)}\}$, where $F_+^{(2D)} = (F_-^{(2D)})^* = \sqrt{2}(\bar{\psi}_1\bar{\psi}_0^* + \bar{\psi}_0^*\bar{\psi}_{-1})$.

The initial dynamics of the system under periodic driving can be understood from the linear stability analysis in Sec. 6.3. When the driving frequency less than the Q2D transverse spin-mode gap, i.e. $\hbar\omega_0 < \Delta_{2D} = \sqrt{q(q + c_1^{(2D)}n_H^{(2D)})}$, only the density mode and F_z spin-modes are unstable, creating patterns in $n_1^{(2D)} \pm n_{-1}^{(2D)}$. When the driving frequency is greater than the gap, we observe transverse spin patterns as well. In the following, we discuss the numerical results for both cases.

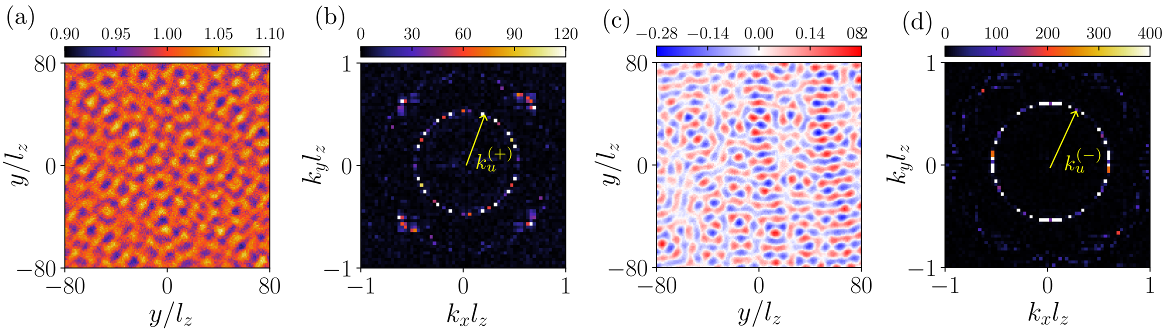

FIGURE 6.6: *Driven Q2D condensate* ($\hbar\omega_0 < \Delta_{2D}$): Total density $n_1^{(2D)} + n_{-1}^{(2D)}$ in the (a) real space and (b) Fourier space. $F_z^{(2D)}$ spin-density $n_1^{(2D)} - n_{-1}^{(2D)}$ in the (c) real space and (d) Fourier space. Here, $\bar{c}_0^{(2D)} n_H^{(2D)} = 0.3\hbar\omega_z$, $\bar{c}_1^{(2D)} n_H^{(2D)} = 0.2\hbar\omega_z$, and $q = -0.3\hbar\omega_z$, and $p = 0$. The driving parameters are $\alpha_0 = 0.4$ and $\omega_0 = 0.3\omega_z$, and the snapshot is taken at $\omega_z t = 980$.

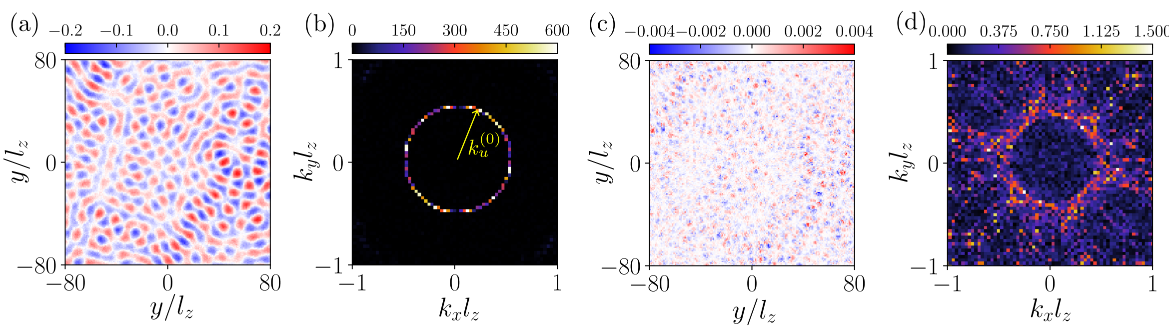

FIGURE 6.7: *Driven Q2D condensate* ($\hbar\omega_0 > \Delta_{2D}$): $F_x^{(2D)}$ spin-density in the (a) real and (b) Fourier space. $F_y^{(2D)}$ spin-density in the (c) real and (d) Fourier space. Here, $\bar{c}_0^{(2D)} n_H^{(2D)} = 0.3\hbar\omega_z$, $\bar{c}_1^{(2D)} n_H^{(2D)} = 0.2\hbar\omega_z$, and $q = -0.3\hbar\omega_z$, and $p = 0$. The driving parameters are $\alpha_0 = 0.4$ and $\omega_0 = 0.6\omega_z$, and the snapshot is taken at $\omega_z t = 600$.

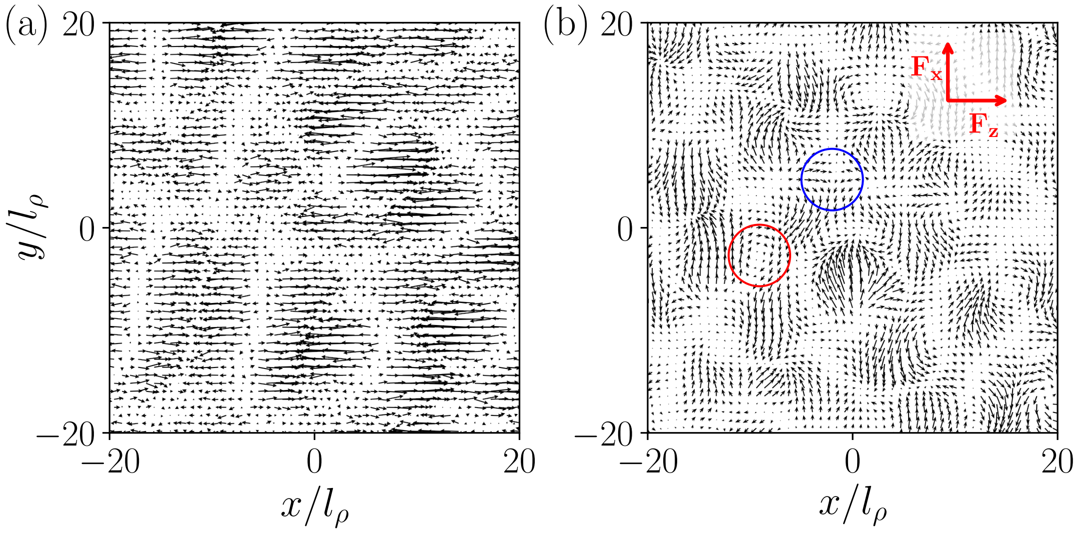

FIGURE 6.8: *Driven Q2D condensate* ($\hbar\omega_0 > \Delta_{2D}$): F_z-F_x spin-texture in the Q2D condensate formed under periodic driving of scattering length a_0, for frequencies (a) $\omega_0 = 0.2\omega_z$ (less than gap) at time $\omega_z t = 980$ and (b) $\omega_0 = 0.6\omega_z$ (greater than gap) at time $\omega_z t = 700$. A spin-vortex (red circle) and antivortex (blue circle) are marked in (b). Here, $\bar{c}_0^{(2D)} n_H^{(2D)} = 0.3\hbar\omega_z$, $\bar{c}_1^{(2D)} n_H^{(2D)} = 0.2\hbar\omega_z$, and $q = -0.3\hbar\omega_z$, and $p = 0$.

When the modulation frequency is less than Δ_{2D}, we do not see any population transfer to the $m = 0$ spin state, as expected. The pattern formed in the total density $n_1^{(2D)} + n_{-1}^{(2D)}$ and spin-density $n_1^{(2D)} - n_{-1}^{(2D)}$ are given in Fig. 6.6. The Fourier transforms of total density and spin density [Fig. 6.6 (b),(c)] reveal the wavelength of the unstable momenta of the density and the spin mode. In the 2D geometry, momenta of the unstable modes lie on a ring in the k_x-k_y space [162]. Again, this is analogous to the case of binary condensate in miscible phase, and the initial phase difference between the $m = \pm 1$ components does not play any role in this dynamics.

When the modulation frequency is greater than the gap Δ_{2D}, we see a population transfer to the $m = 0$ state, similar to what is observed for the Q1D geometry. Here, we see pattern in the total density and F_z spin-density similar to when the frequency was below the gap, along with pattern formation in the $\boldsymbol{F}_\perp^{(2D)}$ spin-component. The initial phase ϕ plays a crucial role in determining the orientation of the spin-density vector. Since we chose $\phi = 0$, the pattern formation occur in the $F_x^{(2D)}$ spin-density vector. We can see this in Fig. 6.7 (a) and (c), where the $F_x^{(2D)}$ and $F_y^{(2D)}$ patterns formed under the driving is given. The Fourier transform of the $F_x^{(2D)}$ also reveals the momenta of the unstable transverse spin-mode $k_u^{(0)}$. The vortices appearing are similar to those encountered for the driven system in the initial polar phase. However, the vortices in the polar phase arise due to the underlying phase vorticity in the $m = \pm 1$ components. For the spin-vortices arising in the AFM phase, such a clear relation

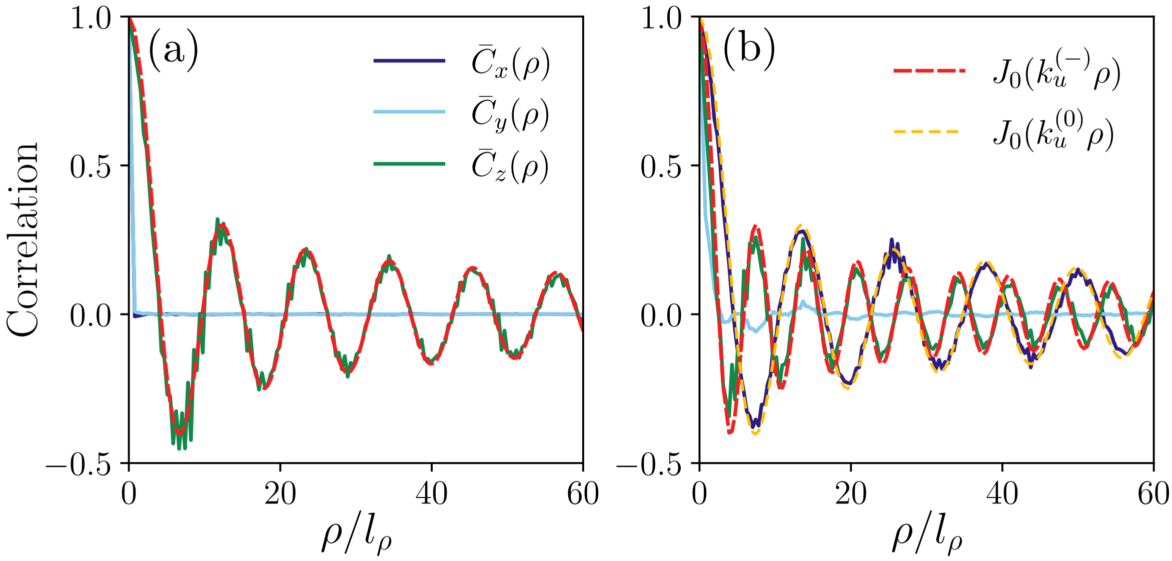

FIGURE 6.9: *Driven Q2D condensate* ($\hbar\omega_0 > \Delta_{2D}$): Radial spin-spin correlation in the Q2D condensate formed under periodic driving of scattering length a_0, for frequencies (a) $\omega_0 = 0.2\omega_z$ (less than gap) at time $\omega_z t = 980$ and (b) $\omega_0 = 0.6\omega_z$ (greater than gap) at time $\omega_z t = 700$. The dashed line denotes the zeroth Bessel function

between the phase vorticity and spin-vorticity could not be identified. Such excitations were also reported in Ref. [195], where anomalous spin-vortices were formed from an unstable ferrodark soliton in Q2D geometry.

We can also visualize the spin-pattern formation in Fig. 6.8, when $\hbar\omega_0 < \Delta_{2D}$ and $\hbar\omega_0 > \Delta_{2D}$, where we see that nature of the F_x-F_z spin-texture patterns are completely different. When $\hbar\omega_0 < \Delta_{2D}$, we see spin domain formations, with the spin-vector aligning along the $F_z^{(2D)}$ axis, whereas when $\hbar\omega_0 > \Delta_{2D}$, we see formation of vortices and antivortices in the spin-texture. Since the $F_y^{(2D)}$ remain close to zero, the spin-vectors are confined to the 2D $F_x^{(2D)}$-$F_z^{(2D)}$ space.

Finally, we also look at the spin-spin correlation function defined as,

$$C_\nu(\boldsymbol{r}) = \frac{\int d\boldsymbol{r}' F_\nu^{(2D)}(\boldsymbol{r}')F_\nu^{(2D)}(\boldsymbol{r}'+\boldsymbol{r})}{\int d\boldsymbol{r}' (F_\nu^{(2D)}(\boldsymbol{r}'))^2}, \quad \nu \in \{x, y, z\}. \tag{6.32}$$

This function is rotationally symmetric in the xy-plane; therefore, we look at the radial correlation function defined as $\bar{C}_\nu(\rho) = (1/2\pi)\int d\varphi C_\nu(\rho,\varphi)$. The radial correlation for the spin density patterns is a Bessel function, and as we can see in Fig. 6.9, the unstable momenta can also be determined from the argument of the Bessel function, as,

$$\bar{C}_z(\rho) \approx J_0(k_u^{(-)}\rho), \quad \bar{C}_x(\rho) \approx J_0(k_u^{(0)}\rho). \tag{6.33}$$

This Bessel function formation is expected as the patterns formed in the condensate are a superposition of many spin-waves travelling along random directions in the xy-plane, but with the same momenta [128].

6.7 a_2 Modulation

In this section, we briefly discuss the case of a_2 scattering length modulation. The Mathieu equations, in this case, is given by,

$$\hbar^2 \frac{d^2 u_+}{dt^2} + \left[\epsilon_1^2(k) + \frac{8\alpha_2 \bar{g}_2 n_H E_k}{3} \cos(2\omega_2 t)\right] u_+ = 0, \tag{6.34}$$

$$\hbar^2 \frac{d^2 u_-}{dt^2} + \left[\epsilon_{-1}^2(k) + \frac{4\alpha_2 \bar{g}_2 n_H E_k}{3} \cos(2\omega_2 t)\right] u_- = 0, \tag{6.35}$$

$$\hbar^2 \frac{d^2 u_0}{dt^2} + \left[\epsilon_0^2(k) + \frac{4\alpha_2 \bar{g}_2 n_H (E_k - q)}{3} \cos(2\omega_2 t)\right] u_0 = 0. \tag{6.36}$$

and resulting the density and spin Floquet exponents are,

$$\sigma_+ = \frac{\alpha_2 \bar{g}_2}{3\hbar^2 \omega_2} \left(\sqrt{\bar{c}_0^2 n_H^2 + \hbar^2 \omega_2^2} - \bar{c}_0 n_H \right), \tag{6.37}$$

$$\sigma_- = \sigma_0 = \frac{2\alpha_2 \bar{g}_2}{3\hbar^2 \omega_0} \left(\sqrt{\bar{c}_1^2 n_H^2 + \hbar^2 \omega_2^2} - \bar{c}_1 n_H \right). \tag{6.38}$$

Here, an extra factor of two appear for the spin-mode density. The consequence of this factor is similar to what had been discussed in case of a_2 modulation in the polar phase. For instance, spin-dynamics dominates for a_2 modulation when $\bar{c}_1 = \bar{c}_0$. In general, the spin Floquet exponent is larger when $0 < \bar{c}_1 n_H < \left(5\bar{c}_0 n_H - 3\sqrt{\bar{c}_1^2 n_H^2 + \hbar^2 \omega_2^2}\right)/4$, a condition which dependents on frequency as well.

6.8 Modulation of both frequency

In this section, we analyze the dynamics that occur under the simultaneous modulation of a_0 and a_2, particularly focusing on the competing instability when modulated at different frequencies (ω_0, ω_2), or equivalently by modulation one scattering length with a combination of two frequencies [201]. Here, we only discuss the results for the Q1D geometry, although qualitatively similar results are obtained for the Q2D geometry as well. With an appropriate choice of driving amplitude, two modes from the same branch (with different momenta) become equally unstable [see. Sec. 5.9.3], i.e. with the same Floquet exponent. The example of such a scenario is given in Fig. 6.10. Here we see competing instability of two unstable modes in the $\epsilon_{-1}(k)$ branch, which is observed from the structure factor (Fourier transform of C_z) plotted in Fig. 6.10 (b) as two distinct peaks. Similar instability can also be observed in the density pattern formation, for instance if $\bar{c}_1 \ll \bar{c}_0$, when the condensate is modulated with two frequencies and appropriately chosen amplitudes.

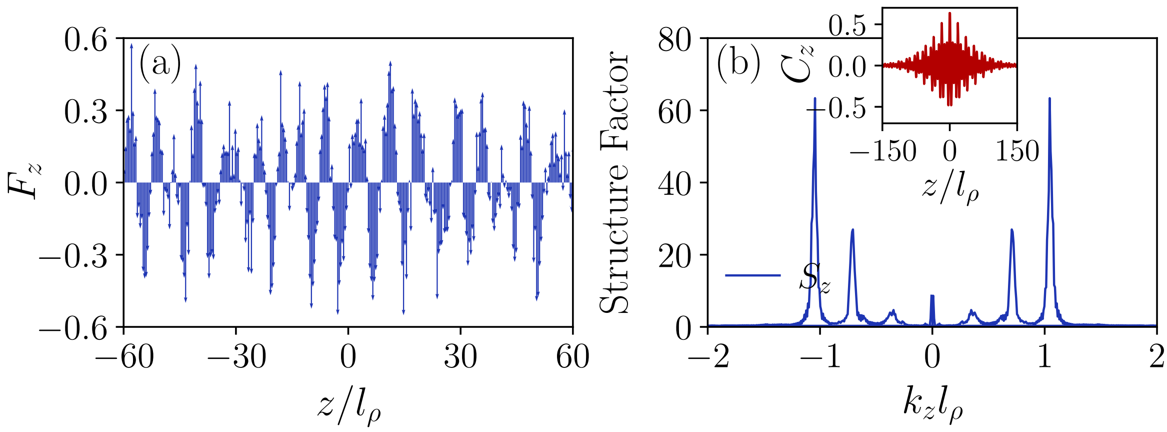

FIGURE 6.10: Results for simultaneous modulation of a_0 and a_2 with $\bar{c}_1 \ll \bar{c}_0$ and $\hbar\omega_{0,2} < \Delta_{1D}$ in Q1D geometry. The values of the parameters $\bar{c}_0^{(1D)} n_H^{(1D)} = 0.4\hbar\omega_\rho$, $\bar{c}_1^{(1D)} n_H^{(1D)} = 0.05\hbar\omega_\rho$, $q = -0.6\hbar\omega_\rho$, $\alpha_0 = 0.2$, $\omega_0 = 0.6\omega_\rho$, $\alpha_2 = 0.15$ and $\omega_0 = 0.3\omega_\rho$. (a) Spin texture for simultaneous modulation of a_0 and a_2 at $\omega_\rho t = 268$. (b) The structure factor reveals the two dominant unstable momenta of the magnon mode. The corresponding C_z correlation is shown in the inset of (b). The correlation is obtained by taking an average from $\omega_\rho t_i = 180$ to $\omega_\rho t_f = 270$ over 40 different realizations of TWA noise.

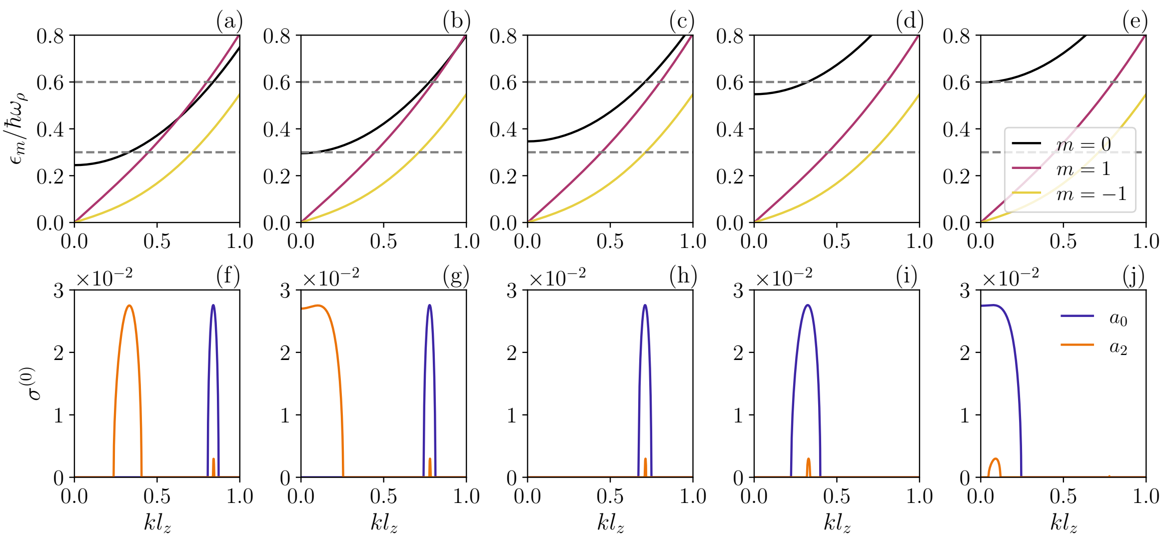

FIGURE 6.11: (a)-(e) The Bogoliubov modes ϵ_m of a Q1D condensate in AFM phase for $\bar{c}_1^{(1D)} n_H^{(1D)} = 0.4\hbar\omega_\rho$, $\bar{c}_1^{(1D)} n_H^{(1D)} = 0.05\hbar\omega_\rho$ (a) $q = -0.2\hbar\omega_\rho$, (b) $q = -0.25\hbar\omega_\rho$, (c) $q = -0.3\hbar\omega_\rho$, (d) $q = -0.5\hbar\omega_\rho$ and (e) $q = -0.55\hbar\omega_\rho$. The modulation frequencies $\omega_0 = 0.6\omega_\rho$ and $\omega_0 = 0.3\omega_\rho$ are indicated by dashed lines. (f)-(j) The Mathieu exponents associated with the unstable spin-mode shown (a)-(e) for modulation amplitudes $\alpha_0 = 0.3$ and $\alpha_0 = 0.217$. The blue peak arises from the a_0 modulation and the orange one arises from the a_2 modulation.

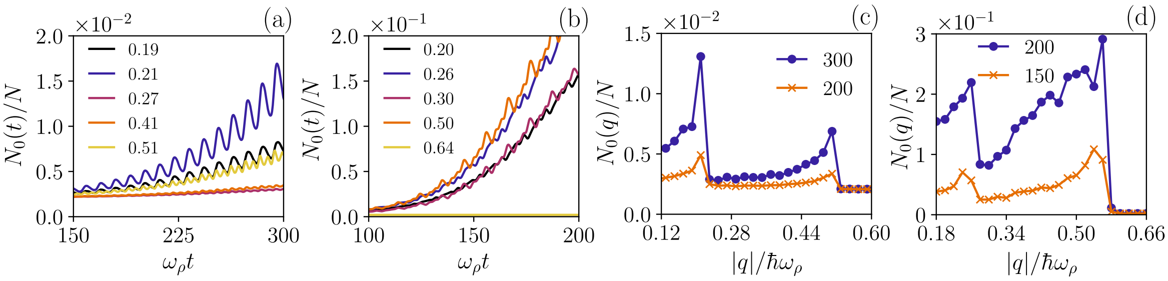

FIGURE 6.12: (a) and (b) shows the population dynamics for different values of $|q|$ (given in the inset in units of $\hbar\omega_\rho$), given in the inset for $\bar{c}_1 = \bar{c}_0$ and $\bar{c}_1 \ll \bar{c}_0$, respectively. (c) and (d) show the total population transferred after two different instants (given in the inset in units of ω_ρ^{-1}) for $\bar{c}_1 = \bar{c}_0$ and $\bar{c}_1 \ll \bar{c}_0$, respectively. For (a) and (c), we took $\bar{c}_0^{(1D)} n_H^{(1D)} = \bar{c}_1^{(1D)} n_H^{(1D)} = 0.1\hbar\omega_\rho$, $\alpha_0 = 0.4$ and $\alpha_2 = 0.235$. For (b) and (d), we took $\bar{c}_0^{(1D)} n_H^{(1D)} = 0.4\hbar\omega_\rho$, $\bar{c}_1^{(1D)} n_H^{(1D)} = 0.05\hbar\omega_\rho$, $\alpha_0 = 0.3$ and $\alpha_2 = 0.217$. For all cases, $\omega_0 = 0.6\omega_\rho$ and $\omega_0 = 0.3\omega_\rho$.

We also investigate the effect of varying the quadratic Zeeman term across the point $\hbar\omega_2 = \Delta_{1D}(q)$, where $\omega_0 < \omega_2$ are the driving frequencies. We chose the amplitudes $\alpha_{0,2}$ such that the Floquet exponents of the two unstable modes are nearly equal Fig. 6.11 [(f)-(g)]. Here, the exponents of the two unstable modes with two different momenta can be approximated as the union of the cases where only one frequency is present [85]. As the gap of the spectrum varies, the exponents of the unstable modes remain constant, since they are independent of q. However, once the $\Delta_{1D} > \hbar\omega_0$, we see a sudden dip in the population transferred to the $m = 0$ component. This is shown in Fig. 6.12 for and $\bar{c}_1 = \bar{c}_0$ [(a),(c)] and $\bar{c}_1 \ll \bar{c}_0$ [(b), (d)], as there is only one unstable mode in $\epsilon_0(k)$ branch when $\Delta_{1D} > \hbar\omega_0$. Even though the Floquet exponent is independent of q, we see a change of population transfer in the simulation. This is attributed to the increase width of the unstable momenta-region near the $\Delta_{1D} = \hbar\omega_{0,2}$ points Fig. 6.11 [(f)-(j)].

6.9 Conclusion

In this chapter, we looked at the dynamics of homogeneous condensate in AFM phase, when the s-wave scattering length is driven about its mean value, in Q1D and Q2D geometry. Similar to the polar phase BEC, density and spin patterns arise in the AFM phase under driving. Using linear stability analysis, we find that spin and density modes become parametrically excited under driving. We also found the relationship between the momenta of the unstable modes, denoted by $k_u^{(\pm,0)}$, and driving frequency as $\hbar\omega_0 = \epsilon_{0,\pm 1}(k_u^{(\pm,0)})$. The transverse spin mode is only unstable if the driving frequency $\omega_0 > \Delta$, the gap of the ϵ_0 branch. The Floquet exponent of the unstable density mode σ_+ depends on the mean spin-independent coefficient $\bar{c}_0$, and that of the unstable spin modes $\sigma_{-,0}$ depends on the spin-dependent interaction coefficient. By inspecting the exponent, we see that the density dynamics dominates when

$\bar{c}_1 \gg \bar{c}_0$, whereas the spin dynamics dominates when $\bar{c}_0 \gg \bar{c}_0$, when the longitudinal and transverse spin modes are both unstable, i.e. when $\omega_0 > \Delta$, the pattern formation occur at the same rate as $\sigma_0 = \sigma_-$.

We study condensate dynamics in Q1D and Q2D geometry by numerically solving the coupled GPE. The initial AFM state was perturbed by adding noise under the TWA prescription, which simulates the quantum fluctuations present in the system. For the Q1D system, the parametric excitation of modes results in sinusoidal density and spin density pattern formation. When the driving frequency $\omega_0 < \Delta_{1D}$, we see patterns in the total density and F_z spin-density with wavelengths $2\pi/k_u^{(+)}$ and $2\pi/k_u^{(-)}$, respectively. In this case, the system is equivalent to a two-component BEC. When $\omega_0 > \Delta_{1D}$, we also see pattern formation in the transverse $F_{x,y}$ spin densities, and a transfer of population to $m = 0$ spin state. The wavelength of the transverse spin density pattern is given by $2\pi/k_u^{(0)}$. When the initial phase between the $m = \pm 1$ components is $\phi = 0$, the spin density pattern forms mainly along F_x. We also see the formation of patterns in F_y, we attribute this to inherent fluctuations of the nematic order.

We see similar dynamics in the Q2D condensate as well, where 2D total density patterns form with wavenumber $k_u^{(+)}$ and F_z spin density patterns form with wavenumber $k_u^{(-)}$. When $\omega_0 > \Delta_{2D}$, we also see spin density pattern in F_x component (for initial phase $\phi = 0$). The radial spin-spin correlation functions are Bessel functions with argument $k_u^{(-)}$ and $k_u^{(0)}$ for F_z and F_x spin patterns, respectively. Therefore, in the F_x-F_z, the spin-texture formed under the periodic driving will be domains along the F_z spin-direction when $\omega_0 < \Delta_{2D}$, and spin vortex antivortex gas when $\omega_0 > \Delta_{2D}$. The patterns formed in all cases are transient due to the initial excitation of the resonant mode, and the condensate destroys continuous driving. We briefly discussed the case of a_2 modulation and competing instability in the presence of two driving frequencies.

Chapter 7

Summary and Outlook

In this thesis, we have investigated the dynamics of driven Bose-Einstein condensates (BECs), focusing on the instabilities that give rise to pattern formation.

In the first part of the thesis, we examined the driven dynamics of a cylindrically confined spin-0 BEC, focusing on the explicit role of the trapping potential. In Chapter 3, we studied the resonance of radial modes in a cylindrical condensate when the interaction strength is modulated at the natural frequencies of these modes, using both Bogoliubov theory and Gross–Pitaevskii equation (GPE) simulations. We established a general resonance condition and explored the resulting dynamics under resonant excitation. Excitation of the transverse monopole mode leads to amplified breathing oscillations, which subsequently decay into pairs of longitudinal density modes, producing longitudinal density patterns. When the driving frequency matches that of the higher radial ($n_r = 2$) mode, annular patterns emerge in the radial density profile. The decay dynamics of these higher modes are more complex due to its high lying nature. At low initial interaction strengths, the decay leads to density waves, while at stronger interactions, the system exhibits centre-of-mass (COM) oscillations due to excitation of the dipole branch modes. We analyze the crossover between these regimes for various interaction strengths.

In Chapter 4, we extend this study to parametric resonances in the cylindrically confined system, focusing on the excitation of Bogoliubov modes at half the driving frequency under periodic modulation of the interaction. Using linear stability analysis and Bogoliubov theory within the quasi-one-dimensional (Q1D) approximation, we show that the unstable wavelengths of the resulting density patterns are determined by the Bogoliubov dispersion. This analysis is validated by extending it to the full three-dimensional condensate, confirming that the Q1D approximation remains valid for weak interactions even at higher driving frequencies. For stronger interactions, radial modes become important and give rise to complex, frequency-dependent pattern formation. In particular, for a certain frequency range, instability of the gapless branch leads to density wave formation, while at higher frequencies, instability of the dipole branch leads to longitudinal COM oscillations.

In the second part of the thesis, we explore the driven dynamics of a spin-1 spinor BEC initialized in various magnetic phases. For a condensate prepared in the fully magnetized ferromagnetic state, the dynamics resemble those of a spin-0 BEC, with parametric excitation resulting in the formation of density waves. However, when the initial state is in the polar or antiferromagnetic (AFM) phase, qualitatively different dynamics emerge. In Chapter 4, we examine the formation of density and spin-density patterns under periodic modulation of the scattering length in quasi-two-dimensional spin-1 BEC initialized in polar phase, where all atoms are in the $m = 0$ spin state. The wavelength of these patterns can be predicted from the Bogoliubov spectrum of the initial state. When the driving frequency is below the spin-mode gap, only density patterns form. When it exceeds the gap, competition between density and spin pattern formation arises. If the spin-independent interaction coefficient c_0 is much larger than the spin-dependent coefficient c_1, the dynamics are dominated by density pattern formation and the reverse leads to dominant spin dynamics. The latter case involves population transfer into the initially unoccupied $m = \pm 1$ and the emergence of spin textures in the transverse spin plane (F_x-F_y). These textures consist of a gas of spin vortices and antivortices, whose number density depends on the driving frequency. Each spin vortex corresponds to a polar-core vortex, composed of a vortex-antivortex pair in the $m = \pm 1$ spin state densities. The radial spin-spin correlation function exhibits a Bessel profile.

We further investigate the AFM condensate in Chapter 6, where both density and spin patterns emerge under periodic driving. Similar to the polar case, dominant spin-independent interactions ($c_0 \gg c_1$) favor spin pattern formation, while dominant spin-dependent interactions ($c_0 \ll c_1$) favor density patterns. When the driving frequency is below the transverse spin-mode gap, we observe in-phase and out-of-phase oscillations of the $m = \pm 1$ components, resulting in patterns in total density and longitudinal spin density. This behaviour closely resembles the response of a binary condensate in the miscible regime. The AFM phase is a symmetry-broken phase. Although the magnetization vanishes isotropically, the spin-nematic tensor exhibits anisotropy in the F_x-F_y plane. This broken symmetry plays a central role when the driving frequency exceeds the transverse spin-mode gap, leading to the formation of transverse spin-density patterns oriented along a specific direction determined by the initial nematic order. The resulting spin texture forms domains below the gap, and a vortex-antivortex gas above the gap. The wavelengths of the longitudinal and transverse patterns are distinct and can be extracted from the Bogoliubov spectrum, which is typically degenerate in the AFM phase. The radial spin-spin correlation again follows a Bessel function profile, and the momenta of the unstable modes can be inferred from its arguments.

Now we outline a few of the possible future outlooks of this thesis. The study can be extended to the nonlinear dynamics of the parametrically excited modes in trapped condensates, as such effects have been shown to cause formation of regular patterns in Q2D systems [60, 162, 201]. The damping of the excitations can also modify the dynamics significantly [162]. Such effects in driven spinor condensates are an interesting problem to look at [23].

The entanglement generation under pair production is also an intriguing topic to explore, in both spinless and spinor condensates. The studies can also be extended to higher spin systems, which host many more ground state phases.

Appendix A

Hamiltonian transformation in Bogoliubov basis

In this appendix, we show that the time-independent Hamiltonian becomes diagonal in its Bogoliubov basis, within a number-conserving framework. Although we consider a cylindrically confined BEC in the thesis, this derivation has not made any assumption on the trap geometry.

Consider the following Hamiltonian,

$$\hat{H}_0 = \int d\boldsymbol{r} \left[\hat{\Psi}^\dagger \hat{h}_0 \hat{\Psi} + \frac{\bar{g}}{2} \hat{\Psi}^\dagger \hat{\Psi}^\dagger \hat{\Psi} \hat{\Psi} \right] \tag{A.1}$$

where $\hat{h}_0(\boldsymbol{r}) = -(\hbar^2\nabla^2/2M) + V_T(\boldsymbol{r})$ with $V_T(\boldsymbol{r})$ being the 3D harmonic trap. Here, $\bar{g}$ is the coefficient of the two-body interaction. We expand the field operator about the mean-field ground state of the Hamiltonian as,

$$\hat{\Psi}(\boldsymbol{r}, t) = \left[\frac{\xi_0}{\sqrt{L_z}} \hat{a}_0 + \delta\hat{\Psi}(\boldsymbol{r}, t) \right] e^{i\mu t} \tag{A.2}$$

where ξ_0 satisfy the time-independent GPE, $[-(\hbar^2\nabla^2/2M) + V_T(\boldsymbol{r}) - \mu + \bar{g} n_H |\xi_0|^2]\xi_0 = 0$. $\hat{a}_0$ annihilates a particle in the condensate mode and $\delta\hat{\Psi}$ contain the portion of the field operator that is orthogonal to the condensate mode, thus representing the non-condensate contribution to it.

Expanding the Hamiltonian around the condensate mode using (A.2), we get,

$$\begin{aligned}
\hat{H}_0 = {} & \frac{\hat{a}_0^\dagger \hat{a}_0}{L_z} \int d\boldsymbol{r} \xi_0^* \hat{h}_0 \xi_0 + \frac{1}{\sqrt{L_z}} \int d\boldsymbol{r} \left[\hat{a}_0 \delta\hat{\Psi}^\dagger \hat{h}_0 \xi_0 + \text{H.c.} \right] + \int d\boldsymbol{r} \delta\hat{\Psi}^\dagger \hat{h}_0 \delta\hat{\Psi} \\
& + \frac{\bar{g}}{2} \frac{\hat{a}_0^\dagger \hat{a}_0^\dagger \hat{a}_0 \hat{a}_0}{L_z^2} \int d\boldsymbol{r} |\xi_0|^4 + \frac{\bar{g}}{L_z \sqrt{L_z}} \int d\boldsymbol{r} \left[\hat{a}_0^\dagger \hat{a}_0 \hat{a}_0 \, |\xi_0|^2 \xi_0 \delta\hat{\Psi}^\dagger + \text{H.c.} \right] \\
& + \frac{\bar{g}}{2L_z} \int d\boldsymbol{r} \left[\hat{a}_0^\dagger \hat{a}_0^\dagger \, (\xi_0^*)^2 \delta\hat{\Psi} \delta\hat{\Psi} + \text{H.c.} \right] + 2\frac{\bar{g}}{L_z} \, \hat{a}_0^\dagger \hat{a}_0 \int d\boldsymbol{r} |\xi_0|^2 \delta\hat{\Psi}^\dagger \delta\hat{\Psi} + O(\delta\hat{\Psi}^3),
\end{aligned} \tag{A.3}$$

where the terms that are of order $\delta\hat{\Psi}^3$ and higher are neglected. This is a valid assumption when the non-condensate population is smaller than the condensate population. Since the total number of atoms N in the system is conserved, we have $\hat{a}_0^\dagger \hat{a}_0 = N - \delta\hat{N}$, where $\hat{a}_0^\dagger \hat{a}_0$ and $\delta\hat{N} = \int d\boldsymbol{r} \delta\hat{\Psi}^\dagger \delta\hat{\Psi}$ are the number operators for the condensate mode and non-condensate modes, respectively. $\delta\hat{N}$ is of order $\delta\hat{\Psi}^2$, therefore we have $\hat{a}_0^\dagger \hat{a}_0^\dagger \hat{a}_0 \hat{a}_0 \approx N^2 - 2N\hat{\delta}N$ when $N \gg 1$.

We collect terms in order of $\delta\hat{\Psi}$, where the Hamiltonian becomes $\hat{H}_0 \approx \hat{H}_0^{(0)} + \hat{H}_0^{(1)} + \hat{H}_0^{(2)}$. The zeroth order term is given by,

$$\hat{H}_0^{(0)} = n_H \int d\boldsymbol{r} \left[\xi_0^* \hat{h}_0 \xi_0 + \frac{\bar{g} n_H}{2} |\xi_0|^4 \right] \equiv E_0 \tag{A.4}$$

This is the mean-field energy of the system, which is obtained by completely neglecting the non-condensate contribution. The linear order term in Hamiltonian vanishes,

$$\begin{aligned} \hat{H}_0^{(1)} &= \hat{a}_0^\dagger \int d\boldsymbol{r}\ \delta\hat{\Psi}^\dagger \left[\hat{h}_0 + \bar{g} n_H\ |\xi_0|^2 \right] \xi_0 + \text{H.c.} \\ &= \mu \hat{a}_0^\dagger \int d\boldsymbol{r}\ \delta\hat{\Psi}^\dagger \xi_0 + \text{H.c.} \\ &= 0. \end{aligned} \tag{A.5}$$

Here, in the first step, we have used the fact that ξ_0 satisfy the time-independent GPE, and the integral vanish in the second step as $\delta\hat{\Psi}$ is orthogonal to the condensate mode.

Finally, collecting the terms of $O(\delta\hat{\Psi}^2)$, we get,

$$\begin{aligned} \hat{H}_0^{(2)} = &\int d\boldsymbol{r} \delta\hat{\Psi}^\dagger \hat{h}_0 \delta\hat{\Psi} + \frac{\bar{g}}{2L_z} \int d\boldsymbol{r} \left[\hat{a}_0^\dagger \hat{a}_0^\dagger\ (\xi_0^*)^2 \delta\hat{\Psi} \delta\hat{\Psi} + \text{H.c.} \right] \\ &+ 2\bar{g} n_H \int d\boldsymbol{r} |\xi_0|^2 \delta\hat{\Psi}^\dagger \delta\hat{\Psi} - \mu \delta\hat{N} \end{aligned} \tag{A.6}$$

Now, we introduce the number-conserving operator $\hat{\Lambda}(\boldsymbol{r}, t) = (1/\sqrt{N}) \hat{a}_0^\dagger \delta\hat{\Psi}(\boldsymbol{r}, t)$, which destroys a non-condensate particle and creates one in the condensate. Here we have $\hat{a}_0^\dagger \hat{a}_0^\dagger \delta\hat{\Psi} \delta\hat{\Psi} = N\hat{\Lambda}\hat{\Lambda}$. The term $\delta\hat{\Psi}^\dagger \delta\hat{\Psi}$ is replaced in an approximate manner as $\delta\hat{\Psi}^\dagger \delta\hat{\Psi} \approx N^{-1} \delta\hat{\Psi}^\dagger \hat{a}_0 \hat{a}_0^\dagger \delta\hat{\Psi} = \hat{\Lambda}^\dagger \hat{\Lambda}$ [29, 30]. Thus we arrive at the following form for the quadratic Hamiltonian,

$$\hat{H}_0^{(2)} \approx \int d\boldsymbol{r} \hat{\Lambda}^\dagger \left(\hat{\mathcal{L}} \right) \hat{\Lambda} + \frac{\bar{g} n_H}{2} \int d\boldsymbol{r} \xi_0^2 \left[\hat{\Lambda}^\dagger \hat{\Lambda} + \text{H.c.} \right] \tag{A.7}$$

where the operator $\hat{\mathcal{L}} = \hat{h}_0 - \mu + 2\bar{g} n_H |\xi_0|^2$.

A.1 Bogoliubov basis

We expand the operator $\hat{\Lambda}$ in the Bogoliubov basis as,

$$\hat{\Lambda}(\boldsymbol{r},t) = \sum_i \hat{b}_i(t)u_i(\boldsymbol{r})e^{-i\omega_i t} + \hat{b}_i^\dagger(t)v_i^*(\boldsymbol{r})e^{i\omega_i t} \tag{A.8}$$

Here $\hat{b}_i$ and ω_i are the quasiparticle operator and corresponding frequency. $\hat{b}_i$ satisfies the bosonic commutation relations, $\left[\hat{b}_i, \hat{b}_j^\dagger\right] = \delta_{ij}$ and $\left[\hat{b}_i, \hat{b}_j\right] = \left[\hat{b}_i^\dagger, \hat{b}_j^\dagger\right] = 0$. The the amplitudes $\{u_i, v_i\}$ are the projection of the usual Bogoliubov amplitudes $\{\tilde{u}_i, \tilde{v}_i\}$ to the space orthogonal to ground state function ξ_0. That is,

$$u_i = \tilde{u}_i - \xi_0 a_i, \quad v_i = \tilde{v}_i + \xi_0 a_i \tag{A.9}$$

where $a_i = \int d\boldsymbol{r}\xi_0\tilde{u}_i = -\int d\boldsymbol{r}\xi_0\tilde{v}_i$ [13]. This ensure that Λ is orthogonal to $\hat{a}_0$. Bogoliubov amplitudes $\tilde{u}_i, \tilde{v}_i$ satisfy the Bogoliubov de-Gennes equation,

$$\begin{pmatrix} \hat{\mathcal{L}} & \bar{g}n_H\xi_0^2 \\ -\bar{g}n_H\xi_0^2 & -\hat{\mathcal{L}} \end{pmatrix}\begin{pmatrix} \tilde{u}_i \\ \tilde{v}_i \end{pmatrix} = \hbar\omega_i\begin{pmatrix} \tilde{u}_i \\ \tilde{v}_i \end{pmatrix}, \tag{A.10}$$

and the orthonormality condition,

$$\int d\boldsymbol{r}\left[\tilde{u}_i\tilde{u}_j^* - \tilde{v}_i\tilde{v}_j^*\right] = \delta_{ij}, \quad \int d\boldsymbol{r}\left[\tilde{u}_i\tilde{v}_j - \tilde{v}_i\tilde{u}_j\right] = 0 \tag{A.11}$$

These functions also posses the following property [13, 117],

$$\int d\boldsymbol{r}\left[\xi_0\tilde{u}_i + \xi_0^*\tilde{v}_i\right] = 0 \tag{A.12}$$

which justifies (A.9). Note that here we assume that ξ_0 can be expressed as a real function which is true for our case. It is not possible to do so in certain cases, such that when ground state contains a vortex. The more general expansion is discussed in Ref. [13].

The following steps are similar to approach done in Ref. [57], which uses a $U(1)$ symmetry breaking approach. Substituting Eqs. (A.8) into Eqs. (A.7) we arrive at,

$$\begin{aligned}\hat{H}_0^{(2)} &= \sum_i \hbar\omega_i \hat{b}_i^\dagger(t)\hat{b}_i(t)\int d\boldsymbol{r}[u_i^* u_i - v_i v_i^*] + \sum_i \hbar\omega_i \int d\boldsymbol{r}|v_i|^2 \\ &+ \frac{1}{2}\sum_{i\neq j} \hat{b}_i^\dagger(t)\hat{b}_j(t)e^{i(\omega_i-\omega_j)t}\int d\boldsymbol{r}\left\{\hbar\omega_j[u_i^* u_j - v_i^* v_j] + \hbar\omega_i[u_j u_i^* - v_j v_i^*]\right\} \\ &+ \frac{1}{2}\sum_{ij} \hbar\omega_i \hat{b}_i^\dagger(t)\hat{b}_j^\dagger(t)e^{i(\omega_i+\omega_j)t}\int d\boldsymbol{r}\left\{-u_j^* v_i^* + v_j^* u_i^*\right\} \\ &+ \frac{1}{2}\sum_{ij} \hbar\omega_i \hat{b}_i(t)\hat{b}_j(t)e^{-i(\omega_i+\omega_j)t}\int d\boldsymbol{r}\left\{v_j u_i - u_j v_i\right\}\end{aligned} \tag{A.13}$$

where we used the relation,

$$\int d\boldsymbol{r} f_1^*(\hat{\mathcal{L}} f_2) = \int d\boldsymbol{r} f_2(\hat{\mathcal{L}}^* f_1^*) \tag{A.14}$$

where $f_{1,2}$ are two arbitrary functions.

We can use Eq.(A.9) and Eq.(A.11) that $\{u_i, v_i\}$ to show that,

$$\begin{aligned}\int d\boldsymbol{r}\left[u_i u_j^* - v_i v_j^*\right] &= \delta_{ij} \\ \int d\boldsymbol{r}\left[u_i v_j - v_i u_j\right] &= 0\end{aligned} \tag{A.15}$$

Using the above relation in Eq.(A.13) and simplifying we finally,

$$\hat{H}_0^{(2)} = \sum_i \hbar\omega_i \hat{b}_i^\dagger(t)\hat{b}_i(t) - \sum_i \hbar\omega_i \int d\boldsymbol{r}|v_i|^2 \tag{A.16}$$

which is diagonal as expected, with the second term being the energy correction due to the quantum fluctuations.

Appendix B

Floquet theory calculation

B.1 Mathieu equation

Consider the following equation,

$$\hbar^2 \frac{d^2 u}{dt^2} + \left[\epsilon_{1D}^2(k) + 2E_k \Delta g_{1D} n_H \cos(\Omega t)\right] u = 0 \tag{B.1}$$

This can be written in the standard form as below,

$$\frac{d^2 u}{d\tilde{t}^2} + [a + 2q \cos 2\tilde{t}\,] u = 0 \tag{B.2}$$

where we used new dimensionless scale of time $\tilde{t} = \Omega t/2$, and $a = 4\epsilon_{1D}^2(k)/\hbar^2\Omega^2$ and $q = 4E_k \Delta g_{1D} n_H/\hbar^2\Omega^2$. It is known that the resonances (instability) then occur when $a = n^2$, where $n = 1, 2, \ldots$ and the first resonance occur form $n = 1$, and the real part of the (dimensionless) Floquet exponent $\tilde{\sigma}$ is given by $\mathrm{Re}\{\tilde{\sigma}\} \approx q/2$ for $q \ll 1$. Therefore the resonant driving frequency satisfy $\hbar\Omega = 2\epsilon_{1D}(k)$ and the exponent in units of t is given by,

$$\mathrm{Re}\{\sigma\} = \frac{\tilde{\sigma}\Omega}{2} = \frac{\Delta g_{1D} n_H E_k}{\hbar^2 \Omega} \tag{B.3}$$

B.2 Floquet exponent

In this appendix, we give the details of calculation of Floquet exponents of Eq. (4.21). Here we follow the method used in Ref. [26] for coupled parametric oscillator.

The general solution to the equation can be expressed in the form,

$$\begin{aligned} \hat{b}_k(t) &= c_k(t)\hat{b}_k(0) + \tilde{c}_k(t)\hat{b}^\dagger_{-k}(0) \\ \hat{b}^\dagger_{-k}(t) &= c'_k(t)\hat{b}_k(0) + \tilde{c}'_k(t)\hat{b}^\dagger_{-k}(0) \end{aligned} \tag{B.4}$$

The coefficients here follow the same equations as the Bogoliubov operators, given by,

$$
\begin{aligned}
\frac{d}{dt}\begin{pmatrix} c_k \\ c'_k \end{pmatrix} &= -i\begin{pmatrix} A + B\cos(\Omega t) & B\cos(\Omega t) \\ -B\cos(\Omega t) & -A - B\cos(\Omega t) \end{pmatrix}\begin{pmatrix} c_k \\ c'_k \end{pmatrix} \\
\frac{d}{dt}\begin{pmatrix} \tilde{c}_k \\ \tilde{c}'_k \end{pmatrix} &= -i\begin{pmatrix} A + B\cos(\Omega t) & B\cos(\Omega t) \\ -B\cos(\Omega t) & -A - B\cos(\Omega t) \end{pmatrix}\begin{pmatrix} \tilde{c}_k \\ \tilde{c}'_k \end{pmatrix}
\end{aligned} \tag{B.5}
$$

where we defined $A = \epsilon_{1D}(k)/\hbar$ and $B = \Delta g_{1D} n_H E_k/\hbar\epsilon_{1D}$. Since the Floquet exponents for both set of equations will be the same, we shall just focus on the the first set of equation, i.e. that of c_k, c'_k. Using Floquet theory, we express the solutions in the form $c_k(t) = e^{i\bar{\sigma}t}p(t)$ and $c'_k(t) = e^{i\bar{\sigma}t}p'(t)$, where functions p and p' are periodic with time period $T = 2\pi/\Omega$. Here we use $e^{i\bar{\sigma}t}$ instead of the usual $e^{\sigma t}$ used elsewhere in the thesis, with $\bar{\sigma} = -i\sigma$. These function can then be expanded in Fourier series, which gives us,

$$
c_k(t) = e^{i\bar{\sigma}t}\sum_{n\in\mathbb{Z}} P_n e^{in\Omega t}, \qquad c'_k(t) = e^{i\bar{\sigma}t}\sum_{n\in\mathbb{Z}} P'_n e^{in\Omega t}, \tag{B.6}
$$

Differentiating both side with respect to time and comparing with Eqs. (B.5),

$$
\begin{aligned}
\dot{c}_k &= e^{i\bar{\sigma}t}\sum_{n\in\mathbb{Z}} i(\bar{\sigma} + n\Omega)e^{in\Omega t}P_n \\
&= -ie^{i\bar{\sigma}t}\sum_{n\in\mathbb{Z}} e^{in\Omega t}\left[[A + B\cos(\Omega t)]\,P_n + B\cos(\Omega t)P'_n\right]
\end{aligned}
$$

This can be expressed as,

$$
\dot{c}_k = -ie^{i\bar{\sigma}t}\sum_{n\in\mathbb{Z}} e^{in\Omega t}\left[AP_n^{(1)} + \frac{B}{2}(P_{n-1} + P_{n+1}) + \frac{B}{2}(P'_{n-1} + P'_{n+1})\right] \tag{B.7}
$$

We follow the same procedure for c'_k, finally arrive at the following recursive relationship between the Fourier coefficients,

$$
\begin{aligned}
(A + \bar{\sigma} + n\Omega)P_n + \frac{B}{2}(P_{n-1} + P_{n+1}) + \frac{B}{2}(P'_{n-1} + P'_{n+1}) &= 0 \\
(A - \bar{\sigma} - n\Omega)P'_n + \frac{B}{2}(P'_{n-1} + P'_{n+1}) + \frac{B}{2}(P_{n-1} + P_{n+1}) &= 0
\end{aligned} \tag{B.8}
$$

This can be can expressed as a matrix equation,

$$\begin{pmatrix} \ddots & \vdots & \vdots & \vdots & \vdots & \vdots & \iddots \\ \dots & \boldsymbol{D}_1 & \boldsymbol{D}_0^{(n-1)} & \boldsymbol{D}_1 & \mathbf{0} & \mathbf{0} & \dots \\ \dots & \mathbf{0} & \boldsymbol{D}_1 & \boldsymbol{D}_0^{(n)} & \boldsymbol{D}_1 & \mathbf{0} & \dots \\ \dots & \mathbf{0} & \mathbf{0} & \boldsymbol{D}_1 & \boldsymbol{D}_0^{(n+1)} & \boldsymbol{D}_1 & \dots \\ \iddots & \vdots & \vdots & \vdots & \vdots & \vdots & \ddots \end{pmatrix} \begin{pmatrix} \vdots \\ \boldsymbol{P}_{n-1} \\ \boldsymbol{P}_n \\ \boldsymbol{P}_{n+1} \\ \vdots \end{pmatrix} = 0 \tag{B.9}$$

where $\boldsymbol{P}_n = (P_n, P'_n)^T$ is a column vector and,

$$\boldsymbol{D}_0^{(n)} = \begin{pmatrix} (A + \bar{\sigma} + n\Omega) & 0 \\ 0 & (A - \bar{\sigma} - n\Omega) \end{pmatrix}, \qquad \boldsymbol{D}_1 = \frac{B}{2}\begin{pmatrix} 1 & 1 \\ 1 & 1 \end{pmatrix} \tag{B.10}$$

are 2×2 matrices. So far during the analysis, we have not made any approximation.

Now, we note that the coefficient B is proportional to the driving amplitude of the interaction Δg_{1D}. Therefore, in the absence of driving, the Fourier coefficients are uncoupled to each other. In presence of a very weak driving, i.e. $B \to 0$, $\boldsymbol{P}_n$ is coupled strongest to $\boldsymbol{P}_{n\pm1}$. We can then neglect the coupling between $\boldsymbol{P}_n$ and $\boldsymbol{P}_{n\pm m}$, where $m > 1$, when the driving amplitude is sufficiently weak. We consider the equation of $\boldsymbol{P}_0$ and $\boldsymbol{P}_1$, whose solution will exist only if the following determinant should vanish,

$$\begin{vmatrix} \boldsymbol{D}_0^{(0)} & \boldsymbol{D}_1 \\ \boldsymbol{D}_1 & \boldsymbol{D}_0^{(1)} \end{vmatrix} = 0 \tag{B.11}$$

We can solve for the Floquet exponent σ to get four roots,

$$\bar{\sigma} = \frac{1}{2}\left[-\Omega \pm \sqrt{4A^2 + \Omega^2 \pm 4A\sqrt{B^2 + \Omega^2}}\right]$$

And assuming $B \ll \Omega$,

$$\bar{\sigma} \approx \frac{1}{2}\left[-\Omega \pm \sqrt{4A^2 + \Omega^2 \pm \left(4A\Omega + \frac{2AB^2}{\Omega}\right)}\right] \tag{B.12}$$

The instability occur when $\bar{\sigma}$ has an imaginary part, which require,

$$(2A - \Omega)^2 < \frac{2AB^2}{\Omega} \tag{B.13}$$

We can see that when $B \to 0$, having instability condition implies $\Omega \to 2A$. This gives us resonant driving frequency, where even an infinitesimally small driving amplitude causes instability. which gives us the resonance condition. At $\Omega = 2A$, the imaginary part of the exponent becomes,

$$\mathrm{Im}\{\bar{\sigma}\} = \pm\frac{B}{2} \tag{B.14}$$

Reiterating the results, we have obtained the resonant condition for driving frequency as,

$$\hbar\Omega = 2\epsilon_{1D}(k) \tag{B.15}$$

and the imaginary part of exponent $\bar{\sigma}$ (real part of σ) that determine the rate of growth of instability at the resonance point

$$\mathrm{Re}\{\sigma\} = \frac{\Delta g_{1D} n_H E_k}{\hbar^2\Omega} \tag{B.16}$$

We see that the Floquet exponents obtained from both Bogoliubov method and linear stability analysis matches.

Appendix C

Properties of $\hat{\mathcal{L}}_Q$ operator

The operator $\hat{\mathcal{L}}_Q$ given in Eq. (4.40) is similar to the usual BdG matrix $\hat{\mathcal{L}}_{BdG}$ in Eq. (3.6), except for the presence projection operator $\hat{Q}$. For a time-independent system, $\hat{\mathcal{L}}_Q$ and $\hat{\mathcal{L}}_{BdG}$ has the same spectrum of eigenvalues,and he eigenvectors $(|u_n\rangle, |v_n\rangle)$ of $\hat{\mathcal{L}}_Q$ is related to the BdG amplitudes $(|u_n\rangle^{(BdG)}, |v_n\rangle^{(BdG)})$ as $|u_n\rangle = \hat{Q}\,|u_n\rangle^{(BdG)}$, and $|v_n\rangle = \hat{Q}\,|v_n\rangle^{(BdG)}$.

We need to first discuss some properties of the eigenvectors of time-independent matrix $\hat{\mathcal{L}}_Q$. If $(|u\rangle, |v\rangle)$ is an eigenvector with eigenvalue $\epsilon > 0$, then $(|v^*\rangle, |u^*\rangle)$ is also an eigenvector, with eigenvalue $-\epsilon$. In addition to this, two eigenvectors with eigenvalues zero, which has the form $(|\xi_0\rangle, |0\rangle)$ and $(|0\rangle, |\xi_0^*\rangle)$, where $|\xi_0\rangle$ is the ground state of the GPE. The eigenvectors also has the orthonormal properties [28],

$$\langle u_n | u_{n'}\rangle - \langle v_n | v_{n'}\rangle = \delta_{nn'} \tag{C.1}$$

$$\langle v_n | u_{n'}^*\rangle - \langle u_n | v_{n'}^*\rangle = 0 \tag{C.2}$$

This also ensure that the excited modes, with $\epsilon \neq 0$, are always orthogonal to the condensate mode as $\langle \xi_0 | u_n\rangle = \langle \xi_0^* | v_n\rangle = 0$ Using the orthonormal properties described above, we can show that any arbitrary set of functions (f_u, f_v) can be expanded in the basis of $\hat{\mathcal{L}}_Q$ as,

$$\begin{pmatrix} |f_u\rangle \\ |f_v\rangle \end{pmatrix} = \alpha_0 \begin{pmatrix} |\xi_0\rangle \\ |0\rangle \end{pmatrix} + \beta_0 \begin{pmatrix} |0\rangle \\ |\xi_0^*\rangle \end{pmatrix} + \sum_{n>0} \alpha_n \begin{pmatrix} |u_n\rangle \\ |v_n\rangle \end{pmatrix} + \beta_n \begin{pmatrix} |v_n^*\rangle \\ |u_n^*\rangle \end{pmatrix} \tag{C.3}$$

The coefficients α_n and β_n are then given by,

$$\begin{aligned} \alpha_0 &= \langle \xi_0 | f_u\rangle, \qquad & \alpha_n &= \langle u_n | f_u\rangle - \langle v_n | f_v\rangle \\ \beta_0 &= \langle \xi_0^* | f_v\rangle, \qquad & \beta_n &= -\langle v_n^* | f_u\rangle + \langle u_n^* | f_v\rangle \end{aligned} \tag{C.4}$$

Bibliography

[1] Dmitry A Abanin et al. "Colloquium: Many-body localization, thermalization, and entanglement". In: *Reviews of Modern Physics* 91.2 (2019), p. 021001.

[2] J. R. Abo-Shaeer et al. "Observation of Vortex Lattices in Bose-Einstein Condensates". In: *Science* 292.5516 (2001), pp. 476–479. DOI: 10.1126/science.1060182.

[3] M. H. Anderson et al. "Observation of Bose-Einstein Condensation in a Dilute Atomic Vapor". In: *Science* 269.5221 (1995), pp. 198–201. DOI: 10.1126/science.269.5221.198.

[4] M. R. Andrews et al. "Observation of Interference Between Two Bose Condensates". In: *Science* 275.5300 (1997), pp. 637–641. DOI: 10.1126/science.275.5300.637.

[5] James R Anglin and Wolfgang Ketterle. "Bose–Einstein condensation of atomic gases". In: *Nature* 416.6877 (2002), pp. 211–218. DOI: https://doi.org/10.1038/416211a.

[6] Antun Balaž and Alexandru I Nicolin. "Faraday waves in binary nonmiscible Bose-Einstein condensates". In: *Physical Review A—Atomic, Molecular, and Optical Physics* 85.2 (2012), p. 023613.

[7] Ryan Barnett, Anatoli Polkovnikov, and Mukund Vengalattore. "Prethermalization in quenched spinor condensates". In: *Phys. Rev. A* 84 (2 Aug. 2011), p. 023606. DOI: 10.1103/PhysRevA.84.023606.

[8] ST Beliaev. "Energy spectrum of a non-ideal Bose gas". In: *Sov. Phys. JETP* 34.2 (1958), p. 299.

[9] Thomas Brooke Benjamin and Fritz Joseph Ursell. "The stability of the plane free surface of a liquid in vertical periodic motion". In: *Proceedings of the Royal Society of London. Series A. Mathematical and Physical Sciences* 225.1163 (1954), pp. 505–515.

[10] Niccolo Bigagli et al. "Observation of Bose–Einstein condensation of dipolar molecules". In: *Nature* 631.8020 (2024), pp. 289–293.

[11] A. T. Black et al. "Spinor Dynamics in an Antiferromagnetic Spin-1 Condensate". In: *Phys. Rev. Lett.* 99 (7 Aug. 2007), p. 070403. DOI: 10.1103/PhysRevLett.99.070403.

[12] P Blair Blakie et al. "Dynamics and statistical mechanics of ultra-cold Bose gases using c-field techniques". In: *Advances in Physics* 57.5 (2008), pp. 363–455.

[13] P. B. Blakie, R. J. Ballagh, and C. W. Gardiner. "Theory of coherent Bragg spectroscopy of a trapped Bose-Einstein condensate". In: *Phys. Rev. A* 65 (3 2002), p. 033602. DOI: 10.1103/PhysRevA.65.033602.

[14] I. Bloch, T. W. Hänsch, and T. Esslinger. "Measurement of the spatial coherence of a trapped Bose gas at the phase transition". In: *Nature* 403.6766 (Jan. 2000), pp. 166–170. ISSN: 1476-4687. DOI: 10.1038/35003132.

[15] Immanuel Bloch, Jean Dalibard, and Wilhelm Zwerger. "Many-body physics with ultracold gases". In: *Rev. Mod. Phys.* 80 (3 July 2008), pp. 885–964. DOI: 10.1103/RevModPhys.80.885.

[16] Nikolai Bogoliubov. "On the theory of superfluidity". In: *J. Phys* 11.1 (1947), p. 23.

[17] E. M. Bookjans, A. Vinit, and C. Raman. "Quantum Phase Transition in an Antiferromagnetic Spinor Bose-Einstein Condensate". In: *Phys. Rev. Lett.* 107 (19 Nov. 2011), p. 195306. DOI: 10.1103/PhysRevLett.107.195306.

[18] T. Boulier et al. "Parametric Heating in a 2D Periodically Driven Bosonic System: Beyond the Weakly Interacting Regime". In: *Phys. Rev. X* 9 (1 Mar. 2019), p. 011047. DOI: 10.1103/PhysRevX.9.011047.

[19] C. C. Bradley et al. "Evidence of Bose-Einstein Condensation in an Atomic Gas with Attractive Interactions". In: *Phys. Rev. Lett.* 75 (9 Aug. 1995), pp. 1687–1690. DOI: 10.1103/PhysRevLett.75.1687.

[20] Leonardo Brito, Lauro Tomio, and Arnaldo Gammal. "Faraday waves on a bubble-trapped Bose-Einstein-condensed binary mixture". In: *Phys. Rev. A* 108 (5 Nov. 2023), p. 053315. DOI: 10.1103/PhysRevA.108.053315.

[21] Marin Bukov, Luca D'Alessio, and Anatoli Polkovnikov. "Universal high-frequency behavior of periodically driven systems: from dynamical stabilization to Floquet engineering". In: *Advances in Physics* 64.2 (2015), pp. 139–226.

[22] E. A. Burt et al. "Coherence, Correlations, and Collisions: What One Learns about Bose-Einstein Condensates from Their Decay". In: *Phys. Rev. Lett.* 79 (3 July 1997), pp. 337–340. DOI: 10.1103/PhysRevLett.79.337.

[23] Xavier Busch, Renaud Parentani, and Scott Robertson. "Quantum entanglement due to a modulated dynamical Casimir effect". In: *Phys. Rev. A* 89 (6 June 2014), p. 063606. DOI: 10.1103/PhysRevA.89.063606.

[24] Salvatore Butera and Iacopo Carusotto. "Numerical Studies of Back Reaction Effects in an Analog Model of Cosmological Preheating". In: *Phys. Rev. Lett.* 130 (24 June 2023), p. 241501. DOI: 10.1103/PhysRevLett.130.241501.

[25] Eugene I Butikov. "Parametric resonance". In: *Computing in Science & Engineering* 1.3 (1999), pp. 76–83.

[26] Marcello Calvanese Strinati et al. "Theory of coupled parametric oscillators beyond coupled Ising spins". In: *Phys. Rev. A* 100 (2 Aug. 2019), p. 023835. DOI: 10.1103/PhysRevA.100.023835.

[27] I. Carusotto et al. "Density correlations and analog dynamical Casimir emission of Bogoliubov phonons in modulated atomic Bose-Einstein condensates". In: *The European Physical Journal D* 56.3 (Feb. 2010), pp. 391–404. ISSN: 1434-6079. DOI: 10.1140/epjd/e2009-00314-3.

[28] Y. Castin and R. Dum. "Bose-Einstein Condensates in Time Dependent Traps". In: *Phys. Rev. Lett.* 77 (27 Dec. 1996), pp. 5315–5319. DOI: 10.1103/PhysRevLett.77.5315.

[29] Y. Castin and R. Dum. "Low-temperature Bose-Einstein condensates in time-dependent traps: Beyond the $U(1)$ symmetry-breaking approach". In: *Phys. Rev. A* 57 (4 1998), pp. 3008–3021. DOI: 10.1103/PhysRevA.57.3008.

[30] Yvan Castin. "Bose-Einstein condensates in atomic gases: simple theoretical results". In: *Coherent atomic matter waves: 27 July–27 August 1999*. Springer, 2002, pp. 1–136.

[31] Peilong Chen and Jorge Viñals. "Amplitude equation and pattern selection in Faraday waves". In: *Phys. Rev. E* 60 (1 July 1999), pp. 559–570. DOI: 10.1103/PhysRevE.60.559.

[32] Terun Chen et al. "Faraday patterns generated by Rabi oscillation in a binary Bose-Einstein condensate". In: *Physical Review A* 100.6 (2019), p. 063610.

[33] F. Chevy, K. W. Madison, and J. Dalibard. "Measurement of the Angular Momentum of a Rotating Bose-Einstein Condensate". In: *Phys. Rev. Lett.* 85 (11 Sept. 2000), pp. 2223–2227. DOI: 10.1103/PhysRevLett.85.2223.

[34] F. Chevy et al. "Transverse Breathing Mode of an Elongated Bose-Einstein Condensate". In: *Phys. Rev. Lett.* 88 (25 June 2002), p. 250402. DOI: 10.1103/PhysRevLett.88.250402.

[35] Cheng Chin et al. "Feshbach resonances in ultracold gases". In: *Rev. Mod. Phys.* 82 (2 Apr. 2010), pp. 1225–1286. DOI: 10.1103/RevModPhys.82.1225.

[36] Shih-I Chu and Dmitry A Telnov. "Beyond the Floquet theorem: generalized Floquet formalisms and quasienergy methods for atomic and molecular multiphoton processes in intense laser fields". In: *Physics reports* 390.1-2 (2004), pp. 1–131.

[37] Logan W Clark et al. "Collective emission of matter-wave jets from driven Bose–Einstein condensates". In: *Nature* 551.7680 (2017), pp. 356–359.

[38] Govinda Clos et al. "Time-Resolved Observation of Thermalization in an Isolated Quantum System". In: *Phys. Rev. Lett.* 117 (17 Oct. 2016), p. 170401. DOI: 10.1103/PhysRevLett.117.170401.

[39] R. Cominotti et al. "Observation of Massless and Massive Collective Excitations with Faraday Patterns in a Two-Component Superfluid". In: *Phys. Rev. Lett.* 128 (21 May 2022), p. 210401. DOI: 10.1103/PhysRevLett.128.210401.

[40] S. L. Cornish et al. "Stable ^{85}Rb Bose-Einstein Condensates with Widely Tunable Interactions". In: *Phys. Rev. Lett.* 85 (9 Aug. 2000), pp. 1795–1798. DOI: 10.1103/PhysRevLett.85.1795.

[41] M. C. Cross and P. C. Hohenberg. "Pattern formation outside of equilibrium". In: *Rev. Mod. Phys.* 65 (3 July 1993), pp. 851–1112. DOI: 10.1103/RevModPhys.65.851.

[42] Siamak Dadras et al. "Experimental realization of a momentum-space quantum walk". In: *Phys. Rev. A* 99 (4 Apr. 2019), p. 043617. DOI: 10.1103/PhysRevA.99.043617.

[43] Siamak Dadras et al. "Quantum Walk in Momentum Space with a Bose-Einstein Condensate". In: *Phys. Rev. Lett.* 121 (7 Aug. 2018), p. 070402. DOI: 10.1103/PhysRevLett.121.070402.

[44] Andrew J Daley et al. "Practical quantum advantage in quantum simulation". In: *Nature* 607.7920 (2022), pp. 667–676.

[45] Franco Dalfovo et al. "Theory of Bose-Einstein condensation in trapped gases". In: *Rev. Mod. Phys.* 71 (3 Apr. 1999), pp. 463–512. DOI: 10.1103/RevModPhys.71.463.

[46] K. B. Davis et al. "Bose-Einstein Condensation in a Gas of Sodium Atoms". In: *Phys. Rev. Lett.* 75 (22 Nov. 1995), pp. 3969–3973. DOI: 10.1103/PhysRevLett.75.3969.

[47] Yijue Ding, José P. D'Incao, and Chris H. Greene. "Effective control of cold collisions with radio-frequency fields". In: *Phys. Rev. A* 95 (2 Feb. 2017), p. 022709. DOI: 10.1103/PhysRevA.95.022709.

[48] André Eckardt. "Colloquium: Atomic quantum gases in periodically driven optical lattices". In: *Rev. Mod. Phys.* 89 (1 Mar. 2017), p. 011004. DOI: 10.1103/RevModPhys.89.011004.

[49] P. Engels, C. Atherton, and M. A. Hoefer. "Observation of Faraday Waves in a Bose-Einstein Condensate". In: *Phys. Rev. Lett.* 98 (9 Feb. 2007), p. 095301. DOI: 10.1103/PhysRevLett.98.095301.

[50] P. J. Everitt et al. "Observation of a modulational instability in Bose-Einstein condensates". In: *Phys. Rev. A* 96 (4 Oct. 2017), p. 041601. DOI: 10.1103/PhysRevA.96.041601.

[51] Bertrand Evrard et al. "Relaxation and hysteresis near Shapiro resonances in a driven spinor condensate". In: *Phys. Rev. A* 100 (2 Aug. 2019), p. 023604. DOI: 10.1103/PhysRevA.100.023604.

[52] D. F. Walls and Gerard J. Milburn. *Quantum optics*. 2nd ed. Springer, 2008.

[53] Michael Faraday. "XVII. On a peculiar class of acoustical figures; and on certain forms assumed by groups of particles upon vibrating elastic surfaces". In: *Philosophical transactions of the Royal Society of London* 121 (1831), pp. 299–340.

[54] F. K. Fatemi, K. M. Jones, and P. D. Lett. "Observation of Optically Induced Feshbach Resonances in Collisions of Cold Atoms". In: *Phys. Rev. Lett.* 85 (21 Nov. 2000), pp. 4462–4465. DOI: 10.1103/PhysRevLett.85.4462.

[55] P. O. Fedichev and G. V. Shlyapnikov. "Critical velocity in cylindrical Bose-Einstein condensates". In: *Phys. Rev. A* 63 (4 Mar. 2001), p. 045601. DOI: 10.1103/PhysRevA.63.045601.

[56] P. O. Fedichev et al. "Influence of Nearly Resonant Light on the Scattering Length in Low-Temperature Atomic Gases". In: *Phys. Rev. Lett.* 77 (14 Sept. 1996), pp. 2913–2916. DOI: 10.1103/PhysRevLett.77.2913.

[57] Alexander L Fetter. "Nonuniform states of an imperfect Bose gas". In: *Annals of physics* 70.1 (1972), pp. 67–101.

[58] Han Fu et al. "Density Waves and Jet Emission Asymmetry in Bose Fireworks". In: *Phys. Rev. Lett.* 121 (24 Dec. 2018), p. 243001. DOI: 10.1103/PhysRevLett.121.243001.

[59] Han Fu et al. "Jet substructure in fireworks emission from nonuniform and rotating Bose-Einstein condensates". In: *Physical Review Letters* 125.18 (2020), p. 183003.

[60] Keisuke Fujii et al. "Stable-fixed-point description of square-pattern formation in driven two-dimensional Bose-Einstein condensates". In: *Phys. Rev. A* 109 (5 May 2024), p. L051301. DOI: 10.1103/PhysRevA.109.L051301.

[61] Juan J Garcia-Ripoll, Victor M Perez-Garcia, and Pedro Torres. "Extended parametric resonances in nonlinear Schrödinger systems". In: *Physical review letters* 83.9 (1999), p. 1715.

[62] S. Giorgini. “Damping in dilute Bose gases: A mean-field approach”. In: *Phys. Rev. A* 57 (4 Apr. 1998), pp. 2949–2957. doi: 10.1103/PhysRevA.57.2949.

[63] Jerry P Gollub and James S Langer. “Pattern formation in nonequilibrium physics”. In: *Reviews of Modern Physics* 71.2 (1999), S396.

[64] Markus Greiner et al. “Quantum phase transition from a superfluid to a Mott insulator in a gas of ultracold atoms”. In: *nature* 415.6867 (2002), pp. 39–44.

[65] Axel Griesmaier et al. “Bose-Einstein Condensation of Chromium”. In: *Phys. Rev. Lett.* 94 (16 Apr. 2005), p. 160401. doi: 10.1103/PhysRevLett.94.160401.

[66] Allan Griffin. “Conserving and gapless approximations for an inhomogeneous Bose gas at finite temperatures”. In: *Physical Review B* 53.14 (1996), p. 9341.

[67] Milena Grifoni and Peter Hänggi. “Driven quantum tunneling”. In: *Physics Reports* 304.5-6 (1998), pp. 229–354.

[68] Christian Gross and Immanuel Bloch. “Quantum simulations with ultracold atoms in optical lattices”. In: *Science* 357.6355 (2017), pp. 995–1001.

[69] M. Guilleumas and L. P. Pitaevskii. “Landau damping of transverse quadrupole oscillations of an elongated Bose-Einstein condensate”. In: *Phys. Rev. A* 67 (5 May 2003), p. 053607. doi: 10.1103/PhysRevA.67.053607.

[70] D. S. Hall et al. “Dynamics of Component Separation in a Binary Mixture of Bose-Einstein Condensates [Phys. Rev. Lett. 81, 1539 (1998)]”. In: *Phys. Rev. Lett.* 81 (20 Nov. 1998), pp. 4531–4531. doi: 10.1103/PhysRevLett.81.4531.

[71] D. S. Hall et al. “Measurements of Relative Phase in Two-Component Bose-Einstein Condensates”. In: *Phys. Rev. Lett.* 81 (8 Aug. 1998), pp. 1543–1546. doi: 10.1103/PhysRevLett.81.1543.

[72] Thomas M Hanna, Eite Tiesinga, and Paul S Julienne. “Creation and manipulation of Feshbach resonances with radiofrequency radiation”. In: *New Journal of Physics* 12.8 (2010), p. 083031.

[73] Tin-Lun Ho. “Spinor Bose condensates in optical traps”. In: *Physical review letters* 81.4 (1998), p. 742.

[74] T. M. Hoang et al. “Dynamic Stabilization of a Quantum Many-Body Spin System”. In: *Phys. Rev. Lett.* 111 (9 Aug. 2013), p. 090403. doi: 10.1103/PhysRevLett.111.090403.

[75] TM Hoang et al. “Parametric excitation and squeezing in a many-body spinor condensate”. In: *Nature Communications* 7.1 (2016), p. 11233.

[76] E. Hodby et al. “Experimental Observation of Beliaev Coupling in a Bose-Einstein Condensate”. In: *Phys. Rev. Lett.* 86 (11 Mar. 2001), pp. 2196–2199. doi: 10.1103/PhysRevLett.86.2196.

[77] Kerson Huang and C. N. Yang. “Quantum-Mechanical Many-Body Problem with Hard-Sphere Interaction”. In: *Phys. Rev.* 105 (3 Feb. 1957), pp. 767–775. doi: 10.1103/PhysRev.105.767.

[78] SeungJung Huh et al. “Universality class of a spinor Bose–Einstein condensate far from equilibrium”. In: *Nature Physics* 20.3 (2024), pp. 402–408. doi: 10.1038/s41567-023-02339-2.

[79] Yuya Imaeda, Kazuya Fujimoto, and Yuki Kawaguchi. “Spin-wave growth via Shapiro resonances in a spinor Bose-Einstein condensate”. In: *Phys. Rev. Res.* 3 (4 Oct. 2021), p. 043090. doi: 10.1103/PhysRevResearch.3.043090.

[80] Shin Inouye et al. “Observation of Feshbach resonances in a Bose–Einstein condensate”. In: *Nature* 392.6672 (1998), pp. 151–154.

[81] Tomoya Isoshima, Kazushige Machida, and Tetsuo Ohmi. “Quantum vortex in a spinor Bose-Einstein condensate”. In: *Journal of the Physical Society of Japan* 70.6 (2001), pp. 1604–1610.

[82] Bjørn Jamtveit and Paul Meakin. “Growth, dissolution and pattern formation in geosystems”. In: *Growth, Dissolution and Pattern Formation in Geosystems*. Springer, 1999, pp. 1–19.

[83] J.-C. Jaskula et al. “Acoustic Analog to the Dynamical Casimir Effect in a Bose-Einstein Condensate”. In: *Phys. Rev. Lett.* 109 (22 Nov. 2012), p. 220401. doi: 10.1103/PhysRevLett.109.220401.

[84] D. S. Jin et al. “Collective Excitations of a Bose-Einstein Condensate in a Dilute Gas”. In: *Phys. Rev. Lett.* 77 (3 July 1996), pp. 420–423. doi: 10.1103/PhysRevLett.77.420.

[85] Sandra M. Jose, Komal Sah, and Rejish Nath. “Patterns, spin-spin correlations, and competing instabilities in driven quasi-two-dimensional spin-1 Bose-Einstein condensates”. In: *Phys. Rev. A* 108 (2 Aug. 2023), p. 023308. doi: 10.1103/PhysRevA.108.023308.

[86] A. V. Joura, J. K. Freericks, and Th. Pruschke. “Steady-State Nonequilibrium Density of States of Driven Strongly Correlated Lattice Models in Infinite Dimensions”. In: *Phys. Rev. Lett.* 101 (19 Nov. 2008), p. 196401. doi: 10.1103/PhysRevLett.101.196401.

[87] Mehran Kardar. *Statistical physics of particles*. Cambridge University Press, 2007.

[88] Adam M Kaufman et al. "Quantum thermalization through entanglement in an isolated many-body system". In: *Science* 353.6301 (2016), pp. 794–800.

[89] Yuki Kawaguchi and Masahito Ueda. "Spinor bose–einstein condensates". In: *Physics Reports* 520.5 (2012), pp. 253–381.

[90] Wolfgang Ketterle. "Nobel lecture: When atoms behave as waves: Bose-Einstein condensation and the atom laser". In: *Rev. Mod. Phys.* 74 (4 Nov. 2002), pp. 1131–1151. DOI: 10.1103/RevModPhys.74.1131.

[91] Toshiya Kinoshita, Trevor Wenger, and David S Weiss. "A quantum Newton's cradle". In: *Nature* 440.7086 (2006), pp. 900–903.

[92] André-Joseph Koch and Hans Meinhardt. "Biological pattern formation: from basic mechanisms to complex structures". In: *Reviews of modern physics* 66.4 (1994), p. 1481.

[93] Ivana Kovacic, Richard Rand, and Si Mohamed Sah. "Mathieu's equation and its generalizations: overview of stability charts and their features". In: *Applied Mechanics Reviews* 70.2 (2018), p. 020802.

[94] H-J Krug, H Brandstädter, and KH Jacob. "Morphological instabilities in pattern formation by precipitation and crystallization processes". In: *Geologische rundschau* 85.1 (1996), pp. 19–28.

[95] Krishna Kumar and Kapil M. S. Bajaj. "Competing patterns in the Faraday experiment". In: *Phys. Rev. E* 52 (5 Nov. 1995), R4606–R4609. DOI: 10.1103/PhysRevE.52.R4606.

[96] K. Kwon et al. "Spontaneous Formation of Star-Shaped Surface Patterns in a Driven Bose-Einstein Condensate". In: *Phys. Rev. Lett.* 127 (11 Sept. 2021), p. 113001. DOI: 10.1103/PhysRevLett.127.113001.

[97] Kazimierz Łakomy, Rejish Nath, and Luis Santos. "Faraday patterns in coupled one-dimensional dipolar condensates". In: *Physical Review A—Atomic, Molecular, and Optical Physics* 86.2 (2012), p. 023620.

[98] Austen Lamacraft. "Quantum Quenches in a Spinor Condensate". In: *Phys. Rev. Lett.* 98 (16 Apr. 2007), p. 160404. DOI: 10.1103/PhysRevLett.98.160404.

[99] LD Landau and EM Lifshitz. "Mechanics". In: (1976).

[100] Samuel Lellouch and Nathan Goldman. "Parametric instabilities in resonantly-driven Bose–Einstein condensates". In: *Quantum Science and Technology* 3.2 (2018), p. 024011.

[101] Ulf Leonhardt and GE Volovik. "How to create Alice string (half-quantum vortex) in a vector Bose-Einstein condensate". In: *arXiv preprint cond-mat/0003428* (2000).

[102] Hongguang Liang et al. “Spin Faraday waves in periodically modulated spin-orbit-coupled Bose gases”. In: *Physics Letters A* 512 (2024), p. 129592.

[103] Nikolas Liebster et al. “Observation of Pattern Stabilization in a Driven Superfluid”. In: *Phys. Rev. X* 15 (1 Feb. 2025), p. 011026. DOI: 10.1103/PhysRevX.15.011026.

[104] Nikolas Liebster et al. “Supersolid-like sound modes in a driven quantum gas”. In: *Nature Physics* (2025), pp. 1–7.

[105] Xinyun Liu and Xinlong Wang. “Polygonal patterns of Faraday water waves analogous to collective excitations in Bose–Einstein condensates”. In: *Nature Physics* 20.2 (2024), pp. 287–293.

[106] Justin Lovegrove, Magnus O. Borgh, and Janne Ruostekoski. “Stability and internal structure of vortices in spin-1 Bose-Einstein condensates with conserved magnetization”. In: *Phys. Rev. A* 93 (3 Mar. 2016), p. 033633. DOI: 10.1103/PhysRevA.93.033633.

[107] Mingwu Lu et al. “Strongly Dipolar Bose-Einstein Condensate of Dysprosium”. In: *Phys. Rev. Lett.* 107 (19 Oct. 2011), p. 190401. DOI: 10.1103/PhysRevLett.107.190401.

[108] K. W. Madison et al. “Vortex Formation in a Stirred Bose-Einstein Condensate”. In: *Phys. Rev. Lett.* 84 (5 Jan. 2000), pp. 806–809. DOI: 10.1103/PhysRevLett.84.806.

[109] Wilhelm Magnus and Stanley Winkler. *Hill’s Equation*. Interscience Publishers, 1966.

[110] Esteban A Martinez et al. “Real-time dynamics of lattice gauge theories with a few-qubit quantum computer”. In: *Nature* 534.7608 (2016), pp. 516–519.

[111] Paul Meakin and Bjørn Jamtveit. “Geological pattern formation by growth and dissolution in aqueous systems”. In: *Proceedings of the Royal Society A: Mathematical, Physical and Engineering Sciences* 466.2115 (2010), pp. 659–694.

[112] Carolyn Meldgin et al. “Probing the Bose glass–superfluid transition using quantum quenches of disorder”. In: *Nature Physics* 12.7 (2016), pp. 646–649.

[113] M.-O. Mewes et al. “Collective Excitations of a Bose-Einstein Condensate in a Magnetic Trap”. In: *Phys. Rev. Lett.* 77 (6 Aug. 1996), pp. 988–991. DOI: 10.1103/PhysRevLett.77.988.

[114] John Miles and Diane Henderson. “Parametrically forced surface waves”. In: *Annual Review of Fluid Mechanics* 22.1 (1990), pp. 143–165.

[115] Takeshi Mizushima, Naoko Kobayashi, and Kazushige Machida. “Coreless and singular vortex lattices in rotating spinor Bose-Einstein condensates”. In: *Phys. Rev. A* 70 (4 Oct. 2004), p. 043613. DOI: 10.1103/PhysRevA.70.043613.

[116] M Modugno and C Tozzo. "Role of transverse excitations in the instability of Bose-Einstein condensates moving in optical lattices". In: *Physical Review A—Atomic, Molecular, and Optical Physics* 70.4 (2004), p. 043625.

[117] S. A. Morgan et al. "Nonlinear mixing of quasiparticles in an inhomogeneous Bose condensate". In: *Phys. Rev. A* 57 (5 1998), pp. 3818–3829. DOI: 10.1103/PhysRevA.57.3818.

[118] Ole G Mouritsen. "Pattern formation in condensed matter". In: *International Journal of Modern Physics B* 4.13 (1990), pp. 1925–1954.

[119] C. J. Myatt et al. "Production of Two Overlapping Bose-Einstein Condensates by Sympathetic Cooling". In: *Phys. Rev. Lett.* 78 (4 Jan. 1997), pp. 586–589. DOI: 10.1103/PhysRevLett.78.586.

[120] Shreyas Nadiger et al. "Stripe and checkerboard patterns in a stack of driven quasi-one-dimensional dipolar condensates". In: *Phys. Rev. A* 109 (3 Mar. 2024), p. 033309. DOI: 10.1103/PhysRevA.109.033309.

[121] Fumiya Nakamura and Yasuhiro Tada. "Impurity effects in a one-dimensional spin nematic liquid". In: *Phys. Rev. B* 109 (10 Mar. 2024), p. 104404. DOI: 10.1103/PhysRevB.109.104404.

[122] R Nath and L Santos. "Faraday patterns in two-dimensional dipolar Bose-Einstein condensates". In: *Physical Review A—Atomic, Molecular, and Optical Physics* 81.3 (2010), p. 033626.

[123] Nir Navon et al. "Emergence of a turbulent cascade in a quantum gas". In: *Nature* 539.7627 (2016), pp. 72–75.

[124] J. H. V. Nguyen et al. "Parametric Excitation of a Bose-Einstein Condensate: From Faraday Waves to Granulation". In: *Phys. Rev. X* 9 (1 Mar. 2019), p. 011052. DOI: 10.1103/PhysRevX.9.011052.

[125] Jason HV Nguyen et al. "Collisions of matter-wave solitons". In: *Nature Physics* 10.12 (2014), pp. 918–922.

[126] Alexandru I. Nicolin. "Resonant wave formation in Bose-Einstein condensates". In: *Phys. Rev. E* 84 (5 Nov. 2011), p. 056202. DOI: 10.1103/PhysRevE.84.056202.

[127] Alexandru I. Nicolin, R. Carretero-González, and P. G. Kevrekidis. "Faraday waves in Bose-Einstein condensates". In: *Phys. Rev. A* 76 (6 Dec. 2007), p. 063609. DOI: 10.1103/PhysRevA.76.063609.

[128] P. O'Connor, J. Gehlen, and E. J. Heller. "Properties of random superpositions of plane waves". In: *Phys. Rev. Lett.* 58 (13 Mar. 1987), pp. 1296–1299. DOI: 10.1103/PhysRevLett.58.1296.

[129] Tetsuo Ohmi and Kazushige Machida. "Bose-Einstein condensation with internal degrees of freedom in alkali atom gases". In: *Journal of the Physical Society of Japan* 67.6 (1998), pp. 1822–1825.

[130] Takashi Oka and Sota Kitamura. "Floquet engineering of quantum materials". In: *Annual Review of Condensed Matter Physics* 10.1 (2019), pp. 387–408.

[131] A. Orlova et al. "Nuclear Magnetic Resonance Signature of the Spin-Nematic Phase in $LiCuVO_4$ at High Magnetic Fields". In: *Phys. Rev. Lett.* 118 (24 June 2017), p. 247201. DOI: 10.1103/PhysRevLett.118.247201.

[132] R Ozeri et al. "Colloquium: bulk Bogoliubov excitations in a Bose-Einstein condensate". In: *Reviews of Modern Physics* 77.1 (2005), pp. 187–205.

[133] D. J. Papoular, G. V. Shlyapnikov, and J. Dalibard. "Microwave-induced Fano-Feshbach resonances". In: *Phys. Rev. A* 81 (4 Apr. 2010), p. 041603. DOI: 10.1103/PhysRevA.81.041603.

[134] Christopher J Pethick and Henrik Smith. *Bose–Einstein condensation in dilute gases*. Cambridge university press, 2008.

[135] D. S. Petrov, M. Holzmann, and G. V. Shlyapnikov. "Bose-Einstein Condensation in Quasi-2D Trapped Gases". In: *Phys. Rev. Lett.* 84 (12 Mar. 2000), pp. 2551–2555. DOI: 10.1103/PhysRevLett.84.2551.

[136] D. S. Petrov, G. V. Shlyapnikov, and J. T. M. Walraven. "Regimes of Quantum Degeneracy in Trapped 1D Gases". In: *Phys. Rev. Lett.* 85 (18 Oct. 2000), pp. 3745–3749. DOI: 10.1103/PhysRevLett.85.3745.

[137] D. S. Petrov, G. V. Shlyapnikov, and J. T. M. Walraven. "Regimes of Quantum Degeneracy in Trapped 1D Gases". In: *Phys. Rev. Lett.* 85 (18 Oct. 2000), pp. 3745–3749. DOI: 10.1103/PhysRevLett.85.3745.

[138] William D. Phillips. "Nobel Lecture: Laser cooling and trapping of neutral atoms". In: *Rev. Mod. Phys.* 70 (3 July 1998), pp. 721–741. DOI: 10.1103/RevModPhys.70.721.

[139] L. P. Pitaevskii and A. Rosch. "Breathing modes and hidden symmetry of trapped atoms in two dimensions". In: *Phys. Rev. A* 55 (2 1997), R853–R856. DOI: 10.1103/PhysRevA.55.R853.

[140] Lev Pitaevskii and Sandro Stringari. *Bose-Einstein condensation and superfluidity*. Vol. 164. Oxford University Press, 2016.

[141] Anatoli Polkovnikov et al. "Colloquium: Nonequilibrium dynamics of closed interacting quantum systems". In: *Reviews of Modern Physics* 83.3 (2011), pp. 863–883.

[142] SE Pollack et al. “Collective excitation of a Bose-Einstein condensate by modulation of the atomic scattering length”. In: *Physical Review A—Atomic, Molecular, and Optical Physics* 81.5 (2010), p. 053627.

[143] Nick P Proukakis et al. *Quantum gases: finite temperature and non-equilibrium dynamics*. Vol. 1. World Scientific, 2013.

[144] E. R. F. Ramos et al. “Coupling collective modes in a trapped superfluid”. In: *Phys. Rev. A* 85 (3 Mar. 2012), p. 033608. DOI: 10.1103/PhysRevA.85.033608.

[145] A. del Río-Lima et al. “Spatial and temporal periodic density patterns in driven Bose-Einstein condensates”. In: *Phys. Rev. A* 110 (5 Nov. 2024), p. 053318. DOI: 10.1103/PhysRevA.110.053318.

[146] J Rogel-Salazar et al. “Methods of quantum field theory for trapped Bose–Einstein condensates”. In: *Journal of Optics B: Quantum and Semiclassical Optics* 6.9 (June 2004), R33. DOI: 10.1088/1464-4266/6/9/R01.

[147] E. E. Rowen et al. “Energy-dependent damping of excitations over an elongated Bose-Einstein condensate”. In: *Phys. Rev. A* 77 (3 Mar. 2008), p. 033602. DOI: 10.1103/PhysRevA.77.033602.

[148] Subir Sachdev. “Quantum phase transitions”. In: *Physics world* 12.4 (1999), p. 33.

[149] LE Sadler et al. “Spontaneous symmetry breaking in a quenched ferromagnetic spinor Bose–Einstein condensate”. In: *Nature* 443.7109 (2006), pp. 312–315.

[150] Komal Sah. “Faraday Patterns in Spinor Spin-1 Bose-Einstein Condensates”. MA thesis. Indian Institute of Science Education and Research Pune, 2019.

[151] Hiroki Saito and Hiroyuki Hyuga. “Dynamical Casimir effect for magnons in a spinor Bose-Einstein condensate”. In: *Phys. Rev. A* 78 (3 Sept. 2008), p. 033605. DOI: 10.1103/PhysRevA.78.033605.

[152] Hiroki Saito, Yuki Kawaguchi, and Masahito Ueda. “Kibble-Zurek mechanism in a quenched ferromagnetic Bose-Einstein condensate”. In: *Phys. Rev. A* 76 (4 Oct. 2007), p. 043613. DOI: 10.1103/PhysRevA.76.043613.

[153] Alessandro Salandrino. “Plasmonic parametric resonance”. In: *Phys. Rev. B* 97 (8 Feb. 2018), p. 081401. DOI: 10.1103/PhysRevB.97.081401.

[154] C. Samuelis et al. “Cold atomic collisions studied by molecular spectroscopy”. In: *Phys. Rev. A* 63 (1 Dec. 2000), p. 012710. DOI: 10.1103/PhysRevA.63.012710.

[155] Christian Schori et al. “Excitations of a superfluid in a three-dimensional optical lattice”. In: *Physical review letters* 93.24 (2004), p. 240402.

[156] Sang Won Seo et al. "Collisional Dynamics of Half-Quantum Vortices in a Spinor Bose-Einstein Condensate". In: *Phys. Rev. Lett.* 116 (18 May 2016), p. 185301. DOI: 10.1103/PhysRevLett.116.185301.

[157] Sang Won Seo et al. "Half-Quantum Vortices in an Antiferromagnetic Spinor Bose-Einstein Condensate". In: *Phys. Rev. Lett.* 115 (1 July 2015), p. 015301. DOI: 10.1103/PhysRevLett.115.015301.

[158] Ashu Sharma and S. C. Sinha. "An Approximate Analysis of Quasi-Periodic Systems Via Floquét Theory". In: *Journal of Computational and Nonlinear Dynamics* 13.2 (Nov. 2017), p. 021008. ISSN: 1555-1415. DOI: 10.1115/1.4037797.

[159] Zeyun Shi et al. "Faraday pattern formations in temporally driven Rydberg-dressed Bose-Einstein condensates". In: *Physical Review A* 108.6 (2023), p. 063317.

[160] A Sornborger and M Parry. "Pattern formation in the early universe". In: *Physical Review D* 62.8 (2000), p. 083511.

[161] Marius Sparn et al. "Experimental Particle Production in Time-Dependent Spacetimes: A One-Dimensional Scattering Problem". In: *Phys. Rev. Lett.* 133 (26 Dec. 2024), p. 260201. DOI: 10.1103/PhysRevLett.133.260201.

[162] Kestutis Staliunas, Stefano Longhi, and Germán J. de Valcárcel. "Faraday Patterns in Bose-Einstein Condensates". In: *Phys. Rev. Lett.* 89 (21 Nov. 2002), p. 210406. DOI: 10.1103/PhysRevLett.89.210406.

[163] Kestutis Staliunas, Stefano Longhi, and Germán J. de Valcárcel. "Faraday patterns in low-dimensional Bose-Einstein condensates". In: *Phys. Rev. A* 70 (1 July 2004), p. 011601. DOI: 10.1103/PhysRevA.70.011601.

[164] Dan M. Stamper-Kurn and Masahito Ueda. "Spinor Bose gases: Symmetries, magnetism, and quantum dynamics". In: *Rev. Mod. Phys.* 85 (3 July 2013), pp. 1191–1244. DOI: 10.1103/RevModPhys.85.1191.

[165] Oleg A Starykh. "Unusual ordered phases of highly frustrated magnets: a review". In: *Reports on Progress in Physics* 78.5 (2015), p. 052502.

[166] J. Steinhauer et al. "Bragg Spectroscopy of the Multibranch Bogoliubov Spectrum of Elongated Bose-Einstein Condensates". In: *Phys. Rev. Lett.* 90 (6 Feb. 2003), p. 060404. DOI: 10.1103/PhysRevLett.90.060404.

[167] J. Steinhauer et al. "Excitation Spectrum of a Bose-Einstein Condensate". In: *Phys. Rev. Lett.* 88 (12 Mar. 2002), p. 120407. DOI: 10.1103/PhysRevLett.88.120407.

[168] J Stenger et al. "Spin domains in ground-state Bose–Einstein condensates". In: *Nature* 396.6709 (1998), pp. 345–348.

[169] S. Stringari. "Collective Excitations of a Trapped Bose-Condensed Gas". In: *Phys. Rev. Lett.* 77 (12 Sept. 1996), pp. 2360–2363. DOI: 10.1103/PhysRevLett.77.2360.

[170] Julian Struck et al. "Quantum simulation of frustrated classical magnetism in triangular optical lattices". In: *Science* 333.6045 (2011), pp. 996–999.

[171] L. M. Symes and P. B. Blakie. "Nematic ordering dynamics of an antiferromagnetic spin-1 condensate". In: *Phys. Rev. A* 96 (1 July 2017), p. 013602. DOI: 10.1103/PhysRevA.96.013602.

[172] L. M. Symes, R. I. McLachlan, and P. B. Blakie. "Efficient and accurate methods for solving the time-dependent spin-1 Gross-Pitaevskii equation". In: *Phys. Rev. E* 93 (5 May 2016), p. 053309. DOI: 10.1103/PhysRevE.93.053309.

[173] Hiromitsu Takeuchi. "Quantum Elliptic Vortex in a Nematic-Spin Bose-Einstein Condensate". In: *Phys. Rev. Lett.* 126 (19 May 2021), p. 195302. DOI: 10.1103/PhysRevLett.126.195302.

[174] G. Thalhammer et al. "Long-Lived Feshbach Molecules in a Three-Dimensional Optical Lattice". In: *Phys. Rev. Lett.* 96 (5 Feb. 2006), p. 050402. DOI: 10.1103/PhysRevLett.96.050402.

[175] M. Theis et al. "Tuning the Scattering Length with an Optically Induced Feshbach Resonance". In: *Phys. Rev. Lett.* 93 (12 Sept. 2004), p. 123001. DOI: 10.1103/PhysRevLett.93.123001.

[176] C Tozzo and F Dalfovo. "Bogoliubov spectrum and Bragg spectroscopy of elongated Bose-Einstein condensates". In: *New Journal of Physics* 5.1 (2003), p. 54. DOI: 10.1088/1367-2630/5/1/354.

[177] T. V. Tscherbul et al. "rf-field-induced Feshbach resonances". In: *Phys. Rev. A* 81 (5 May 2010), p. 050701. DOI: 10.1103/PhysRevA.81.050701.

[178] Naoto Tsuji, Takashi Oka, and Hideo Aoki. "Nonequilibrium Steady State of Photoexcited Correlated Electrons in the Presence of Dissipation". In: *Phys. Rev. Lett.* 103 (4 July 2009), p. 047403. DOI: 10.1103/PhysRevLett.103.047403.

[179] Masahito Ueda. "Quantum equilibration, thermalization and prethermalization in ultracold atoms". In: *Nature Reviews Physics* 2.12 (2020), pp. 669–681.

[180] Michael Uhlmann. "Quantum fluctuations in trapped time-dependent Bose-Einstein condensates". In: *Phys. Rev. A* 79 (3 Mar. 2009), p. 033601. DOI: 10.1103/PhysRevA.79.033601.

[181] Andrew P. C. Underwood et al. "Properties of a nematic spin vortex in an antiferromagnetic spin-1 Bose-Einstein condensate". In: *Phys. Rev. A* 102 (2 Aug. 2020), p. 023326. DOI: 10.1103/PhysRevA.102.023326.

[182] Gunjan Verma, Umakant D. Rapol, and Rejish Nath. "Generation of dark solitons and their instability dynamics in two-dimensional condensates". In: *Phys. Rev. A* 95 (4 Apr. 2017), p. 043618. DOI: 10.1103/PhysRevA.95.043618.

[183] Ivana Vidanović et al. "Nonlinear Bose-Einstein-condensate dynamics induced by a harmonic modulation of the s-wave scattering length". In: *Physical Review A—Atomic, Molecular, and Optical Physics* 84.1 (2011), p. 013618.

[184] Ivana Vidanović et al. "Parametric and geometric resonances of collective oscillation modes in Bose–Einstein condensates". In: *Physica Scripta* 2012.T149 (2012), p. 014003.

[185] A. Vinit and C. Raman. "Precise measurements on a quantum phase transition in antiferromagnetic spinor Bose-Einstein condensates". In: *Phys. Rev. A* 95 (1 Jan. 2017), p. 011603. DOI: 10.1103/PhysRevA.95.011603.

[186] A. Vinit et al. "Antiferromagnetic Spatial Ordering in a Quenched One-Dimensional Spinor Gas". In: *Phys. Rev. Lett.* 110 (16 Apr. 2013), p. 165301. DOI: 10.1103/PhysRevLett.110.165301.

[187] Meiling Wang et al. *Parametric excitations in a harmonically trapped binary Bose-Einstein condensate*. 2025. arXiv: 2505.17409 [quant-ph].

[188] Micheal J. Ward. *Basic Floquet Theory*.

[189] Christof Weitenberg and Juliette Simonet. "Tailoring quantum gases by Floquet engineering". In: *Nature Physics* 17.12 (2021), pp. 1342–1348.

[190] Carl E. Wieman, David E. Pritchard, and David J. Wineland. "Atom cooling, trapping, and quantum manipulation". In: *Rev. Mod. Phys.* 71 (2 Mar. 1999), S253–S262. DOI: 10.1103/RevModPhys.71.S253.

[191] Lewis A. Williamson and P. B. Blakie. "Universal Coarsening Dynamics of a Quenched Ferromagnetic Spin-1 Condensate". In: *Phys. Rev. Lett.* 116 (2 Jan. 2016), p. 025301. DOI: 10.1103/PhysRevLett.116.025301.

[192] K. Wintersperger et al. "Parametric Instabilities of Interacting Bosons in Periodically Driven 1D Optical Lattices". In: *Phys. Rev. X* 10 (1 Feb. 2020), p. 011030. DOI: 10.1103/PhysRevX.10.011030.

[193] Waltraut Wustmann and Vitaly Shumeiko. "Parametric resonance in tunable superconducting cavities". In: *Phys. Rev. B* 87 (18 May 2013), p. 184501. DOI: 10.1103/PhysRevB.87.184501.

[194] Peng Xu and Wenxian Zhang. "Generalized parametric resonance in a spin-1 Bose-Einstein condensate". In: *Phys. Rev. A* 104 (2 Aug. 2021), p. 023324. DOI: 10.1103/PhysRevA.104.023324.

[195] Xiaoquan Yu and P. B. Blakie. "Absence of the breakdown of ferrodark solitons exhibiting a snake instability". In: *Phys. Rev. A* 110 (6 Dec. 2024), p. L061303. DOI: 10.1103/PhysRevA.110.L061303.

[196] Michael P. Zaletel et al. "Colloquium: Quantum and classical discrete time crystals". In: *Rev. Mod. Phys.* 95 (3 July 2023), p. 031001. DOI: 10.1103/RevModPhys.95.031001.

[197] E. Zaremba. "Sound propagation in a cylindrical Bose-condensed gas". In: *Phys. Rev. A* 57 (1 Jan. 1998), pp. 518–521. DOI: 10.1103/PhysRevA.57.518.

[198] Huan Zhang, Sheng Liu, and Yong-Sheng Zhang. "Faraday patterns in spin-orbit-coupled Bose-Einstein condensates". In: *Physical Review A* 105.6 (2022), p. 063319.

[199] Peng Zhang, Pascal Naidon, and Masahito Ueda. "Independent Control of Scattering Lengths in Multicomponent Quantum Gases". In: *Phys. Rev. Lett.* 103 (13 Sept. 2009), p. 133202. DOI: 10.1103/PhysRevLett.103.133202.

[200] Pengfei Zhang and Yingfei Gu. "Periodically and quasi-periodically driven dynamics of Bose-Einstein condensates". In: *SciPost Physics* 9.5 (2020), p. 079.

[201] Zhendong Zhang et al. "Pattern formation in a driven Bose–Einstein condensate". In: *Nature Physics* 16.6 (2020), pp. 652–656.

[202] Chen-Xi Zhu et al. "Parametric resonance of a Bose-Einstein condensate in a ring trap with periodically driven interactions". In: *Phys. Rev. A* 99 (2 Feb. 2019), p. 023619. DOI: 10.1103/PhysRevA.99.023619.

[203] T. Zibold et al. "Spin-nematic order in antiferromagnetic spinor condensates". In: *Phys. Rev. A* 93 (2 Feb. 2016), p. 023614. DOI: 10.1103/PhysRevA.93.023614.